DEVELOPMENT OF A RECOIL DETECTOR AND THE STUDY OF EXOTIC ASYMMETRIC SHAPES IN NUCLEI

Sifiso Senzo Ntshangase

Thesis presented in fulfillment of the requirements for the degree of Doctor of Philosophy at the University of Cape Town

Supervisor: Prof. D.G. Aschman

Dept. of Physics

University of Cape Town

Co-supervisor: Dr. R.A. Bark

Dept. of Nuclear Physics

iThemba LABS

October 2011

DECLARATION

I, the undersigned, hereby declare that the work contained in this thesis is my own original work and that I have not previously in its entirety or in part submitted it at any university for a degree.

Signature: ……

Date: ……

ABSTRACT

A number of interesting physics phenomena have been predicted to occur in the actinide region. These can be studied by measuring fusion-evaporation residues produced in a heavy-ion fusion reaction. However reactions leading to this region are characterized by very low cross-sections and fission is a dominant channel. At iThemba LABS, a recoil detector which separates the fusion-evaporation residues from the fission background using the time-of-flight measurement has been developed. The recoil detector has been used to investigate the predicted phenomena such as hyperdeformation and tetrahedral shapes in the actinide region, and superdeformation in the mass 190 region. Both the hyperdeformation and tetrahedral shapes were investigated in the uranium isotopes ^{230}U and ^{232}U using the reaction ^{232}Th(α, xn) at 61 MeV and 42 MeV beam energy respectively. The superdeformation was investigated in ^{196}Po using the reaction ^{180}W(^{20}Ne, xn) at 110 MeV. The tetrahedral phenomenon was successfully tested, however no conclusion was drawn on hyperdeformation due to low data statistics. A comprehensive set of in-band E2 transitions were observed in the lowest lying negative-parity band of ^{232}U while two new E2 transitions were observed for ^{230}U. These allowed $B(E1;I^- \rightarrow I^+ - 1)/B(E2;I^- \rightarrow I^- - 2)$ ratios to be extracted and compared with systematics in the actinide region. The values are similar to those of their Th and Ra isotones. Therefore these results contradict the tetrahedral prediction in the actinide region.

ACKNOWLEDGEMENTS

I wish to express my sincere gratitude to the following people for making the realization of this thesis possible -bakwethu ngaphandle kwenu lomsebenzi ongaka ubungeke ube yimpumelelo:

- Dr. R.A. Bark, my supervisor, for his willingness to guide, support, motivate, and for being very patient with me. It has been a great pleasure to work with you and you have been the best supervisor I could ever ask for. Your experience, wisdom and professionalism are quite remarkable;
- Prof. D.G. Aschman, my university supervisor, for the guidance and support throughout the duration of the project;
- Prof. R.M. Lieder for motivating me, sharing knowledge and for reading this thesis and give very constructive criticisms;
- Prof. J.F. Sharpey-Schaffer for his willingness to share knowledge and the reading of this thesis and give constructive comments;
- Dr. A. Wilson for allowing me to use her ^{196}Po data and borrowing us her ^{180}W target which was unfortunately destroyed by the ESKOM power failure before we used it;
- Mrs. N.Y. Kheswa for making sure that we had the target and carbon foils;
- The director of iThemba LABS (Dr. Z.Z. Vilakazi) and members of its Program Advisory Committee (PAC) for allocating beam time to this project for several occasions;

- The ion source division (Dr. R. Thomae and Mr. S.S. Ntshangase) and the cyclotron operators for making sure that sufficient quality beam is delivered on target;
- My superiors in the accelerator and engineering department, Dr. J.L. Conradie, Dr. R. Thomae and Mr. D.T. Fourie for understanding when I was busy with the data analysis and writing of this thesis;
- The Pebble Bed Modular Reactor (Pty) Limited (PBMR), South African Nuclear Human Asset and Research Programme (SANHARP), University of Cape Town, Harry Crossley Foundation, Canon Collins Education Trust and Joseph Stone Postgraduate Bursary for funding this project;
- Mr. S Murray for assisting me whenever I had a computer related problem;
- All AFRODITE members, postgraduates students and collaborators who assisted during many weekends of data acquisition and to those who further gave inputs in data analysis and writing;
- Dr. J. G. de Villiers for calculating the magnetic field for the recoil detector;
- Last but not least, the acknowledgements would be incomplete without thanking my family. My parents for loving support, patience and understanding throughout the long duration of this project. My sincere thanks also go to my precious stones- the black diamonds- my kids: Philasande, Zwelezimangaliso and Fanelesibonge for accepting to live without their father over the duration of this project.

This work is dedicated to my parents Mr. Govu James and Mrs Qedizaba Dinah Ntshangase. Bodabezitha ningixolele ngokungabikho ekhaya ekubeni impilo intekenteke ngakubaba. Yiwo lo mshikashika womsebenzi ubungibambile kodwa-ke ngiyibekile induku ebandla, namaBiyela asayokungixolela-AYIDLE IZIBEKELE.

CONTENTS

LIST OF FIGURES

LIST OF TABLES

CHAPTER 1 NUCLEAR PROPERTIES

1.1 Superdeformed, hyperdeformed and tetrahedral shapes

The study of nuclei with exotic shapes is one of the most important fields in modern nuclear structure physics. Superdeformed (SD) nuclei have strongly deformed axially symmetric shapes with a major to minor axis ratio of about 2:1 [Gal93]. On the other hand, hyperdeformed (HD) nuclei correspond to even more elongated shapes with an axis ratio of about 3:1 [Met80, LaF95, LaF96, Thi02]. The SD and HD shapes are shown in Figure 1:1(a) and Figure 1:1(b), respectively. Recently, predictions that nuclei may have tetrahedral shapes have attracted interest [Dud07].

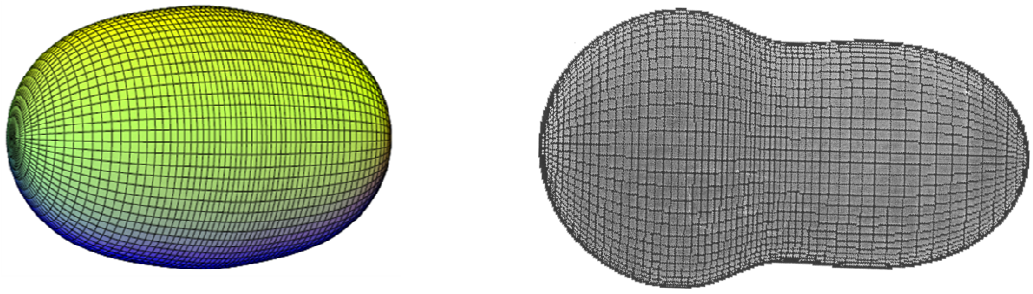

(a) (b)

Figure 1:1. Diagram depicting the shape of (a) superdeformed [Sav96] and (b) hyperdeformed nuclei.

The tetrahedral shape is supposedly rare in atomic nuclei and can be described as a pyramid like structure with rounded edges, as depicted in Figure 1:2. This work concerns itself with an exploration for hyperdeformed and tetrahedral shapes in Uranium nuclei. The theoretical and experimental basis for such shapes will be reviewed in this section.

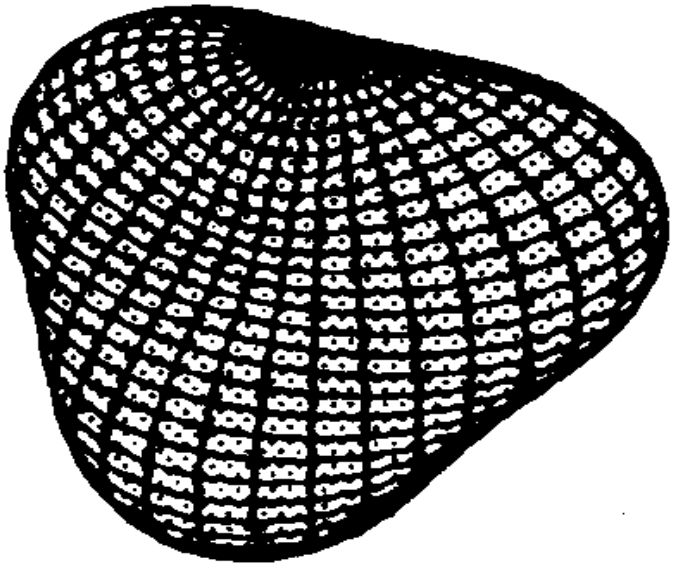

Figure 1:2. Diagram depicted the tetrahedral nuclear shape [Dud02].

1.2 Nuclear deformation

In the absence of universally applicable theories of nuclear structure, attempts have been made to describe nuclear experimental data in terms of various models. Each model is based on a set of simplifying assumptions. A good model can be described as one that can provide a full interpretation of experimental data and predict the possible additional properties of nuclei that can be confirmed experimentally. However each model is usually capable of describing some of the properties of nuclei in certain mass regions or certain shapes. The collective model which best describes nuclear properties, combines the features of the liquid drop model and the spherical or deformed shell model. The present work is based on the study of deformed nuclei which can be described by the deformed collective model.

The nuclear shape can be parameterized in terms of a spherical harmonic or multipole expansion. The nuclear surface is defined by a radius vector R pointing from the origin to the surface. Different shapes of nuclei are mathematically given by an expansion in spherical harmonics $Y(\theta,\phi)$

$$R = R(\theta,\phi) = R_0\left[1+\sum_{\lambda=0}^{\infty}\sum_{\mu=-\lambda}^{\lambda}\alpha_{\lambda\mu}Y_0(\theta,\phi)\right] \qquad (1:1)$$

where R_0 is the radius of a spherical nucleus having the same volume as the deformed ones. The spherical harmonics $Y(\theta,\phi)$ and the coefficients, $\alpha_{\lambda\mu}$ describe the changes of the nuclear shape with their amplitudes multipole order (λ) defining the deformation type. Different $\alpha_{\lambda\mu}$ correspond to different types deformations and the shapes associated with respectively different $\alpha_{\lambda\mu}$ are shown in Figure 1:3.

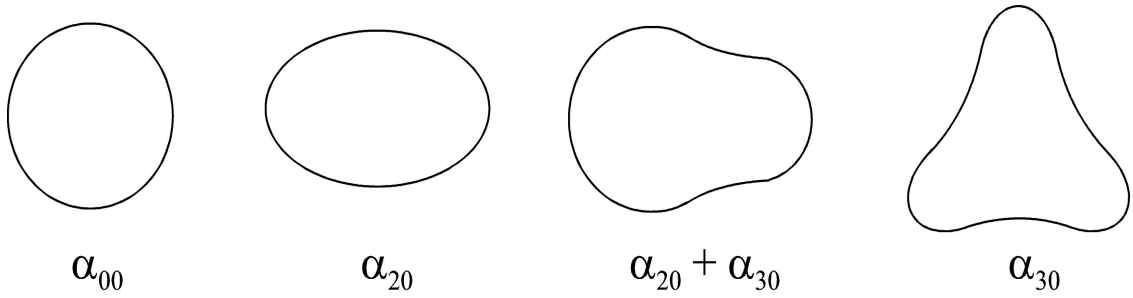

Figure 1:3. The shapes corresponding to the multipole deformations.

In a tetrahedral deformed nucleus, the deformation is characterized by a triaxial octupole deformation α_{32}, together with a near zero quadrupole deformation α_{20}. For the axially symmetric nucleus with quadrupole deformation, the five coefficients namely $\alpha_{2m}:\alpha_{21},\alpha_{22},\alpha_{20},\alpha_{2-1},\alpha_{2-2}$ reduce to only two (α_{20} and $\alpha_{22}=\alpha_{2-2}$). The other $(\alpha_{21}=\alpha_{2-1})$ terms vanish due to symmetry. The coefficients, α_{20} and α_{22} are related to the β_2 and γ deformation parameters as:

$$\alpha_{20}=\beta_2\cos\gamma \tag{1:2}$$

and

$$\alpha_{22}=\frac{1}{\sqrt{2}}\beta_2\sin\gamma \tag{1:3}$$

The deformation parameters β_2 and γ define the size of the quadrupole deformation and deviation from an axially symmetric shape, respectively.

The origin of nuclear deformation can be understood using the two-dimensional harmonic oscillator potential. The resulting single particle energies as a function of quadrupole deformations ($\varepsilon_2\approx\beta_2$) are shown in Figure 1:4. The large shell gaps that

are observed for particular nucleon numbers and nuclear deformation (ε_2) are associated with extra stability and predict "magic numbers" for specific shapes, namely, highly-, super- and hyper-deformed shapes [Wad02]. The corresponding axis ratios and deformation are, the 3:2, 2:1 and 3:1 ratios with $\varepsilon_2 = 0.4, 0.6$ and 0.85, respectively. Beside the predictions of the above mentioned nuclear shapes deformations, recently also the existence of tetrahedral shaped nuclei has been predicted. The tetrahedral shell gaps can be seen in more realistic potentials.

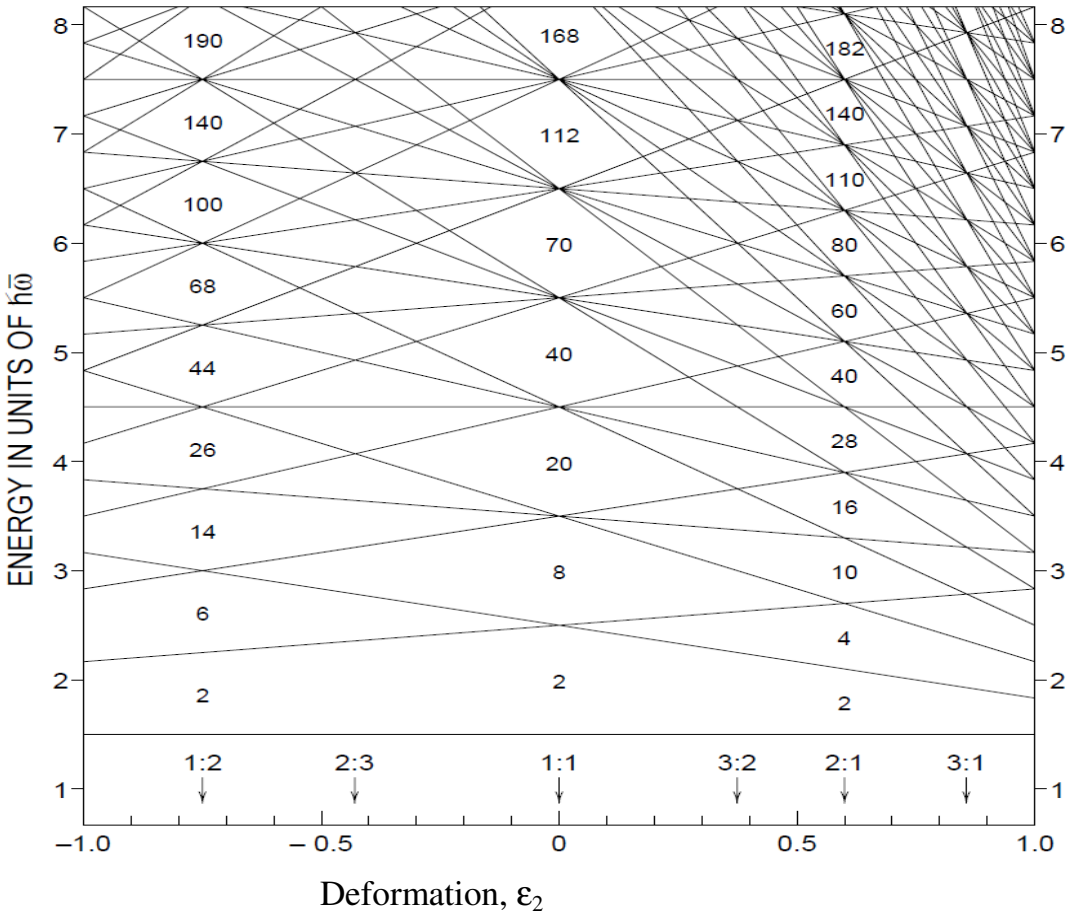

Figure 1:4. The two-dimensional harmonic oscillator energy levels as a function of the deformation parameter, ε_2. The large shell gaps for both prolate $(\varepsilon_2 > 0)$ and oblate $(\varepsilon_2 < 0)$ shapes are marked with numbers. The arrows on the bottom of the figure indicate the deformations of spherical (1:1), highly deformed (3:2), superdeformed (2:1) and hyperderformation (3:1) nuclear shapes, taken from [Boh75,Wad02].

The simple harmonic oscillator is not a realistic potential. It must be modified to better mimic the nuclear potential by adding a spin-orbit term in order to produce the spherical magic numbers (20, 28, 50, 82, etc) which are known to lead to stable nuclei (see Figure 1:5). In certain cases, an orbit is lowered into the next lower major shell by the l^2 and $l \cdot s$ terms. The distortion of the potential affects the single particle energies of the constituent protons and neutrons.

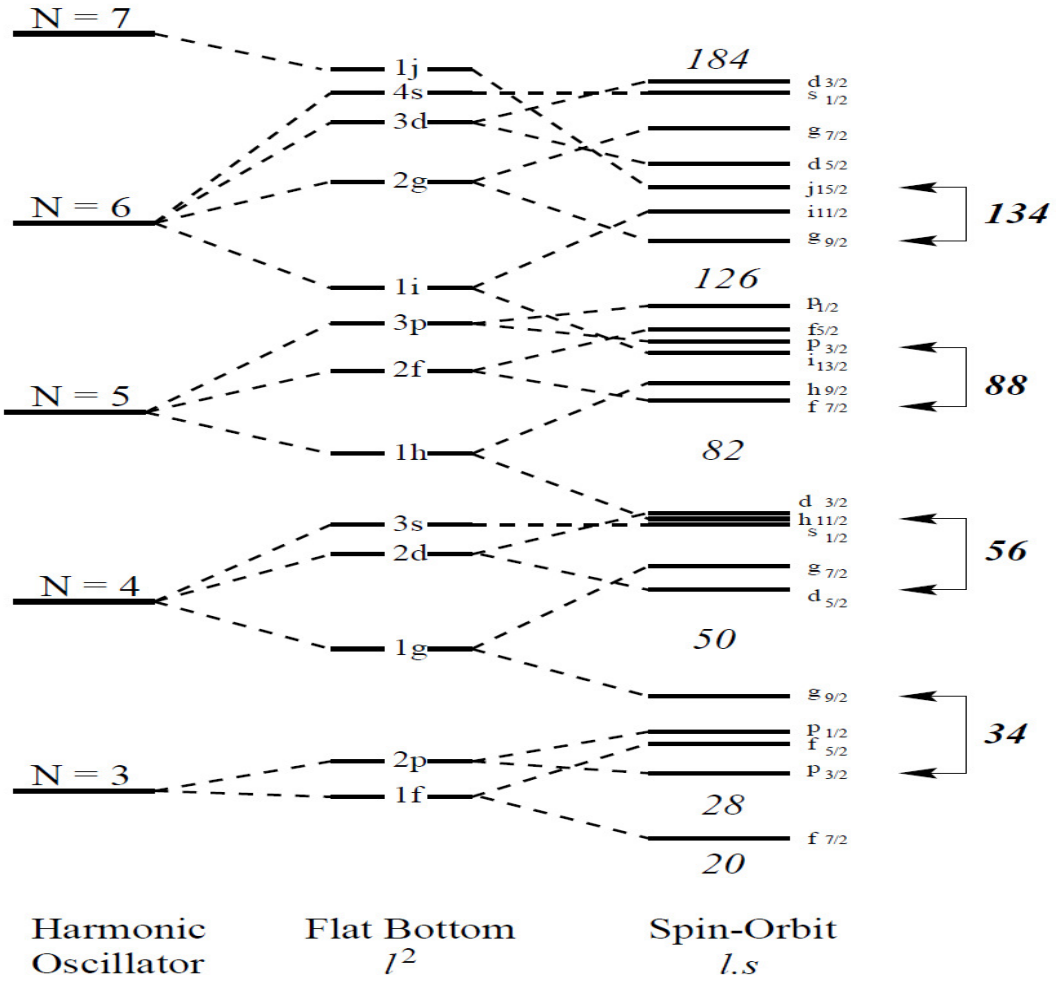

Figure 1:5. Ordering and splitting of energy levels due to the l^2 and $l \cdot s$ terms added to the harmonic oscillator potential. The most important $\Delta l = \Delta j = 3$ couplings are indicated [Nil95].

1.2.1 Favored regions for tetrahedral nuclear shapes

Tetrahedral nuclear shapes are predicted to be particularly stable around tetrahedral shell closures. They can be found for proton and neutron numbers corresponding to the tetrahedral shell gaps. In Figure 1:6 and Figure 1:7, Nilsson model states are shown as a function of the deformation parameter α_{32} for both proton and neutron states, respectively. At proton numbers 70 and 90, gaps corresponding to a tetrahedral deformation with $\alpha_{32} = 0.26$ are observed. These calculations have been carried out for the actinide region but can also describe other mass regions. The calculated shell gaps are similar for protons and neutrons. The gaps at $Z = 70$ and $N = 90$ correspond to the nucleus ^{160}Yb, and it is therefore expected to be another favorable region for tetrahedral shapes.

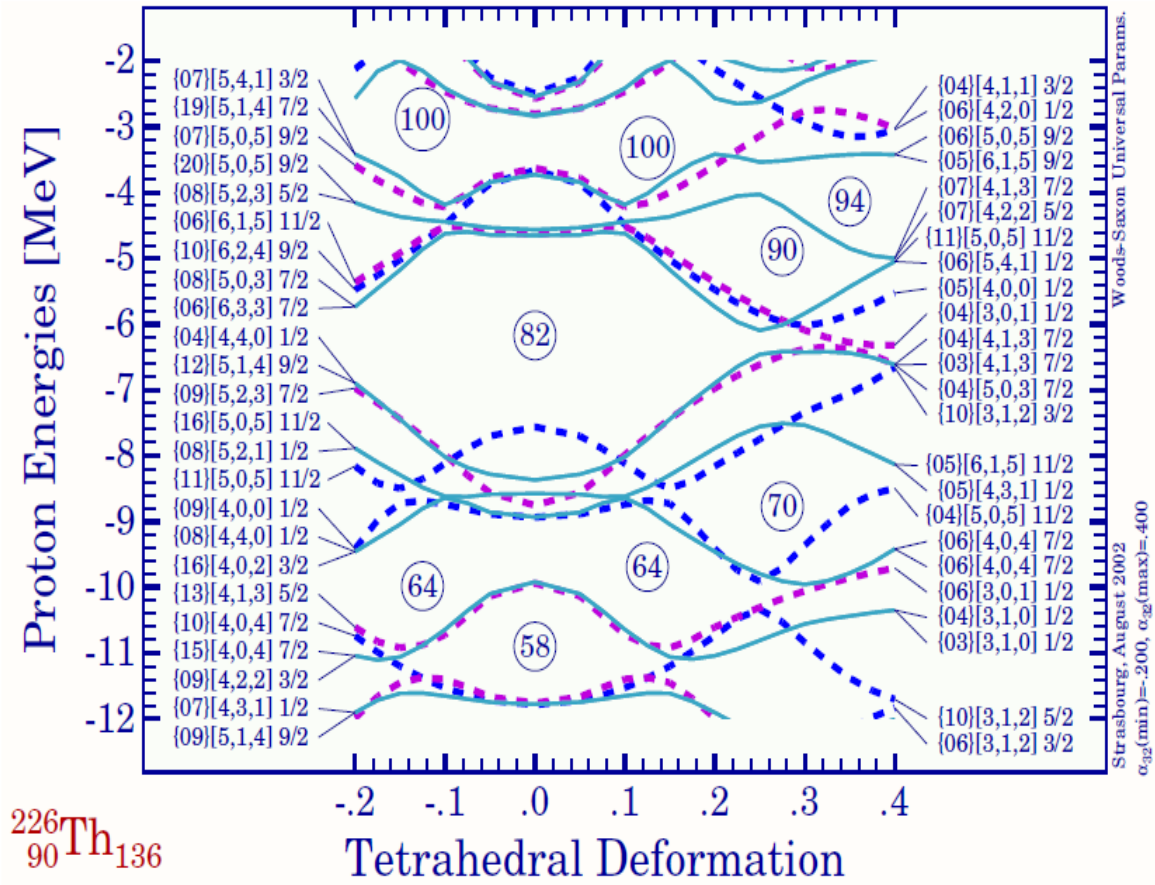

Figure 1:6. Woods-Saxon calculation of single particle proton energies as a function of the tetrahedral deformation parameter, α_{32} [Dud02].

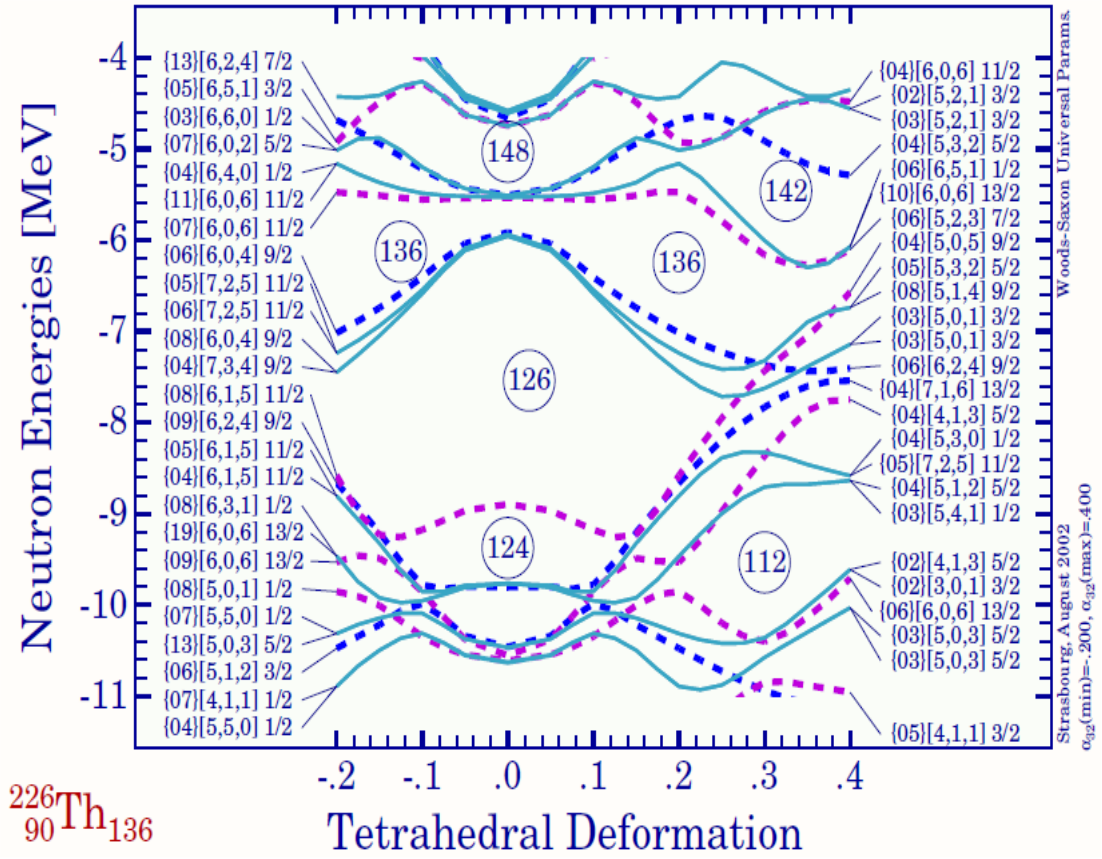

Figure 1:7. Woods-Saxon calculation of single particle neutron energies as a function of the tetrahedral deformation parameter, α_{32} [Dud02].

The calculations show that tetrahedral nuclear shapes, located near the closed shells for tetrahedral nuclei with $(Z,N) = 32, 49, 56, 64, 70, 90, 136$, correspond to nuclei in the Ge, Zr, Ba, Gd, Yb and Th region, respectively [Dud08]. Figure 1:8 shows the regions in the nuclei chart where the possible existence of tetrahedral nucleus has been predicted. The existence of tetrahedral nuclei in the rare earth region and in the actinide region has not been confirmed experimentally as yet [Bar10, Jen10].

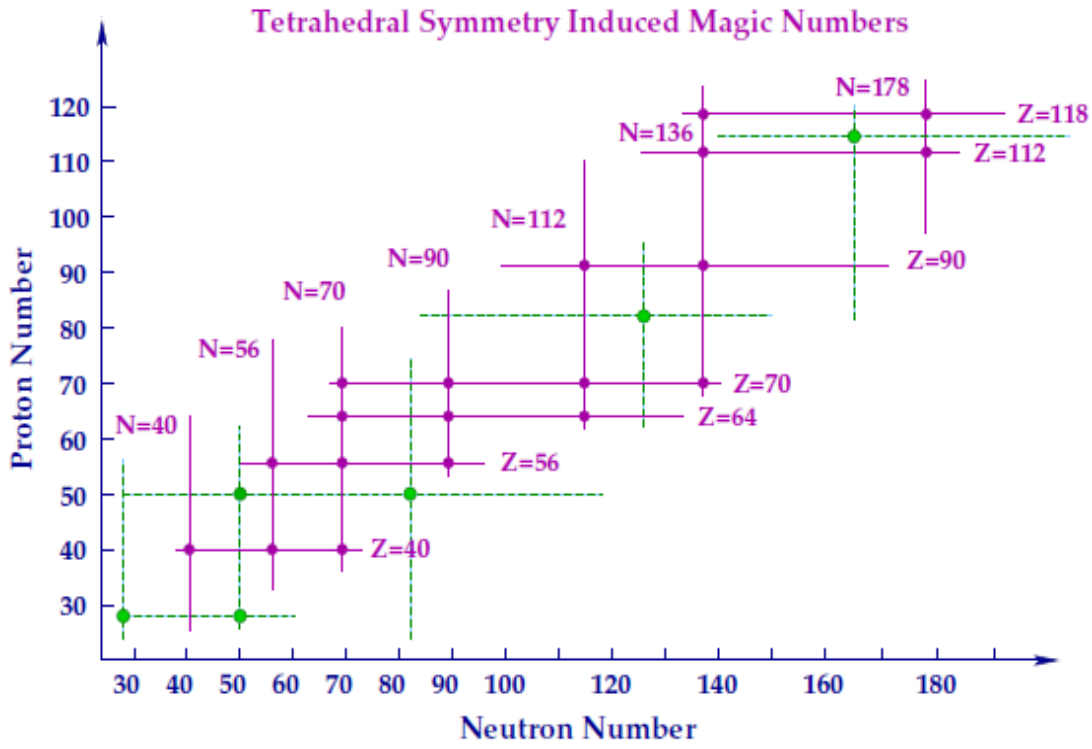

Figure 1:8. Chart of the nuclei showing the predicted regions of tetrahedral shape [Dud08]. The purple lines indicate the tetrahedral shell closures and the green lines indicate the spherical shell closures.

1.2.2 Potential energy surfaces of nuclei in the actinide region

Calculations of the potential energy surfaces performed using the macroscopic-microscopic method with the universal Woods-Saxon potential parametrization [Dud06] are shown in Figure 1:9 and Figure 1:10. Clearly, well-defined tetrahedral minima corresponding to $\alpha_{32} \approx 0.15$ and a vanishing quadrupole deformation ($\alpha_{20} = 0$) deserve attention. These minima are separated from the ground-state minima with a barrier of the order of 1 MeV. Furthermore, Figure 1:9 and Figure 1:10 show that in the calculated nuclear potential, shape coexistence between prolate $\alpha_{20} \approx 0.2$ and tetrahedral $\alpha_{20} = 0$ minima may exist.

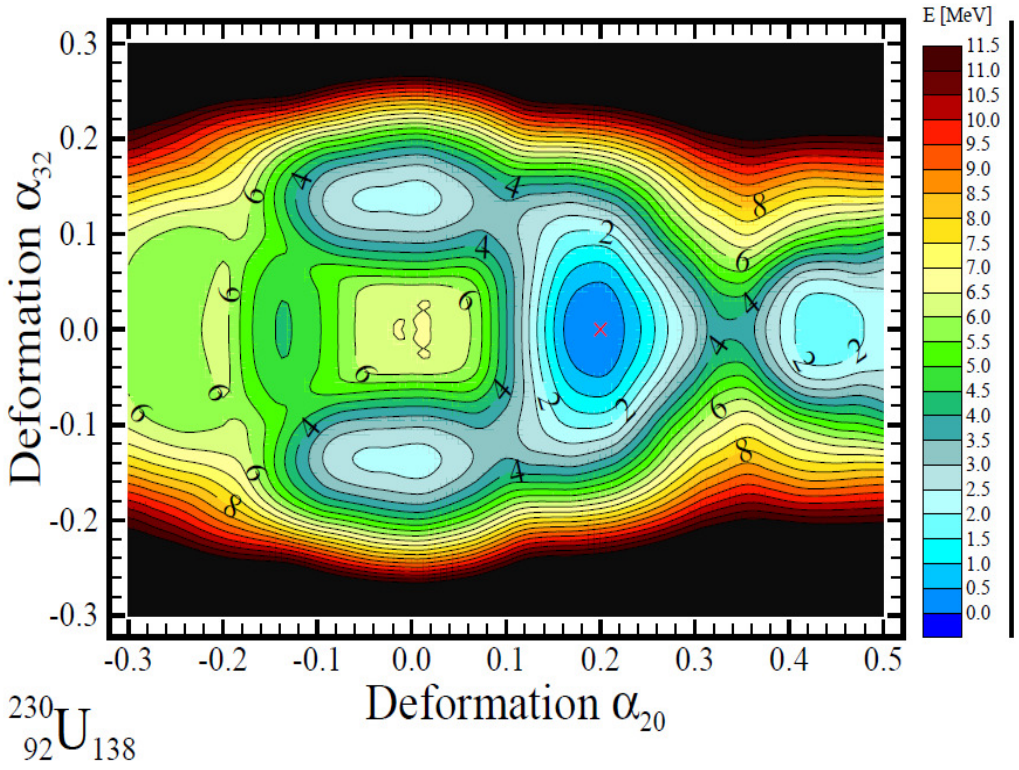

Figure 1:9. Potential energy surface of ^{230}U showing tetrahedral minima [Dud08].

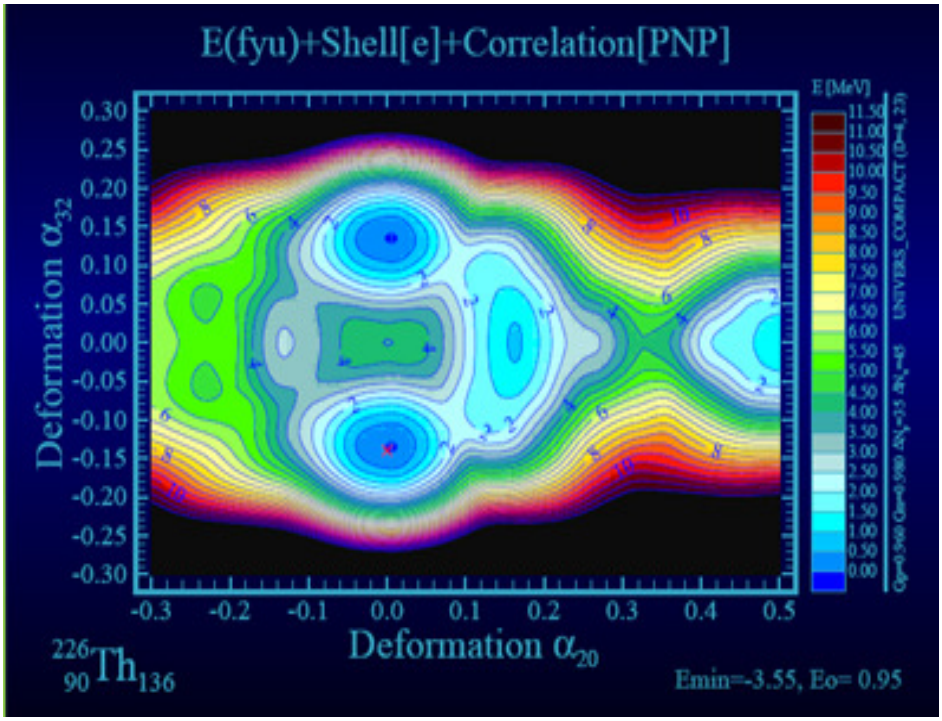

Figure 1:10. Potential energy surface of the doubly magic nucleus ^{226}Th showing minima of tetrahedral shape [Dud08].

1.2.3 The hyperdeformed minima in the actinide region

Potential energy surface calculations predict that the HD minima in the actinide region correspond to reflection asymmetric shapes with an octupole (pear-like) shape as discussed in section 1.1. Surfaces for U and Th nuclei calculated by [Ćwi94, Pas71, Möl73, Berg89, Ben87, Rut94] predict deep HD minima at a quadrupole deformation $\beta_2 = 0.9$, see Figure 1:11. In this figure the shadowed region represent the excitation energy above the first barrier and below the second barrier, where HD transmission resonances have been observed.

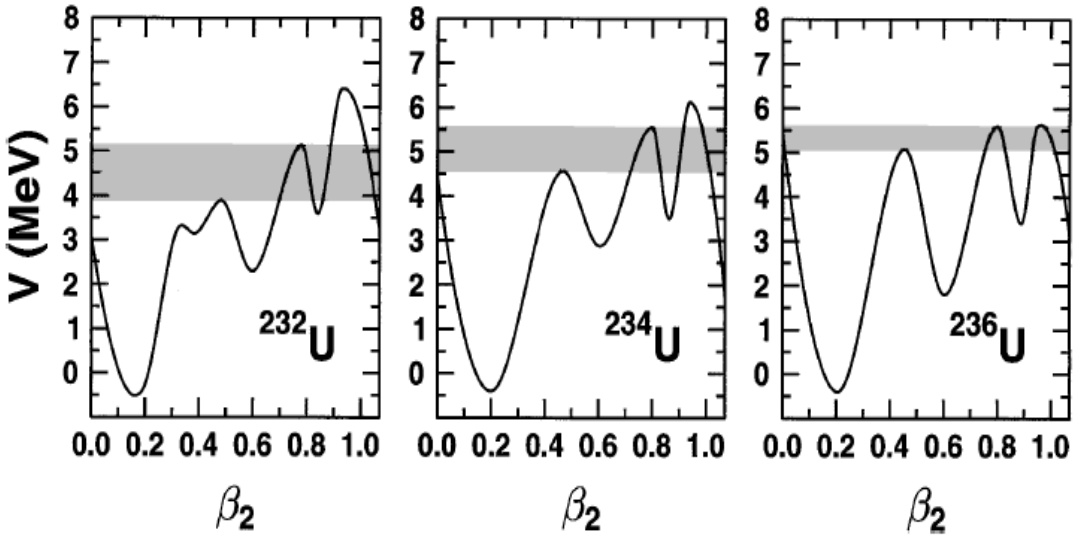

Figure 1:11. Potential energy as a function of quadrupole deformation parameter (β_2) for U isotopes. The energy excitation for studying the hyperdeformed state is marked by horizontally shadowed region and hyperdeformed transition resonances have been observed in the shadowed region [Csi09, Ćwi94].

1.2.4 Shape coexistence

When two or more competing minima exist in the nuclear potential energy surface, corresponding to different shapes of the nuclear mean field, the nucleus can exhibit shape coexistence, as shown in Figure 1:9, Figure 1:10 and Figure 1:11 with excited states located in the respective minima [Woo92]. Such effects often occur in nuclei with near magic numbers of protons and neutrons. In this regime, a spherical configuration competes with a deformed shape corresponding to particle-hole excitations across the shells gaps. Good examples of shape coexistence can be found

in the even-even Hg isotopes where there is coexistence between the weakly deformed oblate ground state, and a more deformed prolate excited state [Lan95]. Some heavy nuclei like Pb exhibit a spherical-prolate-oblate shape coexistence [Lan95, Hee93].

1.3 Energy levels, spin and parity in nuclei

Nuclei exist in different levels corresponding to different arrangements of the nucleons in their allowed states. At low excitation, these levels occur at discrete energies, and each nucleus has its own properties, depending on its internal structure. Each excited state is characterized by quantum numbers that describe it, angular momentum and parity. Figure 1:12 shows a partial sequence of excited states found in the ^{12}C nucleus [Azj90].

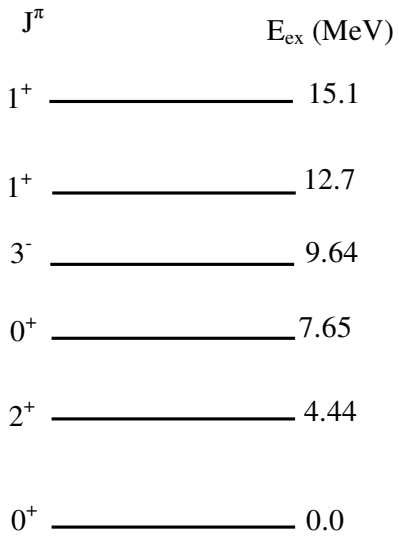

Figure 1:12. Energy levels diagram of some of the excited states of ^{12}C nucleus [Azj90]. The angular momentum (J) and parity (π) of the states are indicated in the left using the notation J^π and excitation energies E_{ex} in the right.

The angular momentum is usually denoted by J and is either an integer or half-integer. The measure of the total angular momentum of a state is in units of $\hbar$. A state has a positive parity if its wave function has the same sign when the spatial coordinates are reversed and a negative-parity if the wave function changes sign under this operation. Figure 1:12 shows these quantum numbers for each excited state in the notation J^π. They determine how an excited state will decay into another state in the

same nucleus via γ–ray decay connecting two states or into a specific state in a different nucleus via beta or alpha decay. Finally, the location of the levels with their spins and parities can be used to provide information about nuclear properties of the nucleus in question, e.g. deformation.

It is not only the energies of the excited minima of exotic shapes, but also their level structure that give important finger prints of their presence. Deformation implies the possibility of rotation. Before the discussion of the rotational structure of exotic shapes, the expected level structure due to the simpler, axially symmetric rotation will be reviewed.

1.4 Nuclear rotations

The most common nuclear shapes are quadrupole shapes. A positive quadrupole moment means that the nuclear shape is prolate, with its polar radius (in z-direction) longer than its equatorial radius (in x-direction). On the other hand, a negative quadrupole deformation is one which a nucleus has an oblate shape, with equatorial radius longer than its polar radius, as shown in Figure 1:13. The shapes shown in Figure 1:13(b) and (c) allow a possible nuclear rotation about the axis perpendicular to the symmetry z-axis.

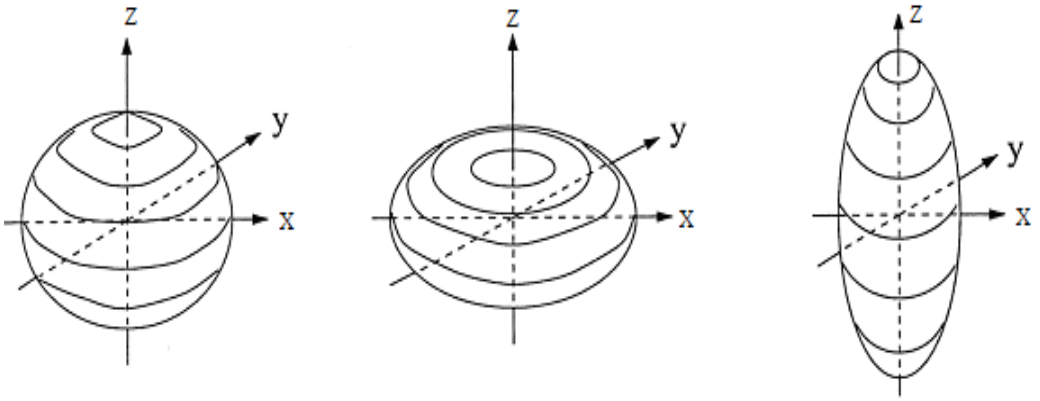

Figure 1:13. Intrinsic quadrupole moments (a) $Q_0 = 0$*, (b)* $Q_0 < 0$ *and (c)* $Q_0 > 0$ *[Bur79].*

1.4.1 Collective motion

In a collective nuclear rotational motion, the nucleons move coherently around the axis perpendicular to the symmetry axis, as illustrated in Figure 1:14(a). The collective nuclear model leads to a regular rotational band of levels such as the ones observed for the ^{158}Er nucleus [Tjø85].

1.4.2 Non-collective (single-particle) motion

Another way to create angular momentum is via single-particle motion. In spherical or weakly deformed nuclei, this is the only mode of creating angular momentum. The angular momentum is generated by the alignment of the nucleon spins along the symmetry axis as shown in Figure 1:14(b). This mode leads to an irregular sequence of states connected by γ–ray transitions with irregular energies and various multipolarities. For example, the ^{147}Gd level scheme shown in Figure 1:14(b) is associated with this mode. The angular momentum vectors, $\vec{j}_i$ for the individual nucleons are summed to produce the total angular momentum vector, $\vec{J} = \sum \vec{j}_i$.

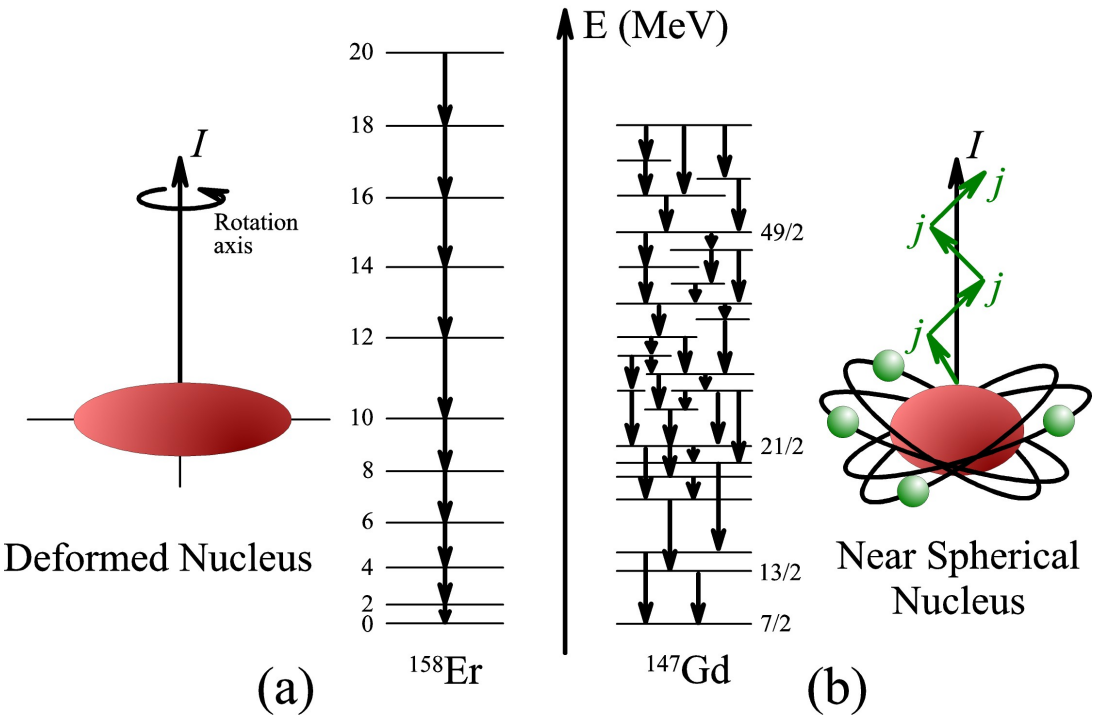

Figure 1:14. Schematic illustration of (a) the collective rotation around an axis perpendicular to the symmetry axis and (b) single-particle motion, generating angular momentum I, by summing the orbital angular mometnum of single particles [Pau03].

1.4.3 Nuclear angular momentum

To describe the interplay between motion of the particles and the collective rotation, consider an axially symmetric deformed nucleus rotating around the x-axis, with an orbiting valence nucleon. The total angular momentum, I, of the nucleus is given by

$$\vec{I} = \vec{R} + \vec{J} \tag{1:4}$$

where $\vec{R}$ is the angular momentum generated by the collective rotation of the core around the rotational axis, and $\vec{J}$ is the intrinsic angular momentum generated by the valence nucleon. The angular momentum coupling given by equation (1:4) is shown schematically in Figure 1:15. The intrinsic angular momentum of the valence nucleons $\vec{J}$ is the sum of the angular momenta of the individual values of the valence nucleons i.e. $\vec{J} = \sum_{i=1}^{A} \vec{j}_i$. The projection of the angular momentum onto the symmetry axis is K and is the same as the projection of $\vec{I}$.The projection of the angular momentum, of a valence nucleon $\vec{J}$ is Ω, thus $K = \sum_{i=1}^{A} \Omega_i$.

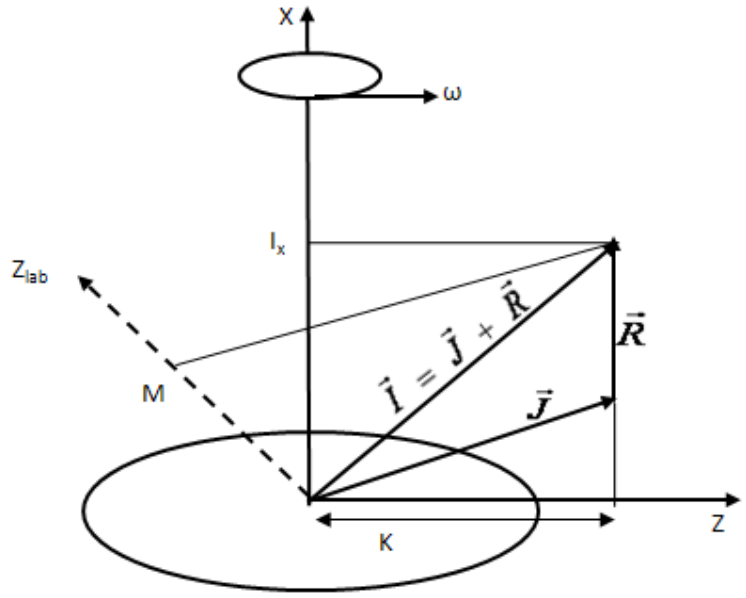

Figure 1:15. Schematic diagram of the coupling of the collective angular momentum, $\vec{R}$ and the intrinsic angular momentum of the valence nucleon, $\vec{J}$. K denotes the projection of the total angular momentum, $\vec{I}$, onto the symmetry axis [Pau03].

The ground state band of an even-even nucleus with a quadrupole deformation consists of levels connected by stretched $E2$ transitions above the 0^+ ground state. Due to pairing, at this point (low spin), all the nucleons are paired such that $\vec{J} = 0$, and the total angular momentum $\vec{I} = \vec{R}$. The energies of the levels for a rigid rotating nucleus are determined by equation (1:5)

$$E = \frac{1}{2\Im}\vec{R}^2 = \frac{1}{2\Im}\vec{I}^2 \tag{1:5}$$

where $\Im$ is the moment of inertia of a rigid nucleus. Quantum mechanically the magnitude of $\vec{I}^2$ is $I(I+1)\hbar^2$. Substituting the eigenvalues of $\vec{I}^2$ into equation (1:5) yields

$$E(I) = \frac{I(I+1)\hbar^2}{2\Im} \tag{1:6}$$

Thus the rigid rotation of a nucleus leads to a sequence of states with energies given by equation (1:6). In nuclei this is very well realized for superdeformed bands. Energies of rotational levels of moderately deformed nuclei do not exactly follow equation (1:6). This discrepancy is due to the fact that they do not behave like rigid rotors [Ben79, Fra81].

1.5 Level structure of tetrahedral and hyperdeformed bands

Tetrahedral and hyperdeformed nuclei have characteristic level structures. The observation of low-lying 1^- and 3^- states in isotopes of Ra and Th nuclei, populated via α-decay, provided the first experimental evidence that some nuclei may possess reflection-asymmetric shapes [Ste55]. In a reflection-asymmetric molecule, such as HCl or NH3, the positive and negative-parity states interleave and follow the $I(I+1)$ formula [Bre94] perfectly. The observed 1^- and 3^- states in the Th and Ra nuclei lie higher in excitation energy than of the corresponding 2^+ and 4^+ states. This leads to the hypothesis that the nucleus is not rigidly octupole deformed and may vibrate around a reflection-asymmetric shape. Figure 1:16 shows that the energies of the lowest-lying negative-parity states in the even-even isotopes of Rn, Ra, Th and U are well correlated to the minima in the potential energy for non-zero β_3. To date there is no actinide nucleus for which a 1^- state has been observed below the first 2^+ state.

Alternating-parity bands, with interleaved states having a spin sequence $I^+, (I+1)^-, (I+2)^+, \ldots$, were first observed in the actinide region in ^{218}Ra and ^{222}Th [Bon83, War83]. Bands with similar structures were also observed in medium mass nuclei such as ^{152,150}Gd and ^{150}Sm [Zol75, Hae77, Suj77]. Ever since this observation, bands of this type have been observed in many nuclei. However, at low spin $(I < 5)$ the bands are not interleaved. The observed displacement can be understood considering Figure 1:17.

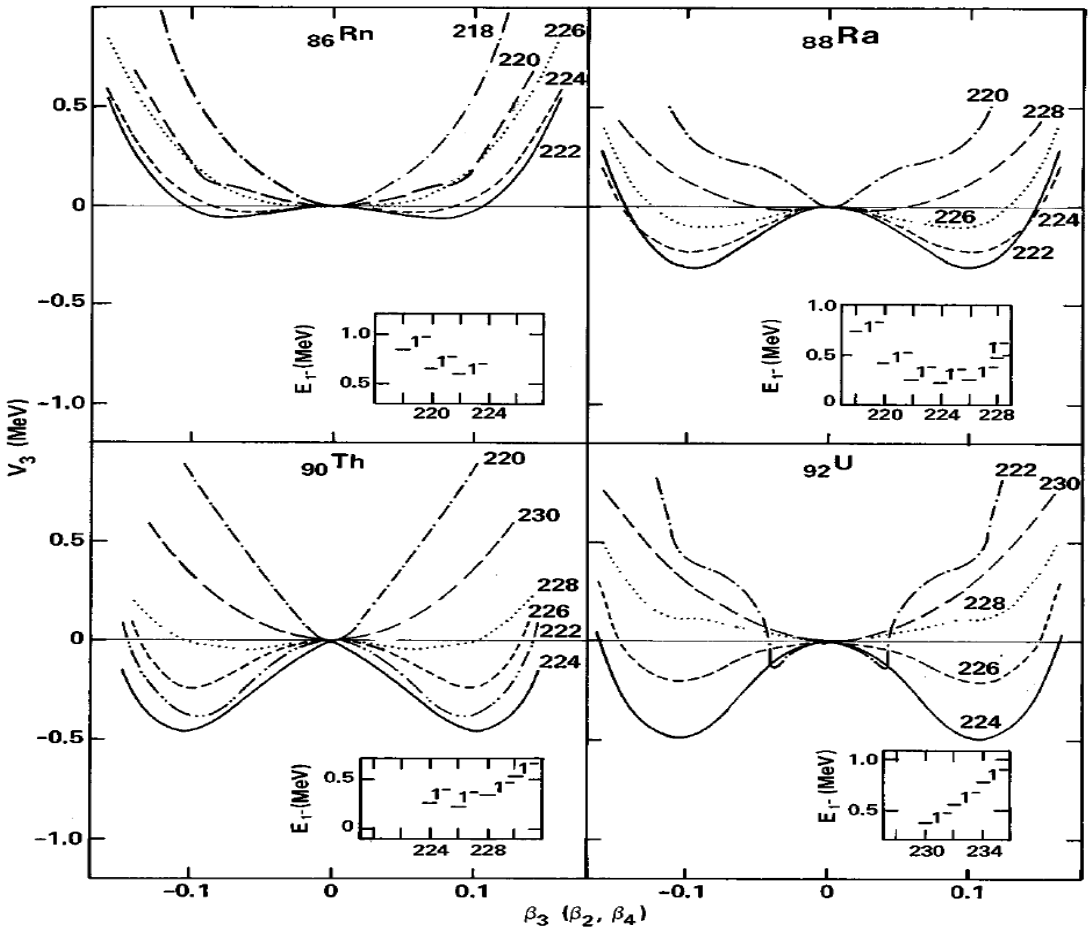

Figure 1:16. Calculated potential energy surfaces for different nuclei plotted as a function of the octupole deformation β_3. In the insets for comparison the lowest-lying negative-parity states for Rn, Ra, Th, and U isotopes are shown. Taken from Nazarewicz et al., [Naz84].

Figure 1:17 shows three different plots of potential energy, V, against β_3. The uppermost potential corresponds to a nucleus with reflection asymmetric shape in its ground state. This nucleus can undergo vibrations about this symmetric shape. The lowermost potential corresponds to a nucleus with a permanent ground state octupole deformation. The potential barrier has two degenerate minima at $\pm\beta_3$ and rises to infinity at $\beta_3 = 0$. The nucleus cannot take on a reflection symmetric shape. The spectrum for an even mass nucleus is characterized by a set of perfectly interleaved states of alternating parity. The potential in the centre is intermediate between the two other potentials. There is a small (<0.5 MeV) potential barrier and the nucleus can tunnel through the barrier to the mirror image shape. This interaction results in the displacement of the two bands. This displacement of states with opposite parity, is known as parity splitting, δE, and can be calculated by

$$\delta E = E(I)^{-} - \frac{1}{2}\left(E(I+1)^{+} + E(I-1)^{+}\right) \qquad (1:7)$$

At spins around $10\hbar$ the parity splitting tends to zero, giving levels schemes similar to that depicted in lower part of Figure 1:17. It seems that the rotational motion acts to stabilize the octupole deformation. The band with negative-parity and the splitting can be explained by dynamics in the octopole deformation degree of freedom [Egi90, Gar98] or by assuming vibrations in the mass asymmetry degree of freedom [Shn02]. The predicted hyperdeformed shape in the U-Th region is octupole (pear-like) [Blo89] with reflection asymmetry as shown in Figure 1:1, implying alternating parity bands for even-even nuclei as shown in Figure 1:17.

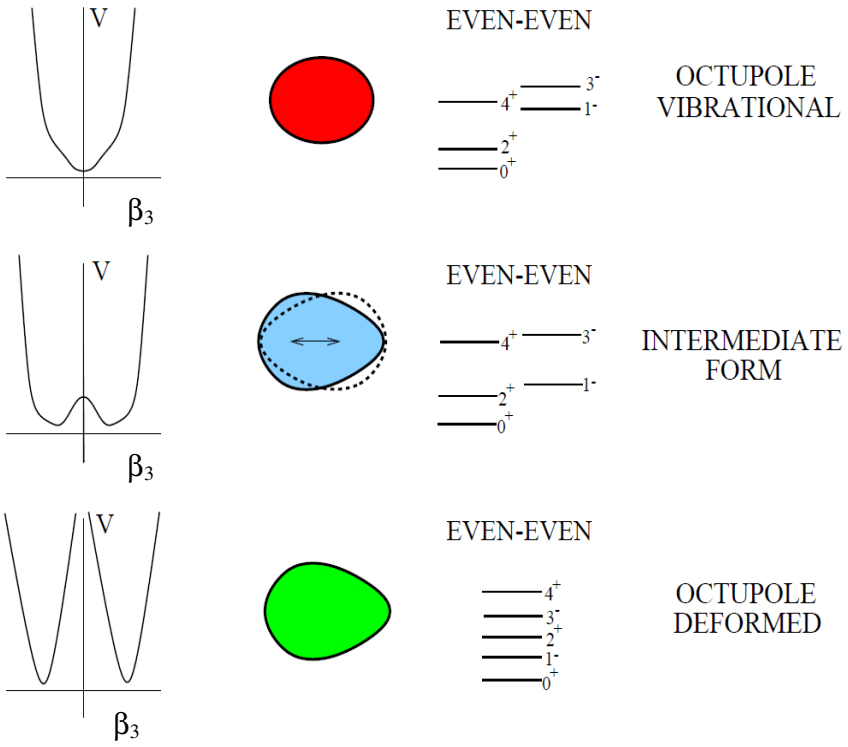

Figure 1:17. Plots of potentials energy, V, as a function of β_3 and associated nuclear shapes and level schemes. The uppermost represent a nucleus with a reflection-asymmetric ground state shape; the lowest corresponds to a static octupole deformed shape and the middle is an intermediate between these two [Ahm93].

The alternating parity levels are expected to be linked by E1 transitions as shown in Figure 1:18 and Figure 1:19. Figure 1:18 shows the rotational band of a pear shaped nucleus while Figure 1:19 compare predicted rotational band of a tetrahedral nucleus according to different predictions [Haf38, Rob79] and [Dud02], respectively. In a pear shaped nucleus, a dipole moment is present unlike in a tetrahedral shaped nucleus. Hyperdeformed bands in nuclei are predicted to have interleaved levels of positive and negative-parity which will decay strongly through E1 emissions. Low energy γ–rays ranging from 50-150 keV with regularly spaced γ–rays energy of about 5 keV are expected. This implies that to test the hyperdeformation prediction it is necessary to experimentally measure the discrete E1 transition connecting the negative-parity levels and the positive ones. This can be compared with the existing results from the fission resonance study [Blo88, Kra98].

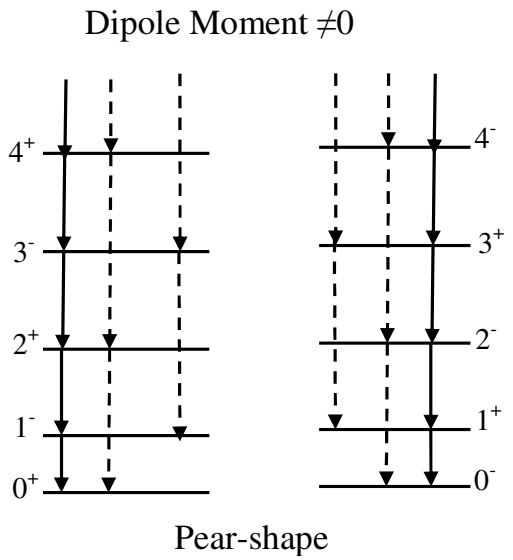

Figure 1:18. Schematic illustration of expected transitions in rotational bands based on pear-shaped (hyperdeformed band) [Dud02]. The solid and dashed lines represent dipole and quadrupole transitions respectively.

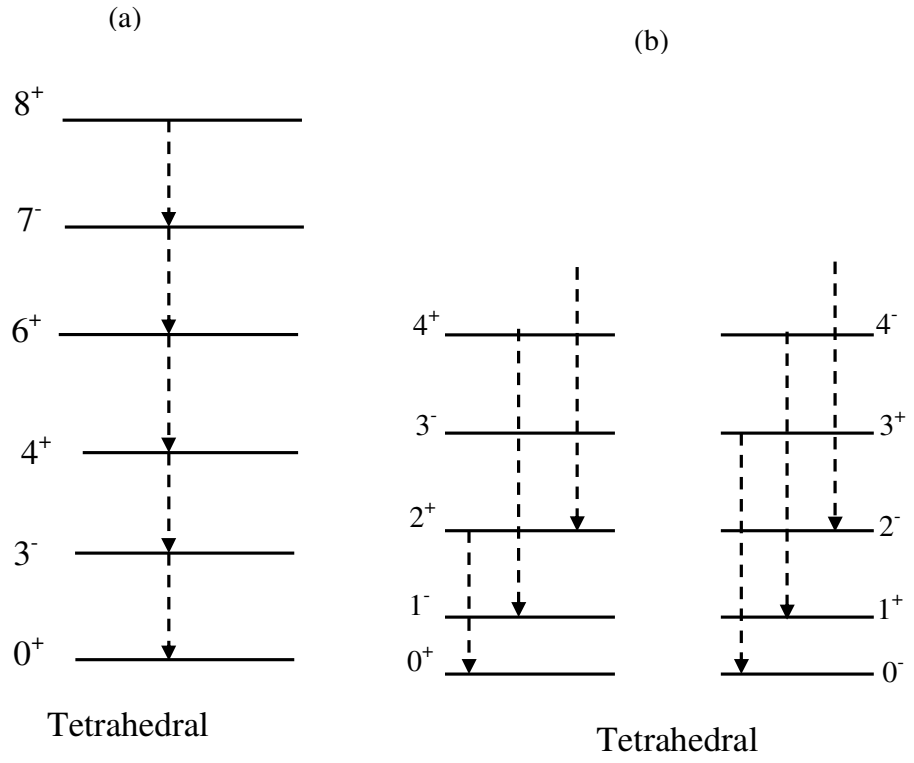

Figure 1:19. Schematic illustration of expected transitions in rotational bands based tetrahedral shaped nuclei according to (a) Hafstad et al., and Robson et al., [Haf38, Rob79] and (b) Dudek et al., [Dud02] .

1.6 Coriolis interaction in actinide nuclei

The alternative parity bands in the actinide nuclei arise due to the fact that in certain cases an orbital is lowered into the next lower major shell by the l^2 and $l \cdot s$ terms [Reg03]. These intruder states lie close in energy to orbits with $l_{\text{int}} - 3$ and $j_{\text{int}} - 3$, and the pairs of orbits with $\Delta l = \Delta j = 3$ can be strongly coupled to form octupole configurations [Dah88,Wie99, Ahm93, War96, But96]. The most important couplings are $(g_{9/2} \rightarrow p_{3/2})$, $(h_{11/2} \rightarrow d_{5/2})$, $(i_{13/2} \rightarrow f_{7/2})$ and $(j_{15/2} \rightarrow g_{9/2})$ [Coc96]. These couplings are shown in the right part of Figure 1:5. Nuclei which have their Fermi surfaces close to these pairs of orbitals will be subjected to octupole correlation effects. The particle numbers close to these coupled orbits are just above the closed shells. This implies that nuclei with both proton and neutron number close to closed shell values will exhibit stronger octupole correlations. It can also be seen in Figure 1:5 that the octupole-driving $\Delta l = \Delta j = 3$ orbits are lying closer together for larger particle numbers, thus heavier nuclei like the one studied in this work should have stronger octupole correlations. As a result, they exhibit a number of spectroscopic properties.

The ground states of even-even deformed nuclei are normally lowered by the pairing gap, Δ, which is typically about 1 MeV for both neutrons and protons. For this reason it is expected that the energy of the lowest excitation mode might be about $2\Delta \approx 2\,MeV$. However, attractive residual interactions significantly lower the energies of some of the excited states, and give rise to low-lying vibrational states. At low spin where residual interactions are more important than the Coriolis force, octupole vibrations are well characterized by their K-quantum numbers. At higher spin, the Coriolis field mixes states with different K values and leads to an alignment of the angular momentum of the octupole phonon along the rotation axis [Nak95]. This phenomenon is called phonon alignment. Furthermore, since octupole phonons carry three units of angular momentum, it is then expected that the maximum alignment $i_{\max} = 3\hbar$. The phonon alignment phenomenon has only been observed in deformed nuclei.

The phonon excitations consist of combinations of many two-quasiparticle states [Ham85]. Some individual quasiparticles associated with high-j intruder orbits experience the Coriolis force and try to align their angular momenta parallel to the rotational axis [Nak95]. At low spin, these individual alignments are prevented by octupole correlations, which couple two-quasiparticles to spin $3\hbar$ [Vog76]. When the Coriolis field becomes strong enough, then the individual quasiparticles are released from the octupole coupling and alignment takes place.

The two nucleons in a given orbit have velocities of opposite sign (time-reversed orbits) and as rotation is induced the Coriolis force acts on each of them. This is shown schematically in Figure 1:20.

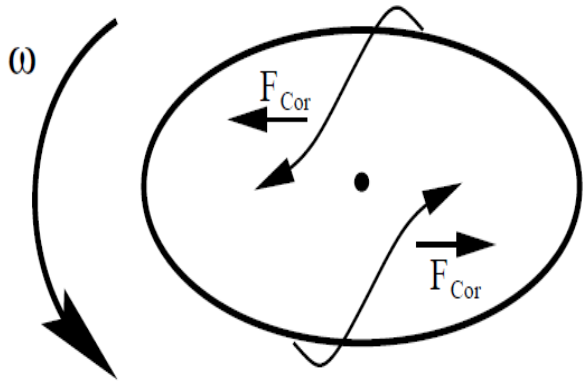

Figure 1:20. Illustration of the Coriolis force, which when the nucleus is rotated, acts to break the pairs of nucleons coupled to $J^{\pi} = 0^{+}$. *The axis of rotation points upwards out of the plane of the paper.*

The classical Coriolis force is given by the expression

$$\vec{F}_{Cor} = -2m(\vec{\omega} \times \vec{V}) \qquad (1:8)$$

Where m is the mass of the particle, $\vec{\omega}$ is the rotational frequency and $\vec{V}$ is the velocity of the particle. Figure 1:20 clearly shows that the Coriolis force acts to break the pair of nucleons which are coupled to $J^{\pi} = 0^{+}$. This phenomenon is known as the Coriolis anti-pairing effect (CAP) [Mot60]. A striking feature of this effect is the

observation of band crossing which occurs in certain nuclei. Band crossing occurs when the Coriolis force, defined in equation (1:8), becomes larger than the pairing energy of the two nucleons in time-reversed orbits, so that the quasi-particle pair breaks up. The band crossing results then from the crossing of the yrast (zero-quasiparticle band) with a two-quasiparticle band. The phenomenon is characterized by a sudden increase in the moment of inertia, along with a decrease in rotational frequency. Thus in a plot of the moment of inertia against the square of the rotational frequency, the moment of inertia bends back and up, hence this effect was originally named backbending.

1.7 Electromagnetic transition rates

Important properties of tetrahedral and hyperdeformed bands are electromagnetic transition rates. The motion of protons and neutrons in a nucleus creates charge and current distributions. Charge distributions can be described by electric multipole moments and they depend on the nuclear shape [Jen95]. On the other hand, current distributions are described through magnetic multipole moments. The electromagnetic radiation field produced when the nucleus emits radiation in the form of γ–rays can be described in terms of a multipole expansion [Bla52, DeS74, Rin80]. The γ–ray transition probability for a γ–ray decaying from state I_i to state I_f (separated by the energy E_γ), with multipole order L, is given by [Eji89, Boh75]

$$T_{fi}(\lambda L) = \frac{8\pi(L+1)}{\hbar L((2L+1)!!)^2}\left(\frac{E_\gamma}{\hbar c}\right)^{2L+1} B(\sigma L, I_i \rightarrow I_f) \qquad (1:9)$$

where σ denotes the type of radiation (electric or magnetic) and the double factorial [Bur63]

$$(2L+1)!! = 1.3.5.....(2L+1) \qquad (1:10)$$

is the amplitude of the oscillating electric or magnetic moment. Quantum mechanically, the radiation is emitted as discrete photons, and the multipole moment amplitude of a transition is replaced by a matrix element, which has the form

$$M_{fi}(\sigma L) = \int \psi_f^* m(\sigma L) \psi_i dv \qquad (1:11)$$

where the integral is carried out over the volume of the nucleus. The wave functions ψ_i and ψ_f refer to the initial and final states of the nucleus, respectively. The multipole operator $m(\sigma L)$ is related to the multipole moment, and it implements the change of the nucleus from its intial to its final state. The values of the reduced transition probabilities $B(\sigma L: I_i \rightarrow I_f)$ are given by

$$B(EL, I_i \rightarrow I_f) = \frac{1}{2I_i+1}\left|\left\langle f \left\| \hat{Q}_L \right\| i \right\rangle\right|^2 \tag{1:12}$$

for electric transitions and

$$B(ML, I_i \rightarrow I_f) = \frac{1}{2I_i+1}\left|\left\langle f \left\| \hat{M}_L \right\| i \right\rangle\right|^2 \tag{1:13}$$

for magnetic transitions. Here $\hat{Q}_L$ and $\hat{M}_L$ are the electric and magnetic multipole operators, respectively. In order to account for the different possible orientations of the angular momenta I_i and I_f the initial and final m-substates have to be taken into account. Derivations of these expressions have been well established and they are discussed in detail in [Rin80]. Experimental techniques for measuring electromagnetic transition rates are lifetime measurements and Coulomb excitation investigations [Ald56, Sch83]. From lifetime measurements electric quadrupole moments can be deduced and in turn the magnitude of nuclear deformation can be extracted.

1.7.1 Electric quadrupole moments

The electric quadrupole moment is one of the lowest multipole orders that results from the distribution of the nucleus charge. Its operator is defined in terms of the nuclear charge density distribution $\rho(r)$:

$$eQ(r) = \int \rho Y_{20} dV = \int \rho(r) r(3\cos^2\theta - 1) d\tau \tag{1:14}$$

where r is the radius vector and θ is the angle it subtends. The integral vanishes for spherically symmetric charge distributions and thus only a deformed nucleus will have a static quadrupole moment. The intrinsic quadrupole moment Q_0 is related [Lob70] to the deformation parameter β_2 as defined by equations (1:2) and (1:3):

$$Q_0 = \frac{3}{\sqrt{5\pi}} ZR^2 \beta_2 \tag{1:15}$$

where R is approximated by $R \approx 1.23A^{1/3}\text{fm}$. As alluded to earlier, Q_0 is positive for prolate and negative for oblate nuclear shapes. The reduced transition probability $B(E2)$ for a quadrupole transition linking states of spins I and $I-2$ is given by the expression

$$B(E2; I_i \to I_f) = \frac{5}{16\pi} e^2 Q_0^2 \left\langle I_i K_i 20 \middle| I_f K_f \right\rangle^2 \tag{1:16}$$

Where $\left\langle I_i K_i 20 \middle| I_f K_f \right\rangle$ is the Clebsch-Gordon coefficient of the transition deexciting a state of spin $I_i = I$ into a state with $I_f = I-2$, given by

$$\left\langle IK20 \middle| I-2K \right\rangle = \sqrt{\frac{3(I-K)(I-K-1)(I+K)(I+K-1)}{(2I-2)(2I-1)}} \tag{1:17}$$

where, K is the projection of the quasiparticle angular momenta onto the symmetry axis of the deformed nucleus.

1.7.2 Intrinsic electric dipole moment

The motion of the protons creates a separation of the centre of charge from the centre of mass, giving an intrinsic electric dipole moment D_0. The intrinsic electric dipole moments D_0 is related to the reduced transition probability $B(E1: I_i \to I_f)$ by the expression [Ahm93]

$$B(E1: I_i \to I_f) = \frac{3D_0}{4\pi} \left\langle I_i 010 \middle| I_f 0 \right\rangle^2 = \frac{3D_0^2}{4\pi} \frac{(I-K)(I+K)}{I(2I+1)} \tag{1:18}$$

The dipole moment can be extracted from experimental data by measuring the ratio of reduced transition probabilities $B(E1)/B(E2)$. This ratio can be calculated from the γ–ray branching ratio λ, for a given state in a rotational band, is given by

$$\lambda = \frac{T_2(E2)}{T_1(E1)} = \frac{i_{E2}}{i_{E1}} \tag{1:19}$$

where i_{E1} and i_{E2} are the γ–ray intensities of the $E1$ and $E2$ transitions, respectively. The transition probabilities are related to the reduced transition probabilities by equation

$$B(E2; I_i \to I_f) = \frac{1}{1.223\times10^{9} E_\gamma^5(E2)} T(E2; I_i \to I_f) \qquad (1{:}20)$$

$$B(E1; I_i \to I_f) = \frac{1}{1.587\times10^{15} E_\gamma^3(E1)} T(E1; I_i \to I_f) \qquad (1{:}21)$$

where E_γ are the E1 and E2 transition energies in MeV respectively. Using equations (1:20) and (1:21) equation (1:19) gives,

$$\lambda = \frac{T_2(E2)}{T_1(E1)} = \frac{1.223\times10^{9} B(E2) E_\gamma^5(E2)}{1.587\times10^{15} B(E1) E_\gamma^3(E1)} \qquad (1{:}22)$$

The reduced in-band transition probabilities are given by equation (1:16) and (1:18)

1.7.3 Collective transition rates

The collective electric and magnetic transition probabilities for deformed nuclei have been deduced by Bohr and Mottelson [Boh75]. The reduced transition probabilities for $E2$ and $E1$ transition, which are important in the context of this work, are given by equation (1:16) and (1:18) respectively. Table A:2 gives electric and magnetic transition rates in terms of the reduced transition probabilities for various multipolarities. They were obtained from equations (A:0:1) and (A:0:2). In this work, only the transition probabilities for the E1 and the E2 transitions were used.

The ratio of the intrinsic electric dipole to electric quadrupole moment can be extracted from experimental data using the ratio of reduced transition probabilities $B(E1)/B(E2)$. If the intensity of an E1 transition is i_{E1} and that of an E2 transition i_{E2}, de-exciting the same level, then the $B(E1)/B(E2)$ ratio can be calculated using equation (1:23)

$$\lambda = \frac{i_{E2}}{i_{E1}} = \frac{1.223\times10^{9} E_\gamma^5(E2) B(E2)}{1.587\times10^{15} E_\gamma^3(E1)\, B(E1)} \qquad (1{:}23)$$

The intensities can be obtained from experimental data and the $B(E1)/B(E2)$ ratio is used to extract the ratio of the intrinsic electric dipole and quadrupole moments, $|D_0/Q_0|$, through the equations (1:16) and (1:18) in the following form

$$\frac{B(E1)}{B(E2)} = 2.4\left[\frac{D_0\langle I_i K_i 10|(I_i-1)K_f\rangle}{Q_0\langle I_i K_i 20|(I_i-2)K_f\rangle}\right]^2 \qquad (1:24)$$

After extracting $B(E1)/B(E2)$ from the data, equation (1:24) can be used to calculate the dipole moment $|D_0|$ if the intrinsic quadrupole moment Q_0 is known.

1.7.4 Electromagnetic properties of tetrahedral and hyperdeformed bands

It is well known that electric dipole moments are directly proportional to E1 transitions and they are enhanced in octupole deformed nuclei. For heavy nuclei, the E1 transition rate is in the range of 10^{-4} to 10^{-7} Weisskopf units (W.u) [Boh58]. However, actinides with $N>140$ have E1 transition rates in the order of 10^{-3} to 10^{-2} W.u. This enhancement can be described in terms of the macroscopic liquid drop model [Boh57, Str56]. In this model, it is assumed that if the nucleus is asymmetric in shape the protons tend to move toward the sharpest end of the pear shape where the curvature of the surface is at optimum. This phenomenon is known as the "lightning rod effect" [Gre99].

It is one of the major objectives of this study to test the tetrahedral prediction by observing in-band E2 transitions in ^{230,232}U to extract $B(E1)/B(E2)$ ratios for comparisons with other nuclei in the actinide region. If the $B(E1)/B(E2)$ ratios of ^{230,232}U and the other actinide nuclei are the same, one could conclude with reasonable certainty that these bands are not of tetrahedral nature but fall into the same class of octuple vibration as their neighbours. The electric dipole interband transition probabilities from the tetrahedral band to the ground state band are expected to be larger as compared to the in-band E2 transition probabilities, especially at the bottom of the tetrahedral band. For tetrahedral bands it is expected that the negative-parity bands deexcite by E1 transitions into the positive-parity band and not by in-band E2 transitions.

1.8 Candidate of the proposed exotic nuclei

The fact that nuclei in different regions of the nuclear chart have different properties means that different physics phenomena can be explored in different regions of the nuclear chart. The candidate nuclei which are predicted to show hyperdeformation and tetrahedral shape and their other features are discussed below.

1.8.1 Hyperdeformed nuclei (HD)

The best evidence for HD shapes in atomic nuclei is in the Uranium (U) -Thorium (Th) region [Blo75, Kra98], but as yet, no discrete γ–rays from HD rotational states have been identified experimentally. The existence of HD states in Th and U isotopes has been established experimentally by studies of fission resonances in (n, f) and (d, pf) reactions [Blo88, Kra98].

Rotational bands of alternating parity with very large moments of inertia based on these minima, have been inferred from (n, f) and (d, pf) work [Kra98]. Levels in such bands would deexcite with about a 30% branch through E1 transitions into the ground band, with most of the remaining intensity being carried away by electrons due to internal conversion as discussed in section 2.5. Only at higher spins, E2 transitions could compete. Gamma–ray energies for these transitions are given by $E_\gamma = 2AI$. The value of A, inferred from measurement of fission resonances, and in agreement with calculations is $\approx 2keV$ [Blo89]. Therefore typical γ–ray energies of transitions de-exciting the HD band into ground band are expected to be between 40 and 120 keV for the spin range $10\hbar$ to $30\hbar$. This corresponds to smaller spacings between γ–rays as compared to the SD transitions of ^{152}Dy shown in Figure 1:21. It is the search for these E1 γ–ray transitions with regularly spacing required to confirm the hyperdeformation hypothesis and this is one of the major motivations for this work and the development of the recoil detector.

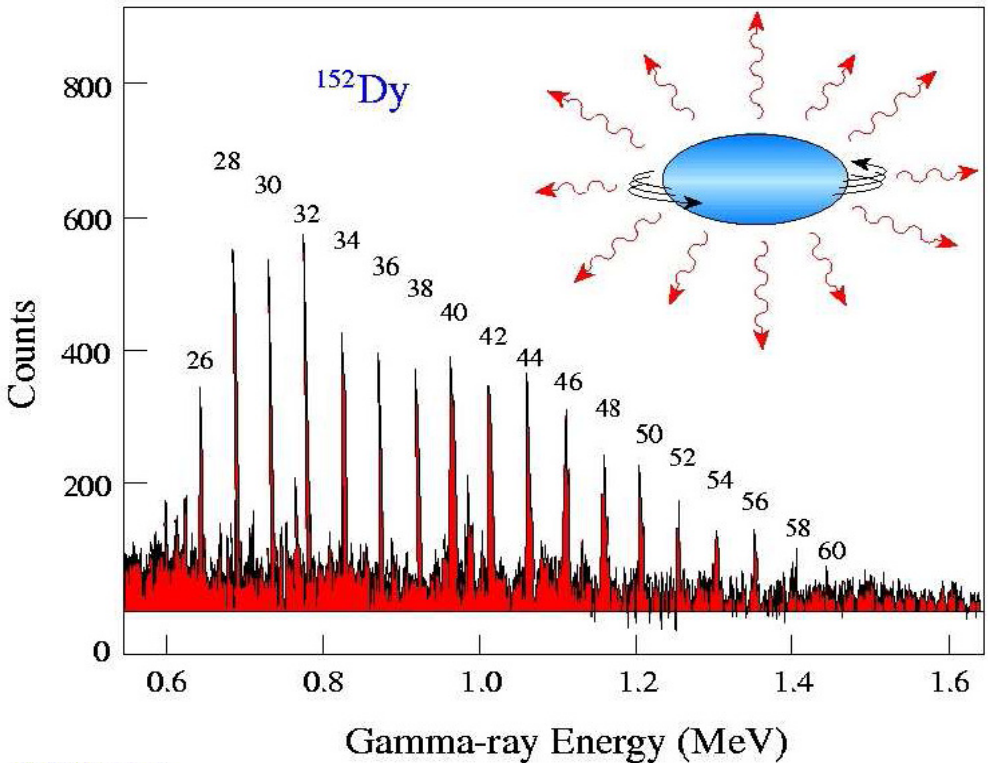

Figure 1:21. γ-ray spectrum of a superdeformed band in ^{152}Dy obtained by summation of gates set on most members of the band [Twi86].

1.8.2 Tetrahedral band

Tetrahedral nuclei are predicted to exist in the rare earth and actinide regions [Dud06] as discussed in section 1.2.1. They are characterized by a triaxial octupole deformation Y_{32}, together with a near-zero quadrupole deformation Y_{20} implying no in-band E2 transition, and this is regarded as a "signature" of tetrahedral shaped nuclei. Several bands in the mass 160 and in the actinide regions have the signature of missing E2 transitions and have consequently been regarded as tetrahedral candidates. Those in the mass 160 region have been studied at iThemba LABS [Bar10a]. In-band E2 transitions have been found in the key nuclei namely ^{160}Yb and ^{154}Gd which have been regarded as tetrahedral candidates. Furthermore, the band mixing calculations have allowed transition quadrupole moments to be deduced and the results indicate large quadrupole moments, consistent with normal prolate deformation.

These results leave the actinide region as practically the last region remaining with tetrahedral candidates that can be reached with stable beams. The prime candidates are the even-even U isotopes $^{230\text{-}234}$U. They have negative-parity bands as shown in Figure 1:22 with missing E2 transitions as reported in [Zey87].

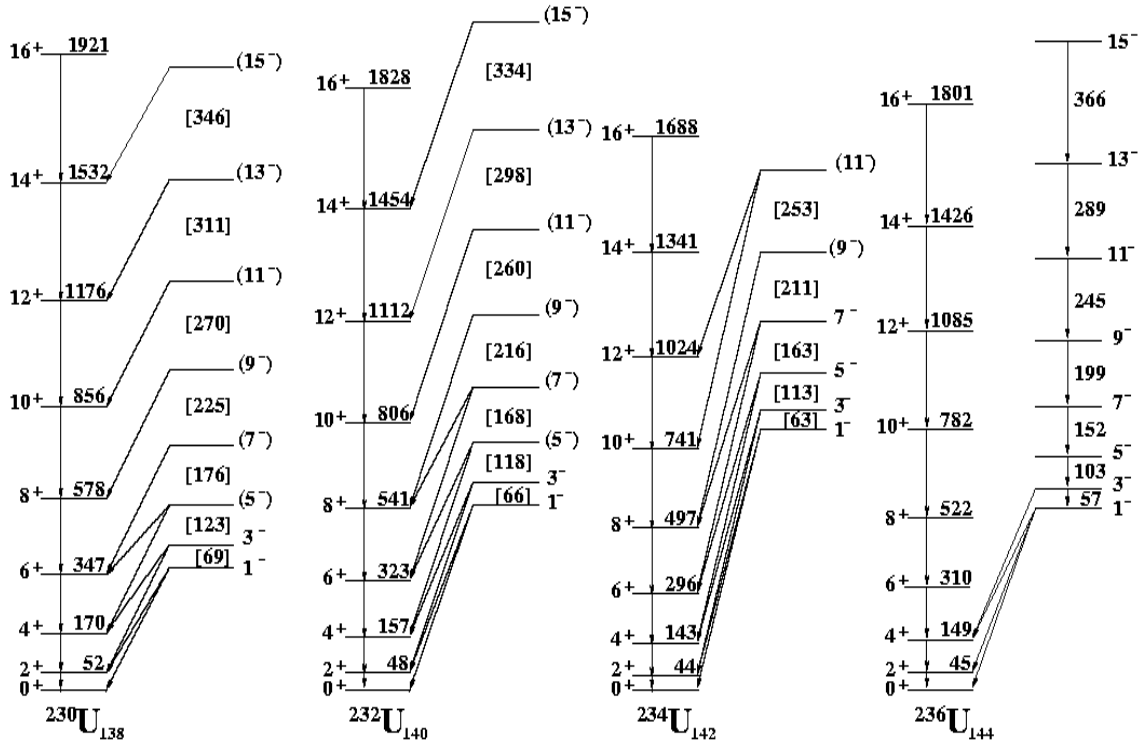

Figure 1:22. Partial level schemes of even-even uranium isotopes $^{230\text{-}234}$U. All nuclei were studied under the same experimental conditions using e-γ and e-e spectroscopy [Zey87]. This method helps to reduce the fission background. In $^{230\text{-}234}$U, the presence of the negative-parity bands have been established only through the observation of the $E1$ transitions to the ground-state bands. The results for $^{230\text{-}232}$U has been confirmed in ref.[Ack93] where two $E2$ transitions depopulating state 13^- and 11^- were tentatively observed. The absence of in-band E2 transitions is the proposed signature of tetrahedral band. In contrast, in ^{236}U no $E1$ transition for states above 3^- have been observed despite the fact that this isotope has been studied with 17 different nuclear reactions [Bro06]. The numbers in square brackets give the energies of the unobserved $E2$ transitions.

1.9 Review of negative-parity bands in the actinide region

In Ra and Th isotopes in-band E2 transitions have been found in their negative-parity bands (see Figure 1:23 and Figure 1:24) [Coc97]. The ground and negative-parity bands in ^{226}Th form interleaved bands and have been interpreted to have a static octupole deformation, and more recently to represent an octupole phonon condensates [Fra08]. Furthermore bands in ^{232,234}Th have been called split bands and have recently been interpreted as octupole vibrational bands. Unlike the even-even Ra and Th isotones the previously reported bands in even-even U nuclei do not show any in-band E2 transitions (*compare Figure 1:22, Figure 1:23 and Figure 1:24)* [Ack93, Coc97].
The calculated in-band E2 transition energies of the U negative-parity bands (see *Figure 1:22)* are nearly identical in energy with those of their Ra and Th isotones (*see Figure 1:23 and Figure 1:24).* All negative-parity bands of the Ra and Th isotones have been understood as octupole vibrational bands in the past. Therefore, one assumes that the negative-parity bands of the U isotopes are also octupole vibrational regardless of the failure to experimentally observe the in-band E2 transitions. It is one of the goals of this work to search for in-band E2 transitions in ^{230,232}U. If they are observed, then their electromagnetic properties through $B(E1)/B(E2)$ ratios can be compared with their isotones in the actinide region. Should their $B(E1)/B(E2)$ ratios be the same as for their isotonic neighbors, one could conclude with reasonable certainty that these bands are not of tetrahedral nature but fall into the same category of octupole vibrational bands as for their Ra and Th isotones.

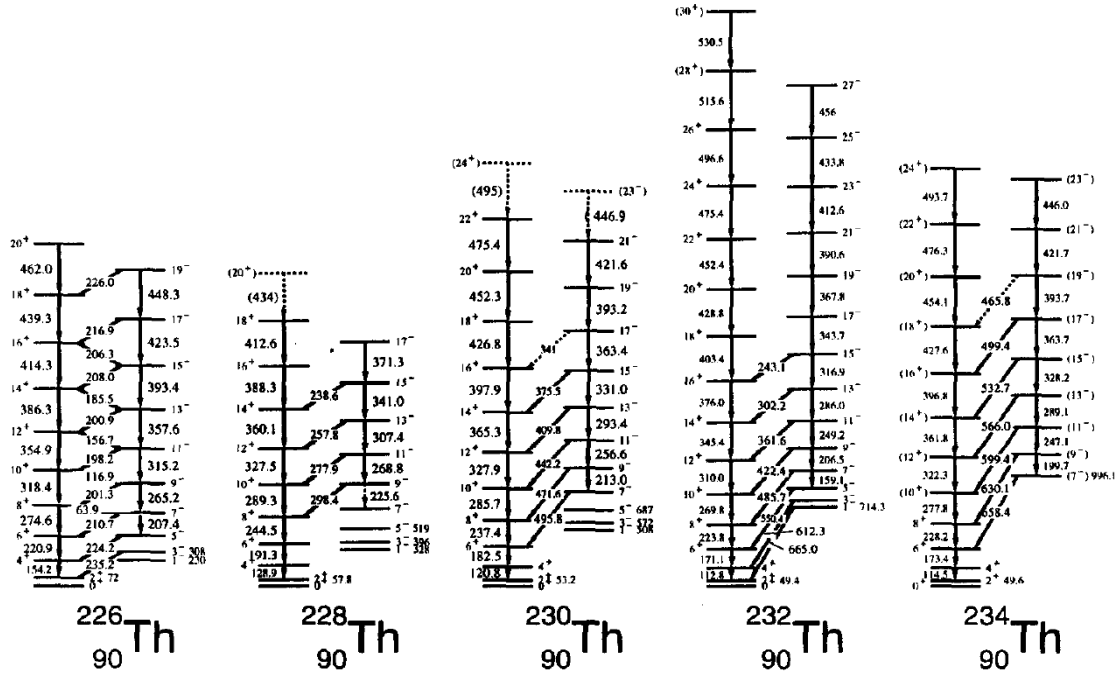

Figure 1:23. Partial level schemes of octupole-deformed Thorium (Z=90) isotopes showing enhanced E1 transitions between the positive-parity ground band and negative-parity states [Coc97].

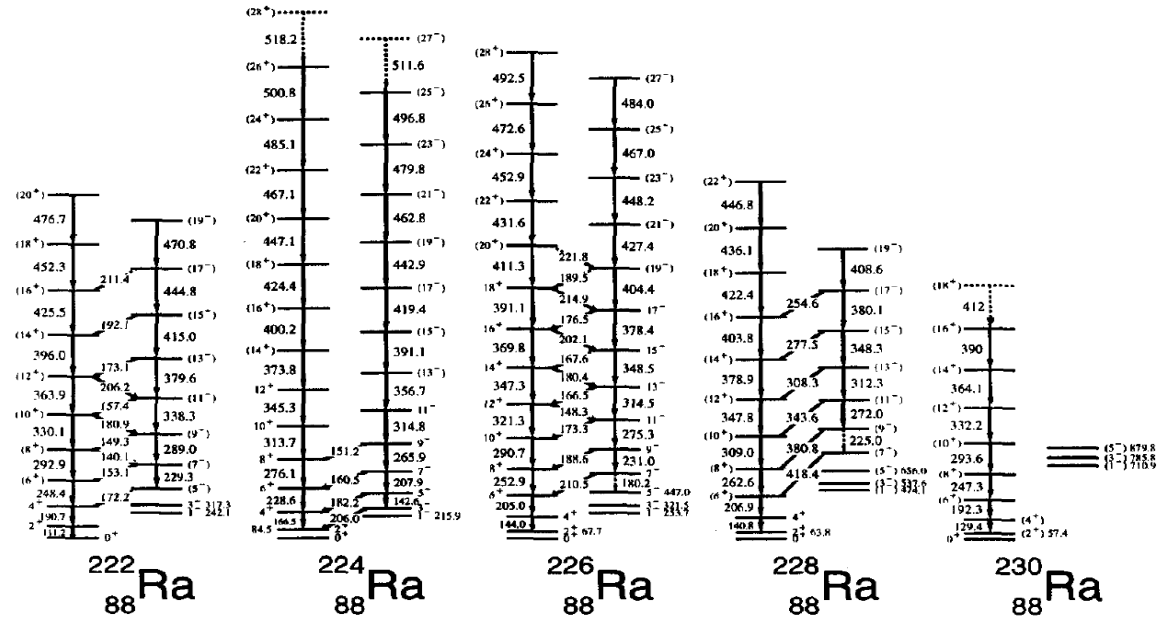

Figure 1:24. Partial level schemes of octupole-deformed Radium (Z=88) isotopes showing enhanced E1 transitions between the positive-parity ground band and negative-parity states [Coc97].

CHAPTER 2 EXPERIMENTAL METHODS

The fact that fission is a dominant channel in reactions leading to the actinide region poses a great challenge in studying nuclei in this region. Challenges in studying these nuclei are discussed in section 2.8. In order to address this, at iThemba LABS a recoil detector, discussed in detail in CHAPTER 4, was built. Reactions used to test the recoil detector are given in Table 2:1 and some results of the tests are discussed in CHAPTER 4. Ultimately the desired experiments, namely Experiment 1 and Experiment 2 were performed. The experimental conditions for the experiments performed and other details are tabulated in Table 2:2. Experiment 1 was proposed and performed by a group of physicists from the Australian National University (ANU) in collaboration with iThemba LABS. This experiment was aimed at searching for superdeformation in ^{196}Po using the reaction ^{180}W(^{20}Ne, 4n) at 110 MeV. For reasons outlined in CHAPTER 4, we performed this experiment using AFRODITE together with the recoil detector.

Table 2:1. Table of reactions used to test the recoil detector.

Reaction	**Beam Energy (MeV)**	**Calculated Cross-section (mb)**	**Target thickness ($\mu g/cm^2$)**	**Fission (%) (calculated**
^{181}Ta(^{20}Ne, 6n)^{195}Bi	125	120	500	78.8
^{198}Pt(α, 5n)^{197}Hg	65	500	200	0.01
^{197}Au(α, 6n)^{195}Tl	65	740	180	0.7
^{180}W(^{20}Ne, 5n)^{195}Po	118	30	1000	74.5
^{232}Th(α, 6n)^{230}U	65	40	150	97.2

In Experiment 2, the reaction ^{232}Th(α, xn) was used to produce the ^{230,232}U isotopes. These isotopes were used to test the described theory of tetrahedral shapes and to search for hyperdeformed states. These theories were to be tested by measuring the γ–ray branching ratios, $B(E1)/B(E2)$. In order to measure $B(E1)/B(E2)$ the nucleus

must be produced at high spin. The creation of the nucleus and the experimental methods used to measure the evaporation residues are discussed in this chapter.

Table 2:2. Summary of experimental details.

Date	**Exp. 1** **Aug-Sep 2006**	**Exp. 2a** **Oct 2009-Apr 2010**	**Exp.2b** **Feb -Apr 2010**
45° CLOVER	0	0	0
90° CLOVER	5	2	5
135° CLOVER	4	4	4
45° LEPS	0	2	0
90° LEPS	3	6	3
135° LEPS	0	0	0
Total number of BGO's	9	6	9
Target	^{180}W, 1mg/cm^2	^{232}Th, 120 μg/cm^2	^{232}Th, 120 μg/cm^2
Beam	^{20}Ne, E=110 MeV	^{4}He, E=61 MeV	^{4}He, E= 42 MeV
Pulse selection	1/4	1/6	1/7
Beam-burst separation	67 ns	244 ns	341 ns
Beam current	~5 pnA	15-40 pnA	15-40 pnA
Recoil velocity (β)	0.93%	0.26%	0.18%
Compound system	^{196}Po (8.8%)	^{230}U (2.4%)	^{232}U (15.4%)
Dominant residual	^{196}Bi(9.3%), ^{193}Pb(7.2%), ^{195}Po(6.8%),^{195}Bi(6.1%)	^{231}U(0.21%), ^{231}Pa(0.02%)	^{233}Pa(0.01%), ^{231}U(0.32%),^{233}U(0.17%)
Fission	58%	97.2%	84.04%
Recoil detector foil	Carbon	Mylar	Mylar
Trigger condition	γ–recoil	γ–recoil	γ–recoil
Aluminum Absorbers	None	0.6 mm on CLOVERS, 1.5 mm on LEPS	0.6 mm on CLOVERS, 1.5 mm on LEPS
No. of weekends	4	6	4
Number of events	33.4×10^6	1.8×10^6	7.0×10^6
Efficiency of a recoil detector	40%	3.5%	7.0%

2.1 The fusion-evaporation reaction

In order to obtain the spectroscopic information on the nuclei studied in this work, typical fusion-evaporation reactions have been used to produce the desired nucleus at high excitation energy. For this kind of reaction to occur, a projectile nucleus must be accelerated by an accelerator to a kinetic energy larger than the Coulomb barrier between the projectile and target nucleus, which is given by

$$E_c(MeV) = \frac{1.44 Z_t Z_p}{1.16(A_t^{1/3} + A_p^{1/3} + 2)} \tag{2:1}$$

where Z_t and A_t are the atomic and mass numbers of the target nucleus and Z_p and A_p are those of the projectile. At iThemba LABS, a Separated Sector Cyclotron (SSC) is used to provide beams of projectiles. The projectile and the target nuclei can fuse together, sharing their nucleons and forming an intermediate excited system, called the compound nucleus. The idea of the compound nucleus, in which mass and excitation energy are equally distributed, was first suggested by Bohr in 1936 [Boh36]. The excitation energy of the compound nucleus formed is given by the following expression

$$E_x = Q + E_b\left(1 - \frac{A_b}{A_p + A_t}\right) \tag{2:2}$$

where E_b is the beam energy in the laboratory reference frame. Q is called a Q-value and is defined as the difference between the masses of the initial (i) and final (f) states:

$$Q = \sum_i m_i - \sum_f m_f = A_p + A_t - m_{CN} \tag{2:3}$$

The highly-excited compound nucleus can either fission or cool down by emitting particles like neutrons (n), protons (p) or α-particles (^{4}He) as depicted in Figure 2:1. In the case of a reaction leading to heavy nuclei, the competition with fission becomes increasingly important with increasing mass number and dominates for actinide nuclei.

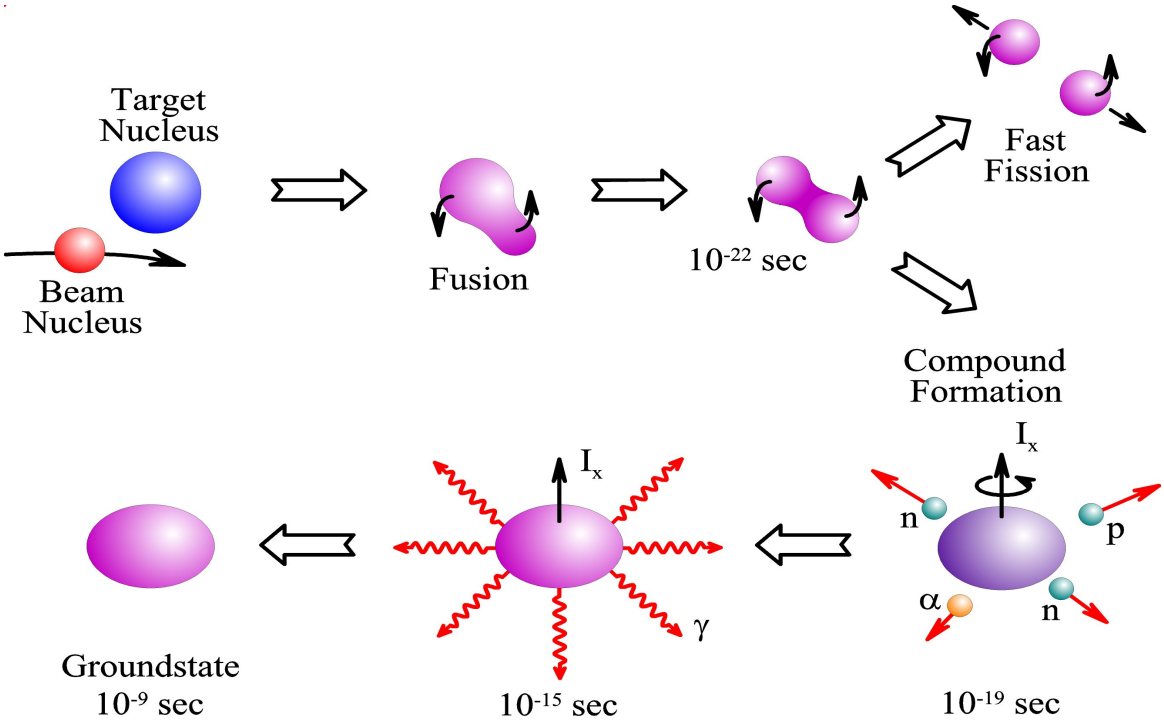

Figure 2:1. Schematic representation of the formation and decay of a compound nucleus through an Heavy Ion Fusion-evaporation (HIFE) reaction.

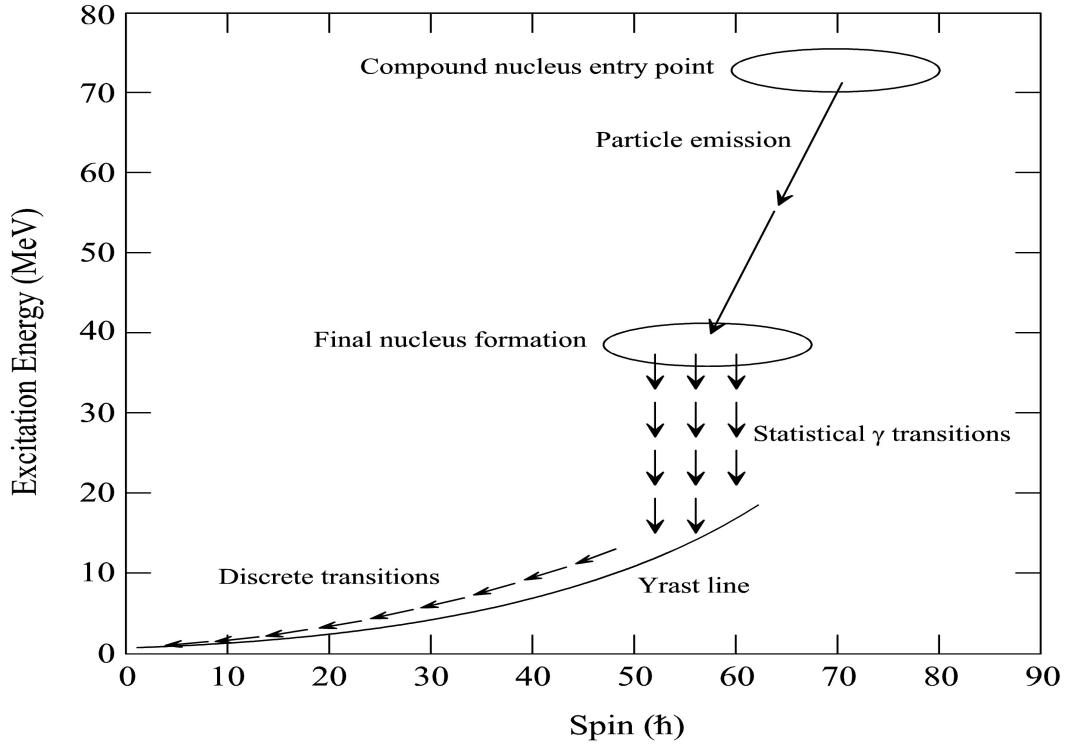

Figure 2:2. Schematic representation of the deexcitation of the final nucleus from the entry states to the ground state [Mab03].

2.2 Fission

For heavy systems, like nuclei in the actinide region, the decay of compound nuclei becomes complicated because fission is a strong channel. The theoretical explanation of fission was first given by Wheeler and Bohr [Whe39]. The fission of a heavy nucleus can take place naturally (spontaneous fission) or under bombardment with neutrons or charged particles. The stability of a nucleus against fission is explained by the liquid-drop model. This model assumes that the long-range Coulomb forces between protons act to disrupt the nucleus whereas the short-range nuclear forces act to stabilize it. The degree of stability is the result of the balance between the relatively weak electromagnetic forces and the strong nuclear force. Although each of these forces result in potentials of several hundreds of MeVs, the height of the fission barrier against fission is about 5-6 MeV for heavy nuclei since the forces partially cancel each other. The height of the fission barrier and consequently the lifetime associated with spontaneous fission of a nucleus depends on the ratio Z^2 / A.

In the first stage of the fission process, the nucleus undergoes a gradual change in shape, in the course of which a neck forms between the pre-formed fragments. The neck gradually grows thinner and at an instance called the scission point it breaks allowing the fragments to move apart in opposite direction with high energies. Those fragments are called primary fragments and decay by β-decay and γ–ray emission. A small fraction of fission fragments also emits neutrons. Finally, stable nuclei are produced.

2.3 Light particle emission

If the compound nucleus survives fission, it first decays by emitting light particles as shown in Figure 2:1. Since the emission of charged particles is hindered by the Coulomb barrier, usually the evaporation of neutrons is a faster process than the evaporation of protons and α-particles. Each particle removes about 5-8 MeV per nucleon and carries a few units of angular momentum, leaving the angular momentum of the residual nucleus slightly reduced. This means that most of the compound nucleus excitation energy is dissipated through particle emission. This process continues until the γ–ray emission probability becomes comparable to the particle

emission probability. Normally this happens when the compound nucleus excitation energy is comparable or (lower than) the particle separation energy.

2.4 γ–ray emission

After particle emission, what remains is often called an "evaporation residue". The residue is generally left in a state of relatively high angular momentum, but small excitation energy (almost of the same order as the particle separation energy). Subsequently, the final nucleus cools down through the emission of γ–rays until the ground state is reached. The γ–ray de-excitation is categorized into statistical or cooling and discrete transitions. The statistical transitions carry away a substantial amount of energy but little angular momentum, de-exciting the nucleus towards the yrast line (comprising the states of lowest excitation energy for a given spin). The discrete transitions follow a path close to the yrast line as indicated in Figure 2:2. These transitions have fairly small energies and take away about 2ħ each. It is these discrete γ–rays that spectroscopists are normally interested in.

2.5 Internal conversion

A competing electromagnetic process to γ–ray emission in the de-excitation of bound nuclear states is internal conversion, where an atomic electron is emitted. In this process, the excitation energy of the nucleus is transferred to one of the atomic electrons, causing it to be emitted. The kinetic energy of the emitted electron depends on the electron binding energy, B_e and the transition energy $(E_i - E_f)$

$$T_e = (E_i - E_f) - B_e \tag{2:4}$$

Electrons in different atomic orbitals have different binding energies, therefore it is possible that for a given transition there are several possible electron energies. From equation (2:4), it can be seen that if the transition energy is smaller than the electron binding energy for a particular shell, then the electrons in that shell cannot be emitted. Conversion electrons are labeled by the atomic shell from which they originated. The principal atomic quantum numbers $n = 1, 2, 3$ correspond to the K, L and M shells, respectively. It is possible to distinguish the shell substructure, thus conversion electrons from the L shell can be labeled L_{I}, L_{II} or L_{III}, if they originated from the

$2s_{1/2}, 2p_{1/2}$ or $2p_{3/2}$ atomic orbitals, respectively. The vacancy left in the atomic shell by a conversion electron causes atomic transitions (X–rays). These X–ray transitions can be used to determine the atomic number Z of the nucleus from which γ–rays under investigation are emitted. The total internal conversion coefficient α_t is defined as the ratio of internal conversion decay probability λ_e to the γ-decay probability λ_γ

$$\alpha = \frac{\lambda_e}{\lambda_\gamma} \tag{2:5}$$

The total decay probability λ_t is

$$\lambda_t = \lambda_\gamma (1 + \alpha_t) \tag{2:6}$$

The internal conversion coefficient depends on the energy E_γ of the transition, the atomic number Z of the nucleus and the principal atomic quantum number n in approximately the following way [Sli65]:

$$\alpha \propto \frac{Z^3}{n^3 E_\gamma^{2.5}} \tag{2:7}$$

Internal conversion coefficients are larger for magnetic transition than for electric transitions, and increase with increasing multipolarity. Measured γ–ray transitions intensities must be corrected for internal conversion to obtain the total intensities, by using equation (2:6) and known values of internal conversion coefficients. This correction has also been applied for the intensity measurements performed in this work.

The calculated internal conversion coefficient (α) plotted as a function of energy for uranium taking into account different multipolarities are shown in Figure 2:3. The calculation indicates that at the energy range of 10-100 keV, the most of the intensities from E2 transition is taken away by internal conversion. Figure 2:3 also indicates that at this energy range the E1 transitions could be easily measured compared to the other multipolarities, and this is why the hyperdeformed experiment aimed at measuring E1 transitions.

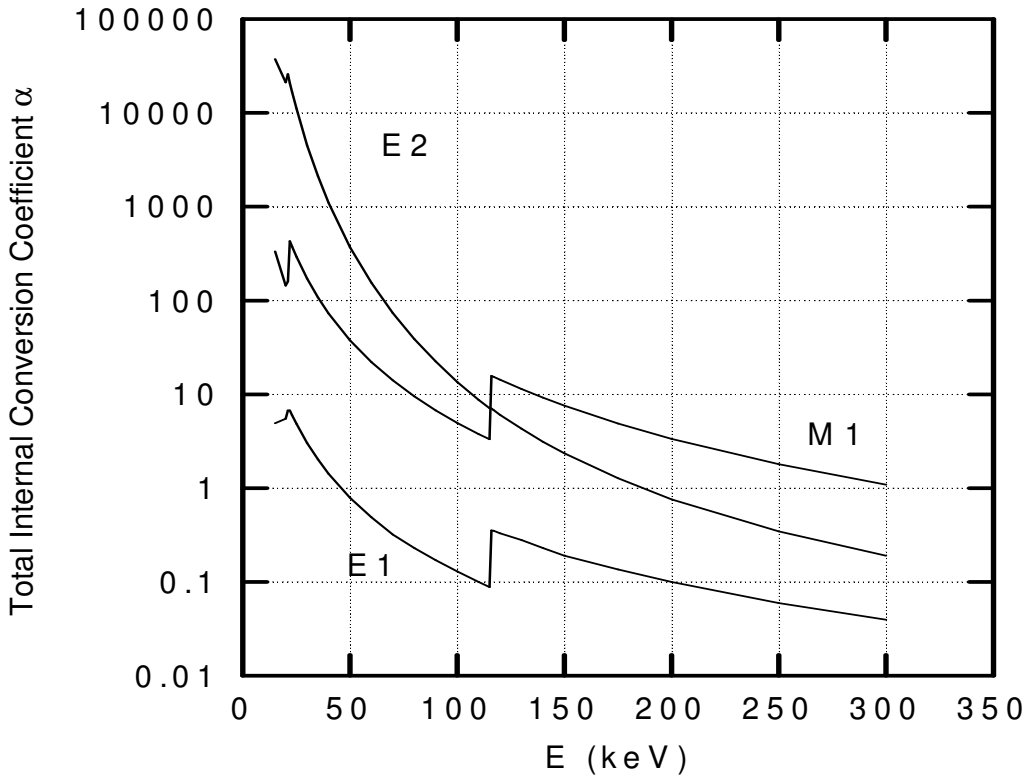

Figure 2:3. The total internal conversion coefficient (α) plotted as a function of energy for U different multipolarities.

2.6 Experiment 1

It is important to identify crucial steps that need to be taken in order to yield a successful experiment. One of the first priorities is choosing the appropriate beam-target combination with a decent probability of yielding the desired isotope at optimum cross-section. Moreover, choosing the appropriate beam energy also remains an intricate and challenging endeavor. Consequently, experimentalists opt to employ a statistical computing program called PACE (Projected Angular Momentum Coupled Evaporation) [Gav80, Gav93]. The program itself employs Monte Carlo simulations to predict cross-sections and angular momenta for the reaction of interest. Moreover, the nucleus of interest (i.e. ^{196}Po-experiment 1) was populated using the ^{180}W (^{20}Ne, 4n) reaction and PACE was used to determine the optimal beam energy for this reaction. The PACE output display is presented in Figure 2:4, and it shows that 110 MeV is the most appropriate beam energy for the desired reaction, since there is minimum contamination at optimum reaction cross-section. This computer program

has also been successfully employed for all experiments of nuclei studied in this current work. The target was a self-supporting metallic ^{180}W foil enriched to 99.9% with a thickness of 1 mg/cm^2.

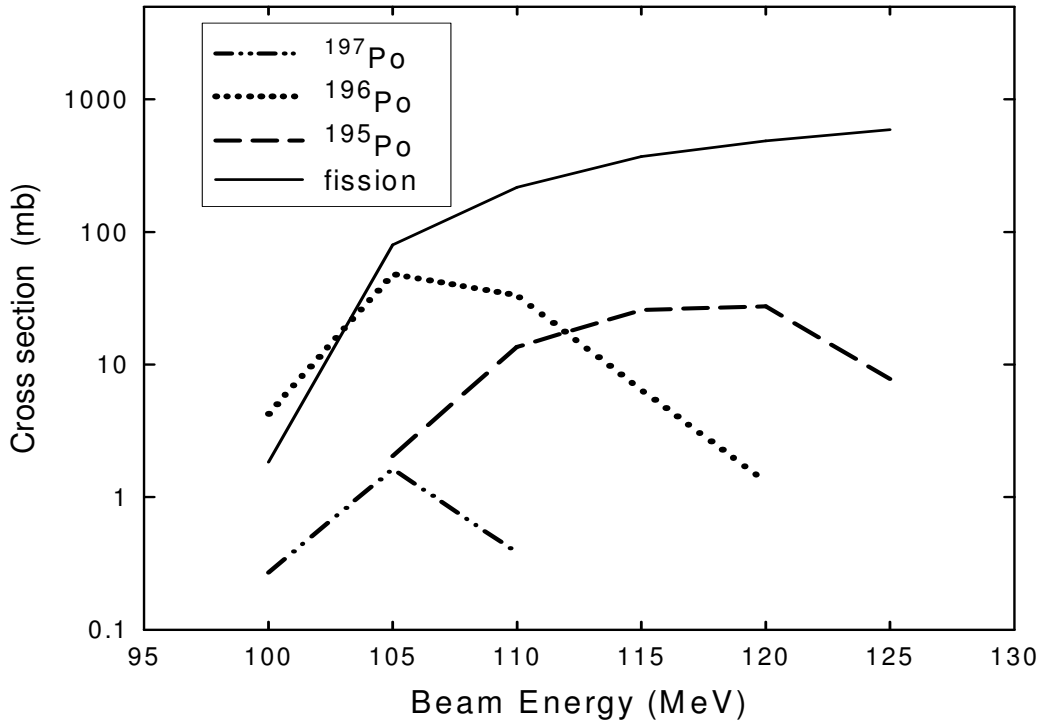

Figure 2:4. Calculated cross-section for the ^{180}W(^{20}Ne, xn) reaction as a function of beam energy.

2.7 Experiment 2

The ^{232}Th(α, xn) reaction was used to produce the uranium isotopes (experiment 2). Calculated excitation functions for $^{230\text{-}233}$U and experimental results for ^{230,232}U are shown in Figure 2:5. Alpha beam energies of 42 MeV and 61 MeV were used to bombard a 120 μg/cm^2 thorium target, with a 20 μg/cm^2 carbon backing on the upstream side, to populate ^{232}U and ^{230}U, respectively. Furthermore, prior to the experiments, the target thickness and materials were confirmed by performing a Particle Induced X–rays Emission (PIXE) analysis [Pro95]. In order to optimize the statistics, an α-beam of high intensity was required. On average, beam currents of 15 pnA and 40 pnA for the 42 and 61 MeV α-beams, respectively, were used. As stated earlier, recoil detector experiments account for time-of-flight measurements.

Consequently, the α-beam was pulsed with 341 ns pulse separation time. After different γ–recoil matrices were constructed an extensive search for the hyperdeformed states and tetrahedral shapes began.

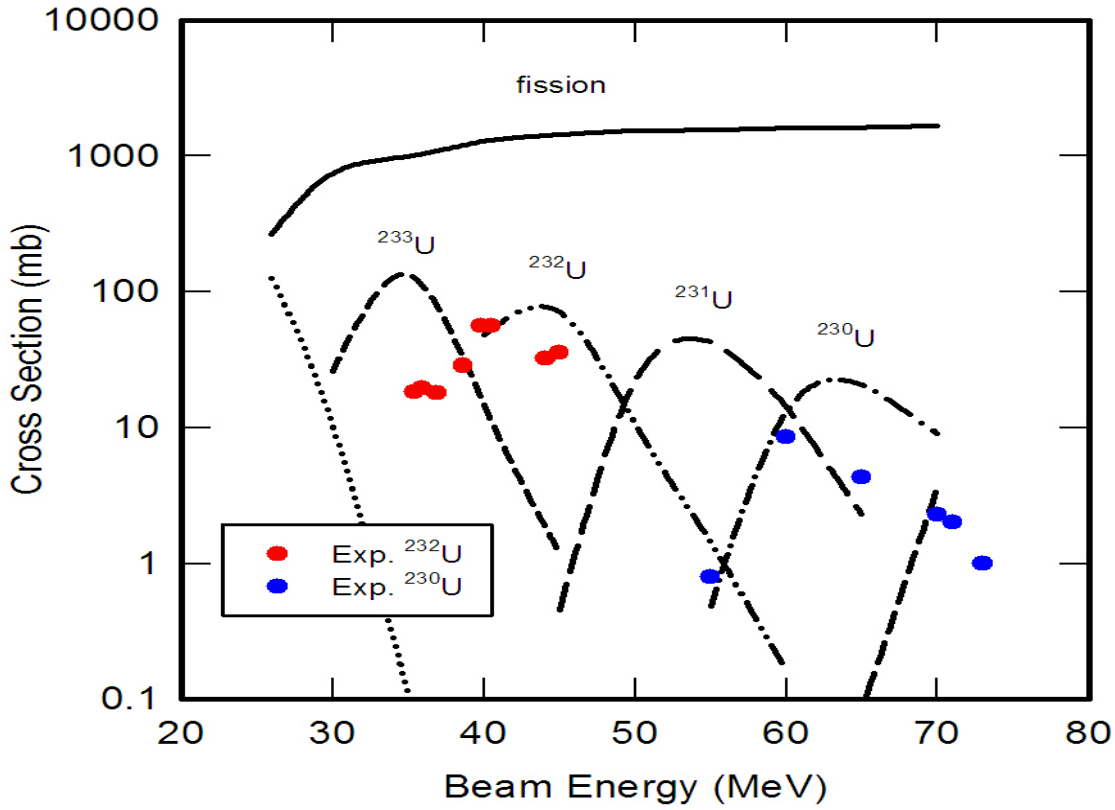

Figure 2:5. Calculated cross-sections for the ^{232}Th(α, xn) reaction as a function of beam energy. They are compared with the experimental excitation functions (symbols) for ^{230,232}U.

2.8 Challenges in studying exotic nuclear shapes

As stated earlier, nuclei in the actinide region (such as U isotopes) are extremely difficult to populate experimentally. Until recently, very little information existed concerning the high spin states of many nuclei which have been predicted to possess exotic nuclear shapes. In the actinide region, these nuclei can be produced using the ^{232}Th(α, xn) reaction. However, this is a reaction in which the production cross-sections of the nuclei of interest diminish, and fission is a dominant channel (see Figure 2:5). Furthermore, the evaporation residues from the ^{232}Th(α, xn) reaction are produced at a very low recoil velocity. The above mentioned factors complicate the

well established method of measuring lifetime using Doppler-shift methods. It is well known that by using lifetime measurements one can extract quadrupole moments, which in turn can be used as a simple test for nuclear deformation and hence tetrahedral predictions. The quadrupole moments can also be extracted by measuring $B(E1)/B(E2)$ branching ratios which are related to the intrinsic dipole moment (*see equation (1:24)*). CHAPTER 4 discusses the recoil detector which deals with challenges facing the detection of evaporation residues of the exotic nuclei.

2.9 Germanium detector arrays

The array of HpGe detectors called AFRODITE was used to detect the γ–rays from the excited nucleus. Discrete-line γ–ray spectroscopy requires a detection system that offers high efficiency, excellent energy resolution and a large peak-to-total (P/T) ratio [Lie97]. Nowadays, most γ–ray spectroscopy experiments employ high-resolution germanium detectors surrounded by Compton-suppression shields, to improve the P/T ratio.

The germanium detector is a semiconductor detector consisting of a large reverse-biased p-n junction diode. At the junction between the p-type and n-type material, the migration of electrons from the n-type material and the holes from the p-type material give rise to a region of net zero charge, called the depletion region. The applied high voltage creates an electric field across the depletion region. Any γ–ray interacting with the germanium, through the processes photoelectric effect, Compton scattering and pair production produce electron-hole pairs in the depletion region, which move in the electric field. Since the depletion region is the active part of the germanium detector, its volume is required to be as large as possible. A certain reverse-bias is needed to fully deplete the diode. The width of the depletion region is proportional to $\left(\frac{V}{N}\right)^{1/2}$, where V is the bias voltage and N is the impurity concentration in the germanium crystal of the detector. Chemically pure germanium can only maintain a depletion region of a few millimeters before electric breakdown takes place. To increase the width of the depletion region, the impurity concentration N of the Ge crystal has to be reduced. To achieve this goal in the past, lithium-drifted Ge detectors have been introduced, known as Ge(Li) detectors. The Ge(Li) detectors are

manufactured by adding lithium donor atoms to the Ge material. The donor lithium atoms exactly balance the acceptor impurities, resulting in a very low net impurity level. This allows the depletion region to be extended over the whole of the lithium drifted region. Nowadays high-purity Ge detectors are used. This became possible by advanced manufacturing techniques. High-purity germanium, or HPGe, has impurity concentrations of around one part in 10^{12}, allowing depletion depths of several cubic centimeters to be achieved. High-purity germanium detectors have also the advantage with respect to Ge(Li) detectors, that they can be stored at room temperature. Ge(Li) detectors must be stored at 77 K, to prevent lithium drifting out of the depletion volume, which destroys the detector. However, when HPGe detectors are exposed to neutrons, as in-beam spectroscopy experiments, they should be permanently cooled as well, to keep the effects of neutron-damage small. In HPGe neutron scattering causes dislocation defects in the crystal. The levels produced by the dislocations in the paring gap become occupied by electrons under normal experimental conditions. These electrons are released if the crystal is warmed up to room temperature. On recooling the crystal, electrons trapped by the now empty dislocations produce a low-energy tail to γ–ray photo peaks. The normal cure for this is to place a strong γ–ray source in front of the detector to produce enough electrons to fill the electron traps caused by the dislocations from the neutron damage. To make the electric field in the Ge detector as homogeneous as possible, the front edge of the crystal is rounded off. State-of-the-art Ge detectors have active volumes of approximately 450 cm^3.

The average energy of an electron-hole pair in Ge is 2.96 eV. Thus an incident γ–ray, with an energy of several hundred keV, produces a large number of electron-hole pairs in the Ge detector, leading to a good energy resolution due to low statistical fluctuations. This is the most desirable property of the HPGe detectors. HPGe detectors operate at a temperature of around 77 K, in order to reduce the noise of electrons which may be thermally excited across the small band gap of 0.665 eV in Ge at room temperature. The cooling is achieved through a thermal contact of the Ge crystal with a Dewar of liquid nitrogen, using a copper rod known as a “cold finger”.

2.9.1 AFRODITE array

AFRODITE *is an acronym* standing for *AFRican Omnipurpose Detector for Innovative Techniques and Experiments* [New98]. The AFRODITE array comprises two sets of High Purity Germanium (HPGe) detectors; Low Energy Photon Spectrometers (LEPS) and CLOVER detectors. A photograph of AFRODITE is shown in Figure 2:6. AFRODITE detectors are supported by a rhombicubioctahedron shaped aluminum frame with 18 square and 8 triangular faces. For the experiments discussed on this work, the two faces at 0^o and 180^o of the support frame with respect to the beam direction were occupied by the beam pipe and the recoil detector chamber. One square face at 90^o with respect to the beam direction is used for the target system. The remaining 15 square faces are usually available for mounting of detectors as shown in Figure 2:6. The nine CLOVER detectors of the AFODITE array have a total photo-peak efficiency of $P_{ph} = 0.016$ for the 1.33 MeV γ–ray transition of ^{60}Co.

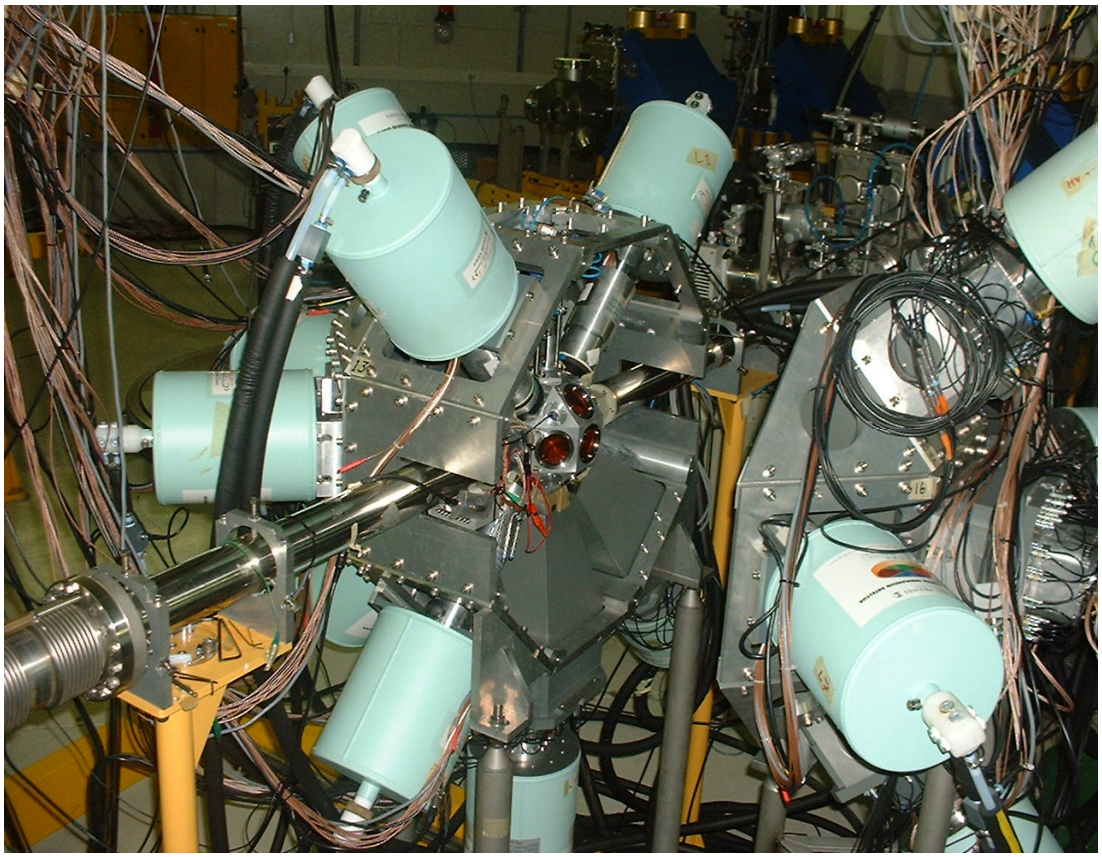

Figure 2:6. Photograph of the AFRODITE array with mounted gamma detectors (LEPS and CLOVER detectors).

2.9.2 CLOVER detectors

The CLOVER detector was developed for the γ-detector array EUROBALL [Lie97, Mos91, Nol94]. A photograph of the CLOVER detector is shown in Figure 2:7. It is a composite detector consisting of four separate n-type coaxial HPGe crystals which are arranged about 0.2 mm apart [Jon95] as shown in Figure 2:8. The Ge crystals with dimensions of 70 mm in length and 50 mm in diameter have a 36 mm tapering length and a front width of 41 mm. Four separate HPGe crystals are packed in a common cryostat as shown in Figure 2:8 and they are called elements of the CLOVER detector. These elements provide a large photo peak efficiency as well as high multiplicity because of their granularity. Each CLOVER element has its own electronics to ensure independence. The granularity of the CLOVER detector decreases Doppler broadening effects. Ultimately, CLOVER detectors are coupled to an automated liquid Nitrogen (LN_2) filling system which fills their Dewars after every twelve hours.

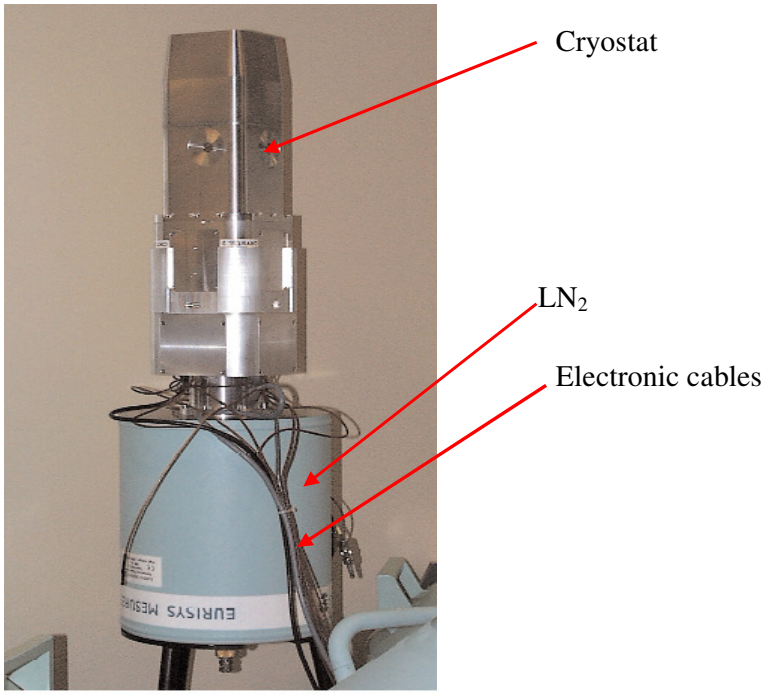

Figure 2:7. Photograph of a CLOVER detector, showing the tapered rectangular cryostat, the cylindrical liquid nitrogen (LN_2) Dewar and the cabling of the built-in preamplifiers for the four elements. Photograph taken from AFRODITE.

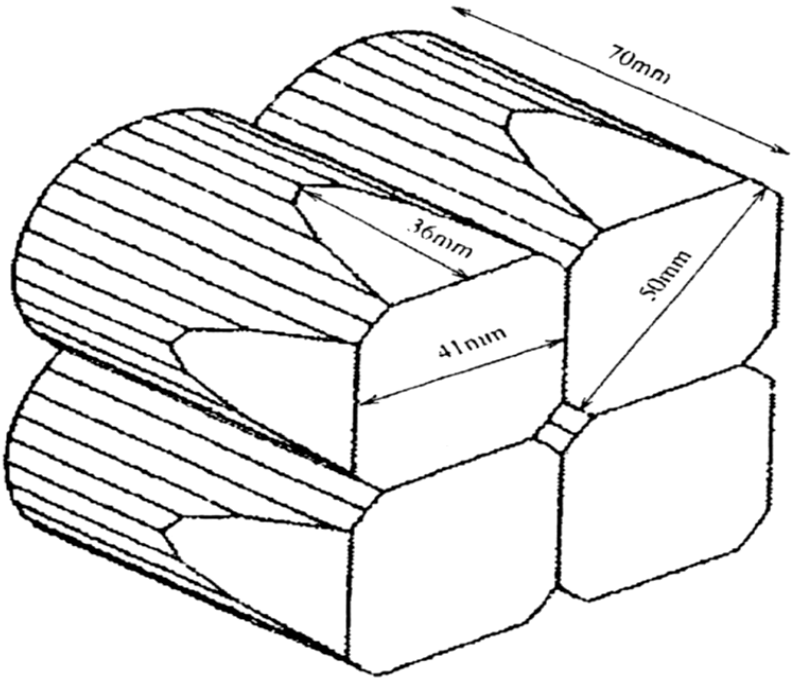

Figure 2:8. Schematic sketch of the four separate n-type coaxial HPGe crystals comprising the CLOVER detector [Jon95].

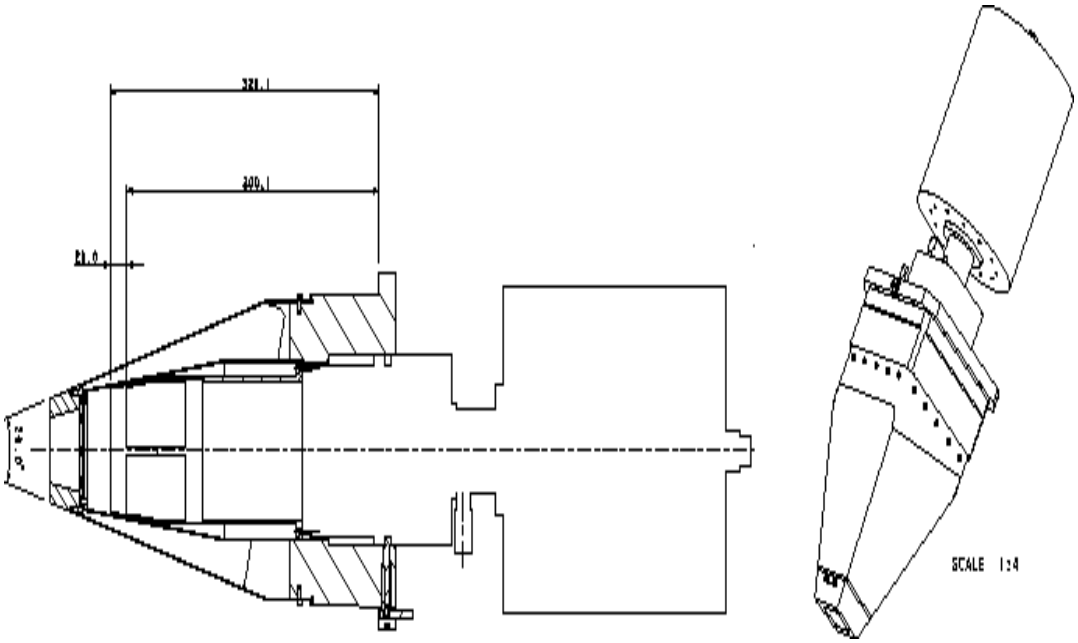

Figure 2:9. Schematic sketch of the CLOVER detector with its Compton-suppression shield (left) and a 3D view (right). Taken from [Hib93].

Specifications of the CLOVER detector [Lie97, New98]:

- Distance from the crystal surface to the target centre: $D_{tc} = 196\,\text{mm}$
- Distance from the detector end-cap to the crystal surface: $D_{ec} = 20\,\text{mm}$
- Total opening angle: $\Theta = 23.2^{\circ}$
- Solid angle per detector: $\Omega_{Ge} = 1.34\%$ of 4π (for a 0.2 mm distance between crystals)
- Photo-peak efficiency (for 1.33 MeV): $\varepsilon_{ph}\,\Omega_{Ge} = 17.8 \times 10^{-4}$
- Add-back factor (for 1.33 MeV): 1.56
- Peak-to-total ratio (for 1.33 MeV): $(P/T)_{Ge} = 0.30$

2.9.3 LEPS detectors

LEPS detectors consist of a single p-type HPGe crystal with dimensions of 60 mm diameter and 10 mm thickness which is electrically segmented into four quadrants. The LEPS detectors are most suitable for the detection of low energy γ–rays due to their high relative efficiency at low energies (30-300 keV). The Dewars of the LEPS detectors are filled with liquid nitrogen (LN_2) every 24 hours. Figure 2:10 shows a photograph of a LEPS detector. It is worth mentioning that in these experiments, NORDBALL LEPS detectors were used in addition to the iThemba LABS LEPS detectors. Unlike the iThemba LABS LEPS detectors, these LEPS detectors are not segmented.

Figure 2:10. Photograph of a LEPS detector.

Specifications of the LEPS detectors [New98]:

- The distance from crystal surface to the target centre: $D_{tc} = 119\,\text{mm}$ for a 4 mm gap between the target chamber and the end-cap.
- The distance from the detector end-cap to the crystal surface: $D_{ec} = 15\,\text{mm}$
- The total opening angle: $\Theta = 28.3^{\circ}$
- The solid angle per detector: $\Omega_{Ge} = 1.57\%$ of 4π
- Photo-peak efficiency: $(P/T) \approx 0.48$

2.10 AFRODITE electronics and data acquisition system

The block diagram of the AFRODITE electronics is shown in Figure 2:11. In the experiments studied in this work, eight CLOVER detectors and iThemba LEPS plus two NORDBALL LEPS detectors were used. As discussed in section 2.9.2, the CLOVER detectors provide four channels corresponding to each crystal. The signals from the LEPS detector preamplifiers were then amplified by CAEN N568 amplifiers. These amplify and shape the LEPS detector signal in a form compatible with both linear and fast signals. The fast signals produced by the amplifier were fed into a Constant Fraction Discriminator (CFD) where they were transformed from analog into logic signals. These were then fed into a FAN IN circuit connected to a Gate and Delay Generator (G&DG). The FAN IN unit was operated in an OR mode for the input signals from the four elements of a LEPS detector. The ORed LEPS detector signals were fed into a multiplicity unit which produced a selectable logic output signal depending on the number of multiplicity inputs that have fired. The fast signals were also fed into a second Gate and Delay generator (G&DG) which delayed the signals until the arrival of a start signal for the 4418/T TDC, where the LEPS times were measured.

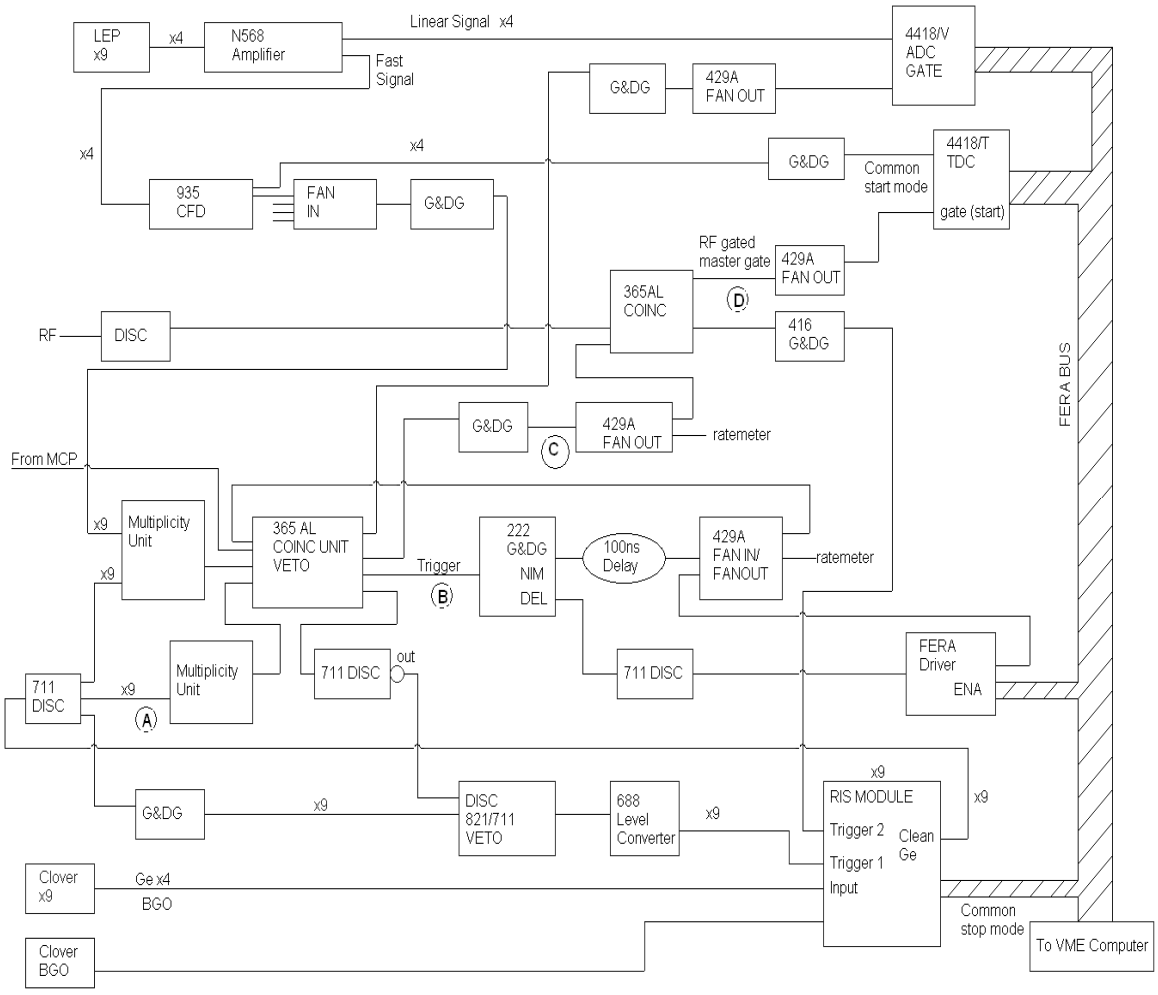

Figure 2:11. Block diagram of the AFRODITE array electronics.

The RIS modules perform the signal processing for the CLOVER detectors. These modules have integrated circuits, which perform many of the functions already described for the LEPS detectors, in one unit. As shown schematically in Figure 2:12 and Figure 2:13, respectively, the RIS modules include the standard fast–slow processing circuits as well as a circuit to create a veto signal, if a Ge and a BGO detector fires, to suppress Compton-scatter events and to produce a "clean Ge" signal. The "clean Ge" signal was fed into the trigger logic consisting of two multiplicity units, the first of which was set to two for these experiments, i.e. for an event to be counted the trigger demanded that a suppressed CLOVER detector had fired. The second unit also accepted logic signals from the LEPS detector. The output from both multiplicity units can be "AND"ed in the 365 AL coincidence unit. In this way, more

complex trigger conditions can be demanded. Once the trigger signal was generated, it was fanned out to the various ADC'S and TDC's and RIS modules. In one branch, Silena 4418/V ADC modules were gated to digitize the energies of the LEPS detectors. Another branch enables the digitization of energy and time in the RIS module by routing the clean Ge signal of the RIS module back, into its "trigger" input, which initiates the module to commence conversion.

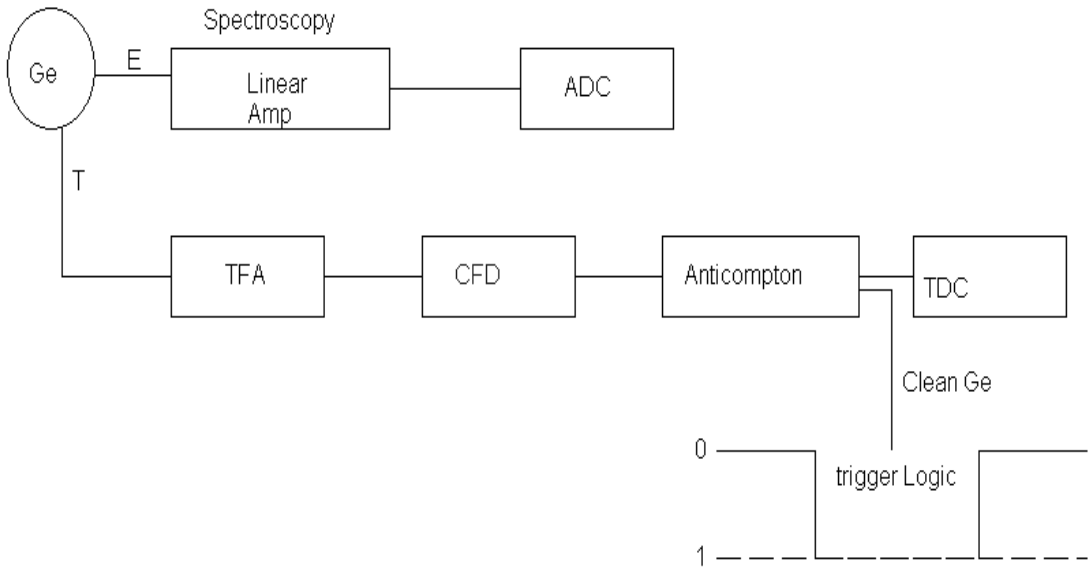

Figure 2:12. Part of the electronics which processes signals from the CLOVER detectors in the RIS modules.

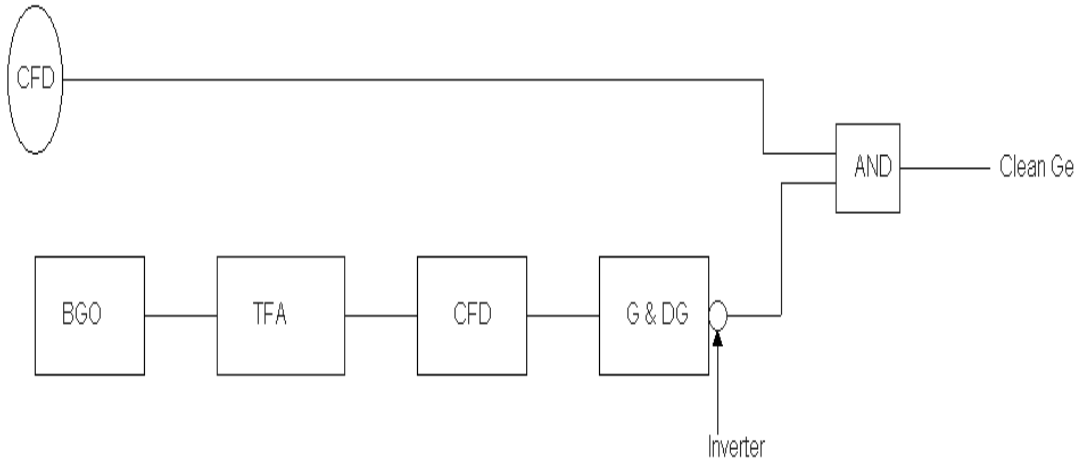

Figure 2:13. The Compton-suppression electronics of the RIS module using the BGO-detector signals.

A further branch of the trigger logic was used to create a radio-frequency (RF) gated trigger signal, being used both to gate the various TDC modules and to provide a time reference. The timing diagram is shown in Figure 2:14. The cyclotron RF signal provides the time reference. The pulse selection was 244 and 341 ns for ^{230}U and ^{232}U measurements, respectively. The arrival of two clean Ge signals at the coincidence unit, Ge1 and Ge2, generates a trigger signal, which is true during the time when both logic signals overlap. The width of the clean Ge signals was set to half the time between beam bursts, in this case about 180 ns. This defines the coincidence window. In this example, Ge2 is delayed with respect Ge1, and a delayed trigger signal is generated at B (*see Figure 2:11*). The trigger signal is stretched by a gate and delayed generator at C and gated with the RF signal to produce the RF-gated trigger signal at D (*see Figure 2:11*). This signal was fanned out to the TDC modules (4418/T) of the LEPS detectors, where it serves as a "common start" for the time measurement in the TDC. The individual timing signals were delayed such as to arrive after the common start, and each signal "stops" the TDC allowing the time to be measured. The RIS modules also have an internal TDC, which operates in a common Stop mode. The RF gated trigger is used as the common stop, by applying it to the trigger 2 input. The RIS and 4418/T (TDC) and 4418/V (ADC) modules are readout via a FERA BUS by a VME module called F2VB and the data are sent to a Linux workstation. This workstation allows the RIS modules to be controlled and to write the data to tape.

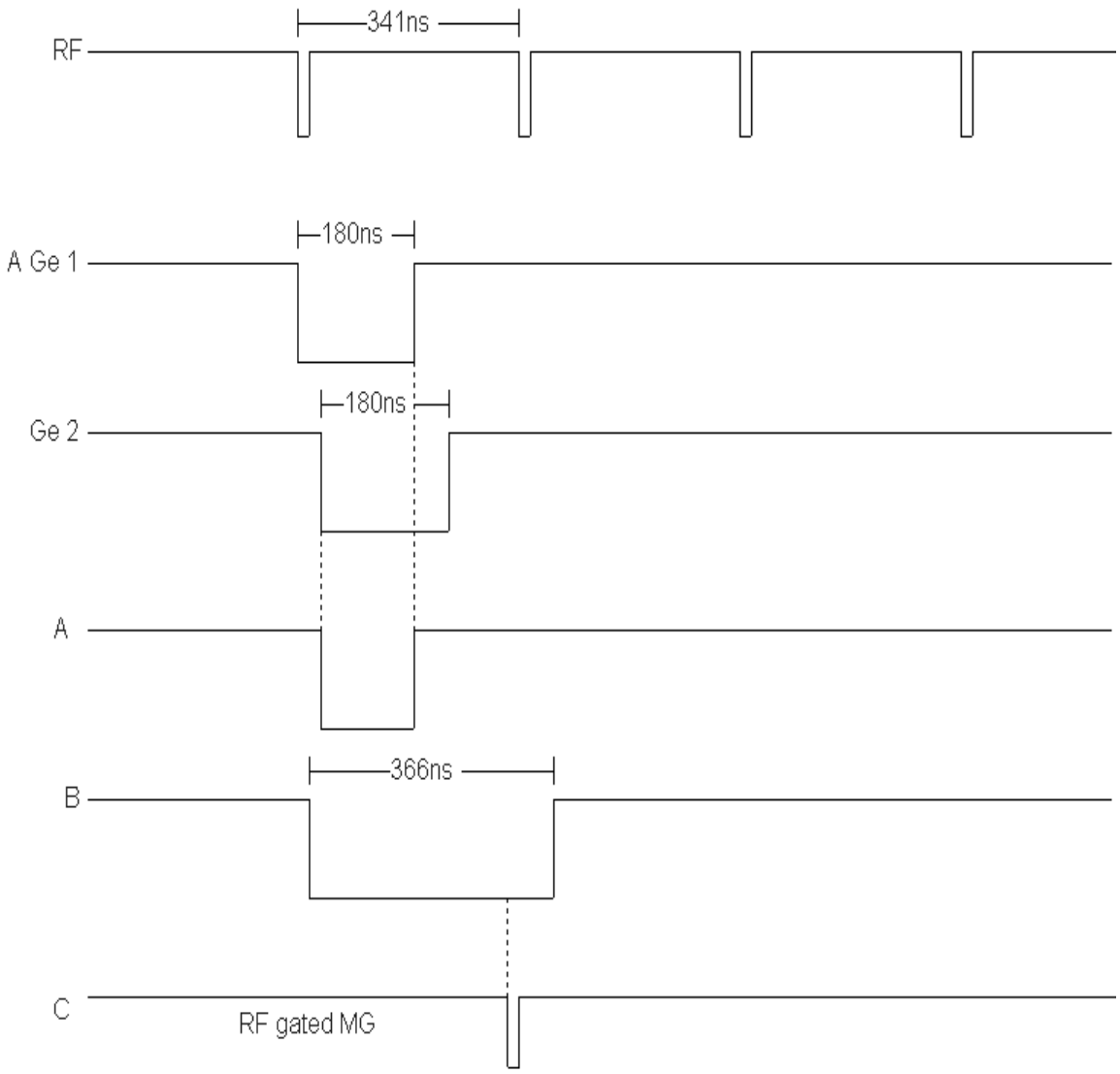

Figure 2:14. The RF time signal in coincidence with the Germanium detector time signal.

CHAPTER 3 DATA ANALYSIS METHODS

The data acquired during the experiments have been stored onto the magnetic Digital Linear Tapes (DLT). At the end of each experiment the data is dumped from the tapes to disc where the data can be replayed to transform the event data to suitable forms in order to facilitate the analysis. Before or after the experiment is performed the following processes have to be done in order to understand the data and ultimately construct a coincidence matrix *(discussed in section 5.1).*

3.1 Energy calibrations

At iThemba LABS, beamtime is only available on weekends for physics experiments. Therefore all the measurements discussed were performed over weekends. The energy calibration data were obtained before and after each weekend of the experiments in singles mode using ^{152}Eu and ^{133}Ba radioactive sources. Before the measurement, each of the above mentioned sources were placed independently in front of the detectors such that all the detectors can detect the γ–rays emitted by the source. The data were collected for about thirty minutes per run and the data was saved for both CLOVER and LEPS detectors.

Thereafter, centroids of the photopeaks from saved source (^{152}Eu and ^{133}Ba) spectra were determined using the SFIT program. This program finds the centroids of the ^{152}Eu and ^{133}Ba sources automatically and those that it fails to fit are normally determined by using the GF3 program [Rad95]. Unlike the SFIT program the GF3 program allows the user to manually fit the peak and find the centroids. The centroids were then fed to the SCAL program which fits an energy calibration to each detector, in the form $E = a_0 + a_1 x + a_2 x^2$, where x is a channel number. Thereafter the program named DOP_COR was used to determine the gain matching coefficients, which map the channels to calibration of $E = 0.5x'$ keV, $E = 0.2x'$ keV for CLOVERS and the LEPS respectively, where x' are new channels as shown in Figure 3:1. The DOP_COR program gives the option of including the Doppler shift correction.

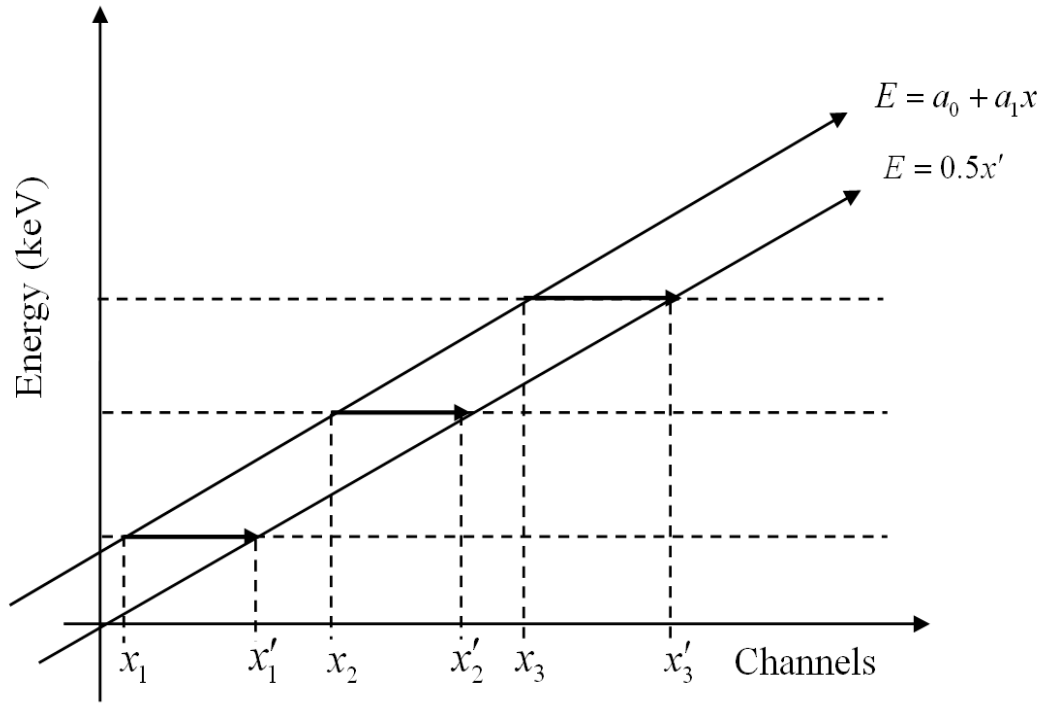

Figure 3:1. Shows how the energy calibration was performed. The arrows indicate mapping direction from one equation to the other with x' on the x-axis which shows the new channel ultimately used in the analysis in these measurements.

3.2 Doppler shift correction

The Doppler-shift corrections for the detected γ–rays were necessary in both measurements since thin targets were used. The recoiling residual nucleus emits γ–rays subjected to an energy shift given by

$$E_\gamma = E_0(1 + \beta \cos\theta) \tag{3:1}$$

where E_γ is the Doppler shifted γ–ray energy, E_0 is the unshifted γ–ray energy, $\beta = v/c$ (v is the recoil velocity of the nucleus and c is the speed of light) and θ is the angle between the detector and the beam axis. Doppler shifts for the emitted γ–rays were measured using the CLOVER detectors located at 135º. The Doppler shift was obtained by setting $\beta = 0$ and obtaining the shift in energy of the well known strong peaks of the recoiling nucleus and using equation (3:1) to calculate a correct β.

The calculated average β for experiments 1 and 2 were 0.93% and approximately 0.2%, respectively (*see* Table 2:2).

3.3 Gain drift corrections

The in-beam data stored on the disc were sorted in order to trace any possible gain drifts that might have occurred during the execution of the experiments. Investigation lead to the conclusion that there were some gain drift almost every eight hours in experiment 1. Figure 3:2 shows how the gain changed with time. Investigation into the source of such gain drift has been done by Ntshangase et al., [Nts07]. It was established that temperature variations in the AFRODITE vault might have an effect on the amplifiers and the rest of the electronics such that drifts occurred in the output signals. Therefore gain drift corrections were done before any data analysis. The corrections were done by using a correctly calibrated spectrum obtained from the first runs of the experiment, referred as in-beam reference spectrum (IRS). Well known strong peaks like the 511 keV, tungsten X–rays were used to choose IRS and to correct the drift. All data runs were collected in a GF3.spe file and were compared. Ultimately every eight hours worth of data had its own coefficients and the data was presorted to the disc.

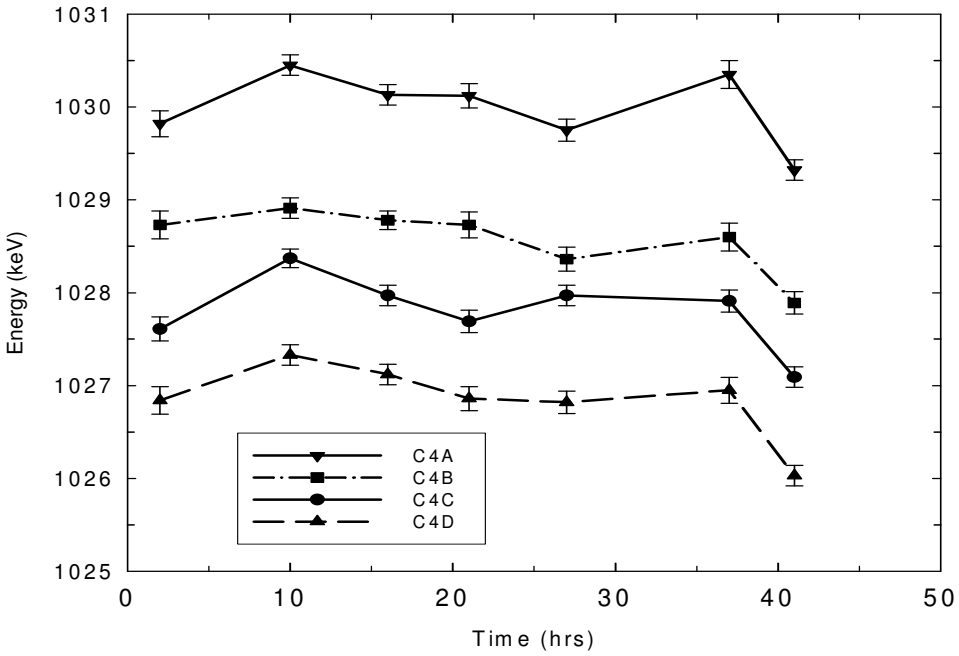

Figure 3:2. Plot showing the gain drift in the four elements of CLOVER 4 caused by temperature variation.

3.3.1 Addback

Both iThemba LABS CLOVERS and LEPS detectors are made up of four crystal elements as discuss in section 2.9.2. Gamma rays can be fully absorbed in a single crystal or can be first detected in one crystal and Compton scatter to another crystal where it can in turn get detected. The energy deposited to the first crystal can be added to the energy deposited in the second crystal to recover the total energy. This technique is called addback and is very important in increasing the photo peak efficiency.

3.3.2 Efficiency calibration

The efficiency calibration measurements of the AFRODITE CLOVER and LEPS detectors were performed at the end of the experiments by using ^{152}Eu and ^{133}Ba radioactive sources. Unlike the energy calibration discussed in section 3.1, when performing the efficiency calibration the source must be positioned exactly at the target position one at a time. The data were recorded event-by-event and later sorted offline, in order to obtain the addback of the energies deposited to different individual crystal elements. The relative efficiency curves for various AFRODITE settings, for different experiments discussed in CHAPTER 2, are shown in Figure 3:3. The efficiency was fitted to the equation (3:2).

$$In(eff) = \left[\left(A + Bx + Cx^2\right)^{-G} + \left(D + Ey + Fy^2\right)^{-G}\right]^{1/G} \qquad (3:2)$$

where A, B and C describe the efficiency at low energies and D, E and F describe the efficiency at high energies. The parameters x and y are given by equation (3:3) and (3:4) respectively. G is an interaction parameter between the low and high energy region and it determines the efficiency in the turn over region.

$$x = \log(E_\gamma / 100) \qquad (3:3)$$

$$y = \log(E_\gamma / 1000) \qquad (3:4)$$

The relative efficiency for all the curves were obtained using the RADWARE Software Effit program [Rad95]. The efficiency for CLOVERS and LEPS

respectively drop at energies below 150 keV and 100 keV. The maximum detection efficiency for CLOVERS occurs at 150 keV and at 100 keV for the LEPS detectors. It decreases monotonically with increase in as shown in Figure 3:3. This decrease in efficiency on both detectors is caused by the decrease in cross-section of both the photoelectric effect and Compton scattering as a function of γ–ray energy.

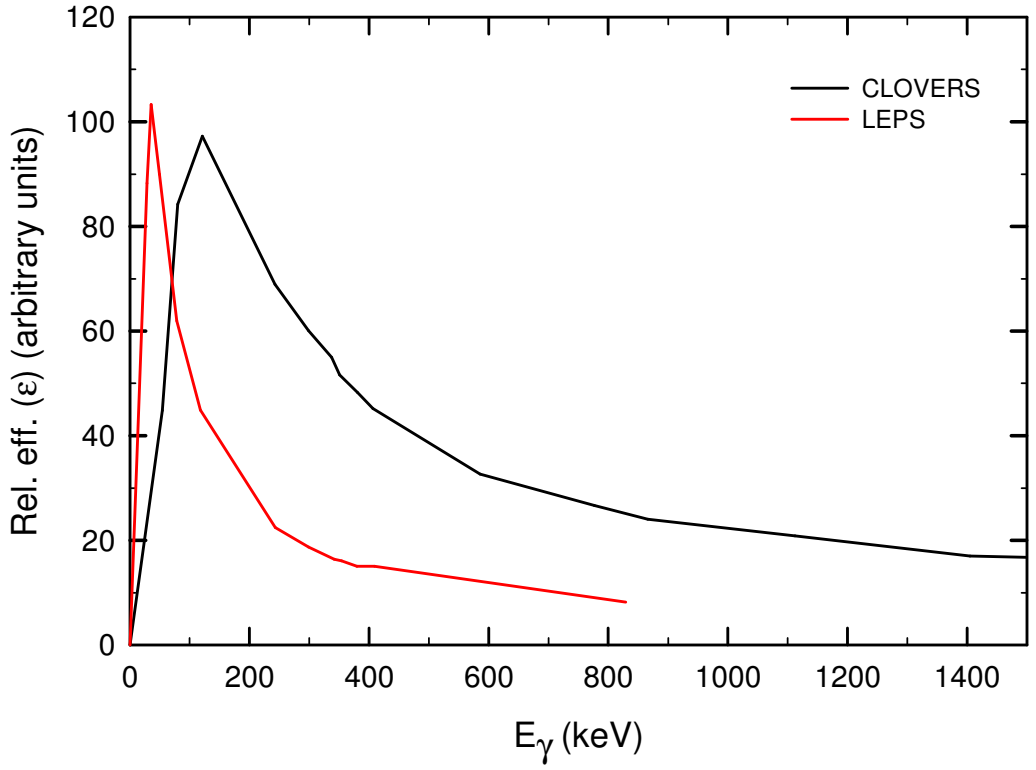

Figure 3:3. The relative efficiency (ε) for the 8 LEPS and 8 CLOVER detectors measured with ^{133}B and ^{152}Eu radioactive sources mounted on target position.

3.4 Transition intensities

Measured γ–rays intensities play a very important role in determining the branching ratios, $B(E1)$ and $B(E2)$, which in this work will be used to test the tetrahedral predictions. The intensity of a γ–ray transition (I_γ) is given by:

$$I_\gamma = \frac{S}{\varepsilon} \qquad (3:5)$$

where S is the area under the γ–ray peak and ε the efficiency of the detector for a γ–ray (discussed in section 3.3.2). The total transition intensity, I_t is given by:

$$I_t = I_\gamma(1+\alpha) = \frac{S}{\varepsilon}(1+\varepsilon) \tag{3:6}$$

Where α is the electron conversion coefficient which gives the probability of electron emission relative to γ emission [Kra88] defined as:

$$\alpha = \frac{I_e}{I_\gamma} \tag{3:7}$$

The electron conversion coefficient ranges from very small to very large values. The internal conversion coefficients for U are shown in Figure 2:3.

3.5 Time calibration

The desire to make all prompt time peaks for both CLOVER and LEPS detectors to be at the same position i.e. channel 1000, requires a time calibration as shown in Figure 3:4. Therefore the time was calibrated by finding the prompt peak position and the separation of the beam pulse using GF3 program. Knowing the RF frequency the separation in terms of seconds can be known. Therefore the separation of the successive beam pulses in terms of channels and in terms of time can be used to calculate the slope (m) in channels/seconds units. The separations between the beam pulse was about 341 ns for experiment 2. These pulses have smaller amplitudes than the "prompt" peak since they are caused by γ–rays being detected outside the co-incidence window and they can be seen in Figure 3:4.

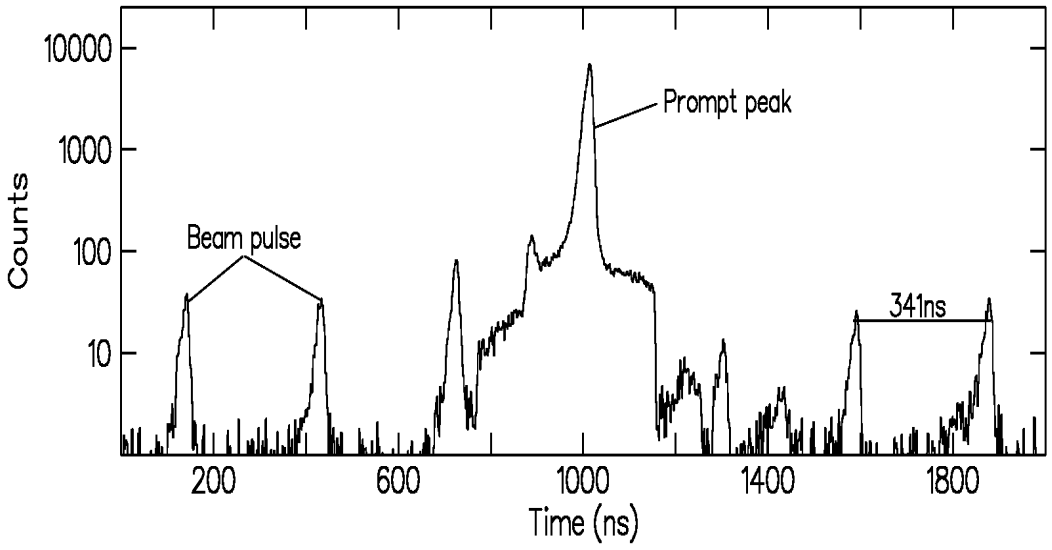

Figure 3:4. Time spectrum.

Figure 3:5 shows how the time gain matching was performed. First, the time dispersion, m, was determined from the separation of the peaks in the spectrum. The slope m can be obtained by using

$$m = \frac{341ns \times number\ of\ \ pulses}{(x_i - x_f)} \tag{3:8}$$

where x_i and x_f are the centroids of the initial and final time peaks. The prompt peak at channel x_0 was assumed to occur at time $t_0 = 1000$.

One has to map the time $t = mx + C$ onto $t = x'$, where x' are the new channels and C is constant. In order to determine x' the two equations can be equated since the time interval are equal.

$$x' = t = mx + C \tag{3:9}$$

$$t_0 = 1000 = mx_0 + C \tag{3:10}$$

From these equation C becomes

$$C = 1000 - mx_0 \tag{3:11}$$

By substituting equation (3:11) in equation (3:9) , one gets

$$x' = mx + 1000 - mx_0 \tag{3:12}$$

So finally

$$x' = m(x - x_0) + 1000 \tag{3:13}$$

Therefore using this method all the prompt peaks can be calibrated in such a way that they are positioned at channel 1000.

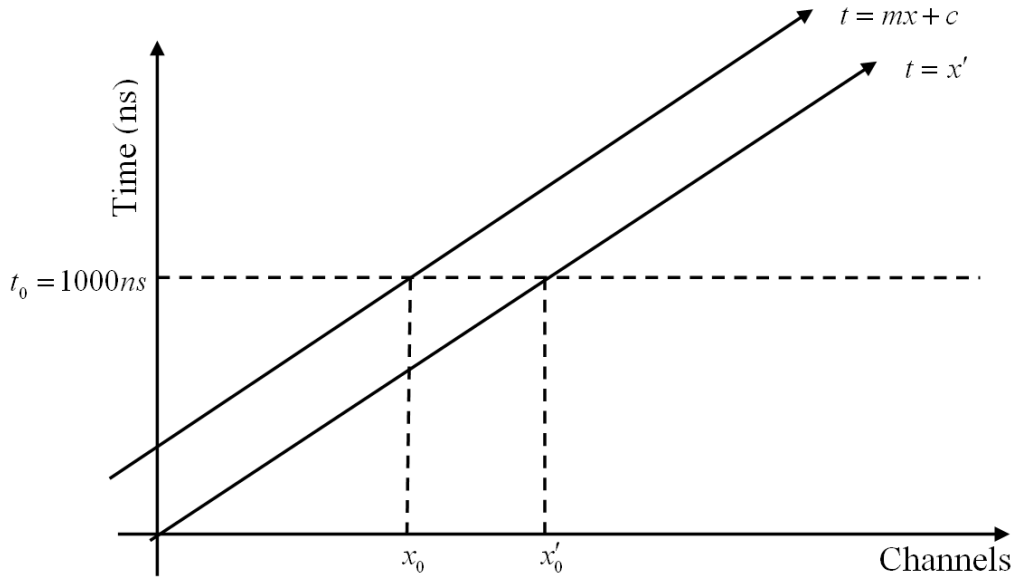

Figure 3:5. Time gain matching.

3.6 Coincidence matrices

As stated in CHAPTER 2, a very large number of data sets was collected during fusion-evaporation reaction experiments. After these data have been stored on magnetic tapes/hard drives, they then need to be sorted and converted into matrices compatible with the RADWARE software. A matrix is a two dimensional ($E_{\gamma 1}$, $E_{\gamma 2}$) energy histogram with the energy of one photon on one axis and the energy of a coincident photon on the other axis. In principle, when a gate is set on a particular photopeak using channel numbers from the total projection (ungated spectrum), a coincidence spectrum comprised of all the γ–rays in coincidence with it is observed. The calibration parameters discussed in sections 3.1 and 3.5 were used in the MTsort program [Cre06] which matched the energies and the times and updated a matrix. The total projection of the matrix is formed by the projection of all the counts onto one energy axis resulting in a one-dimensional γ–ray spectrum. Since the recoil detector was used together with AFRODITE, the matrices constructed demanded a γ–recoil condition. After a γ–recoil matrix has been created, it is necessary to convert the two dimensional spectra into a (.mat) RADWARE format [Rad95] which, can be analyzed

in GF3 program. The eg2mat program is used to do this conversion. The converted matrix or γ–recoil matrix with dimension of (4096×4096) channels has a dispersion of 0.5 and 0.2 keV (or channels) for CLOVERS and LEPS detectors respectively. These γ–γ matrices are used to construct the nuclear level schemes (discussed in section 5.1).

CHAPTER 4 ITHEMBA LABS RECOIL DETECTOR

4.1 Development of the iThemba LABS recoil detector

Currently at iThemba LABS only stable beams can be produced therefore the only way to study ^{230,232}U is to use the ^{232}Th(α, xn) reaction and measure the γ–rays from the evaporation residues using AFRODITE. Nevertheless AFRODITE alone is not sufficient to detect γ–rays from U evaporation residues as they are obscured by fission background and target X–rays. This is evident in Figure 4:1 which shows coincidence projection spectra obtained using the reaction ^{232}Th(α, xn) at beam energies of 42 MeV and 61 MeV using AFRODITE alone. The 106 keV and 140 keV lines are due to Th Coulomb excitation, the 198 keV line is an Al γ–ray and the 417 keV and 440 keV lines are from contaminants. The arrows indicate the locations of the relevant U transitions.

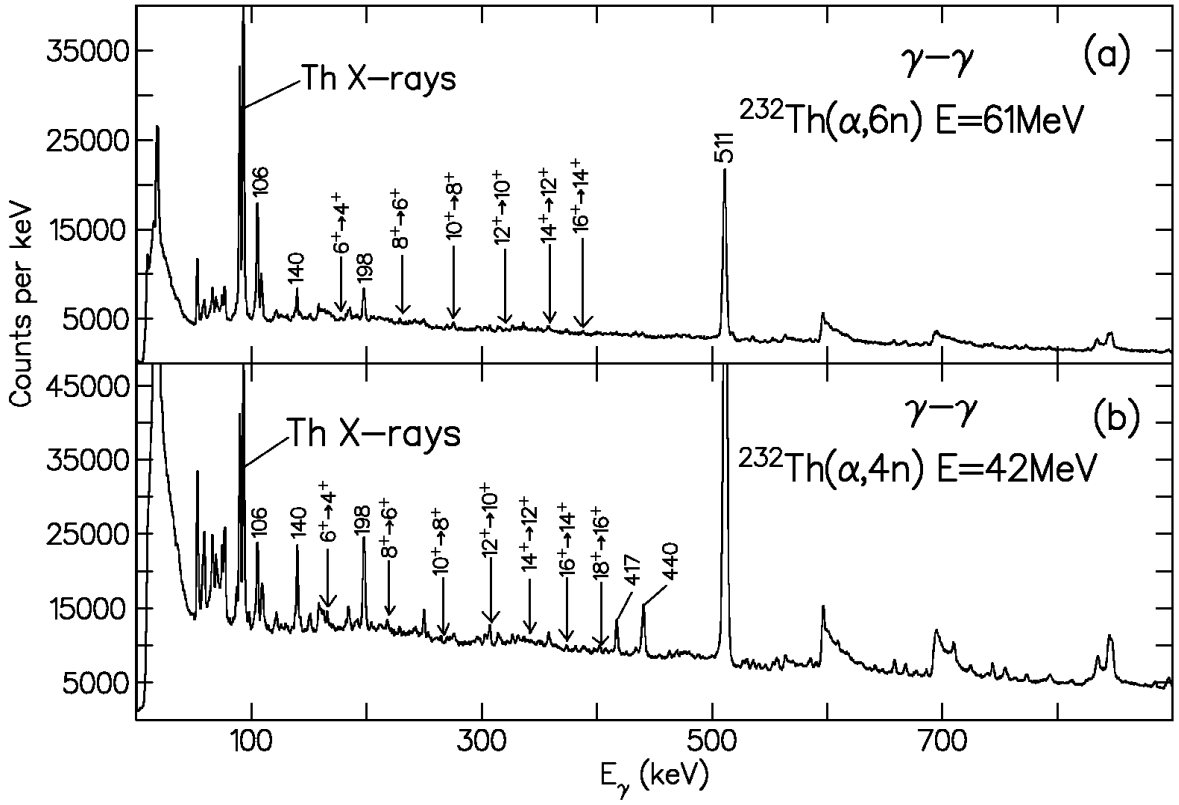

Figure 4:1. CLOVER energy total projection spectra obtained without the recoil detector in reaction ^{232}Th(α, xn) at beam energy 61 MeV and 42 MeV. The arrows indicate the energies of the relevant U transitions.

As stated above, the background from fission is too high such that it becomes impractical to effectively measure γ–rays from the evaporation residues with AFRODITE alone. In order to enable the detection of the weak evaporation residue signal produced in heavy-ion reactions, the fission background and target X–rays have to be reduced. To meet this requirement, a recoil detector which separates the fusion-evaporation residues from background was designed and developed to increase the sensitivity of AFRODITE. This chapter discusses the two versions of the recoil detector which were developed as part of this work. The first version is closely modeled on Ward's detector [War83]. However, this version presents a lot of challenges, as a result it could not suppress the background to the desired level. A second version had to be designed and developed from scratch. This newly designed recoil detector successfully reduced the background. The operation principles of both the Ward modeled recoil detector and the new recoil detector are outlined in this chapter.

4.1.1 Principle of operation

Recoil detectors have been used extensively in the field of nuclear physics, [Bec94, Lei95, Lei97]. The recoil detector described in this thesis was designed at iThemba LABS based on the design of Ward et al., [War83] which in turn was based on the design of Zebelman et al., [War83, Zeb77]. A schematic drawing of the Ward design is shown in Figure 4:2. The recoil detector of Ward was able to reduce fission background to a useful level; its results are shown in Figure 4:3. This design was chosen because of its ability to detect low energy recoils, distinguish among ions, and its ability to fit into the already existing AFRODITE array at iThemba LABS. It operates on the principle that when a beam strikes the target, recoils and fission fragments are produced. The ions produced, recoiling out of the target, and scattered beam projectiles, are allowed to pass through a thin foil placed behind the target. The ions are distinguished from each other using their signal amplitudes and time-of-flight. The ion time-of-flight is measured relative to the Radio Frequency (RF) of the Separate Sector Cyclotron (SSC). When the ions pass through the foil, electrons are released, and they are accelerated in an electric field by applying a negative voltage to the foil and by grounding a grid behind it. The accelerated electrons are directed by a magnetic field onto a Micro Channel Plate (MCP) detector, where they are multiplied and detected. The time-of-flight of the ions is in a range of tens of nanoseconds for the

Po experiment. In the case of the U measurement, the time-of-flight was at the range of hundreds of nanoseconds. Therefore, an MCP was chosen because of its fast time response. The MCP has a time resolution better than 1 ns.

The number of electrons released in the foil is proportional to the energy loss (dE/dx) of the ions passing through the foil [Cle73]. The energy loss dE/dx is proportional to the square of the atomic number (Z^2) of the ions. This implies that a smaller number of electrons are released by low-Z projectiles of the beam compared to the heavy recoils and fission fragments, which means that the signals of the low-Z projectiles can be differentiated from those of the recoils and fission fragments using their amplitudes. However the recoils and fission fragments release almost the same number of electrons, so they have comparable signal amplitudes. However, both fission fragments and scattered beam can be rejected using the fact that recoils have quite different times of flight from the target to the foil. This makes the time-of-flight measurements fundamental for the recoil detector.

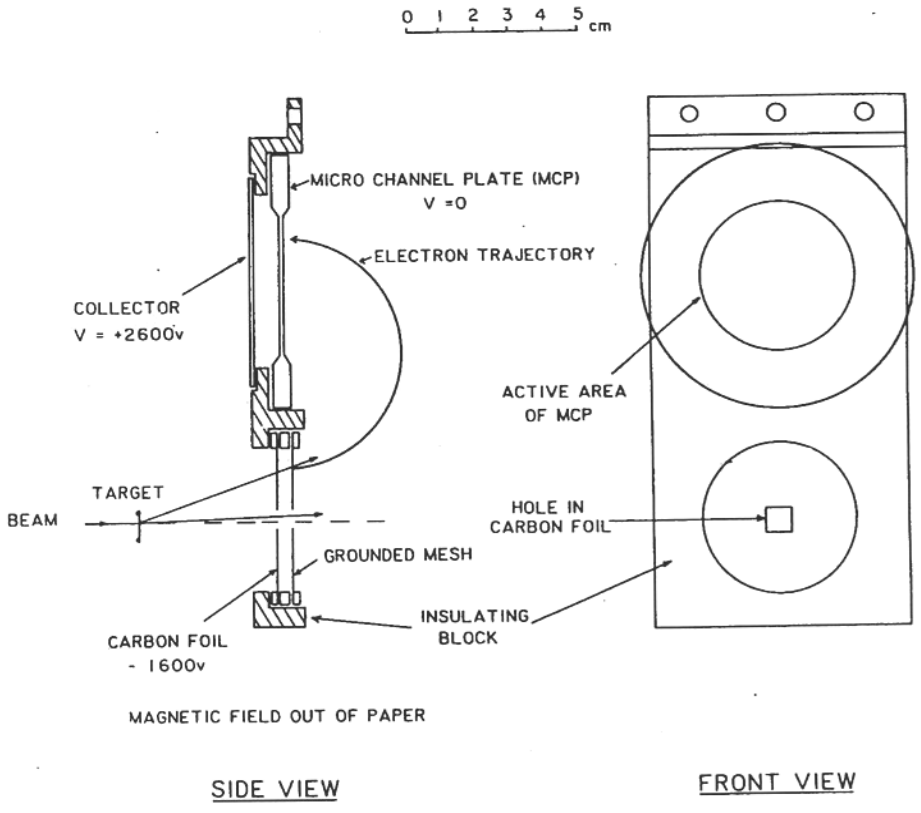

Figure 4:2. Schematic drawing of the recoil detector designed by Ward et al [War83].

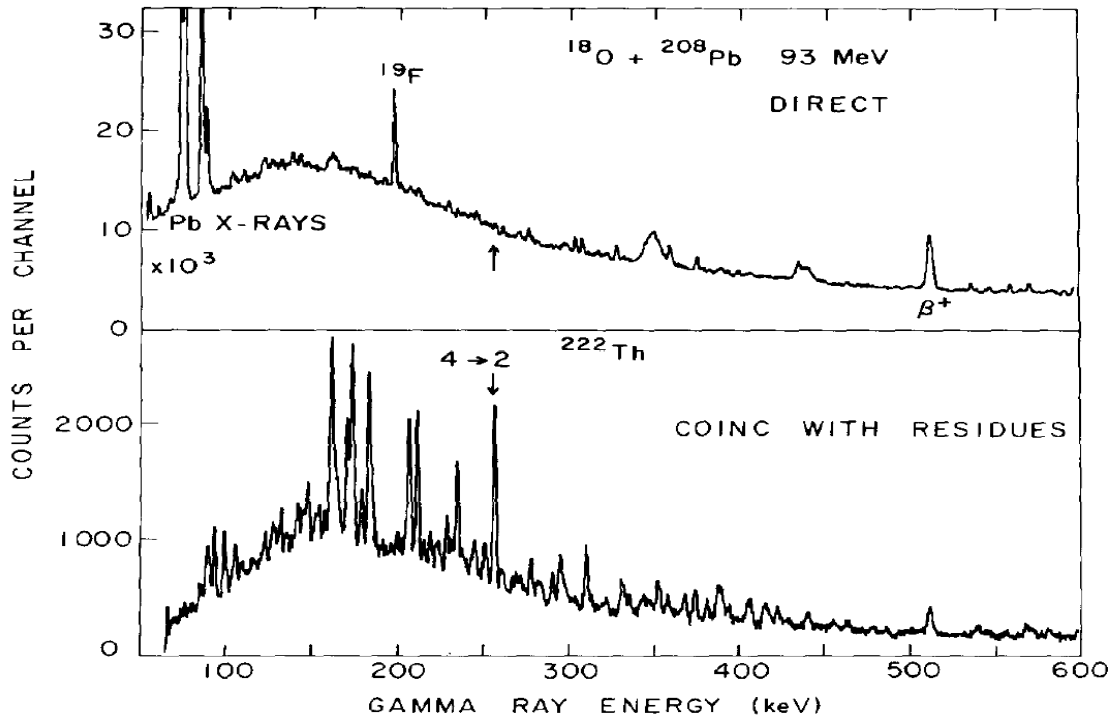

Figure 4:3. The direct γ-ray spectrum, and γ-ray spectrum in coincidence with residues for the reaction $^{208}Pb(^{18}O, 4n)^{222}Th$. The γ-ray peaks observed in coincidence were largely masked by high background in the direct spectrum. The arrow marks the expected position of the prominent $4^+ \rightarrow 2^+$ transition in ^{222}Th [War83].

4.1.2 Design considerations

When the recoil detector was designed it was essential to take the time-of-flight measurement into consideration. Since the reactions of interest are ^{232}Th (α, xn) reactions, therefore the ^{232}Th (α, 6n) ^{230}U reaction was used as the model reaction. The recoiling ^{230}U nuclei were calculated to have a velocity of v/c ~ 0.3% and a recoil energy of about 1 MeV. On the other hand, the alpha projectiles have a velocity of v/c ~ 19 % and the fission fragments have velocities of v/c ~ 4 % for energies of about 100 MeV. The calculated flight times of the various nuclei, using a distance of 65 mm between the target and the foil, for the ^{232}Th (α, 6n) ^{230}U reaction are: 1ns for the alpha projectiles, 5 ns for fission fragments and 68 ns (minimum) for the recoils. Clearly, by using this method, the different ions produced in a reaction can be distinguished.

The recoils produced by a light beam incident on a heavy target, as the ^{232}Th (α, 6n) ^{230}U reaction have very low energies. This determines the target thickness to be used in such kinds of experiments, since low-energy recoils produced in the reaction cannot escape from a target which is too thick. Therefore, the target thickness specifications were determined using the Monte Carlo code SRIM [Sri06]. Using the ^{232}Th (α, 6n) ^{230}U reaction it was established that recoils cannot escape from a target with a thickness greater than 200 μg/cm^2.

The recoils are produced along the beam path within the target. They are slowed down due to electronic scattering and deflected away from the beam direction by nuclear scattering. Since with the code SRIM one can only calculate the scattering of the incident particles (recoils) for a given thickness of target, SRIM calculations were carried out for a range of thicknesses and the average for all thicknesses was taken.

In order to maximize the acceptance angle, the recoil detector foil must be positioned as close as possible to the target. However, this distance is limited by the necessity to accommodate the AFRODITE low-energy photon LEPS detectors to be placed in close geometry. Therefore the foil was located 65 mm behind the target. The area of the foil is limited by the size of the Micro Channel Plate (MCP), since with a single dipole magnet it is not possible to focus electrons from a large foil onto a small MCP. The largest available MCP is of 75x93 mm^2 dimension; therefore the size of the recoil detector foil was chosen to have the approximately same dimension. The size of the MCP allows a maximum scattering angle of about 30º for the recoils in the target.

The MCP is rate limited to about 10^7 particles (or electrons) per second (pps). Allowing the beam to hit the foil will unnecessarily saturate the MCP. Therefore a hole was made in the foil centered around the beam line to allow the beam to pass through without hitting the foil. The disadvantage of this hole is that it results in the loss of geometrical efficiency for detecting the recoils and therefore its size must be accurately estimated in order to minimize the efficiency loss. Since the ion scattering depends on the energy of the projectile and its atomic mass, the size of the hole in the foil was calculated. The number of ions scattered as a function of angle was

calculated and the results are presented in Figure 4:4. In this plot the percentage of 11.1 MeV polonium ions scattered into a cone subtending a given scattering angle is shown for a tungsten target of 500 $\mu g/cm^2$ thickness.

Figure 4:4 and Figure 4:5 show examples of the calculated scattering angles in lab coordinates of the recoils and projectiles, respectively, for the $^{180}W(^{20}Ne, xn)^{196}Po$ reaction at a beam energy of 110 MeV. The produced ^{196}Po nuclei have a recoil velocity of v/c = 1.1%. In order to calculate the size of the hole, the SRIM code was used to calculate the effects of multiple scattering in the target, for the ^{20}Ne projectiles and for the produced ^{196}Po recoils. The size of the hole for the ^{20}Ne projectiles and the ^{196}Po recoils was calculated, assuming that the beam current is 1 pnA, which is equivalent to 6.25×10^9 pps. Since the MCP is rate limited to about 10^7 pps (particles per second), the hole must reduce the number of particles per second from 10^{10} pps to10^6 pps assuming that about 10 electrons are created and detected per ion. The scattering cone was calculated to have an opening angle of 10º, for which a fraction of only $\sim 2\times10^{-4}$ of the projectiles are scattered outside this angle as indicated in Figure 4:5. A hole in the detector foil corresponding to an opening angle of 10º results in a loss of 35% of the scattered recoils as shown in Figure 4:4. However the foil subtends an angle of 30º within which 85% of the recoils are scattered. Therefore, the geometric efficiency of the detector is 50%.

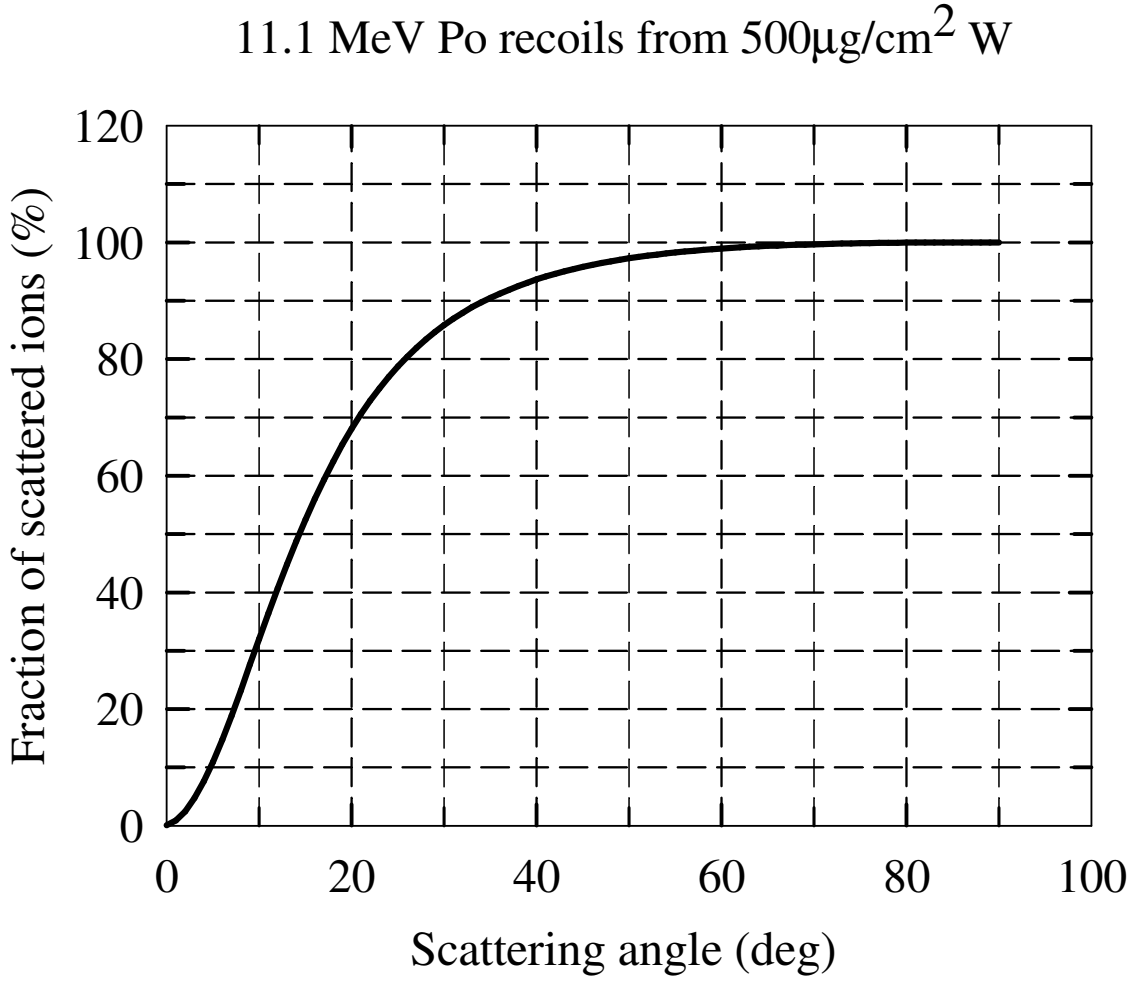

Figure 4:4. The percentage of ^{196}Po ions scattered through a given angle after passing the ^{180}W target plotted as a function of scattering angle.

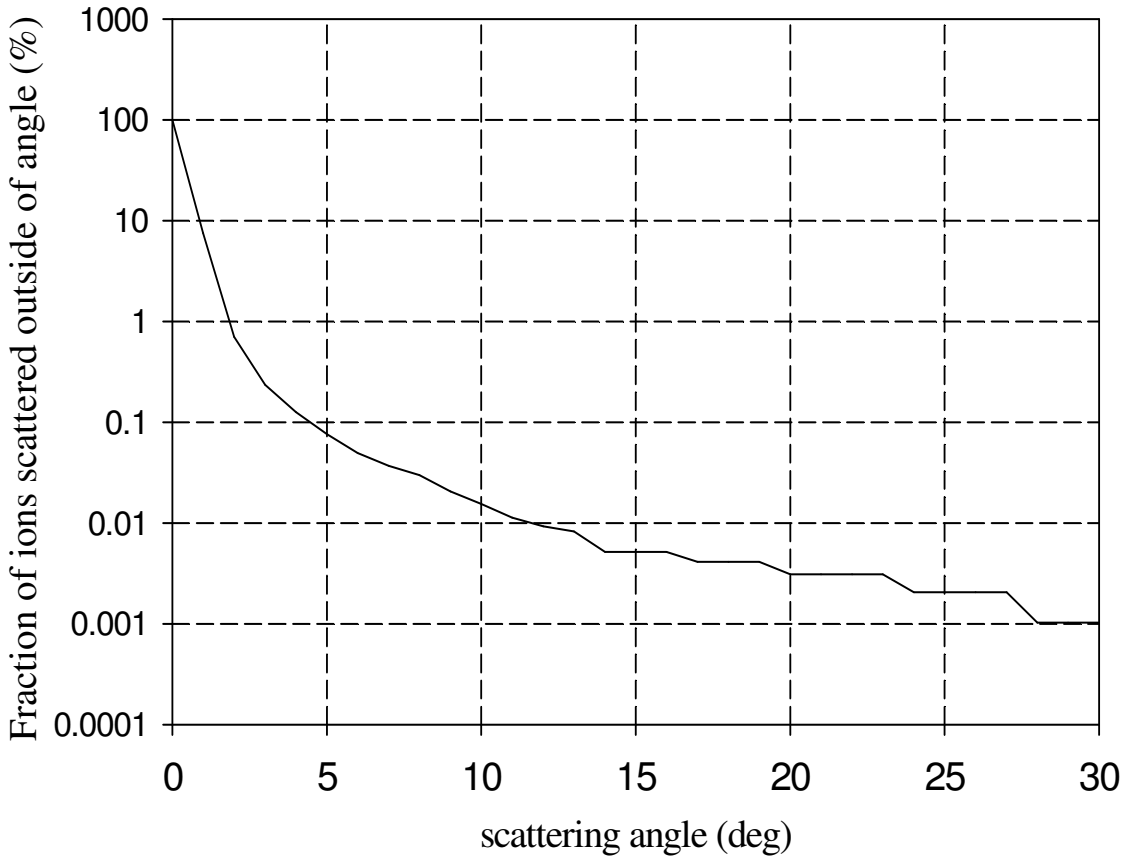

Figure 4:5. The percentage of scattered ions outside of angle, when ^{20}Ne passing through the target ^{180}W, plotted as function of angle.

In contrast, for the ^{232}Th(α, 4n) reaction a 150 μgcm^{-2} target was used and the average energy loss of the recoils is about 600 keV. For this reaction the SRIM calculations indicate that, at the maximum angle (30º) about 65% of the transmitted ions should strike the foil as can be seen in Figure 4:6. Figure 4:4 and Figure 4:6 show, that the scattering angles of the recoils also depend on the recoil energy. For example it can be noticed that, at a scattering angle of 20º, more ^{196}Po than ^{230}U particles are scattered. This is due to the fact that the nuclear scattering cross-section decreases with increasing recoil velocity [Lie09], considering the fact that v/c = 1.1% for ^{196}Po and 0.3% for ^{230}U. Furthermore the number of electrons produced is proportional to Z^2, since more electrons have a potential of saturating the MCP, beams of ions with larger atomic mass numbers i.e. A>20 are not suitable for the recoil detector, since the recoil

detection efficiency decreases with increasing projectile mass. It must be noted that the SRIM calculation for the Po does not take into account the spread in recoil velocities caused by neutron evaporation. However, the calculations are largely correct because the neutron evaporation would introduce a spread of only ~ ±6% to the velocities of the energetic Po evaporation residues. Unlike the $^{180}W(^{20}Ne, xn)^{196}Po$ reaction, the SRIM calculations for the $^{232}Th(\alpha, 6n)$ reaction shown in Figure 4:6 must be corrected for neutron evaporation. In this case, neutron evaporation changes the velocities recoils by approximately ±25%. Figure 4:7 and Figure 4:8 show the calculated time-of-flight for the $^{232}Th(\alpha, 6n)^{230}U$ and $^{232}Th(\alpha, 4n)^{232}U$ recoils considering only the straggling in the target.

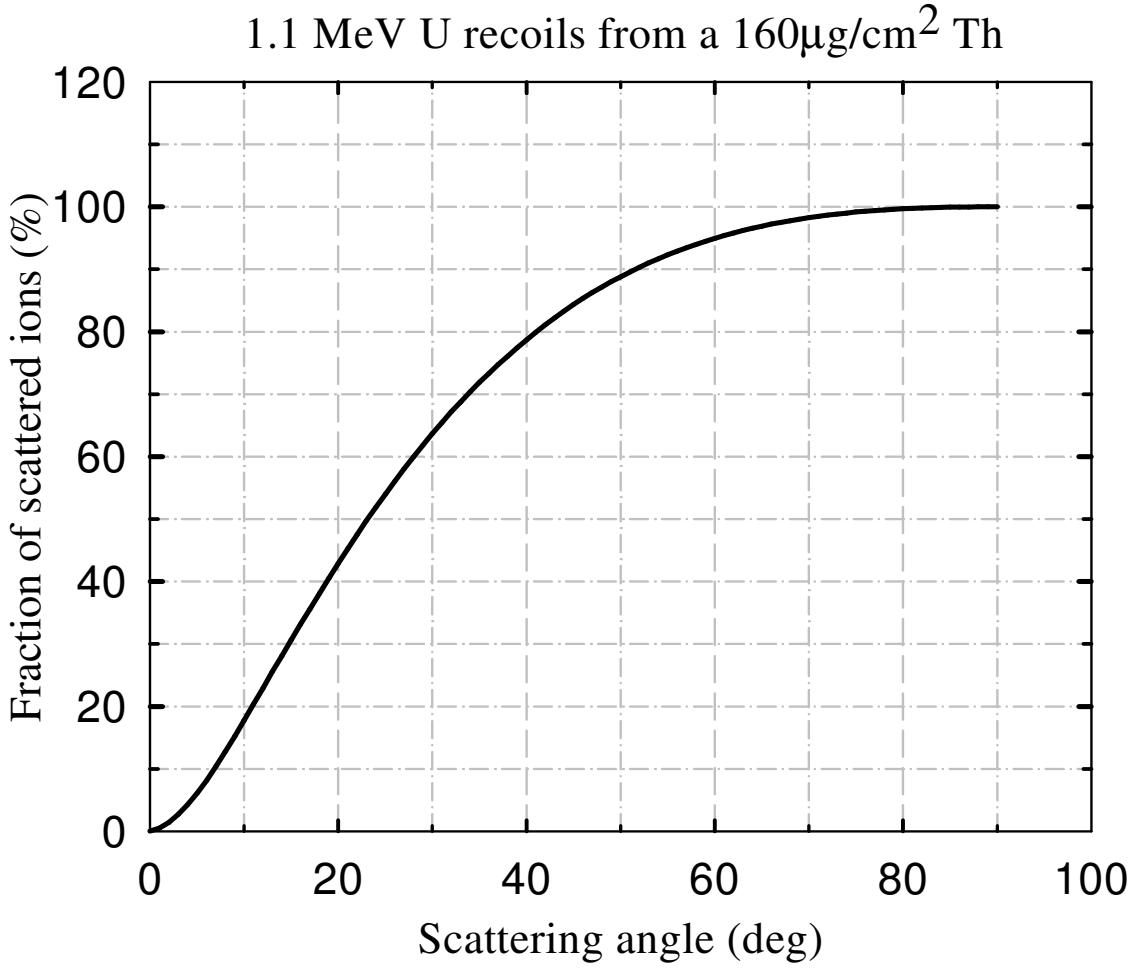

Figure 4:6. The percentage of scattered ions as a function of scattering angle in lab coordinates.

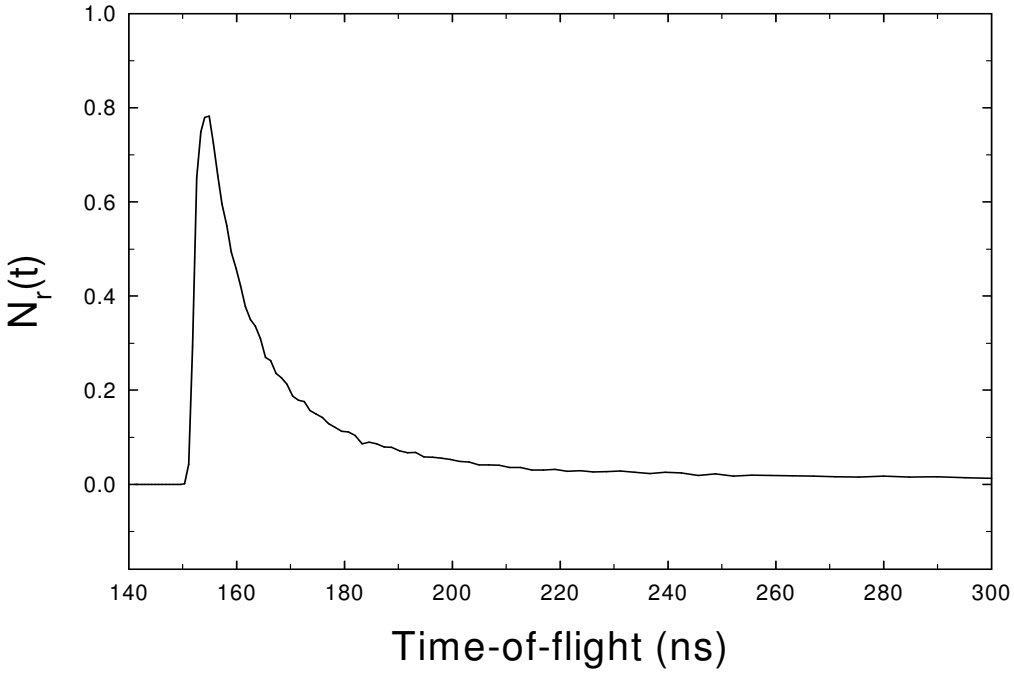

Figure 4:7.Calculated time-of-flight for the 1.06 MeV ^{230}U recoils using SRIM.

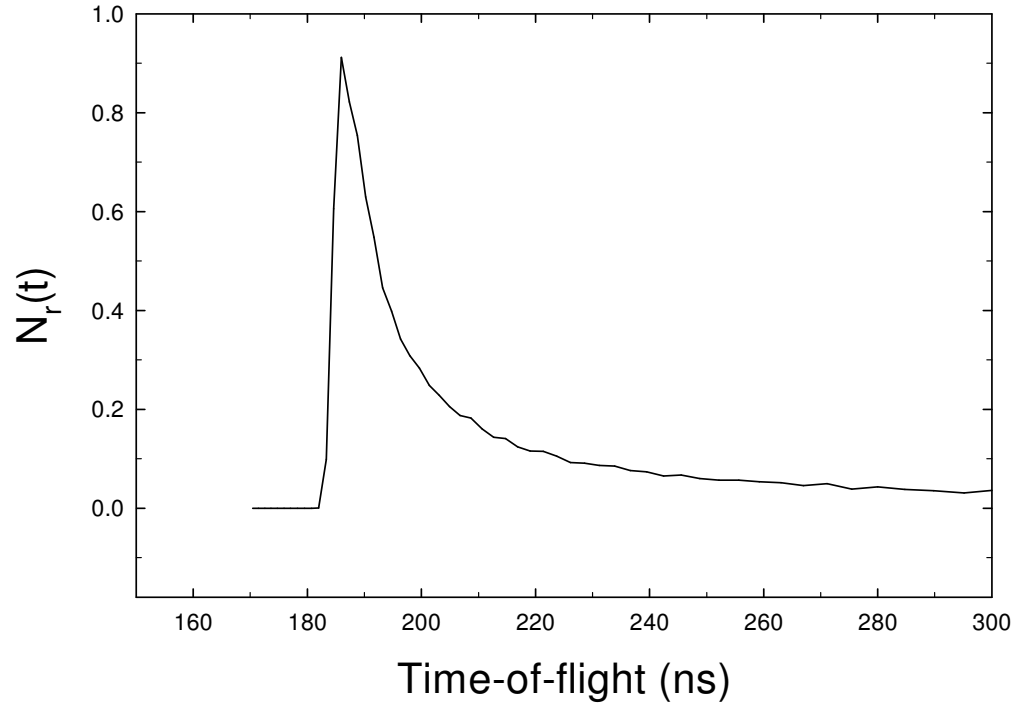

Figure 4:8. Calculated time-of-flight for the 0.725 MeV ^{232}U recoils using SRIM.

Assuming that the neutrons are emitted at a mean energy of 1.8 MeV (as given by PACE) and converting this energy into a neutron momentum, allows the recoil momentum for the evaporation residue to be calculated. This adds a spread to the initial recoil velocities of σ= 0.07% v/c. Thus there is a distribution of initial velocities which we assume is Gaussian. Recoils at each initial velocity v' will straggle through the target and arrive at the foil with velocity distribution n(v,v'), as shown in Figure 4:9. Weighting the n(v,v') by the Gaussian distribution of initial recoil velocities gives the total velocity distribution, $N_R(v)$, or the number of recoils that arrive at the foil with velocity v averaged over all starting velocities.

$$N_R(v) = N\int_0^{\infty} n(v,v')\exp\left(-\frac{1}{2}\left(\frac{v-v_0}{\sigma}\right)^2\right)dv' \qquad (4:1)$$

where $\sigma = \sqrt{\sum \sigma_v^2}$ is the width obtained by assuming the emitted neutrons have energy up to 1.8 MeV as indicated in the PACE calculation.

N is a normalization factor,

v_0 is the recoil starting velocity before neutron evaporation,

This equation was evaluated numerically and converted to the time-of-flight distribution shown in Figure 4:10. The measured results and the calculated time of fight are compared in section 6.2. Note that a broader peak is predicted, together with a rather long tail, which is largely due to straggling.

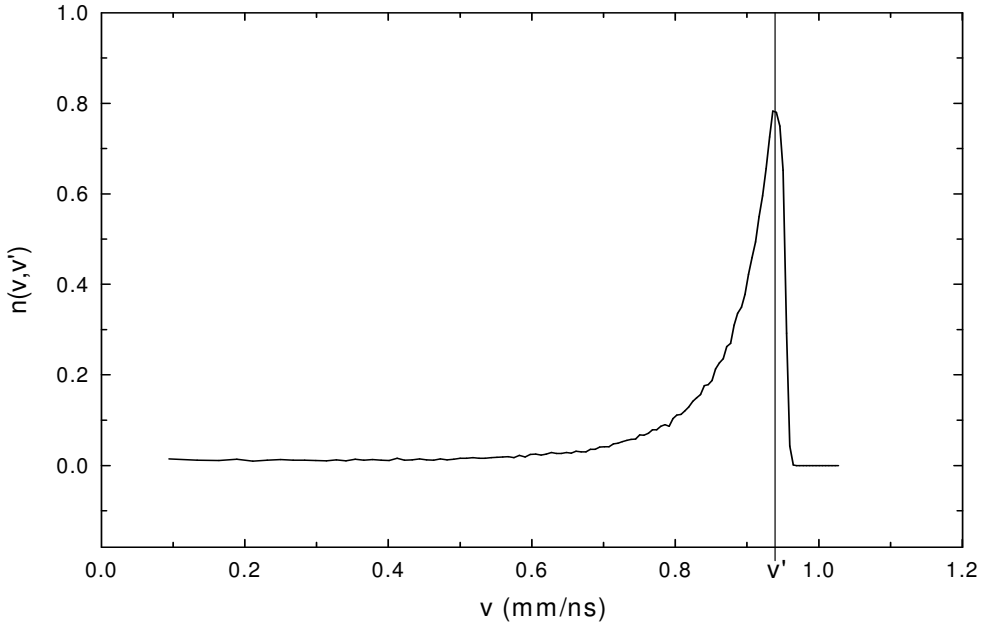

Figure 4:9. Calculated velocity distribution for the 1.06 MeV ^{230}U recoils using SRIM.

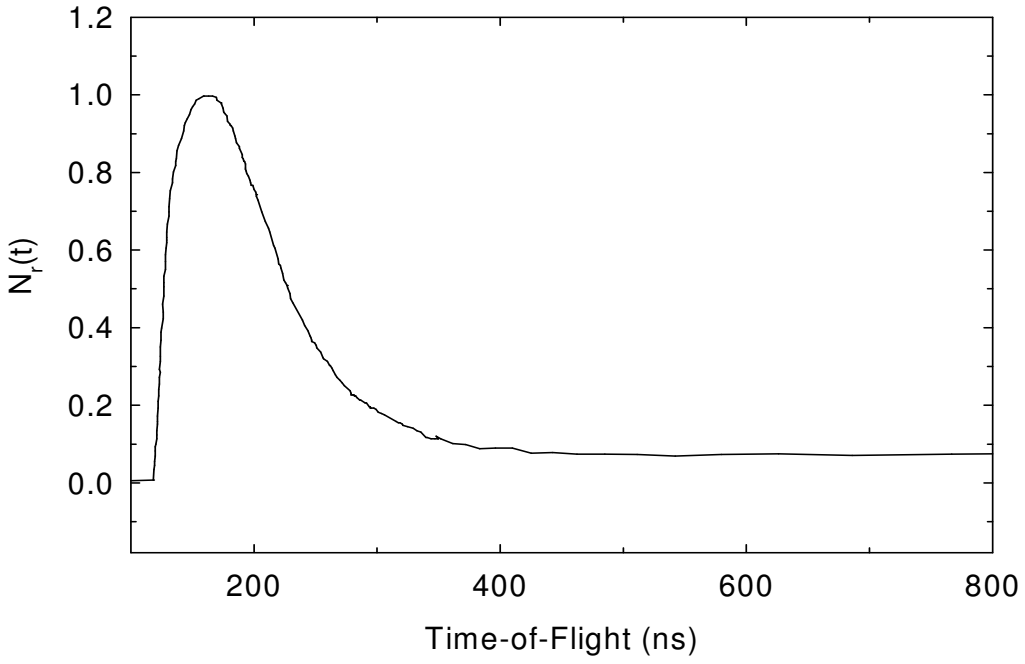

Figure 4:10. Calculated time-of-flight taking into consideration the neutrons' contribution and straggling in the target for $^{232}Th(\alpha,xn)$ at 61 MeV.

Considering the fact that the produced U recoils are at a very low energy, the thickness of the carbon foil was chosen such that it allows them to pass through. For an example, in the ^{232}Th (α, 4n)^{232}U reaction, a 10 μg/cm^2 foil is used, since the Uranium recoils have small recoil energies. In the carbon foil of this thickness the 0.725 MeV ^{232}U recoils loss 0.17 MeV. The created electrons are emitted with a typical energy of 50 eV and a cosine angular spread [Bru54, Sch80, Has92]. The created electrons are accelerated by a grid in the presence of the magnetic field. They are well focused by accelerating them to about 1.6 keV, which is close to the maximum MCP efficiency. The strength and geometry of the required magnetic field to deflect the electrons onto the MCP has to be determined. Due to the thickness of the recoil detector carbon foil, the process of mounting and handling the foil also posed a challenge in these experiments. The entire process of mounting the carbon foil is discussed in APPENDIX B.

4.1.3 Specifications of the Micro Channel Plate (MCP) used for the recoil detector

A micro channel plate (MCP) is a very fast device which converts charged particles and photons into a signal. They are available in different shapes with different physical and electrical specifications. Figure 4:11 shows the geometry of the MCP used for the recoil detector, with its connectors placed on the side. Its dimensions are given in Figure 4:11 and its physical and electrical specifications are tabulated in Table 4:1.

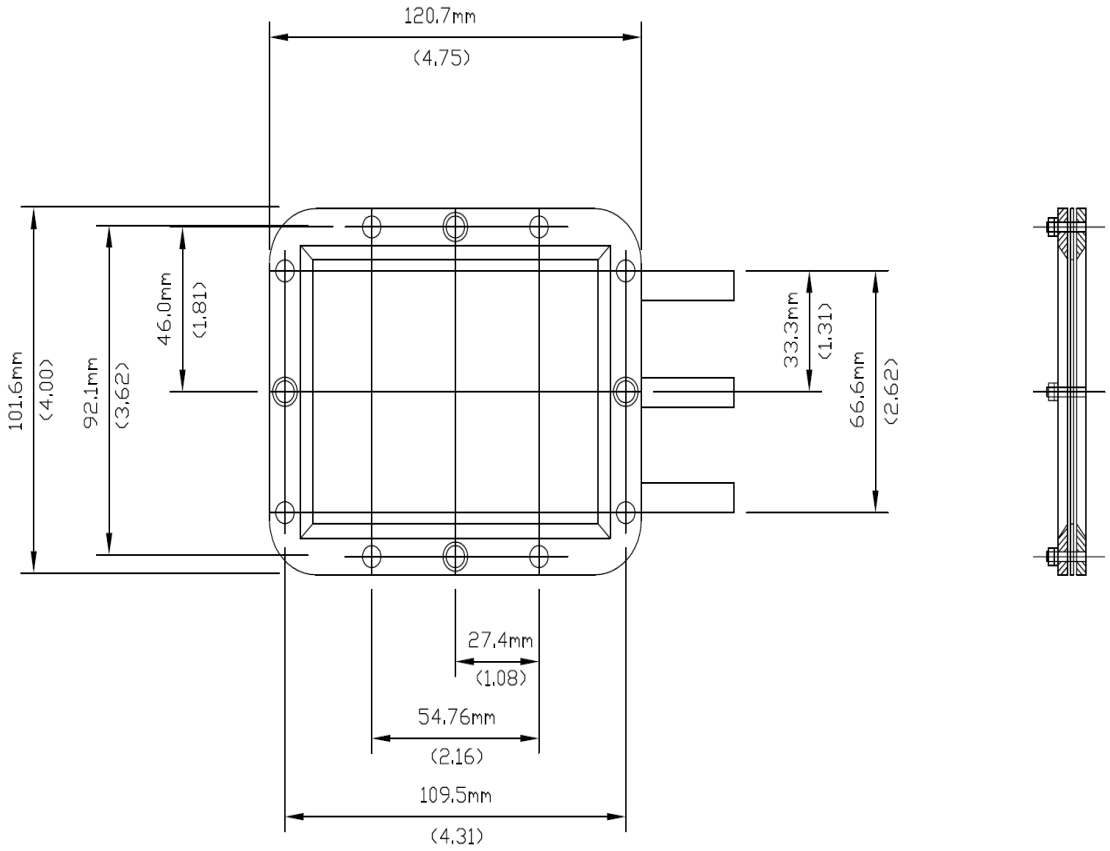

Figure 4:11. Schematic drawing and dimensions of the MCP used for the recoil detector. The electrical contacts to the front and back faces of the MCP and the anode are shown on the right-hand side.

Table 4:1. The electrical and physical specifications of the MCP used for the recoil detector, taken from the MCP manual.

Physical characteristics of MCP	**Specifications**
Dimensions of the sensitive area	75 mm x 93 mm
Center to Center Spacing	32 μm Nominal
Pore Size	25 μm Nominal
Bias Angle	8º ± 1º
Open Area Ratio	45% Minimum
Electrical characteristics of the MCP	**Specifications**
Electron Gain at 2000 V	4×10^6
Bias Current Range at 2000 V	75-300 μA
Resistance	7-27 MΩ Reference
Pulse Height Distribution at 2000 V	175% Maximum
Linear Output Current Density ($\mu A cm^{-2}$)	Typical 10% of Bias Current Density

The MCP is formed by a number of small tubes of same the dimensions like a honey comb. Theses tubes are called channels and when electrons or charged particles enter them they are accelerated by the electric field due to the voltage V_D applied to the electrodes of the MCP, as shown in Figure 4:12. The accelerated electrons move in a circular path and hit the wall of the tube and release further electrons. In this way the electrons are further accelerated and are multiplied by producing secondary electrons when the wall is hit. This process is repeated up to the end of the channel and it simultaneously takes place in all the channels in which radiation ended. Ultimately, at the end of the channels a multiple of secondary electrons are released, resulting in a charge signal, which is then converted into a voltage signal by the signal processing electronics. The MCP may consist of several stages and their gains are shown in Figure 4:13. A single stage MCP cannot exceed a gain of 10^4 due to noise [Tec94]. This noise is caused, e.g., by ion feedback, the response to ionized gases remaining in the tubes. Other noise contributions are discussed in the section 4.1.4. However, more gain can be achieved when two MCP's are used in a so-called "chevron arrangement" as shown in Figure 4:14. This arrangement increases the gain and reduces the noise coming from positive ion feedback [Lam01]. Figure 4:13 indicates that the maximum applied voltage is 1 kV for the single-stage, 2 kV for the double-stage and 3 kV for

the triple-stage MCPs. So clearly, the applied voltage is increased by 1 kV per stage. Furthermore, the gain increases exponentially with each stage and the applied voltage. The MCP for the recoil detector was chosen such that a signal of 50 mV, at 50 Ω impedance, and a width of 5 ns is produced by 50 electrons released from a 10 μg/cm^2 carbon foil by a uranium ion. Ohms law, $V = IR$, and the current law $I = \frac{\Delta Q}{\Delta t}$ were used to calculate the gain required for the recoil detector. The instantaneous current is given by

$$I = \frac{V}{R} = \frac{50\,mV}{50\,\Omega} = 1\,mA \tag{4:2}$$

Therefore the charge can be calculated using the current law as follows:

$$\Delta Q = I\Delta t = 1\,mA \times 5\times 10^{-9}\ s = 5\times 10^{-12}\ C = 30\times 10^{6}\,\text{electrons} \tag{4:3}$$

These calculations indicate that 50 emitted electrons should be multiplied to 30 x 10^6 electrons. This amplification can be achieved with a gain of $\approx 10^6$. A two-stage MCP was chosen in order to achieve this (see Figure 4:13). The MCP detection efficiency depends on the energy of the electron. Figure 4:15 shows the detection efficiency of the MCP as a function of electron energy. The MCP maximum efficiency of about 70% can be achieved with 0.5 keV electrons and with the 1.6 keV energetic electrons expected from the foil after accelerated by the grid, detection efficiency of about 50% is expected (see Figure 4:15).

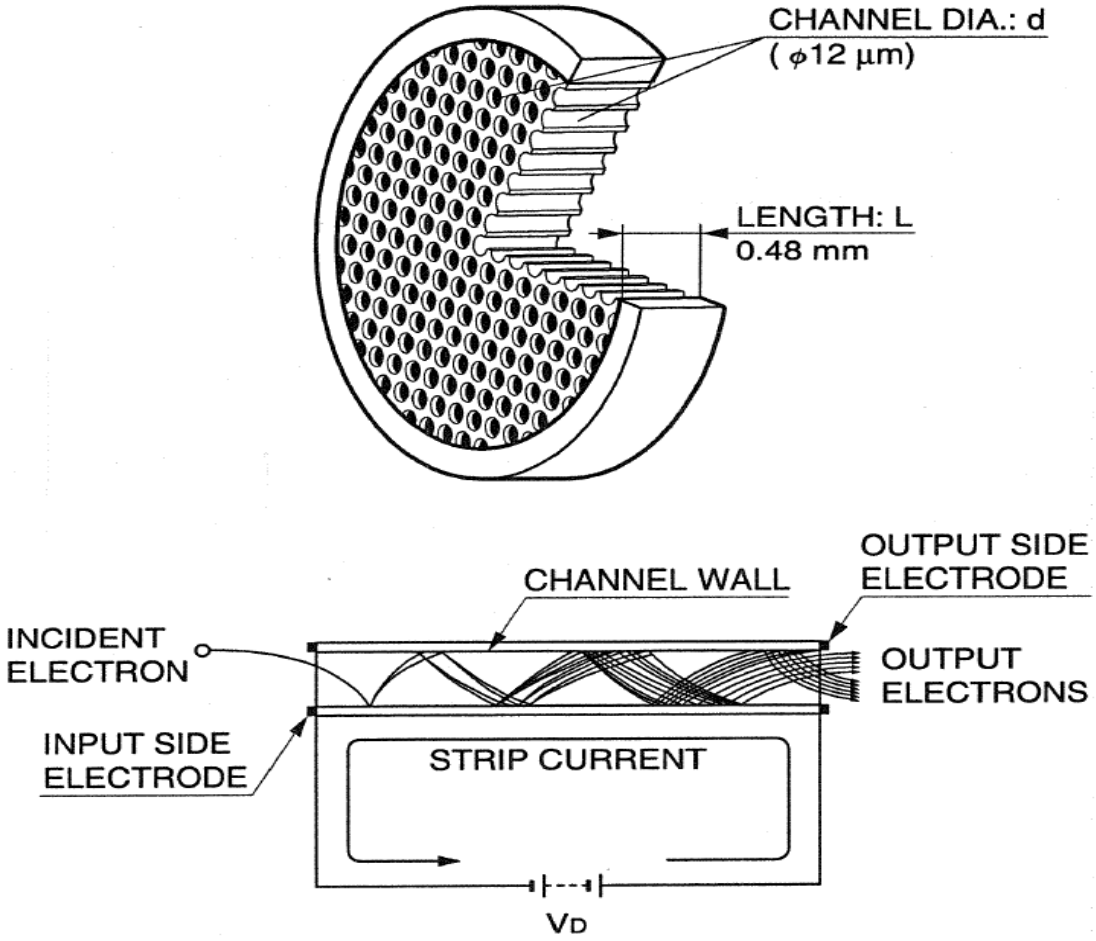

Figure 4:12. Schematic construction of the MCP [Tec94] (upper portion) and operating principle of a single channel (lower portion).

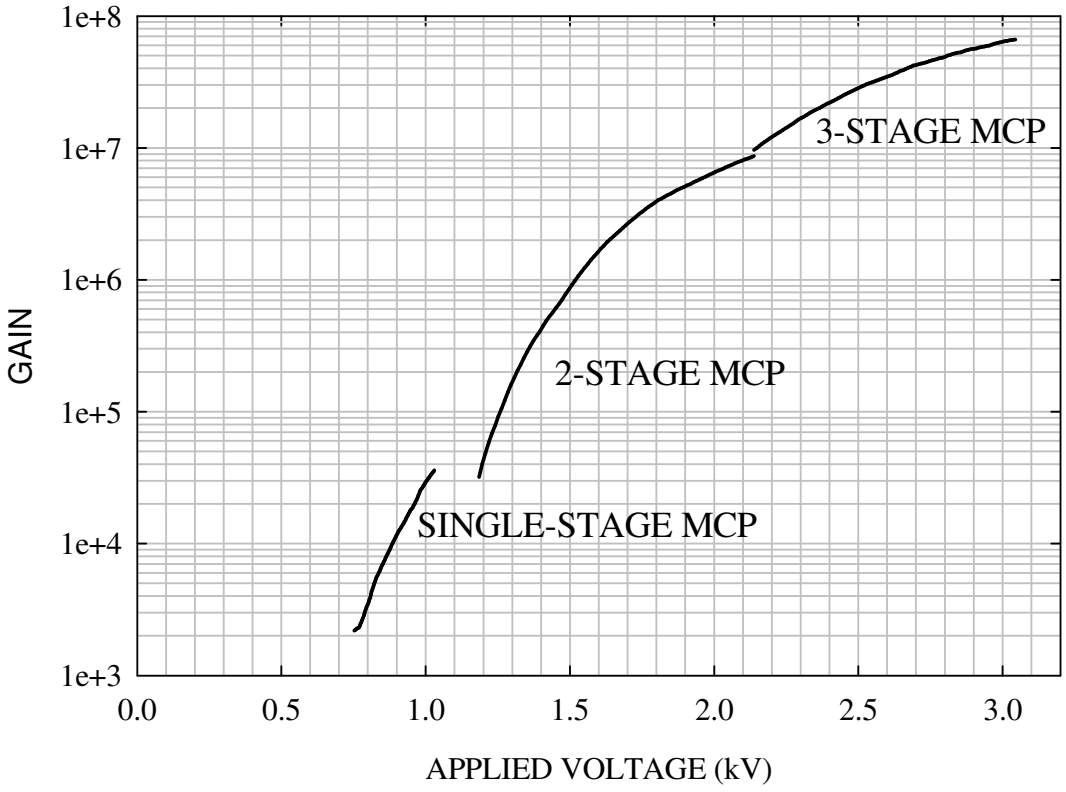

Figure 4:13. The gain characteristics of MCP's consisting of several stages [Tec94].

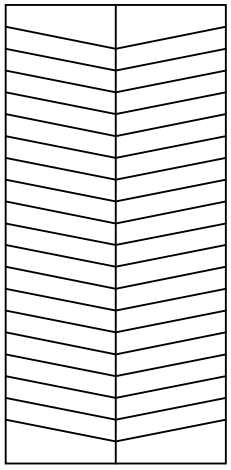

Figure 4:14. The chevron arrangement of a two-stage MCP.

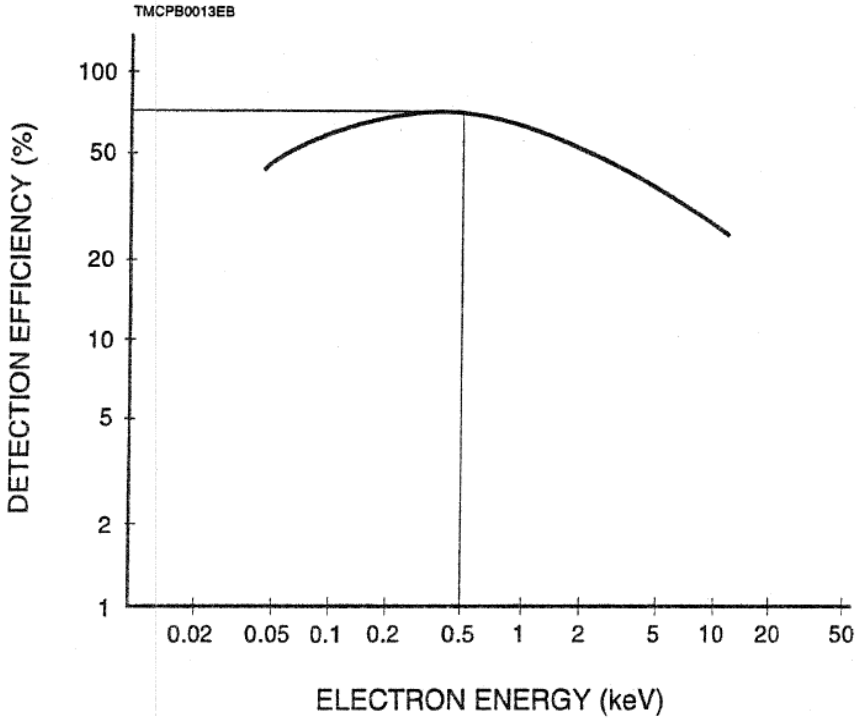

Figure 4:15. Detection efficiency of the MCP as a function of electron energy [Tec94].

4.1.4 Vacuum requirements

The MCP can only work at a vacuum less than 10^{-6} mbar due to dark current which increases with pressure. The dark current results from many factors including thermionic and electric field emissions from the channel walls, ionization of residual gases, local discharge by a high electric field and the photoelectron emission of the MCP support [Tec94, Lam01]. Therefore, a high voltage can only be applied to the MCP if and only if this vacuum requirement is fulfilled. Failure to comply with this requirement might damage the MCP. The recoil detector MCP must always be kept under vacuum. The manufacturer has measured the dark current at the specified vacuum and found it to be 2.0 counts/sec/cm^2. This measurement was performed at an acceleration voltage of –300 V and a MCP bias of 2200 V. At this bias the gain was measured to be 2.1×10^7. Another precaution which has to be taken into consideration is to avoid using oil pumps since the oil vapour can damage the MCP by depositing oil on the MCP channels and covering the emissive surface. Therefore only oil-free pumps were used to pump down the recoil detector chamber, the beam line and the beam dump during the conduction of tests and experiments.

4.1.5 The characteristics of the recoil detector magnet

In order to create a magnetic field the recoil detector is equipped with magnets. A permanent magnet was chosen, as compared to an electromagnet, for simplicity. Various types of permanent magnets exist, depending on the material they are made of. For our recoil detector, sheet magnets were used, since they can be easily cut into any desired shape and were fitted on the sides of the recoil detector chamber. These magnets are made of a flexible rubber-like plastic with barium or strontium ferrite powder imbedded. The magnets were placed on the outside of the chamber such that a homogenous field is produced inside, especially in the volume through which the electrons fly from the foil to the MCP. Some of the design parameters of the recoil detector are shown in Table 4:2. These parameters were calculated using the following equations which were taken from [Zeb77]. The electron bending radius r is:

$$r = 3.38\frac{\sqrt{V}}{B} \quad \text{cm} \tag{4:4}$$

where V is the voltage applied to the foil and B is the magnetic field created by the magnets.

The time-of-flight of an electron at rest accelerated in an uniform field is:

$$t_y = \frac{33.7d}{\sqrt{V}} \quad \text{ns} \tag{4:5}$$

where d is the distance in the field free region. The time-of-flight for a 180^0 deflection is:

$$t_B = \frac{179}{B} \quad \text{ns} \tag{4:6}$$

The exit angle can be calculated using equation (4:7)

$$\theta = \frac{\omega t}{2} \quad \text{rad, } \textit{where} \quad \omega = 1.7\times10^{-2}B \tag{4:7}$$

For other derivations of the recoil detector parameters see APPENDIX C. In order to ensure the field lines between the poles are parallel, additional magnetic material or a belt of magnets must be added at the edges of the magnet. The magnets that were placed on the edges are called shims. To ensure that the magnetic field is parallel the dimensions and positions of the shim magnets must be identified. Therefore, more detailed calculations were performed by Garret de Villiers of iThemba LABS using the program Vector Fields [Vec_1]. The path of the electrons in the magnetic field is

shown in Figure 4:16. Garret found that shims of $15\times15\,\mathrm{mm}^2$ thickness were needed to make the field parallel as indicated in Figure 4:16, where the image is almost of the same size as the object. Other Vector Fields calculations are shown in APPENDIX D.

Table 4:2. The parameters of the recoil detector calculated using the equations (4:4) to (4:7).

Parameters	**Value**	**Unit**
Magnet		
Radius of curvature r	6.25	cm
Field B	22	G
Pole gap	14	cm
Acceleration voltage V	1655	V
Approximate time-of-flight t	8.1	ns
Acceleration region		
Carbon foil diameter	8	cm
Foil-grid distance	1	cm
Time-of-flight	0.81	ns
Exit angle θ	0.31	rad
Anode (MCP)		
Maximum Applied voltage	2000	V
Shim magnets		
Dimensions	60×7.5	cm
Thickness	0.1	cm

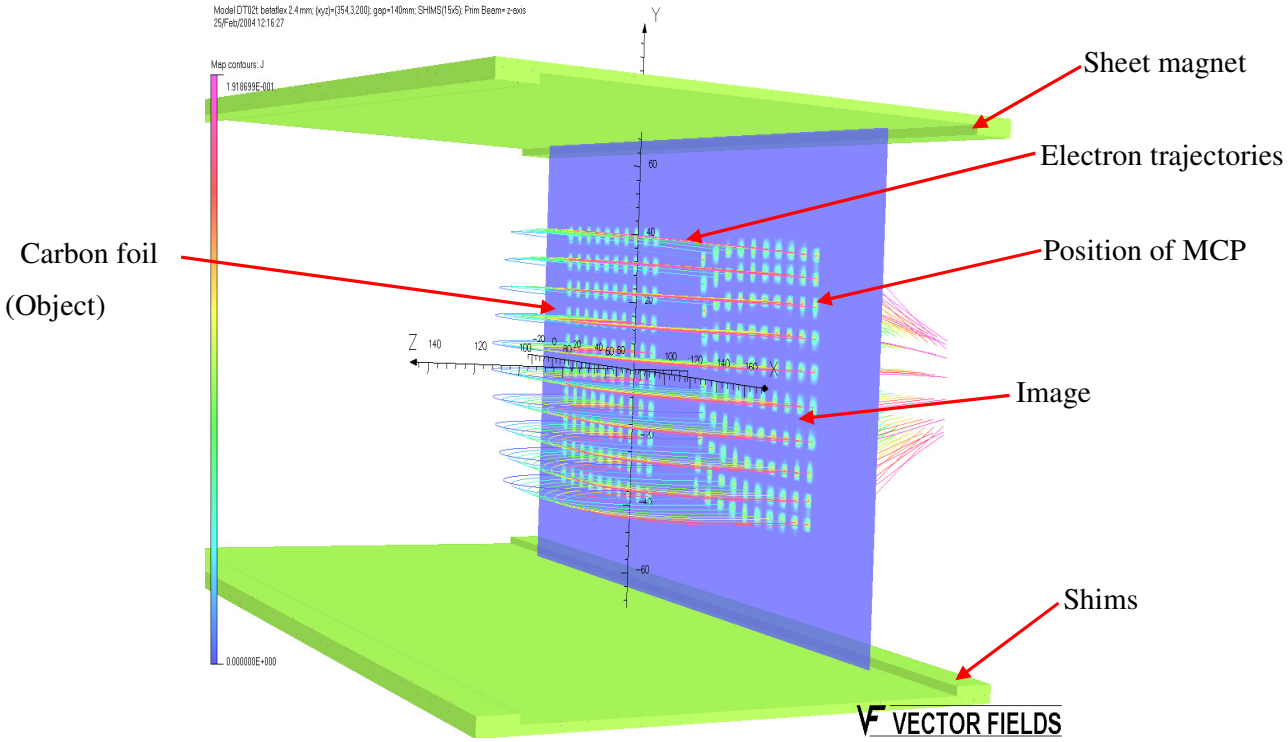

Figure 4:16. The trajectories of electrons in the magnetic fields. The electrons move initially in z-direction and are bent in the magnetic field, which is oriented in y-direction. Remarkably, the object is almost preserved by the image.

4.1.6 Mechanical construction

Considering the fact that the MCP of the recoil detector requires a very good vacuum, to be operated at high voltage, the mechanical design and construction must provide for this requirement. Firstly, the electrons emitted from the foil have to be directed onto the MCP. Therefore, the space for the magnets, the foil and the grid must be optimized. Since a negative high voltage has to be applied to the foil it must be mounted so that it is isolated from ground. Since the MCP needs a positive bias whereas a negative high voltage is used to accelerate electrons from the foil, measures were taken to avoid the high voltage cables from touching each other. The fact that in the reaction to be studied recoils of very small energy are produced, thin fragile carbon foils have to be used.

4.1.7 Pumping method

In order to avoid breaking of the foil when pumping down, a systematic procedure to pump down and vent the chamber was established. Initially, a fore pump is used to pump the chamber down to a pressure of 10^{-1} mbar. Immediately after pressure of 10^{-1} mbar has been reached, a turbo pump is switched on. It further pumps the chamber down through a small hole until a pressure of 10^{-4} mbar is achieved. At this pressure, the turbo molecular pump is closed until the pressure in the recoil detector chamber, the pressure before the main valve that separate the recoil detector chamber and the beam line upstream are equal at a pressure of about 10^{-1} mbar. Then the system can be pumped down through the main valve, hence the valve can be opened and the turbo molecular pump can be switched on. Due to the sensitivity of the foils, the recoil detector chamber is vented through a very small hole. Furthermore due to the sensitivity of the carbon foil, the arm like pipe in both Figure 4:17 and Figure 4:18 has been made such that both sides pumping of carbon are pumped simultaneously in order to balance the pressure that may otherwise break the foil. Beam focusing on the target requires a ruby viewer and a camera. All these requirements were taken into consideration in both the process of designing and constructing the recoil detector chamber and taking into account that the recoil detector with all its components has to fit into the AFRODITE array.

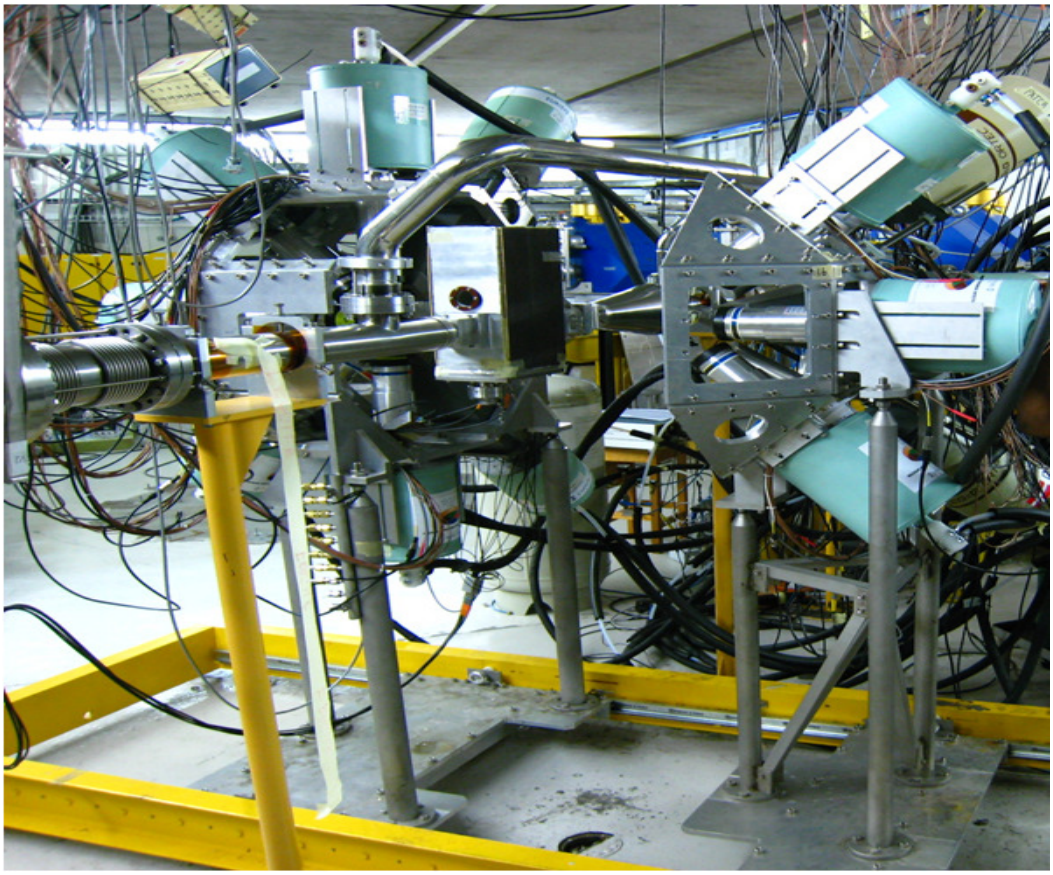

Figure 4:17. The recoil detector chamber mounted in the beam line of the AFRODITE array viewed from downstream.

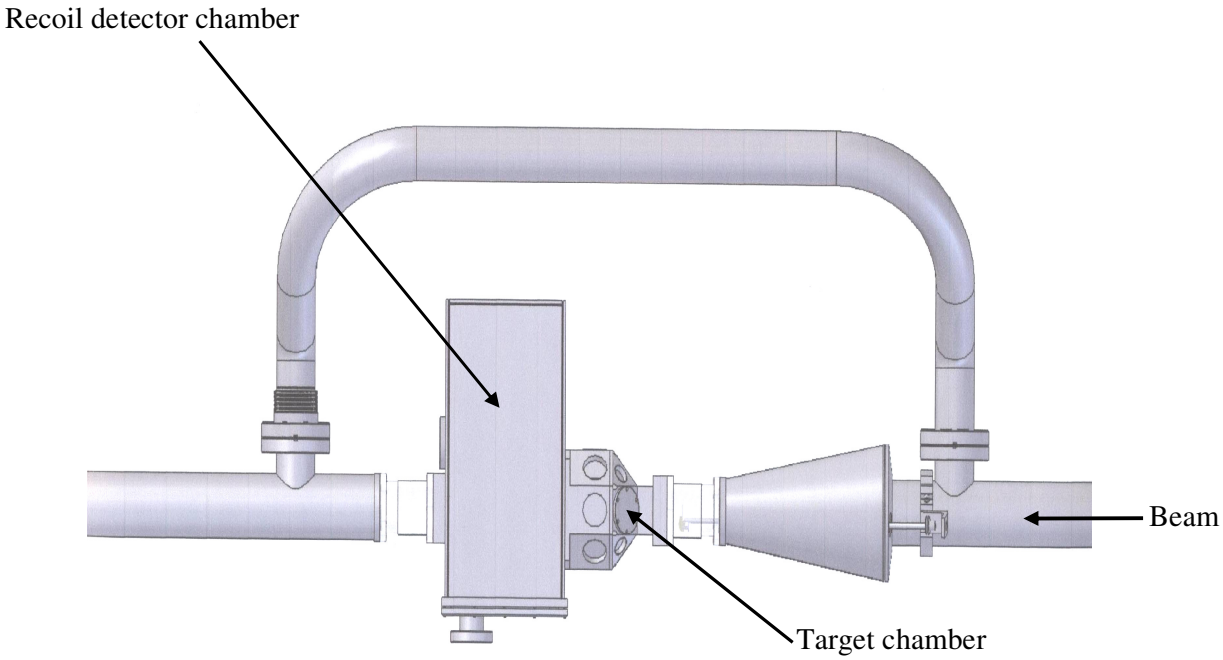

Figure 4:18. Schematic drawing of the recoil detector arrangement.

In Figure 4:17, a photograph of the recoil detector chamber mounted in the AFRODITE beam line is shown. Figure 4:18 shows a side view schematic picture of the arrangement that was used in this work. The single hemisphere target chamber at the center is equipped with 1 mm thick aluminum windows to allow γ–rays of energies less than 100 keV to be detected by LEPS detectors (positioned around the target chamber). The rectangular shaped box attached to the target chamber, is the recoil detector chamber which houses the recoil detector components including the MCP, grid, foil and electronics. The components are mounted on an insulating assembly plate (2) which is screwed to the base plate (1) of the recoil detector chamber as shown in Figure 4:19, other components are shown in the figure as well. By dismounting the base walls access can be gained to the inside of the chamber. The insulating assembly plate isolates the High Voltage (HV) from the chamber which is made of aluminum. The bottom half of the assembly plate contains a recess for the carbon foil, onto which a plate for connecting a negative voltage to the foil is mounted. A spacer (4) separates the grid from the foil. At the top half of the assembly plate the MCP is mounted as can be seen in Figure 4:21, where the MCP is shown, mounted with its connectors facing up. A plate (6) prevents electrons on non-circular orbits reaching the MCP. The base plate contains a tube and a flange (3), (5) to mount the electrical feed-throughs for the high voltages and the signals from the recoil detector electronics.

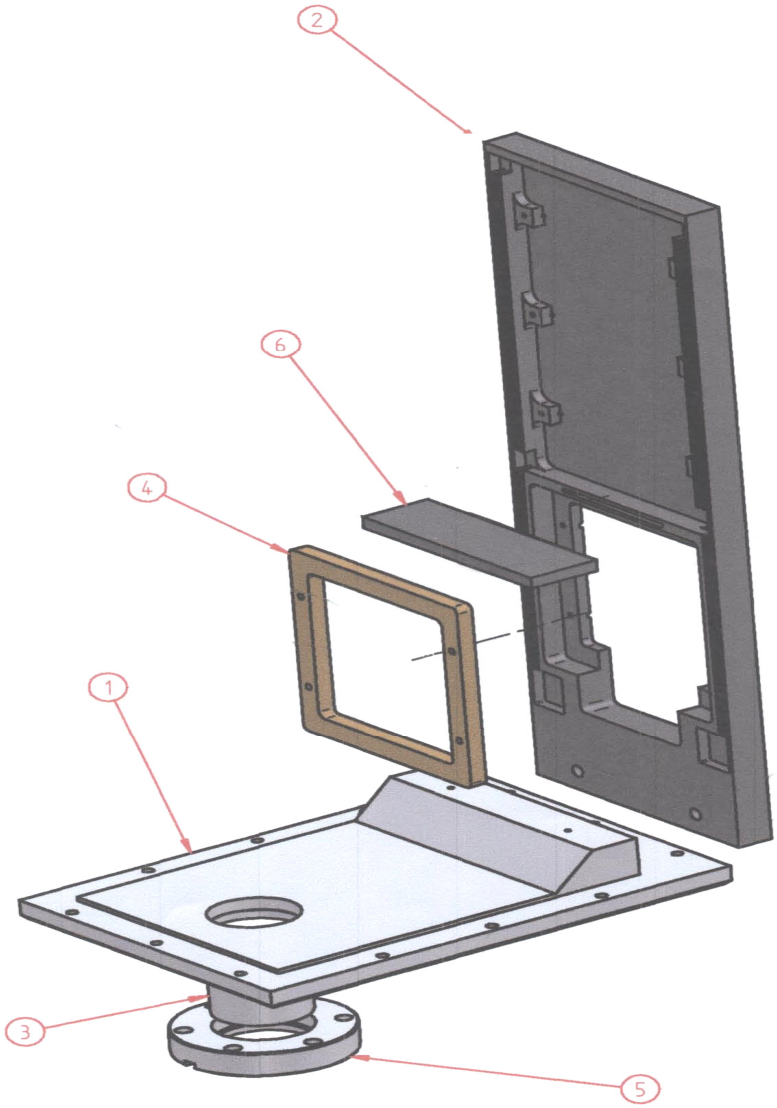

Figure 4:19. The insulating assembly plate (2) and its base plate (1) with tube and flange (3 and 5) to mount the feed-throughs, the spacer (4) and shield (6) used in experiment 1, as described in the text.

4.1.8 Electronics of the MCP

Figure 4:20 shows the circuit diagram of the MCP. Considering the fact that the electronics will be placed under vacuum, a special type of High voltage resistor, imported from Japan, which is tolerant to high temperatures, was used to avoid out gassing. The part of the electronics placed inside the chamber is shown in Figure 4:20. The resistors of R_1 = 1 MΩ and R_2 = 0.1 MΩ act as a voltage divider which allows different voltages to be applied to the anode and the MCP tube, needed to accelerate

the electrons inside the MCP. A capacitor of 2 nF was used to decouple the detector signal from the HV. Hence, an AC pulse is further amplified.

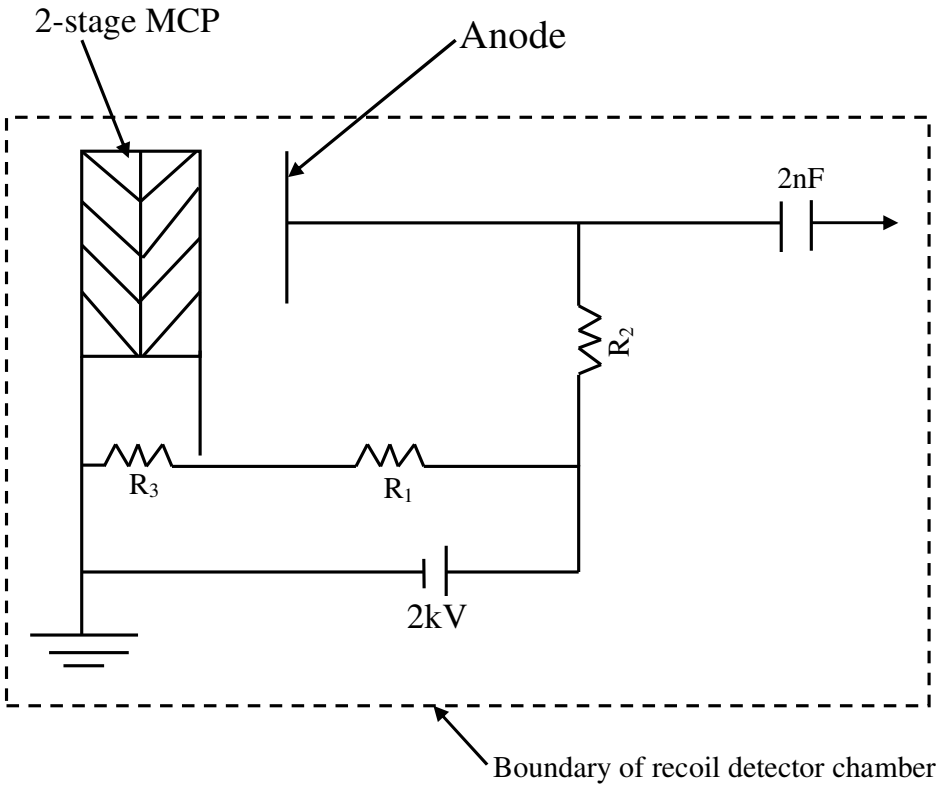

Figure 4:20. The circuit diagram of the used double-stage MCP. R_1 = 1 MΩ, R_2 = 0.1 MΩ and R_3 =2 MΩ are resistances.

The sides of the insulating assembly plate have grooves, as can be seen in Figure 4:19, which accommodate the cables from the feed-throughs to the MCP and to the other components of the recoil detector like the foil and the grid, as shown in Figure 4:21. These cables are connected to the feed-throughs in the flange attached to the base plate, as shown in Figure 4:21.

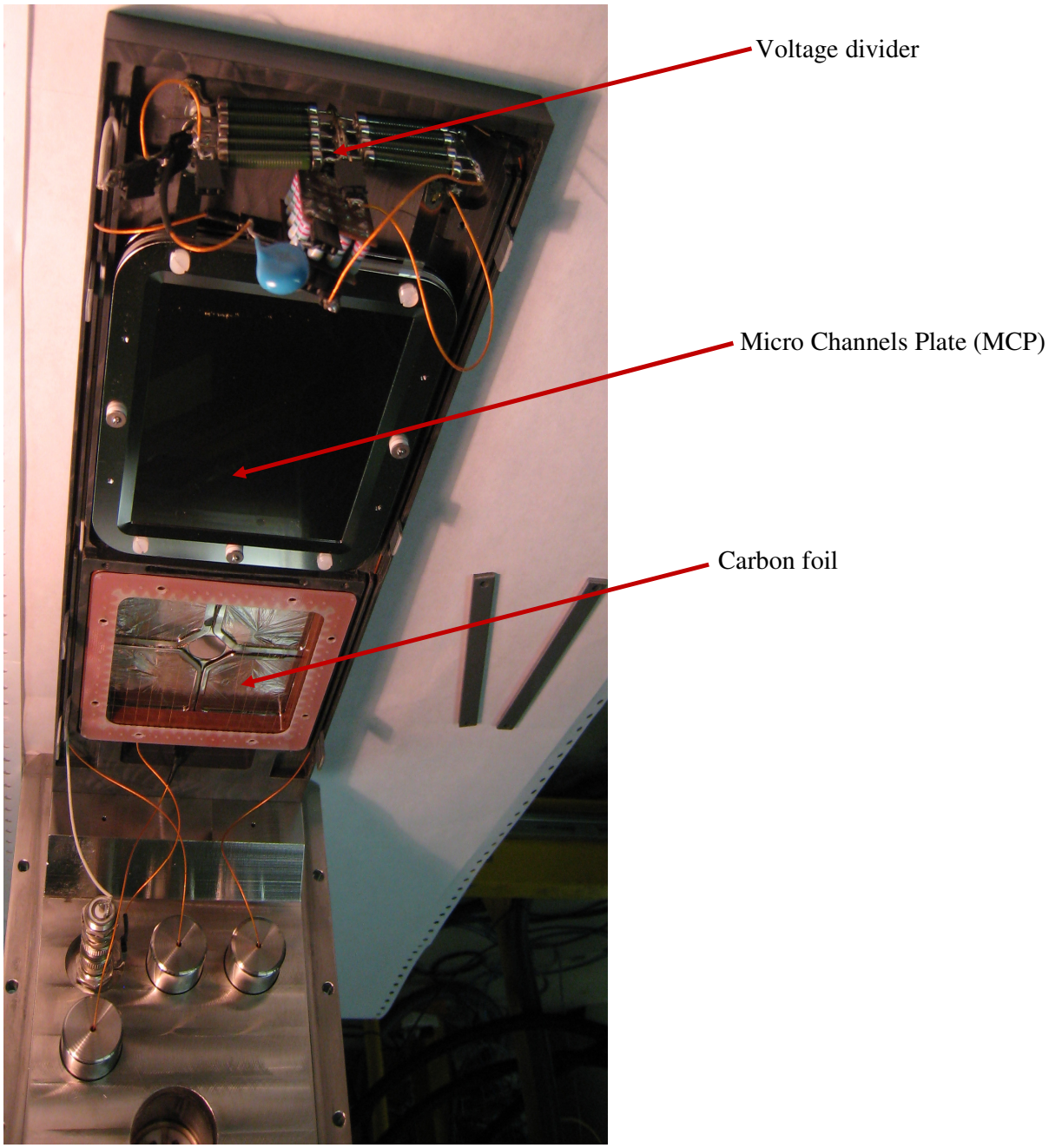

Figure 4:21. Photograph of the assembly plate with the mounted foil and MCP attached to the base plate of the recoil detector chamber.

At the right-hand side of the target chamber shown in Figure 4:18, a conical pipe can be seen which accommodates an external camera, and controls for a ruby viewer used to focus the beam as mentioned in section 4.1.6. The viewer can be moved perpendicular and parallel to the beam direction. This ruby can be flipped up and down to put it into the beam or take it out. It is controlled automatically by a long rod

attached to a piston, the movement of which is activated by compressed air. This allows the ruby to be moved up and down remotely from the control room during the focusing of the beam at the target position.

4.1.9 Test of the recoil detector with a ^{252}Cf fission source

The recoil detector was tested using a spontaneous fission ^{252}Cf source before any in-beam test or experiment was performed. The source was placed in a position facing the MCP so that fission fragments and electrons from the source would randomly hit the MCP. The circuit block diagram for the recoil detector used in the first test is shown in Figure 4:20. However, the resistors of the voltage divider have been changed to $R_1 = 240$ kΩ and $R_2 = 166$ kΩ. Before the test took place the chamber was pumped down as described in the previous section. Two days were used to pump the recoil-detector chamber down to a pressure of 1.2×10^{-6} mbar. Thereafter the high voltage was applied very slowly as required by the MCP up to 2 kV. This voltage results in a gain greater than 10^6 . A negative high voltage of about 1100 V has been applied to the recoil-detector foil, with the grid grounded. During this procedure, the output signal from the MCP is closely monitored with an oscilloscope. At about 1700 V, which is almost equal to the calculated MCP bias voltage, the signals shown in Figure 4:22 were observed. The signals were superimposed by a ringing, which was caused by a mismatch of the impedance and reflection at the feed-through. In order to confirm that these signals came from the MCP the voltage at the foil was reduced. This resulted in a decrease of the signal until it disappeared and reappeared when the voltage on the foil was increased again, above the threshold, as required to obtain the correct electron trajectories for the electrons to hit the MCP.

In order to improve the MCP signal, various modifications have been made during the test phase. The circuit diagram shown in Figure 4:20 was modified to the circuit diagram shown in Figure 4:23. In order to make the signal cable as short as possible, to reduce ringing and reflections, the MCP was turned upside down, in such a way that its connectors became closer to the feed through. The preamplifier and amplifier were also placed as close as possible to the chamber. Furthermore, a test was done with a potentiometer between signal and ground of the oscilloscope 1 MΩ input impedance on the oscilloscope with the potentiometer resistance close to 50 Ω in order to match the impedance. After all these the MCP signal shown in Figure 4:24

obtained when testing with the ^{152}Cf source. Ultimately Experiment 1 was performed under these conditions using reaction ^{180}W(^{20}Ne,6n) at 110 MeV beam energy.

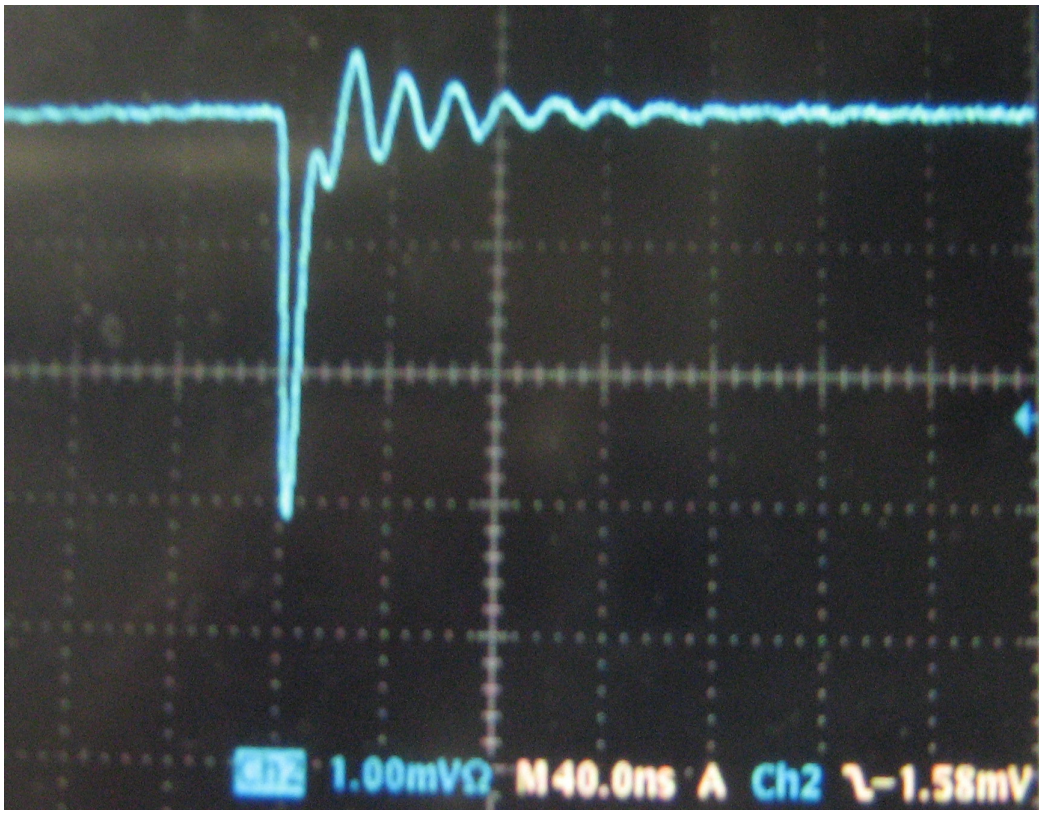

Figure 4:22. Signals observed in the first test of the MCP with a ^{252}Cf fission source.

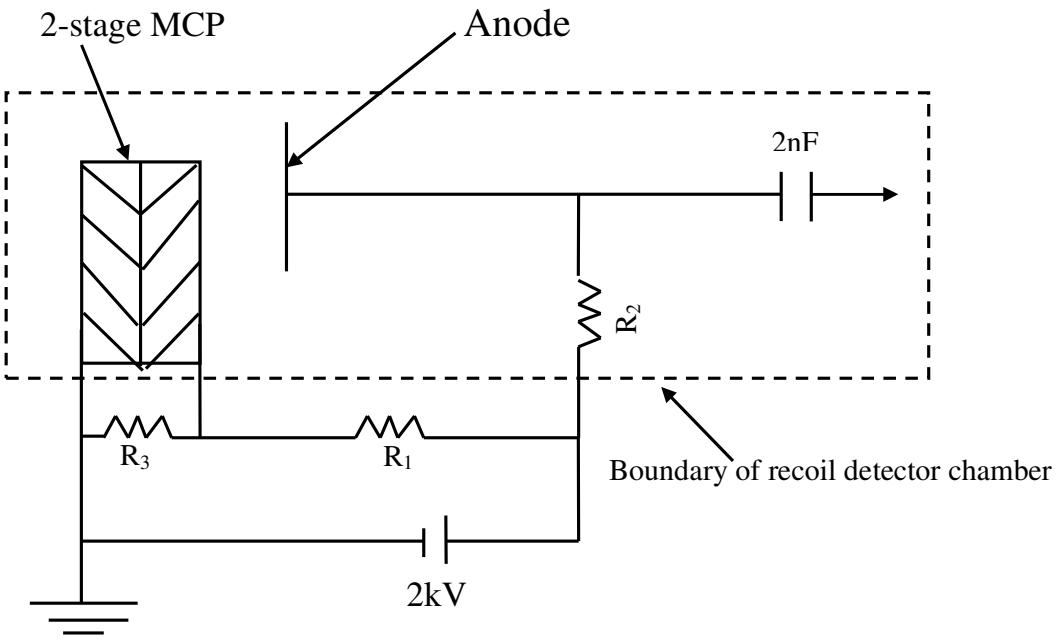

Figure 4:23. The circuit diagram of the recoil detector for the test with a ^{252}Cf fission source. R_1 = 240 kΩ , R_2 = 166 Ω and R_3 = 2 MΩ are resistances. The dotted line indicates the boundary of the recoil detector chamber.

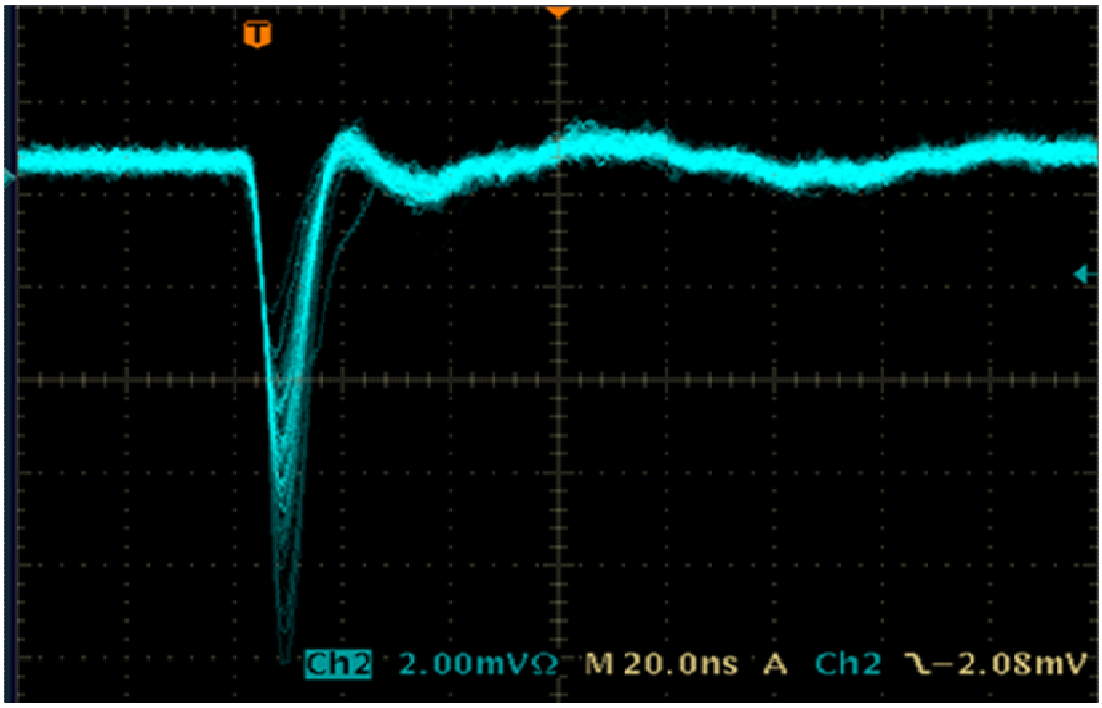

Figure 4:24. MCP signals observed with the ^{252}Cf fission source after the modifications described in the text had been made.

4.1.10 The recoil detector signal processing electronics

The recoil detector signal processing electronics circuit diagram and timing diagram are shown in Figure 4:25 and Figure 4:26 respectively. The signal from the MCP detector was pre-amplified and passed through a Fast Timing Amplifier in order to provide a fast amplified signal for timing purposes. The Timing Amplifier output signal was then split into two. The first signal was used in the oscilloscope to monitor the MCP signal. The other signal was fed into a Constant Fraction Discriminator (CFD) as shown in Figure 4:25. Here the signal was converted into a fast logic pulse, for any signal that exceeded a low level threshold which was set to remove the noise. The logic signal from the CFD was delayed for 524 ns and then passed through a second Discriminator to re-generate the signal.

This delay was necessary to bring the MCP signal in alignment with the "clean Ge" signal (see Figure 2:12) for incorporation in the trigger. The timing diagram is shown in Figure 4:25. Recoils should be delayed with respect to the beam pulse. To select these events the MCP time signal was "AND" with a delayed RF signal (see Figure 4:25"C"), which was stretched (in this example, 160 ns to 524 ns see Figure 4:25) to accommodate a large spread in recoil velocities.

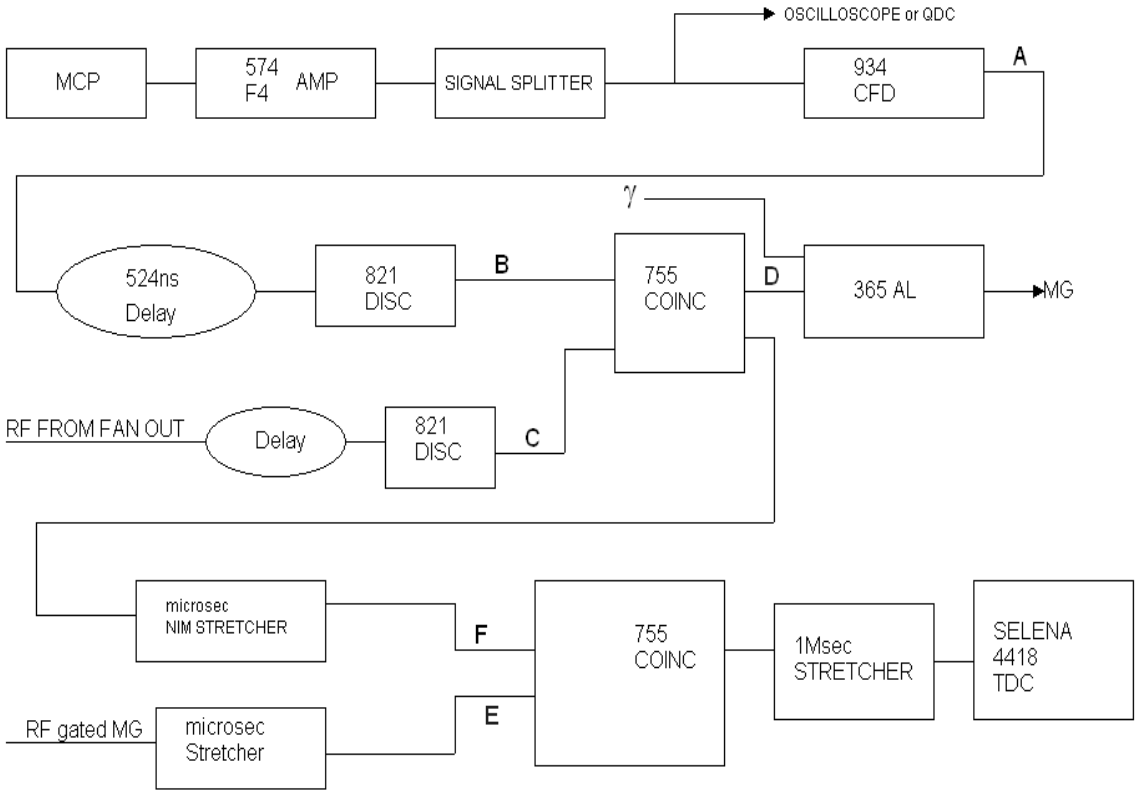

Figure 4:25. The circuit diagram for the recoil detector electronics.

The output of the 755 coincidence unit thus represents the detection of a "recoil" see Figure 4:25 "D", which then goes into the 365 AL (Figure 2:11) to be "ANDED" with the γ–ray logic signal from AFRODITE, and to form a master gate. A further branch of signal Figure 4:25 "D" is used to form the MCP time in the Silena 4418 TDC. Here the signal is digitized and fed into a Versa Module Europa (VME) computer. The further processing of events is then controlled by the data acquisition system. The task of the acquisition code, which runs on a Linux workstation, is to read data from VME modules, construct events from this data, and save these events to disk or tape and transmit them to the online sorting code which runs on the same workstation.

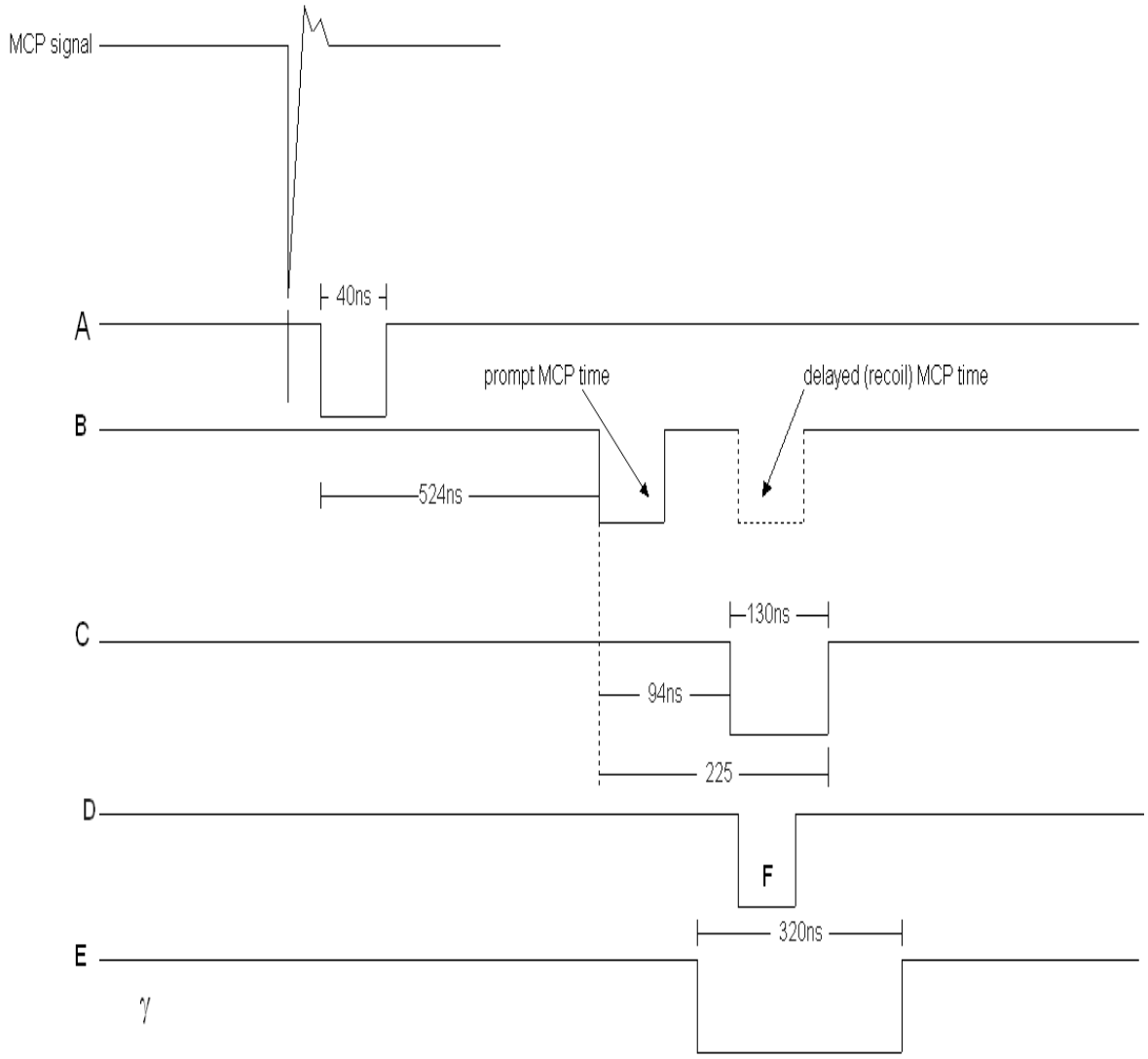

Figure 4:26. The corresponding recoil detector time signal. Letters corresponding to signals seen at the locations in the circuit diagram in Figure 4:25.

4.1.11 In-beam tests of the recoil detector with Ne projectiles

After the source tests of the recoil detector, test experiments were carried out using the ^{181}Ta(^{20}Ne, 6n)^{195}Bi reaction at a beam energy of 125 MeV and the ^{180}W(^{20}Ne, 4n)^{196}Po reaction at a beam energy of 110 MeV. The major motivation for performing the former experiment was to study the evolution of magnetic rotational bands in ^{195}Bi and for the latter, to identify and study superdeformed states in ^{196}Po. The ^{181}Ta(^{20}Ne, 6n)^{195}Bi reaction has previously been used by Mabala et al., [Mab03] to identify magnetic rotational bands using the AFRODITE array. However, that investigation

suffered from fission background and target X–rays. Since the main objective for the development of the recoil detector was to suppress the fission background, this experiment was repeated for the recoil detector. Furthermore, the use of ^{20}Ne induced reactions had the purpose to check the behaviour of the recoil detector with the heaviest beam which could be used with our recoil detector, as discussed in section 4.1.2.

The spectra shown in Figure 4:27 were obtained in the ^{181}Ta(^{20}Ne, 6n)^{195}Bi experiment. Figure 4:27(a) shows a total projection of a γ–γ coincidence spectrum while Figure 4:27(c) shows a γ–recoil coincidence spectrum. A remarkable reduction of the background and the neutron peak is obtained by triggering on the recoils. Furthermore, the Coulomb excitation lines (135 and 166 keV) of the target are eliminated and the ^{195}Bi transitions are remarkably visible. From this measurement it was deduced that the recoil detector worked with an efficiency of at least 45% at 2 pnA beam current. Even though the Ta target used was 500μg/cm^2 thick, the SRIM code calculations indicated that a target of 700μg/cm^2 thickness would give an efficiency of about 55%. It was expected that the efficiency of the recoil detector would drop as the beam current increases because the MCP needs to recharge after amplifying the electrons from the beam pulse. When the time between events becomes comparable to the recharge time constant, a significant loss in efficiency was expected. For example, Ward et al. [War83] reported a 50% loss in efficiency when the beam current was increased by a factor of ten. However the test was only performed with a beam current of about 1 pnA. Therefore, the question of efficiency-count rate dependence remained unanswered. The tests revealed that a large count rate came from electrons which did not originate from the carbon foil. They presumably resulted from gas ionization and δ-electrons. In order to suppress these electrons, the use of a baffle to allow only electrons from the foil to reach the MCP was proposed. Another problem to be solved, was to reduce the ringing which remained in the MCP signal (*see Figure 4:24*), as already known from the ^{252}Cf source test. Fortunately, the first undershoot occurred at 30 ns, just after the arrival of the Bi recoils at about 25 ns, therefore they can be discriminated by time gates. The amplitude of the undershoot restricts, however, the setting of the discriminator level, which reduces the efficiency.

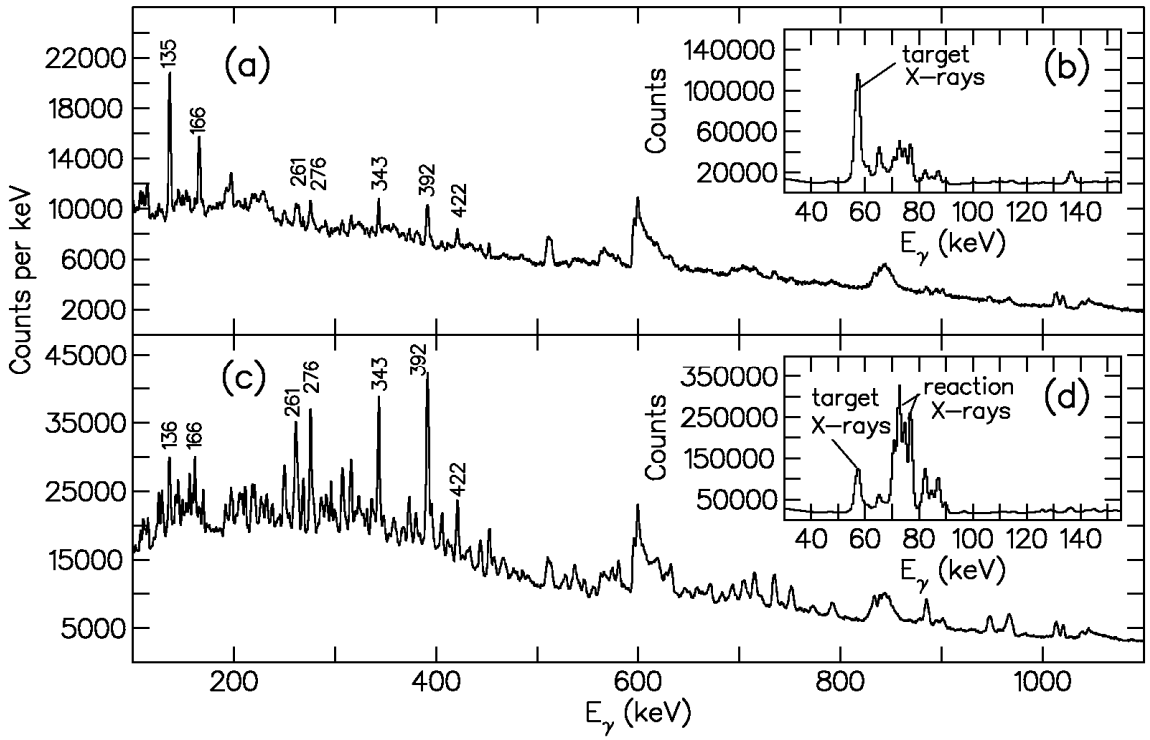

Figure 4:27. Spectra obtained in the ^{181}Ta(^{20}Ne, 6n)^{195}Bi experiment. Upper portion: total projection of the γ–γ coincidence matrices. Lower portion: total projection of the γ–γmatrix with a recoil gate (γ–γ–recoil coincidence spectrum).

The ^{180}W(^{20}Ne, 4n)^{196}Po experiment was performed using the same setting as for the ^{181}Ta(^{20}Ne, 6n)^{195}Bi experiment. Figure 4:28 (a and b) show the total projections of γ–γ and γ–γ–recoil coincidence matrices, respectively. Clearly, a remarkable suppression of the background is observed in the latter spectrum. This background suppression is also accompanied by a much enhanced appearance of γ–rays from ^{196}Po.

As stated earlier, there was a limit on the amount of beam current that could be used. This is due to the fact that the efficiency drops with an increase in the beam current. Consequently, 2 pnA was chosen as the upper limit for heavy induced reactions like ^{20}Ne. This was not expected to be a problem with the α-induced reactions for which the recoil detector was designed, as the electron production is approximately proportional Z^2, so a reduction in δ-electrons of about a factor of $(10/2)^2 = 25$ could be expected.

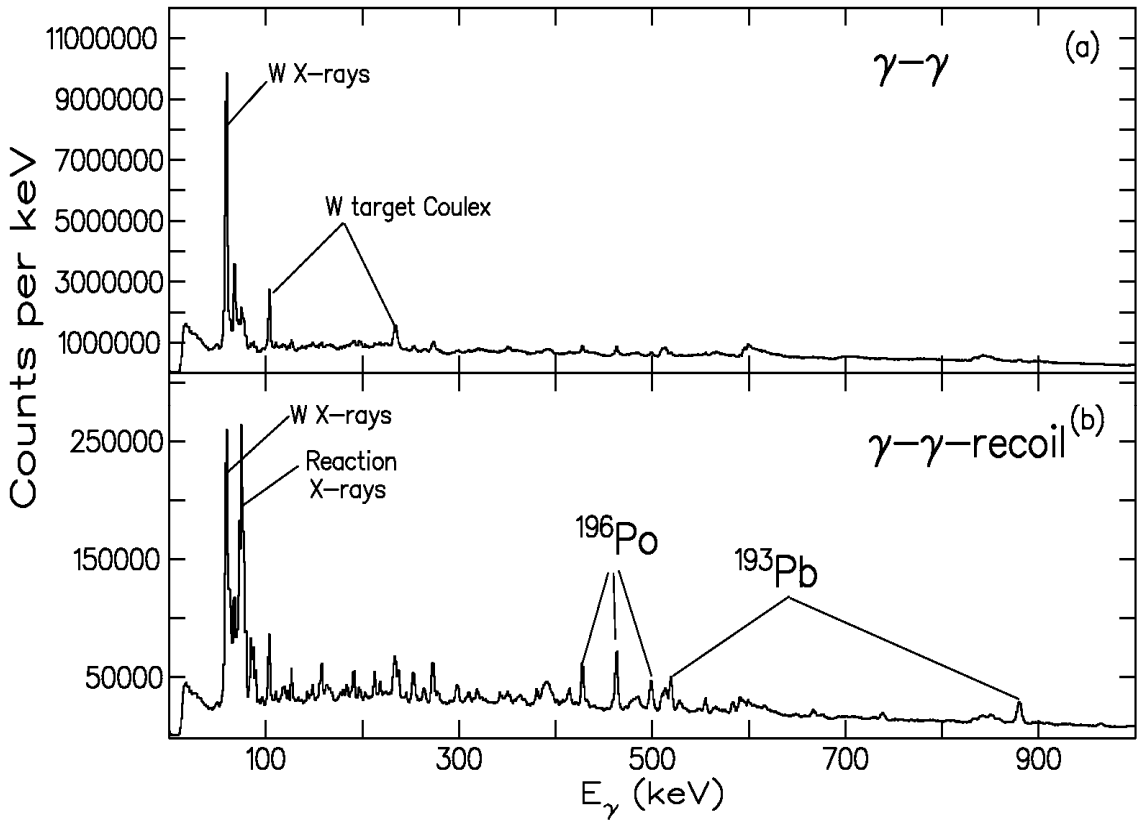

Figure 4:28. Spectra obtained in the $^{180}W(^{20}Ne, 4n)^{196}Po$ experiment. Upper portion: total projection of a coincidence spectrum. Lower portion: total projection of a γ–γ–recoil coincidence spectrum.

4.1.12 Recoil detector test with alpha beams

For use with an α-particle beam, test experiments using the $^{197}Au(\alpha, xn)$ reaction were carried out as well. The beam energy was 65 MeV, target thickness was 180 μg/cm^2 as given in Table 2:1 and the carbon foil thickness was 12 μg/cm^2. The major reaction products from this reaction are ^{195}Tl and ^{196}Tl. The γ–rays from these two nuclei were observed. In Figure 4:29 a γ–ray singles (upper portion) and a γ–recoil coincidence spectrum (lower portion) are shown. Not only the prompt γ–rays from the Tl isotopes were observed, but also γ–ray lines resulting from beta decay. In addition, the 384 keV line, de-exciting the $3/2^+$ level in ^{195}Tl was also observed. This level is fed from its 3.6 s $9/2^-$ isomer, as can be seen in the partial level scheme of ^{195}Tl shown in Figure 4:30. In the recoil-gated γ–ray spectrum the 384 line almost

vanished as can be seen in the lower portion of Figure 4:29. The remaining intensity of this line is probably due to the MCP threshold being set to low and triggering in noise. The statistics in the recoil gated γ–ray spectrum are about 1% of that of the γ–ray singles spectrum. This is rather small compared to the predicted efficiency. The low efficiency is probably caused by most of the recoils not leaving the target. This would explain the presence of the 384 keV line and the γ-ray energies resulting from β-decay in the singles spectra shown in the top panel of Figure 4:29. A comparison of the spectra of the 90º and 135º CLOVER detectors suggested that about half of the recoils did not leave the target (this agrees with SRIM estimates for targets at 200μg/cm^2 thickness) with the rest being trapped in the carbon foil and chamber walls.

This observation implies that either the stopping powers for Tl in carbon and Au obtained using the SRIM code, were wrong or that the carbon foil and the target were much thicker than believed. Therefore, the thicknesses of both the target and the carbon foil were measured and confirmed using Rutherford backscattering at the Material Research Department (MRD) of iThemba LABS. It was concluded that the stopping powers calculated with the SRIM code were underestimated by ≈50% and that thinner foils would be required.

After this test experiment, carbon foils of 4 μg/cm^2 thickness were obtained from Peter Maier-Komor of the Technical University of Munich, Germany. However it proved difficult to mount these fragile foils. Therefore, the big frame was subdivided into quarters, such that the fragile foils could be mounted onto smaller frames, the areas of which add up to the required frame size of $27 \times 20\,\mathrm{mm}^2$. The measurement was repeated with 4 μg/cm^2 thick carbon foil. This time, the recoil detector worked, but the recoil signal amplitude was much smaller than expected. This meant that the signal-to-noise ratio was not better than for the Ne induced reactions. For example, although the background was noticeably reduced with the α-beam, the signal from the recoils were not as strong as expected. Presumably because even with a 4 μg/cm^2 carbon foil, the recoils exited the back of the foil with very low energy, such that the signal-to-noise ratio remained the same. The detector would be severely rate-limited as in the Ne case.

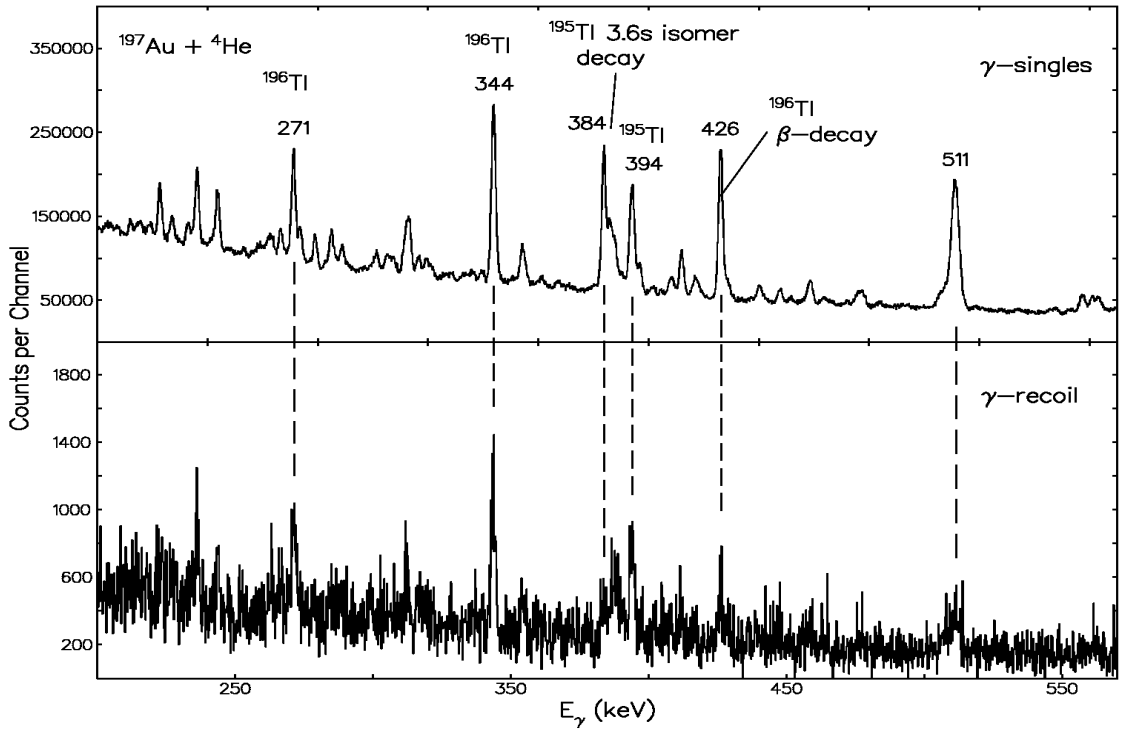

Figure 4:29. Upper portion: singles spectrum obtained in a $^{197}Au(\alpha,nx)$ reaction at 65 MeV. Lower portion: recoil gated γ-ray spectrum.

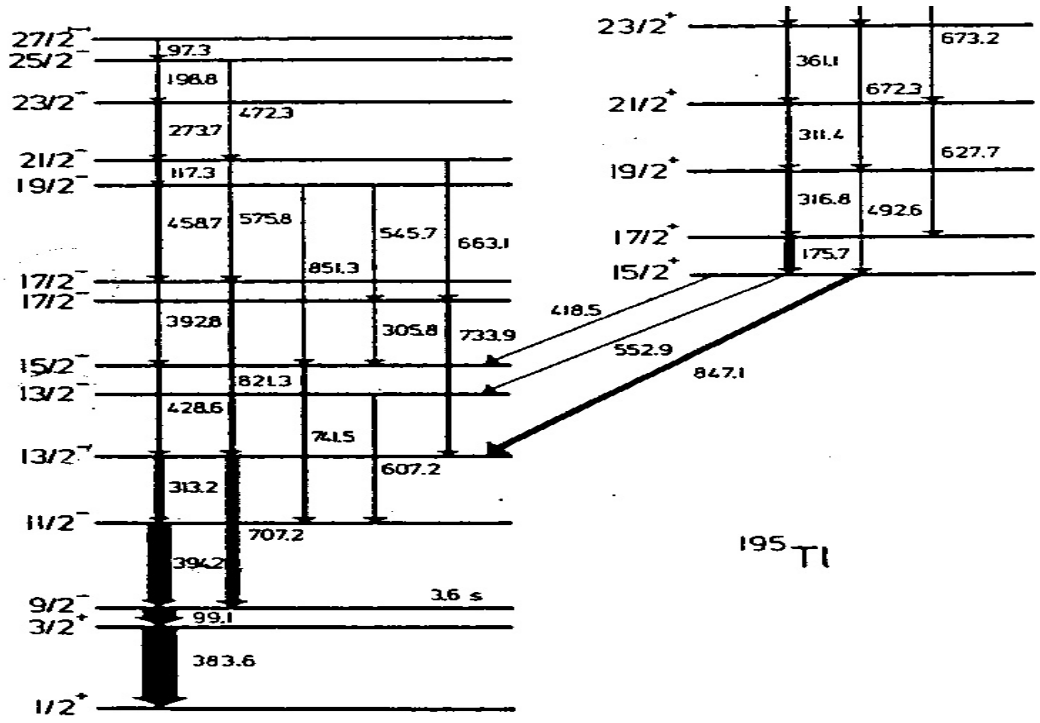

Figure 4:30. Partial level scheme of ^{195}Tl [Lie78].

After numerous tests of the recoil detector some efficiency limitations of the detector were deduced. One was that the MCP eventually was saturated by beam related electrons. For the ^{20}Ne beams used in the recoil detector tests, the saturation current is about 2 pnA. Since the production of electrons increases as a function of Z^2, where Z is the atomic number of the accelerated projectiles, it was expected that higher α-beam currents could be used. Indeed the pulses from the α-projectiles were much smaller in amplitude than those from Ne projectiles. Also the signals produced by the recoils were far smaller in the α-induced reactions compared to Ne induced reactions and therefore a larger amplification was needed. For α-induced reactions the signal to noise ratio was almost the same as for the Ne induced reactions, but the saturating beam current was not determined.

4.1.13 Modified recoil detector

The main reason for redesigning the recoil detector was because recoils barely got through the carbon foil, even when it was only 4 μg/cm^2 thick. This brought about a very small signal, which could barely be been above the noise. In hindsight, it might have worked better with a much bigger hole in the carbon foil. But to avoid the problem of recoils barely getting through the foil and very small signals, it was decided to detect electrons emitted from the front face of the foil, rather than the back. Moving the foil further back from the target comes at the price of reducing the geometrical efficiency up to half, for both alpha and Ne induced reactions. Furthermore, generally only a factor of two smaller number of electrons is emitted from the front face of the foil as compared to the back face [Has92]. But in case of the recoils produced in alpha-induced reactions, it is likely that more electrons are emitted from the front than from the back face. This is because the number of produced electrons depends on the recoil energy [Has92]. In the case of low-energy recoils, as for the U nuclei, the recoils of about 600 keV energy are slowed down by electronic stopping to an energy of about 100 keV in the foil. Using these energies to estimate the number of electron yields results in about five electrons emitted from the back face as compared to nine from the front face, thus giving a stronger signal in the new arrangement. Since we were radically redesigning the recoil detector, we also decided to address some of the other problems, like the ringing and background. Figure 4:31

show the picture of the newly designed recoil detector chamber mounted in the beam line of the AFRODITE array.

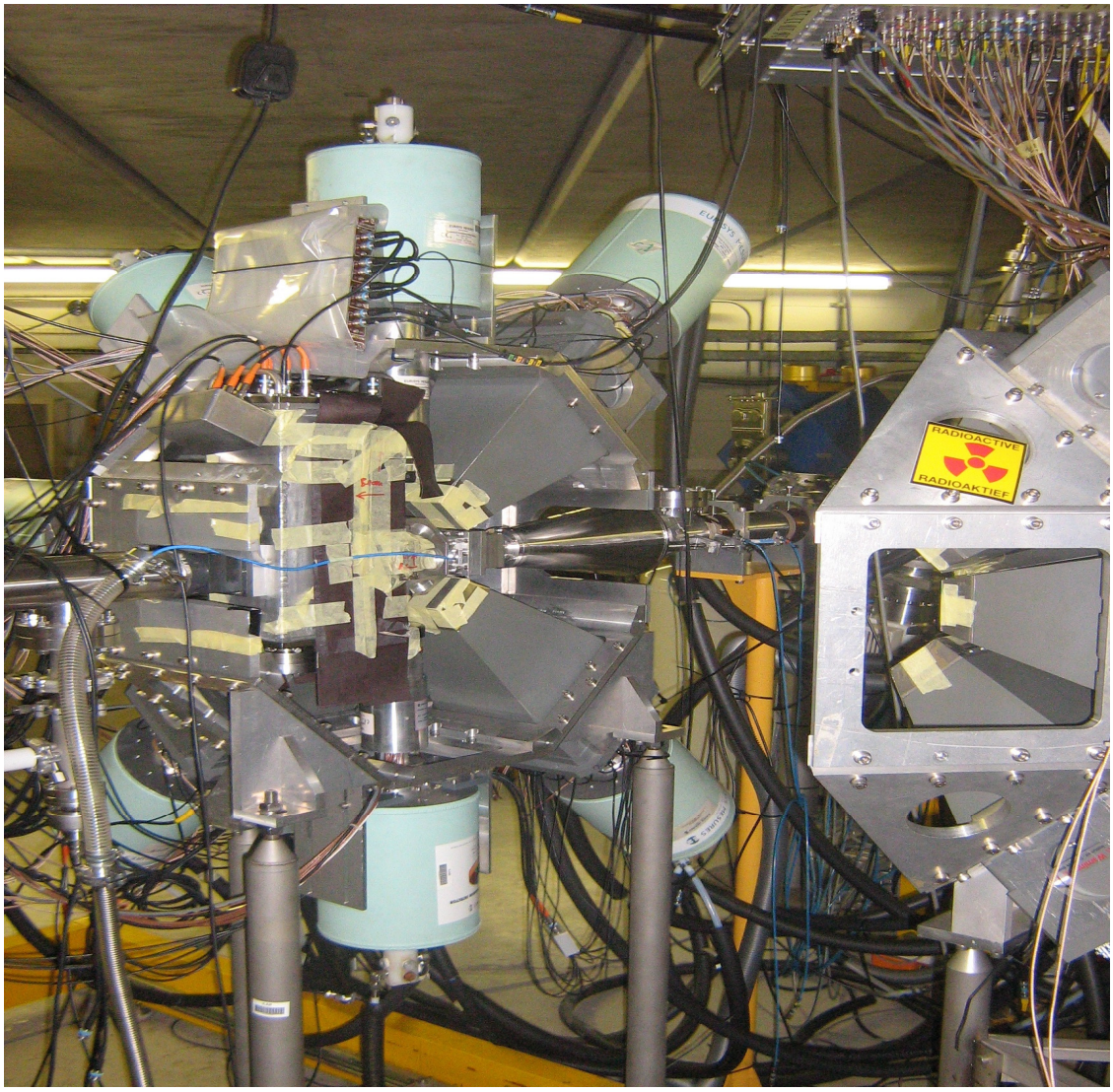

Figure 4:31. The new recoil detector chamber mounted in the beam line of the AFRODITE array.

The distance between the target and the foil was increased to 145 mm and the MCP was turned around in order to detect the electrons from the front face (see Figure 4:32). The resulting effect on the efficiency is discussed later on in this section. In order to deflect unwanted δ-electrons away from the MCP, magnets were placed behind the target. These magnets were attached to a collimator which was inserted to shield the foil from the beam projectiles potentially scattered further upstream. In Figure 4:33, the collimator and the small magnets which were attached to the

collimator are shown. These magnets provide a field of 1 kG, however the field was not perfectly uniform. Making the ^{232}Th(α, 6n) reaction as a model, the time-of-flight of the 1.1 MeV ^{230}U recoils would now be 153 ns, the fission fragments would be 11.2 ns, and the alpha beam particles 2.7 ns. It was estimated that the detection efficiency would now be a maximum of 16%.

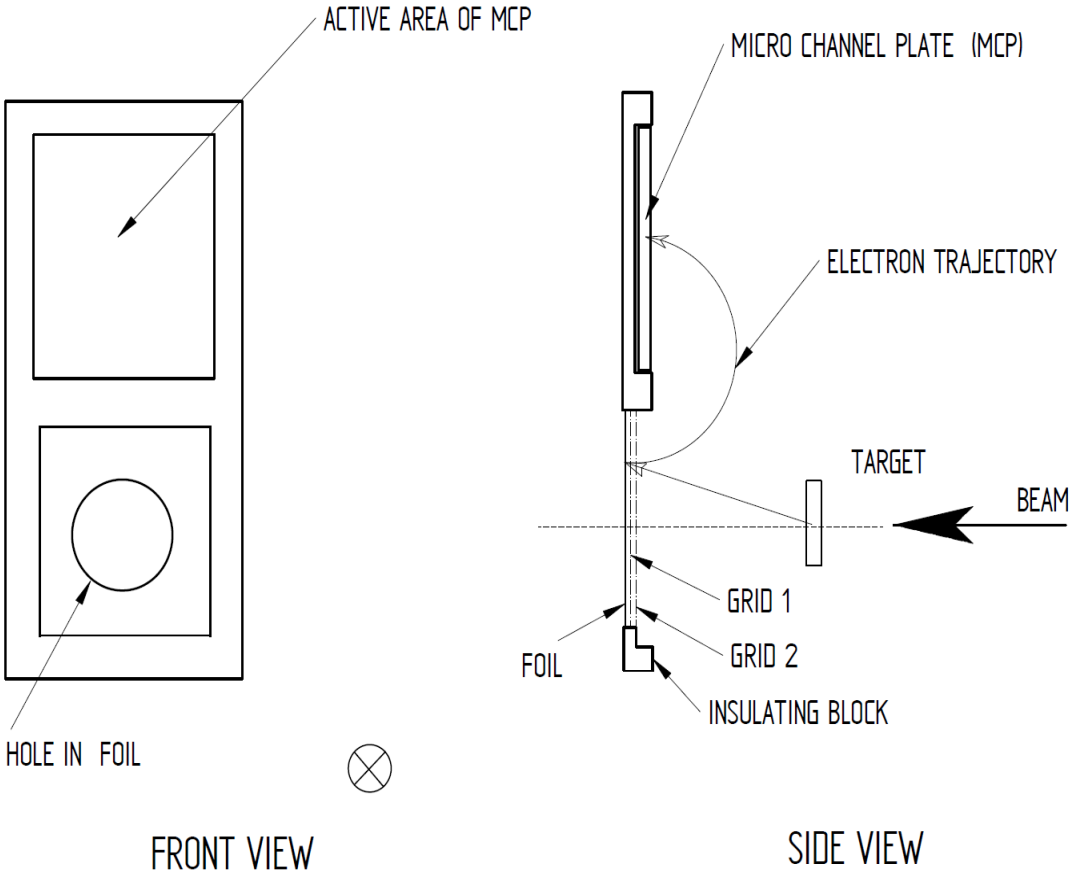

Figure 4:32. The new design of the recoil detector showing that the MCP was turned around so that the electrons emitted from the front face of the foil, as viewed from the target, are observed.

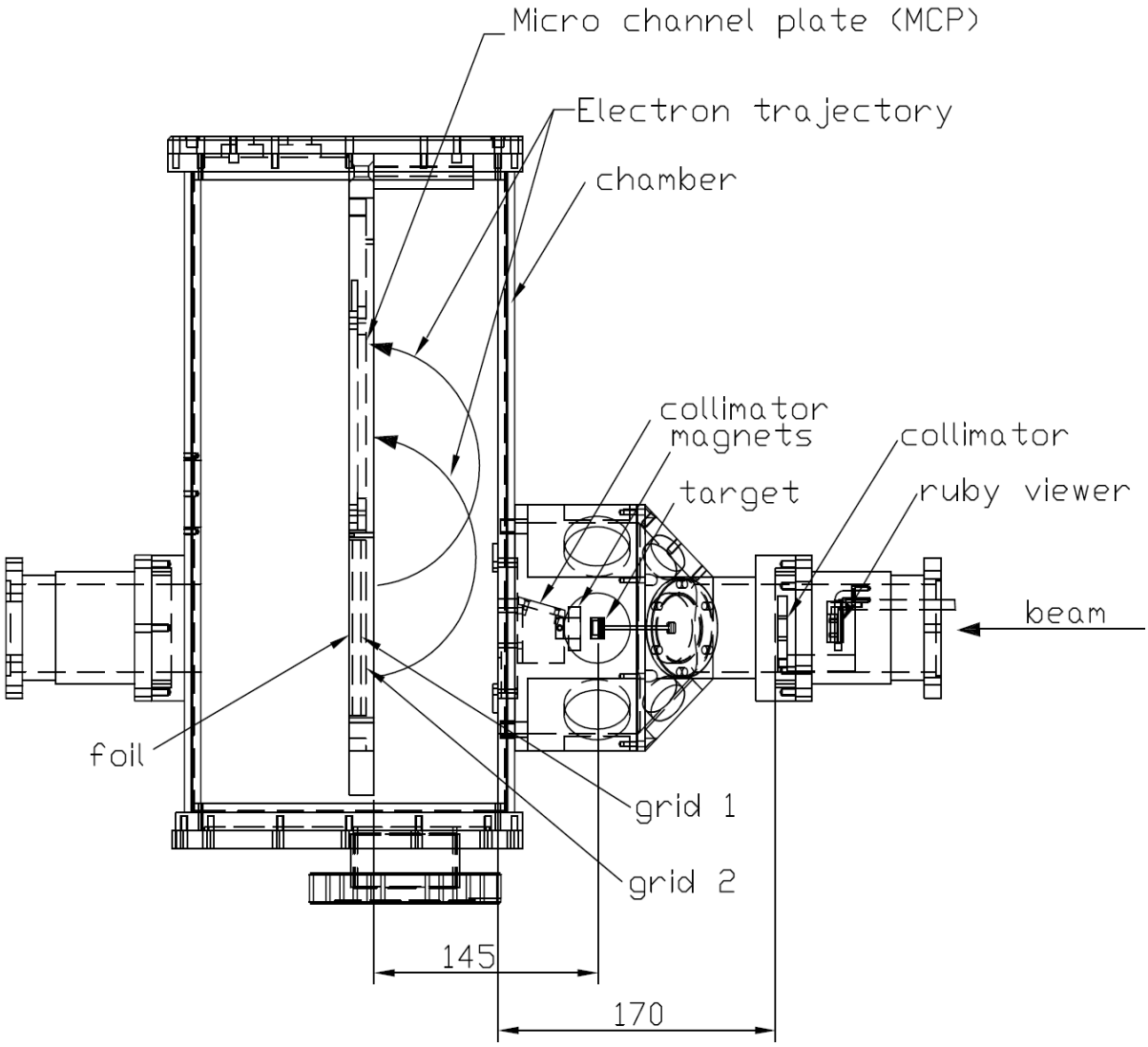

Figure 4:33. Design of the collimator with the attached magnets, which deflect the δ-electrons from the target.

In the test experiments it was established that the main limitation on the maximum beam current (I_{sat}) arose from beam induced electrons. Therefore the recoil detector had to be modified in order to minimize the detection of these electrons by the MCP. The sources of the beam induced electrons were assumed to be the following:

- Beam halo by-passing the target and striking the carbon foil
- Beam scattered from the target into the carbon foil
- Residual gas ionization by the beam
- δ-electron production in the target by the beam

In order to reduce the beam halo, a collimator system was designed, satisfying the condition that the pumping efficiency was not severely reduced. The electrons from the scattered beam can be minimized by making the size of the hole in the foil large enough to allow both the focused and scattered beam to pass through it without hitting the foil. Furthermore it is of utmost importance that the beam is well focused on the target to minimize the number of scattered projectiles. Since the ruby viewer is located 30 cm upstream, it is difficult to focus the beam because focusing the beam at the ruby viewer position does not necessarily mean that it is focused at the target position. The focusing procedure was improved by placing another viewer about 3 m upstream. Viewing the beam in the 3m upstream ensured the beam was focused in the target, avoiding focusing the beam at only one location.

The electrons from residual gas ionization and δ-electrons were minimized by placing a turbo pump as close as possible to the recoil detector chamber, housing the MCP. Due to the geometry of the AFRODITE array, the pump could be mounted only at a distance of about one meter from the foil. This change in the design allowed the vacuum in the chamber to be improved, hence resulting in a reduction of residual gas ionization.

Another advantage of the new configuration was that very thin carbon foils were not necessary. Aluminum coated Mylar foils of 680 $\mu g/cm^2$ thickness were used instead, hence simplifying the handling of the detector and the pumping procedure. The MCP electrodes were now placed even closer to the feed-throughs (see Figure 4:34) and this resulted in a reduction of the ringing in the MCP signal. The larger distance between the foil and target also delayed the recoils such that the recoils arrive at a time later than any ringing. This allowed very low thresholds to be set and therefore U recoils of lower energy to be detected. Table 4:3 shows some of the parameters of the modified recoil detector.

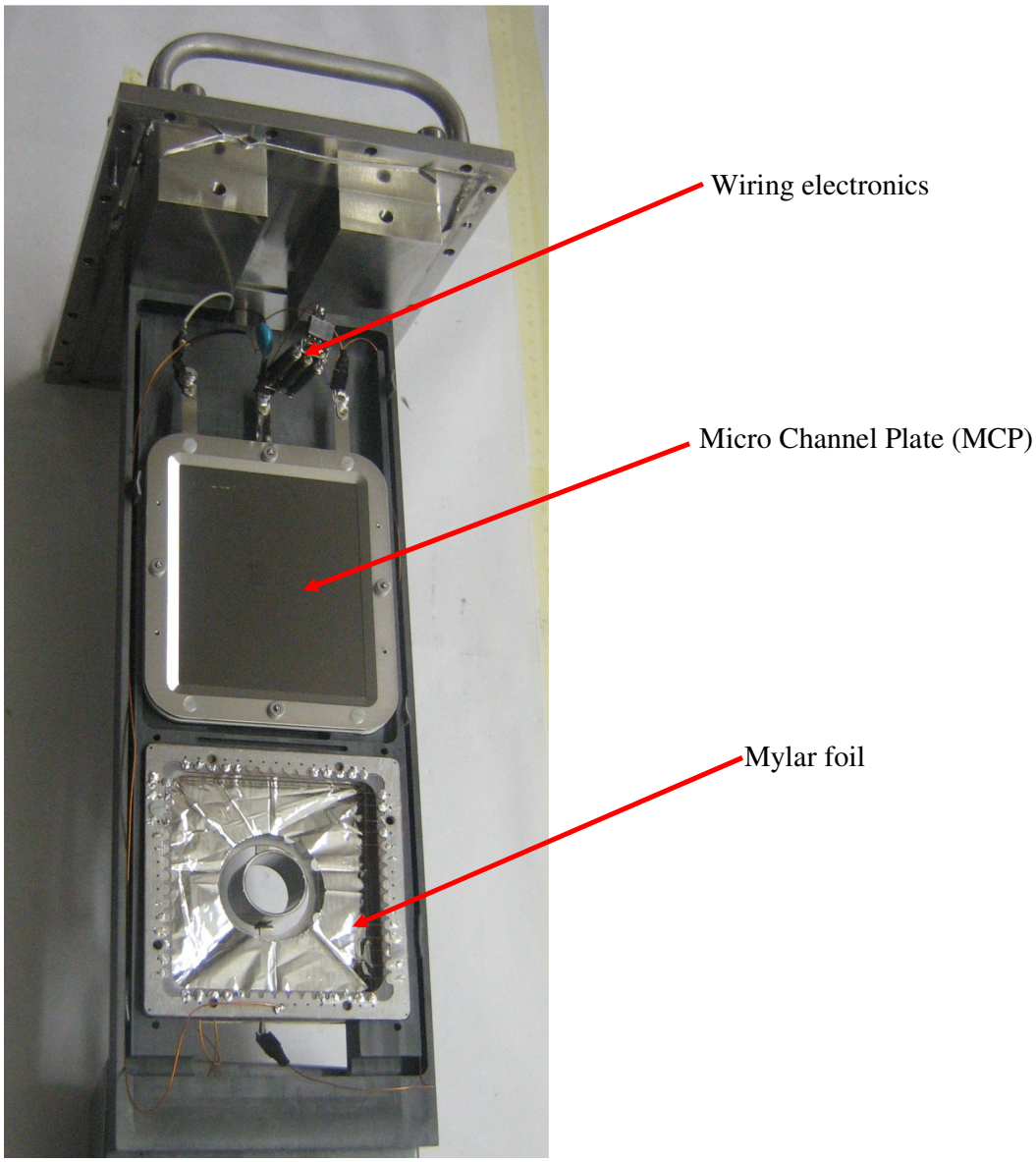

Figure 4:34. Photograph of the assembly plate on which the internal components of the recoil detector are mounted. It is attached to the top plate of the recoil detector chamber.

Table 4:3. Parameters of the modified recoil detector.

Parameters	Value	Units
Magnet		
Radius of curvature r	6.25	cm
Field B in the MCP chamber	22	G
Pole gaps	14	cm
Field B in the collimator vicinity	1000	G
Acceleration region		
Small hole in Mylar foil	2.3	cm
Big hole in Mylar foil	4.0	cm
Mylar foil active area with small hole	107.4	cm^2
Mylar foil active area with big hole	99.0	cm^2
Foil to the first grid distance	1	cm
Foil to the second grid distance	1	cm
Exit angle θ	0.33	rad
Accelerating Voltage in the foil	400	V
Distance from the target to the foil	14.5	cm
Voltage on the second grid	400	V
MCP Anode		
Maximum applied voltage	2070	V

4.1.14 Tests of the redesigned recoil detector

As for the previous version of the recoil detector, the new recoil detector was first tested using a ^{252}Cf source. A very good MCP signal without ringing, shown in Figure 4:35, was obtained, giving the "green light" for in-beam test experiments. The first in-beam experiment was performed using the $^{197}Au(\alpha, xn)$ reaction at 65 MeV. The recoil detector was equipped with a Mylar foil instead of a fragile carbon foil. This experiment demonstrated that the redesigned recoil detector worked with an efficiency of about 10% without any further loss of efficiency up to the maximum beam current of 20 pnA, that the SSC was able to deliver during the test. However the selectivity of the recoil detector was still not up to 100% as target X–rays were still

visible in the spectrum at a few percent level. Subsequently, experiments using the ^{232}Th(α, xn) reaction at 42 and 61 MeV were carried out. In this reaction the fission cross-section is dominant, forming 97 % and 84 % for the 61 and 42 MeV cases, respectively, according to PACE calculations. This leaves the ^{230}U and ^{232}U evaporation channels with only 2.4% and 15.4% of the reaction cross-section respectively.

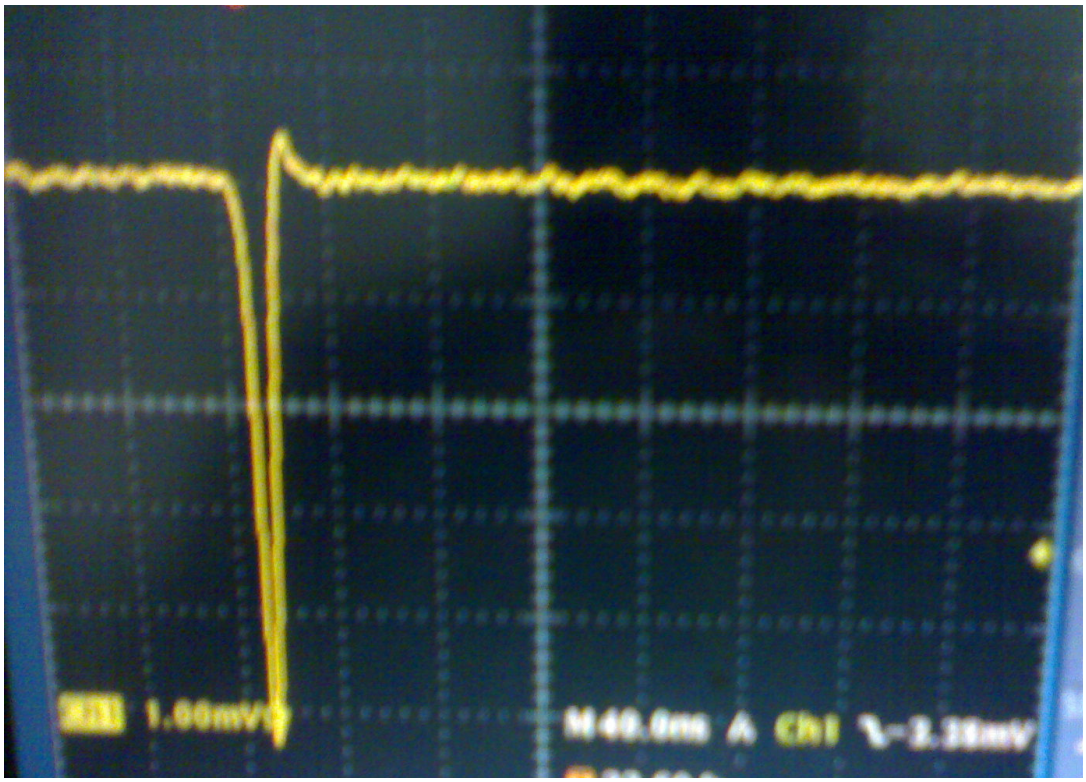

Figure 4:35. Signals obtained with the redesigned recoil detector.

Figure 4:36 and Figure 4:37 show the "time-of-flight" spectra for the two experiments. These spectra were measured by stopping a Time to Amplitude Converter (TAC) with the MCP signal and starting it with a signal from the cyclotron RF. The separation of the beam pulses was about 341 ns as shown in Figure 4:36 This separation is long enough to detect recoils with energies as low as 270 keV. The initial energies of the recoils, produced with 42 MeV and 61 MeV α-beams, are 725 keV and 1063 keV, respectively, but they are slowed down in the target. The time-of-flight spectrum in the 42 MeV data is very similar to that calculated in section 4.1.2. The 61 MeV data shows a broader recoil peak. The reason for this will be discussed in

CHAPTER 6. Another feature that can be seen in Figure 4:37 is that some of the recoils extend to the next beam pulse and unfortunately they do not fall inside the co incidence window. Therefore they cannot be counted as good events. This affects data statistics negatively. Not only that, actually the counts in the valley (see Figure 4:36) are a combination of the background and recoils.

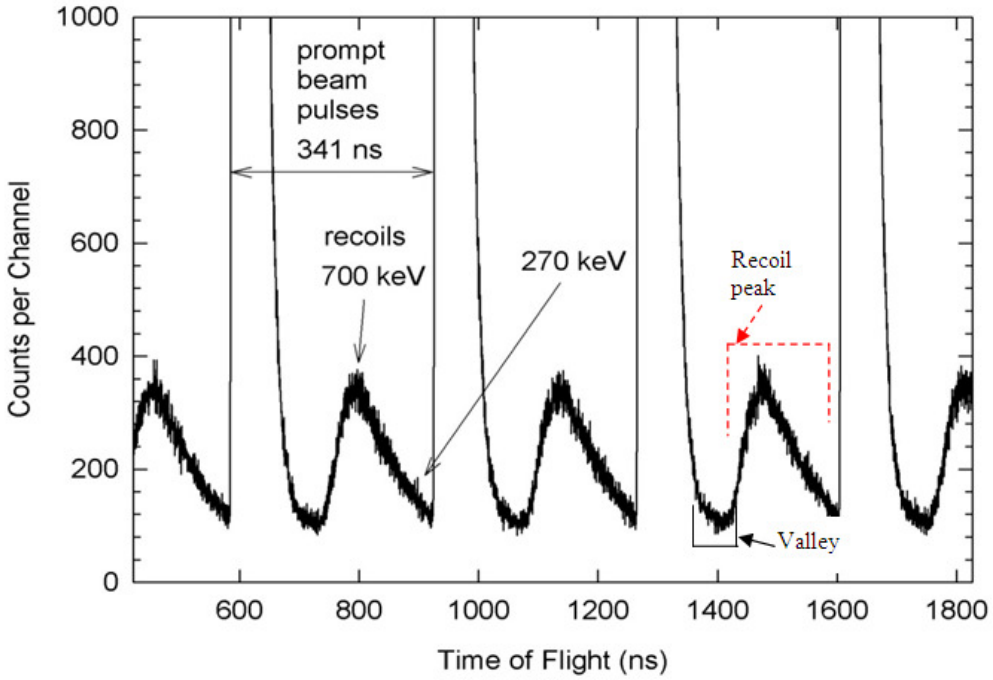

Figure 4:36. Number of particles detected as a function of the time-of-flight, measured at a beam current of 5 pnA for the reaction $^{232}Th(\alpha, 4n)$ at 42 MeV.

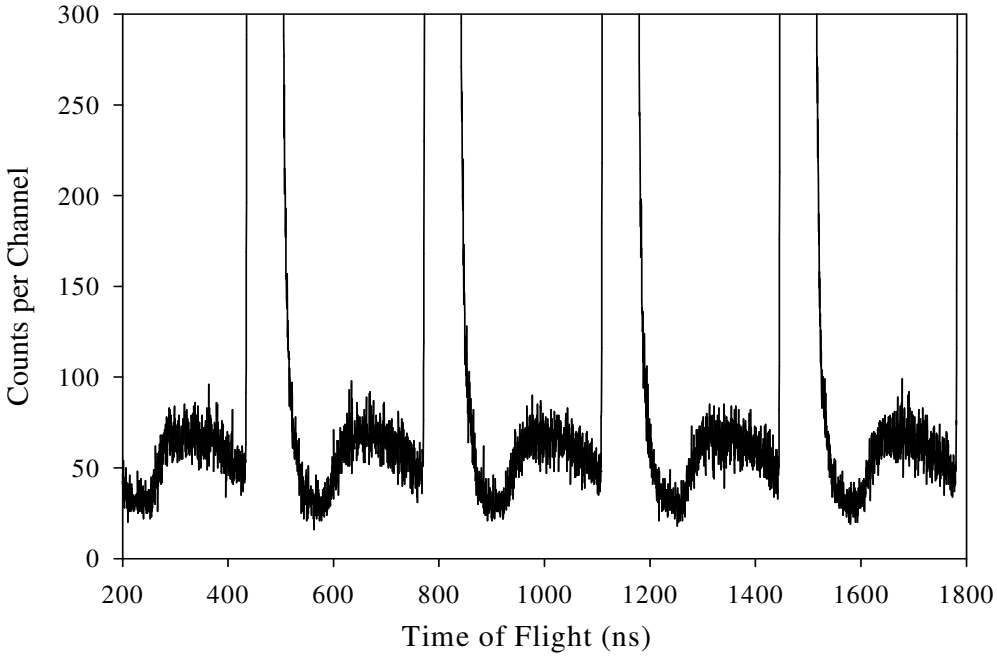

Figure 4:37. Number of particles detected as a function of the time-of-flight, measured at a beam current of 5 pnA for the reaction $^{232}Th(\alpha, 6n)$ at 61 MeV.

These results were obtained after considerable effort to optimize the performance of recoil detector, in particular, to reduce the background below the recoil peak. These efforts are the subject of the next sections.

4.2 Background reduction

Reducing the background to a desired level was one of the challenges in performing the experiments using the recoil detector. Some of the results are shown in Table 4:4. Figure *4*:*38* shows the number of particles detected as a function of the time when doing a test without beam. It could be seen that only few counts (see Figure *4*:*38*) are detected when there is no beam hitting the target. These counts are presumably random counts caused by dark current and due to radioactivity caused by the use of the beam prior to recording the spectrum. When beam is applied, but with the target removed, the spectrum shown in Figure 4:39 was observed. Peaks corresponding to the passage of the beam are seen together with a much higher background

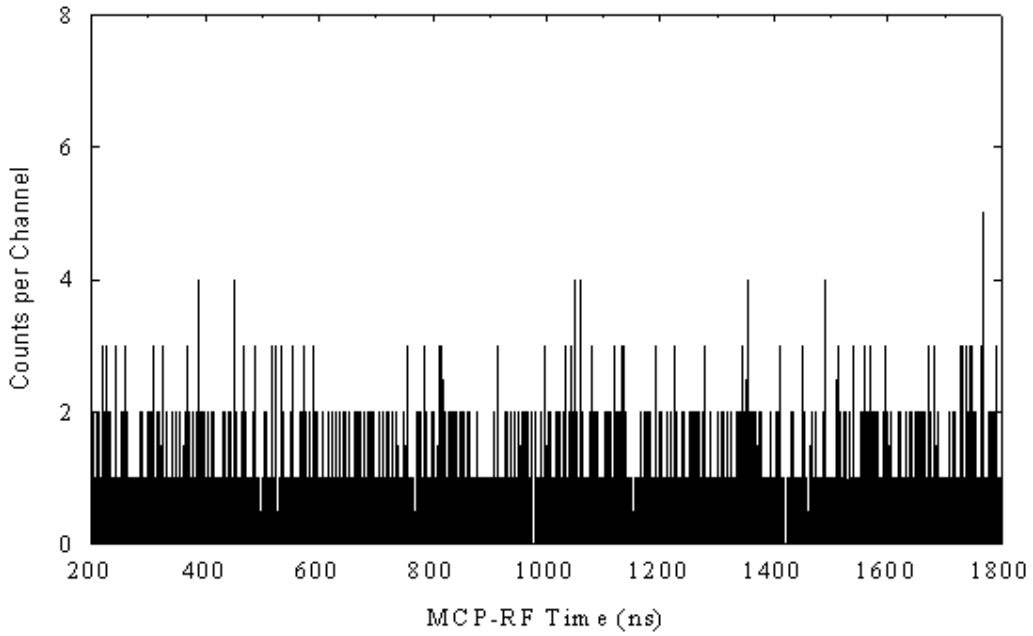

Figure 4:38. Number of particles detected as a function of the time-of-flight, measured without beam on target, in ten minutes.

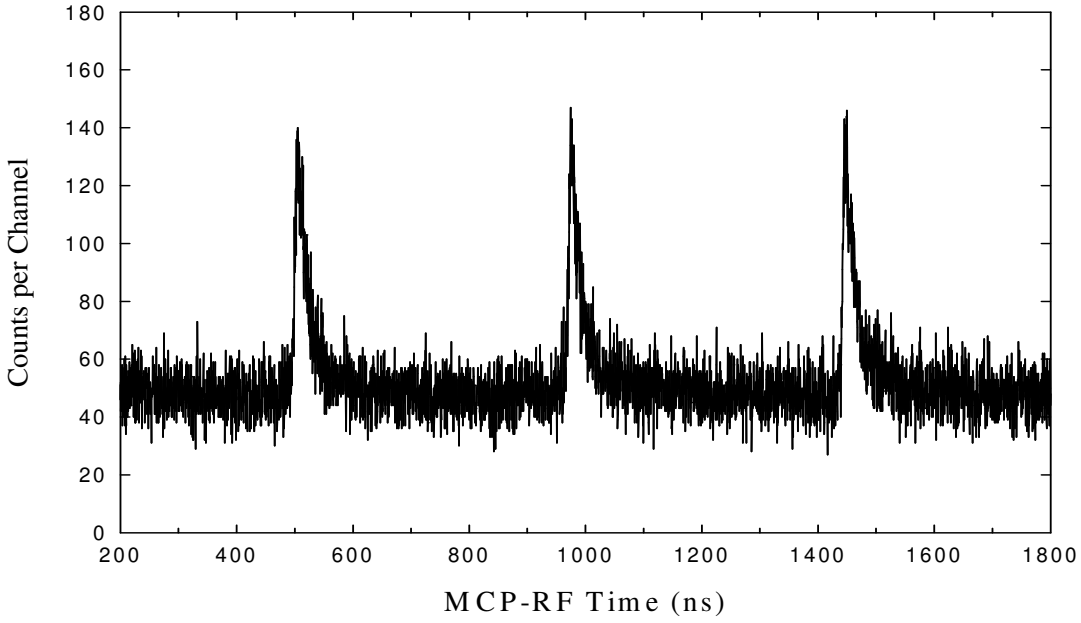

Figure 4:39. Number of particles detected as a function of the time-of-flight, measured at a beam current of 5.5 pnA with 0 V on the grid and without a target, in ten minutes.

The fact that there is considerable background between the beam pulse suggested that the background could be caused by slow moving positive ions from residual gas ionization striking the foil and ejecting electrons. As a result an investigation was undertaken by checking the effect of the vacuum on the background.

4.2.1 Effect of pressure

Simple tests were performed by turning off vacuum pumps and allowing the pressure to gradually increase. The results of the test are shown in Figure 4:40. The pressure measurements plotted in Figure 4:40 were taken 1 m from the MCP. This was the closest position where the pump and the gauge could be placed (as discussed in 4.1.13). There are high chances that the pressure in the chamber was worse than the measured one. The tests supported the hypothesis that the background was produced by positive ions - with bad vacuum (and hence a higher rate of gas ionization) a lot of background events, almost equal to the recoil events were detected, (see Figure 4:40, the green points). Meaning that the background increased with an increase in pressure.

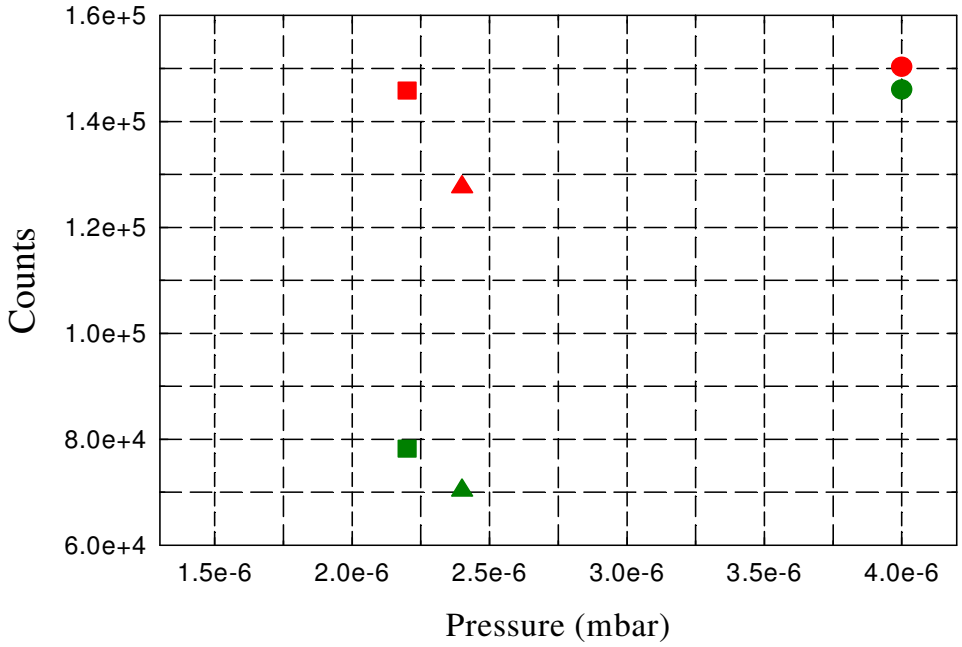

Figure 4:40. The plot shows the effect of vacuum on the peak to background ratio.The green points and red points represents the background events and the recoils events respectively. The counts were obtained from the recoil peak and the valley.

4.2.2 Effect of grid voltage

In order to address the background caused by the positive ions, a positive biased shield was placed around the sensitive foil to shield it from the positive ions. In this way the background was reduced to less than one percent. To provide a uniform, electric field-free region for the electrons to orbit into the MCP, an additional grounded grid was placed in front of the positively biased grid. The grids function using the principle described in Figure 4:41. The magnetic field was also reduced by a factor of two, resulting in a reduction of the acceleration voltage to about 400 V.

The applied voltages create the electric fields as indicated in Figure 4:41(b) and the potentials shown in Figure 4:41(c). As a result the positive ions were deflected away from the foil. Therefore applying 400 V to the grid and 300 V to the foil reduced the background almost completely. Figure 4:39 and Figure 4:42 shows the results obtained when using a beam current of 5.5 and 30 pnA, without and with a grid voltage respectively on an empty target. Evidently positive-ions have a huge contribution to the production of background. The effect of the grid is summarized in Table 4:4. All the thresholds in this thesis were taken from the threshold monitor which is ten times the actual threshold [Ort_1].

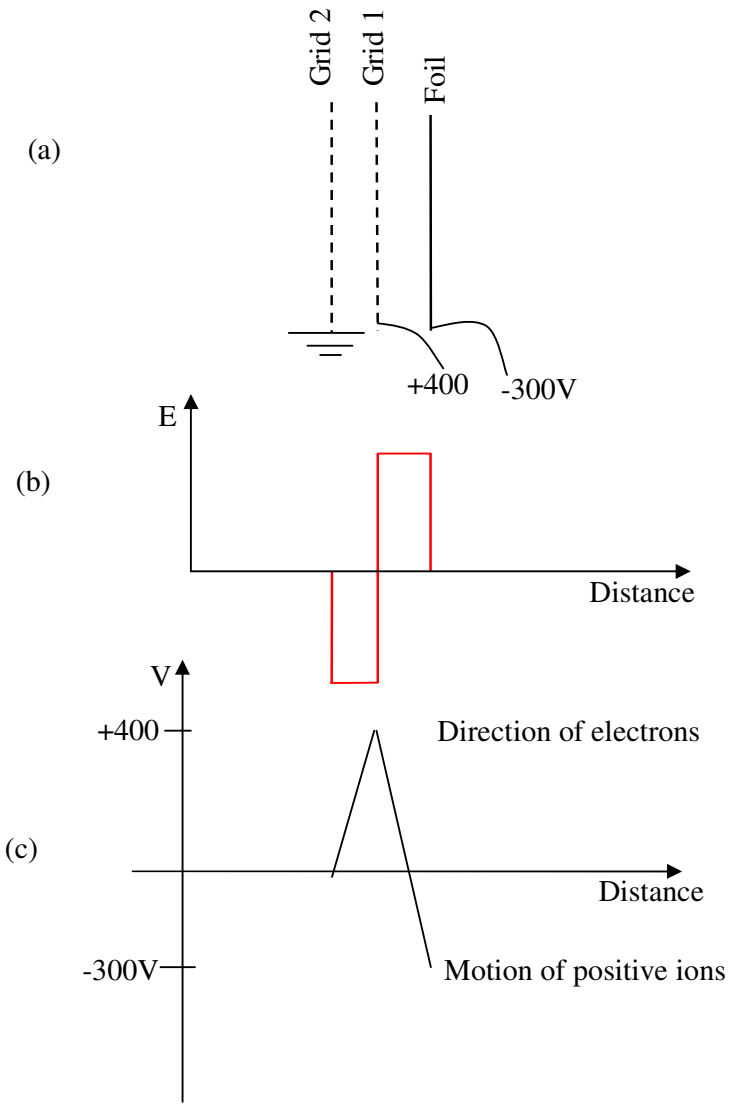

Figure 4:41. The diagram showing the function of grid 1 and grid 2.

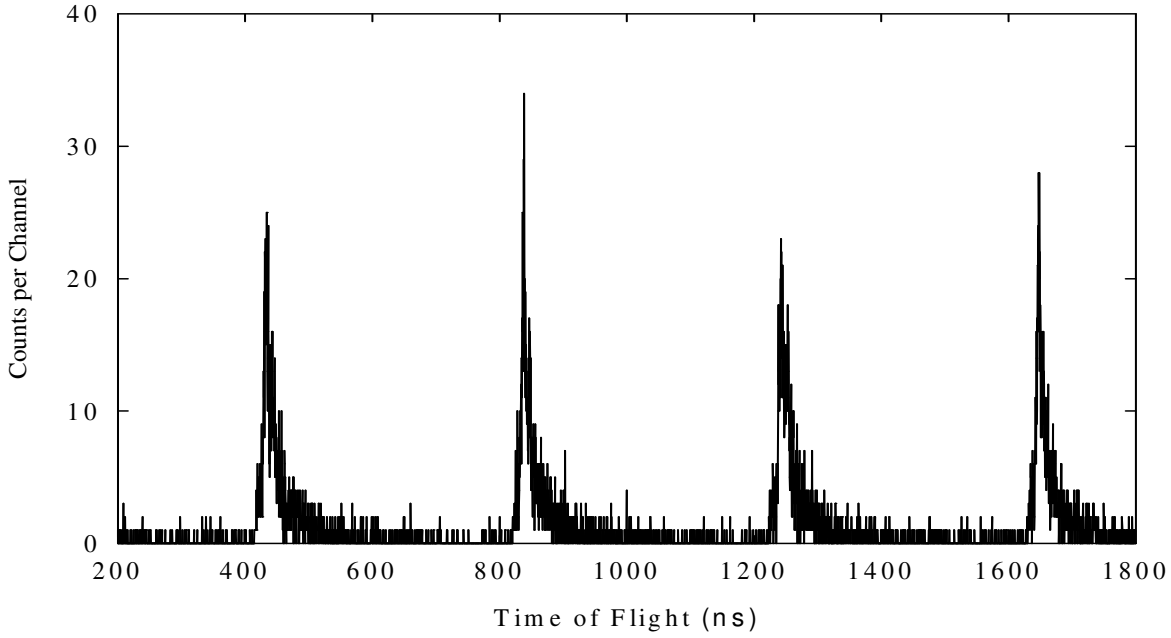

Figure 4:42. Number of particles detected as a function of the time-of-flight, measured at beam current of 30 pnA, using reaction ^{232}Th(α, 4n) on an empty target at 42 MeV with grid voltage of 400 V.

Table 4:4. Table shows the effect of the additional downstream grid on the MCP background. All measurements were performed for a period of 10 minutes.

Beam (pnA)	**Discriminator level (V)**	**Target Position**	**Deflection grid voltage**	**Background counts**
10	1.3	out	on	100
10	1.3	out	off	25000
0	0.5	in	on	250
30	0.5	out	on	1000
30	0.5	in	on	16000

Figure 4:43 compares the results obtained with 0 and 400 V on the grid for ^{232}Th(α, xn) at 42 MeV. There is a remarkable improvement on the peak to background ratio

on the results obtained when running with 400 V on the grid. The grid is used to repel positive ions, and this prevents them from hitting the foil, hence reducing the background.

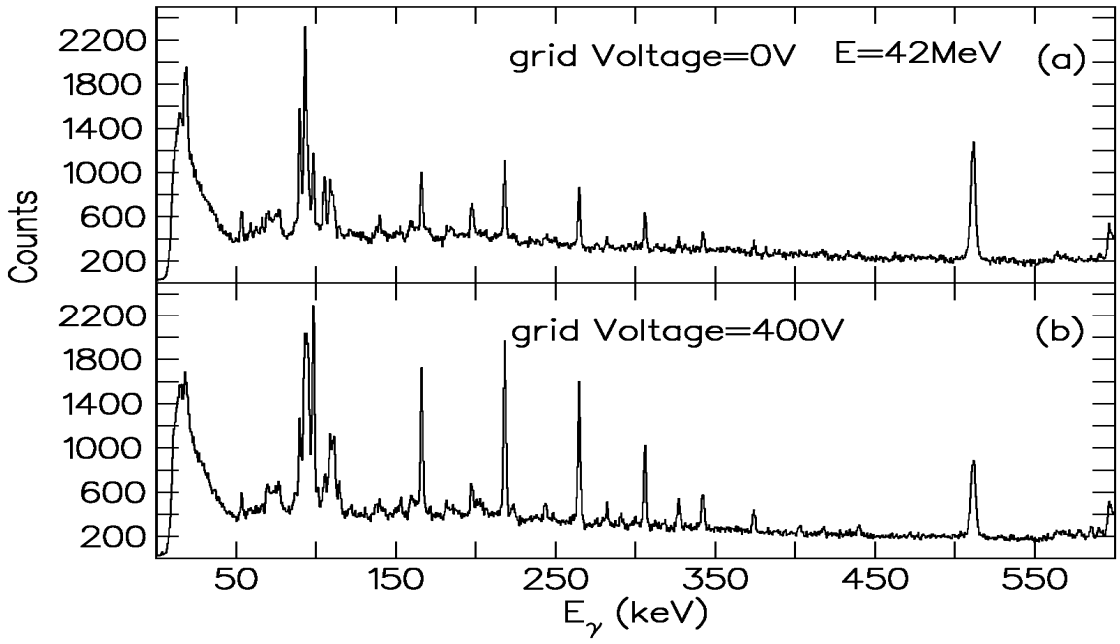

Figure 4:43. Comparison of spectra obtained using the reaction ^{232}Th(α, xn) at beam energy of 42 MeV at different grid voltages and 3.5 V CFD setting.

4.2.3 Effect of increasing beam current

One of the requirements for better performance of the recoil detector is well focused beam. However focusing gets poorer with an increase in beam current. Figure 4:36, Figure 4:44, Figure 4:37 and Figure 4:45 compare the level of background for different beam currents at the respective beam energies. For the ^{232}Th(α, 4n) reaction, the ratio of the peak to valley (P/V) is approximately 2.5 at a beam current of 5 pnA compared to P/V of 1.3 for 30 pnA (see Figure 4:36 and Figure 4:44). Furthermore the P/V for ^{232}Th(α, 6n) reaction is about 1.5 and 1.2 for 5 and 20 pnA, respectively (see Figure 4:37 and Figure 4:45). This evidence clearly shows that increasing the beam current degrades the performance of the recoil detector. At the same time, beam time is a very special commodity at iThemba LABS. Therefore taking into consideration, the reaction cross-section and the beam time, it is clear that a compromise has to be made when choosing the beam current, so that better statistics and good data can be

obtained. The decision however, is made on the basis of the quality of the recoil time-of-flight spectrum formed in coincidence with at least one γ–ray. These are shown for the two reactions in Figure 4:46 .

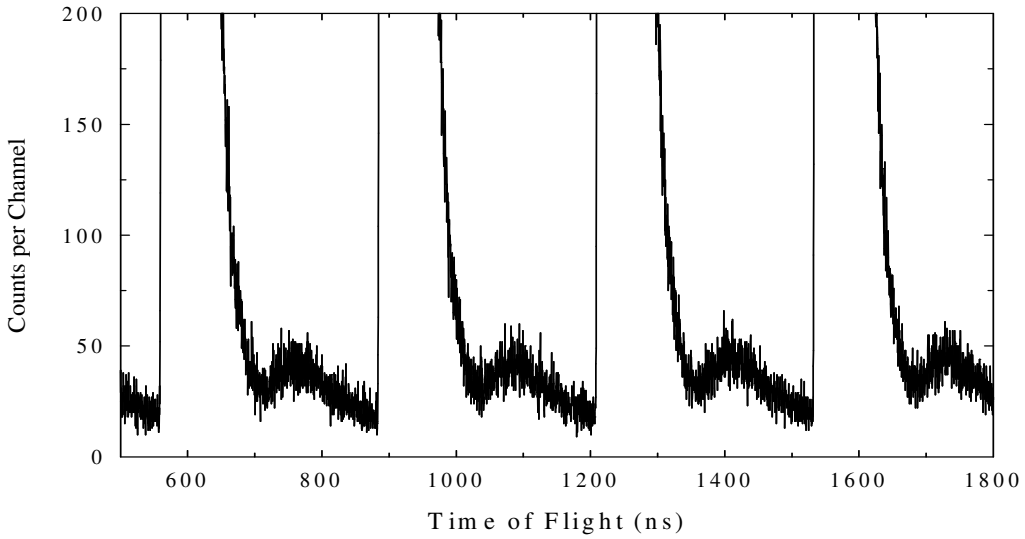

Figure 4:44. Number of particles detected as a function of the time-of-flight, measured at a beam current of 30 pnA and the reaction $^{232}Th(\alpha, 4n)$ at 42 MeV.

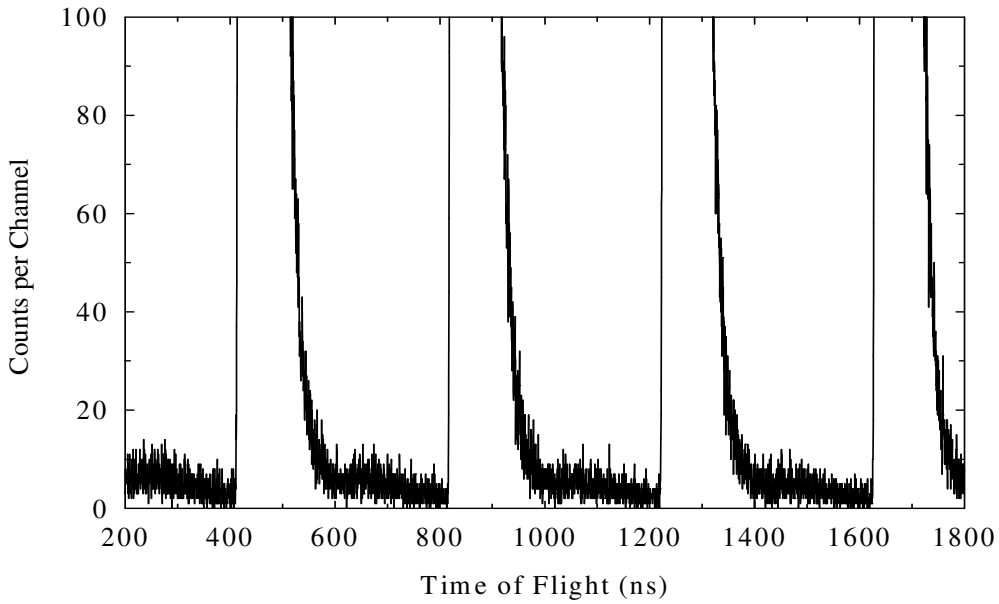

Figure 4:45. Number of particles detected as a function of the time-of-flight, measured at a beam current of 20 pnA for the reaction $^{232}Th(\alpha, 6n)$ at 61 MeV.

The requirement of the detection of at least one γ–ray considerably reduces the background, implying that much of the background in the recoil detector does not produce a γ–ray. Note the wiggles in the MCP time spectra and the peak at 100 ns were caused by some electronics effects.

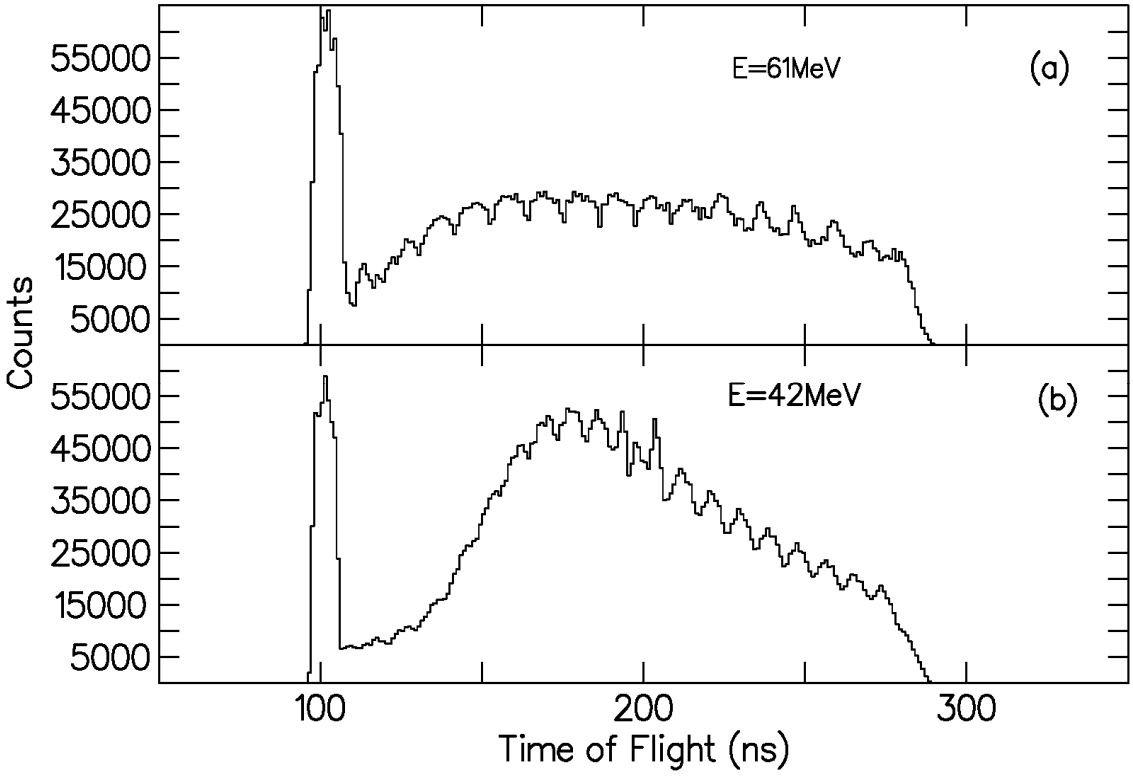

Figure 4:46. The time-of-flight measurement performed with γ–recoil co-incidence at (a) 61 MeV and (b) 42 MeV using the reaction $^{232}Th(\alpha, xn)$.

4.2.4 Foil Voltage

The designed accelerating voltage applied to the foil was about 2000 V, but above a voltage of 1100 V a large background appeared between the beam pulses. Since the level of background was a function of the voltage, the foil voltage was reduced to about 500 V. Although this reduced the background the reasons were never understood. This actually gives the maximum detection efficiency of the recoil detector as indicated in Figure 4:15.

4.2.5 Effect of the hole

Theoretical calculations indicate that a small hole in the foil can improves the recoil detector efficiency. However in the experiment with the small hole the recoil detector caused more background to be detected. Figure 4:47 compares the results obtained using (a) small of 23 mm in diameter and (b) a big hole of 40 mm in diameter in the reaction ^{232}Th(α, xn) at 61 MeV with 2 pnA. This lead to the decision to use the big hole in the experiments.

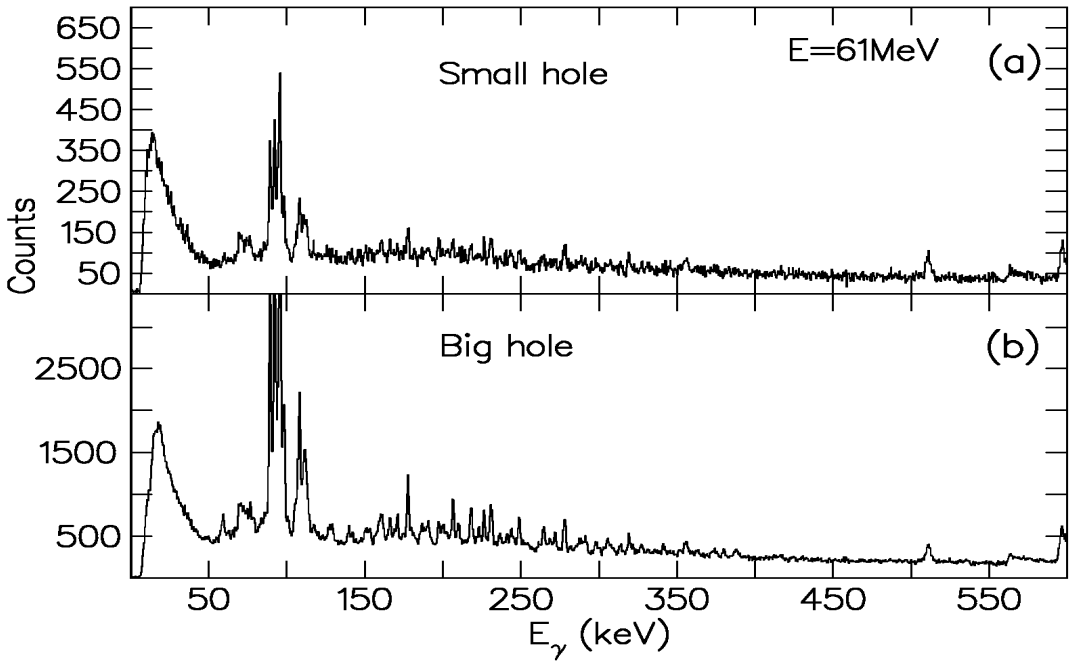

Figure 4:47. Comparison between the spectra obtained using a foil with (a)small hole (23 mm diameter) and (b) big hole (40 mm diameter).

Beside the origin of background discussed above, additional background is detected due to random coincidences in the time gates. Examples of such gates are the γ–γ and the γ–recoil gates. The fission, Coulomb excitation, β-decay and X–rays all emit gamma rays which by coincidence fall within the set time gate. The time gate for the coincidence was set to be 200 ns. On the other hand the scattered beam, gas ionization and ringing can knock out an electron in the foil which coincides with electrons knocked out by recoils. If these arrive at the same time in the recoil gate of 300 ns then the background event will be detected. Using the known recoil and gates

and the peak to the background information the probability of detecting these unwanted events can be calculated.

4.2.6 Constant Fraction Discriminator (CFD)

In order to better understand the background a Charge to Digital Convertor was obtained and implemented in the later weekends. The circuit diagram of the QDC is shown in Figure 4:48. Figure 4:49 compares the data obtained at different CFD thresholds namely, 1.5 and 4.0 V. In Figure 4:50 which is a projection of Figure 4:49, two broad peaks for the CFD threshold of 4.0 V are observed (see Figure 4:49(a)). The high peak at higher channels corresponds to the evaporation residues while the lower peak corresponds to the background. Evidently with CFD threshold of 1.5 V the background peak became more dominant such that the evaporation peak is shadowed. Its position is marked by the arrow and is not visible because the background tail extends to higher channels.

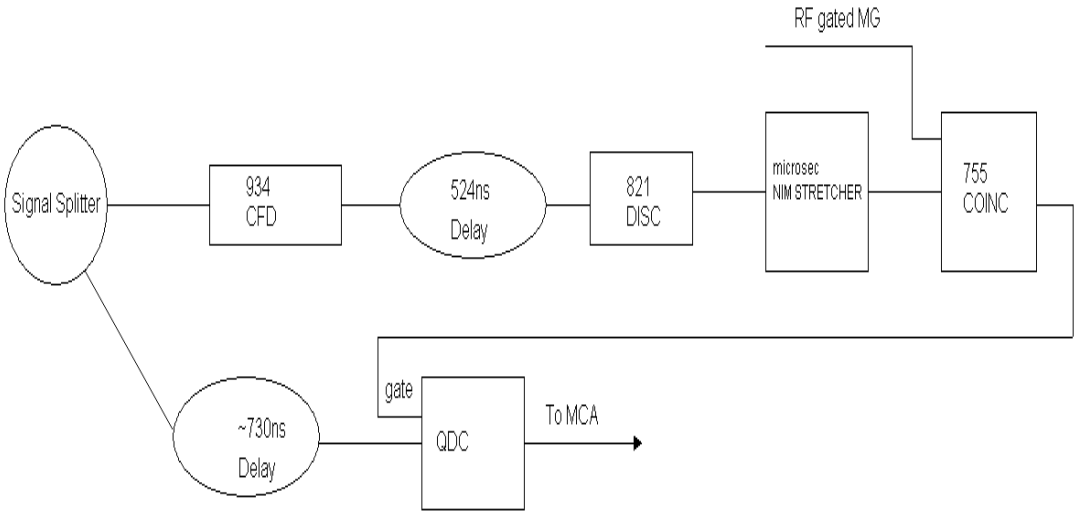

Figure 4:48. The circuit diagram for the Charge to Digital Convertor (QDC).

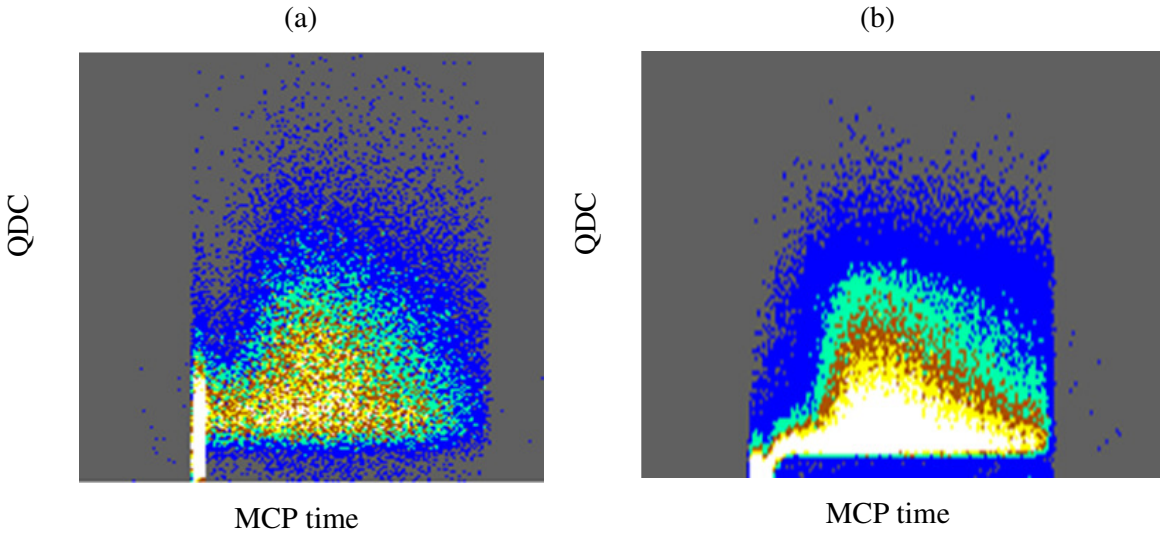

Figure 4:49. The energy of the measured products plotted as a function of time, obtained when running with a Charge to Digital Convertor (QDC) setup at different CFD setting i.e. (a) CFD = 4 V and (b) CFD = 1.5 V at beam energy of 61 MeV.

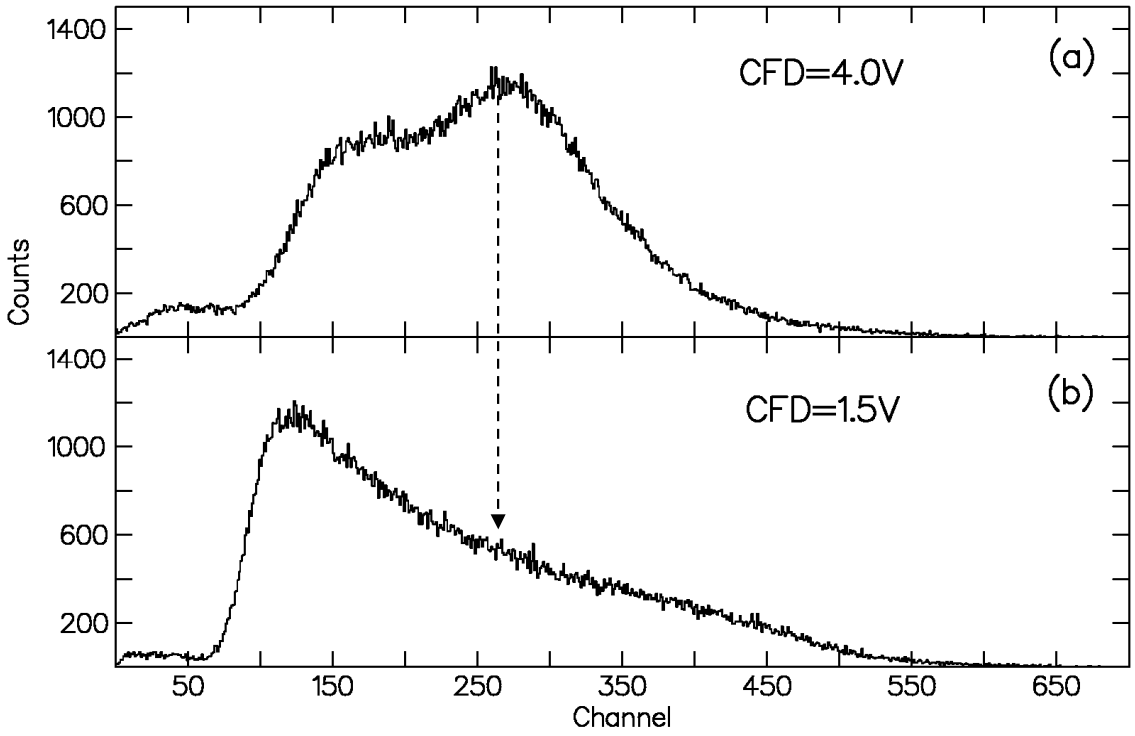

Figure 4:50. The Charge Digital Convertor (QDC) spectra for the $^{232}Th(\alpha, xn)$ at E = 61 MeV for different CFD setting i.e. a projection of Figure 4:49.

Furthermore the effect of the CFD can also be seen in Figure 4:51 which compare – recoil CLOVER spectra obtained at different CFD thresholds. These spectra were attained at the same amount of time. Although there are high statistics for low threshold, the bulk of the events are background events (see peak to background ratio in Figure 4:51(c). At the same time setting the threshold too high gives very good data but at a price of lower statistics, this can be seen when comparing Figure 4:51 (a) and Figure 4:51 (c). A two-dimensional software gate was also applied to the QDC-MCP time spectra to optimize statistics and signal-to-noise ratio. Figure 4:37 and Figure 4:50 shows that the background and the recoils overlap, therefore even though setting the CFD high gives a better peak to background ratio, it also cuts away recoils. Therefore, just like with the beam current, when setting the CFD threshold, a compromise had to be made, so that better statistics and good data could be achieved. Eventually an intermediate threshold of 3.5 V was used to perform the experiment, but this still pick up some background (*see Figure 4:51(b)*).

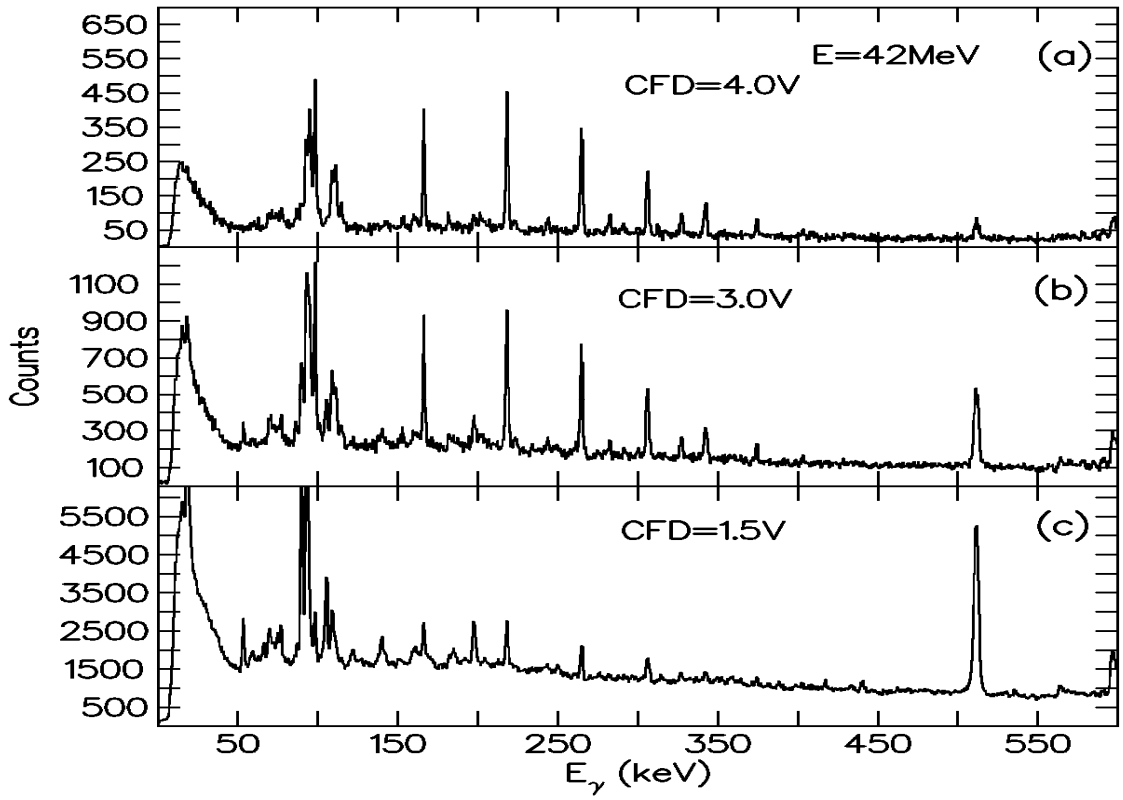

Figure 4:51. Comparison of CLOVERS spectra obtained using ^{232}Th(α, xn) at 42 MeV at different CFD threshold.

Ultimately when all the discussed parameters were optimized, data were collected. Figure 4:52 and Figure 4:53 compare the coincidence spectrum and the γ–γ–recoil spectrum results obtained after all the recoil detector's components were optimized. The results clearly show that after optimizing all the components the recoil detector reduced the background to a desired level.

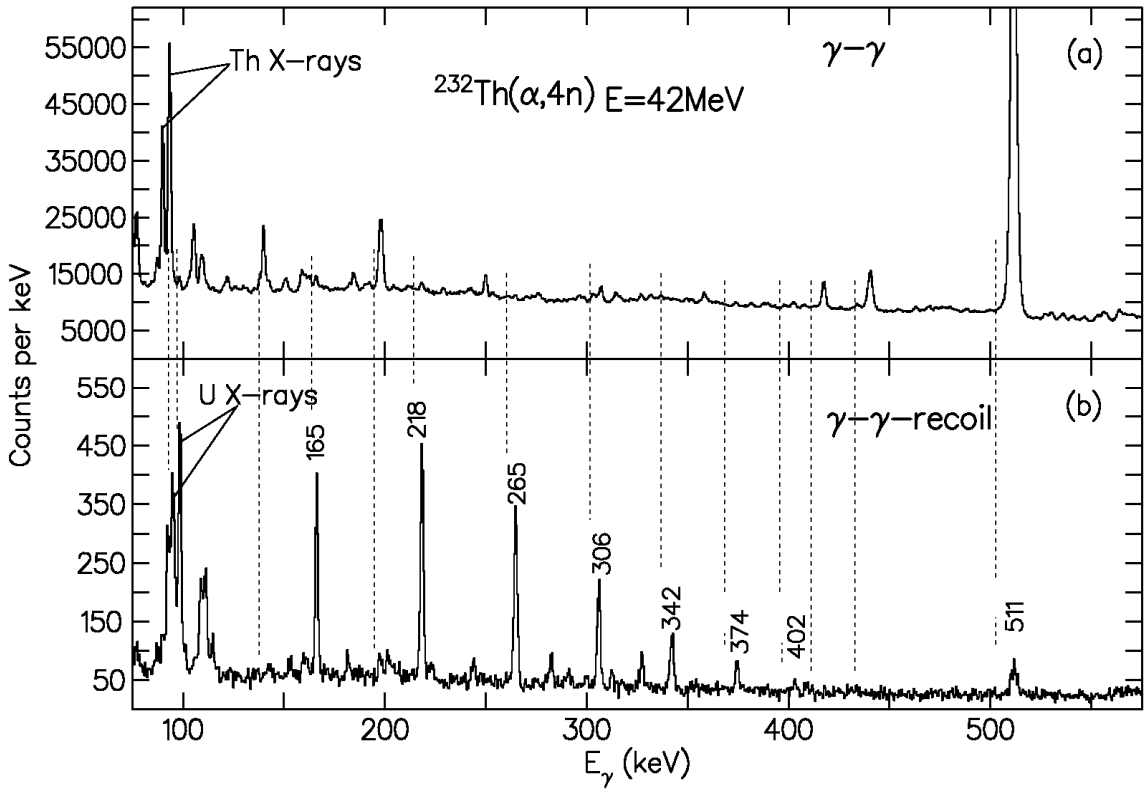

Figure 4:52. Spectra obtained in the ^{232}Th(α, 4n) experiment at beam energy of 42 MeV using the redesigned recoil detector. Upper portion: total projection spectrum. Lower portion: recoil gated total projection spectrum.

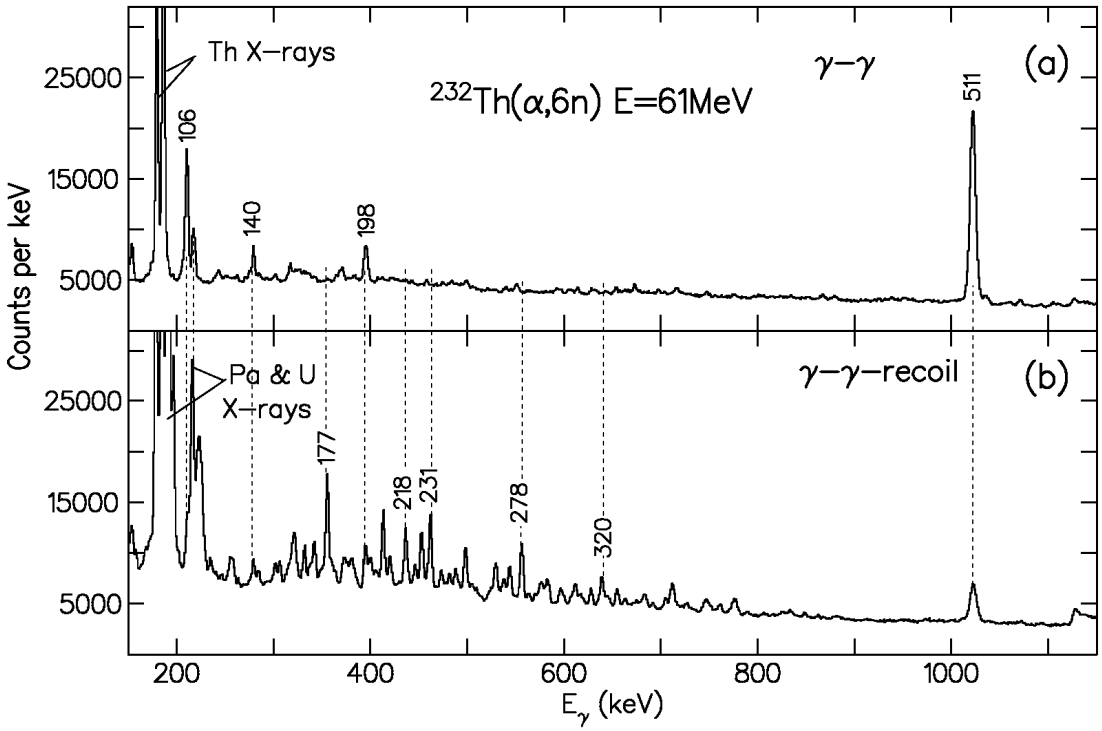

Figure 4:53. Spectra obtained in the ^{232}Th(α, 6n) experiment at beam energy of 61 MeV using the redesigned recoil detector. Upper portion: total projection spectrum. Lower portion: recoil gated total projection spectrum.

4.3 Efficiency of the recoil detector

The recoil detector efficiency could be obtained by comparing the gated data to the γ–recoil data corrected for charge or by performing the two coincidence modes concurrently. Figure 4:54 shows the spectra of the results obtained by performing the γ and the γ–recoil coincidence modes. The arrows in Figure 4:54(a) indicate the energies of the U transitions, but these transitions cannot be observed because of the severe fission background. Although there are few statistics in the γ–recoil spectrum (see Figure 4:54(b)) partly because the test was done for a short period of time, the U transition are clearly observed. Of interest was the complete disappearance of the 511 keV line. With the modified recoil detector, for the ^{232}Th(α, 4n) reaction the recoil detector efficiency was measured to be 7% while for the ^{232}Th(α, 6n) the efficiency could not be deduced because the ^{230}U lines are not seen at all in the results which are not recoil gated. The reaction X–rays and the 218 keV transition were used to deduce the efficiency.

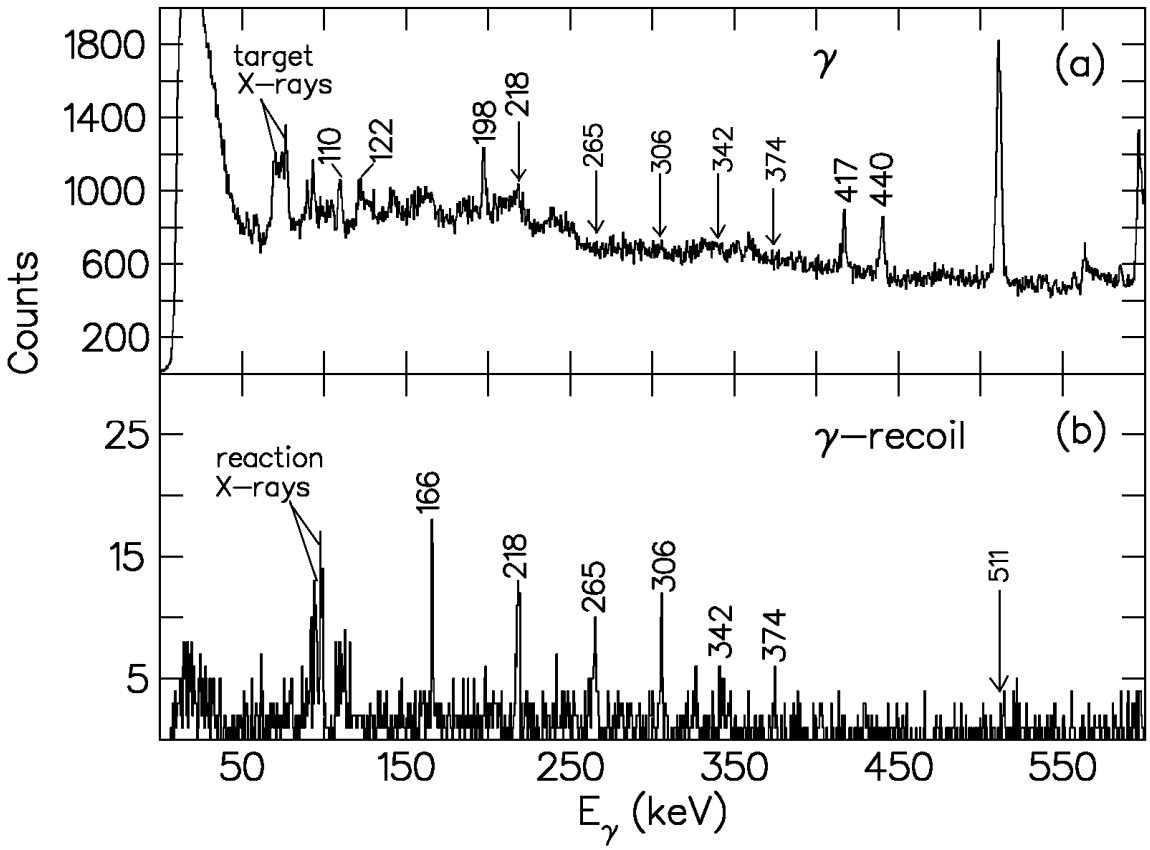

Figure 4:54. The (a) γ single CLOVER spectra (b) γ–recoil CLOVER spectra taken concurrently. This is used to determine the efficiency of the recoil detector for the reaction ^{232}Th(α, 4n) at beam energy of 42 MeV, at beam current of 15 pnA.

CHAPTER 5 RESULTS

5.1 The construction of the level schemes

As stated in section 3.6, the acquired data were sorted into a γ–recoil matrix in order to analyze γ–rays which are in coincidence. The total projections for the CLOVER detectors are shown in the spectra of Figure 5:1, Figure 5:2, and Figure 5:3, for the different reactions and beam energies which were used. Figure 5:4 shows the total projection spectrum for the LEPS detector.

In order to study the quantum mechanical properties (excitation energy, angular momentum, etc) of a de-exciting nucleus, a level scheme must be created (using the program ESCL8R) [Rad95]. ESCL8R is a program for graphics-based analysis of coincidence data for the deduction of the level schemes. The placement of γ–ray transitions in the level scheme results from the coincidence relationships that can be established using γ–γ matrices and γ–γ–γ cubes. In addition, these multi-dimensional arrays can be triggered by particle detectors. In this work, since AFRODITE was used together with the recoil detector, a γ–recoil trigger was used.

When sorting the matrix, the CLOVER/LEPS time was always gated at the prompt peak as shown in Figure 5:5. This is done to ensure that only prompt γ–rays are allowed to contribute to the matrix. It is very important that the gate is not too wide so as to not accommodate the next beam pulse. Furthermore, since the recoil detector was used in this work, there was an MCP time gate in addition of the CLOVER/LEPS time gates. Figure 5:6 and Figure 5:7 show the MCP time spectra with positions of time gates for the different measurements.

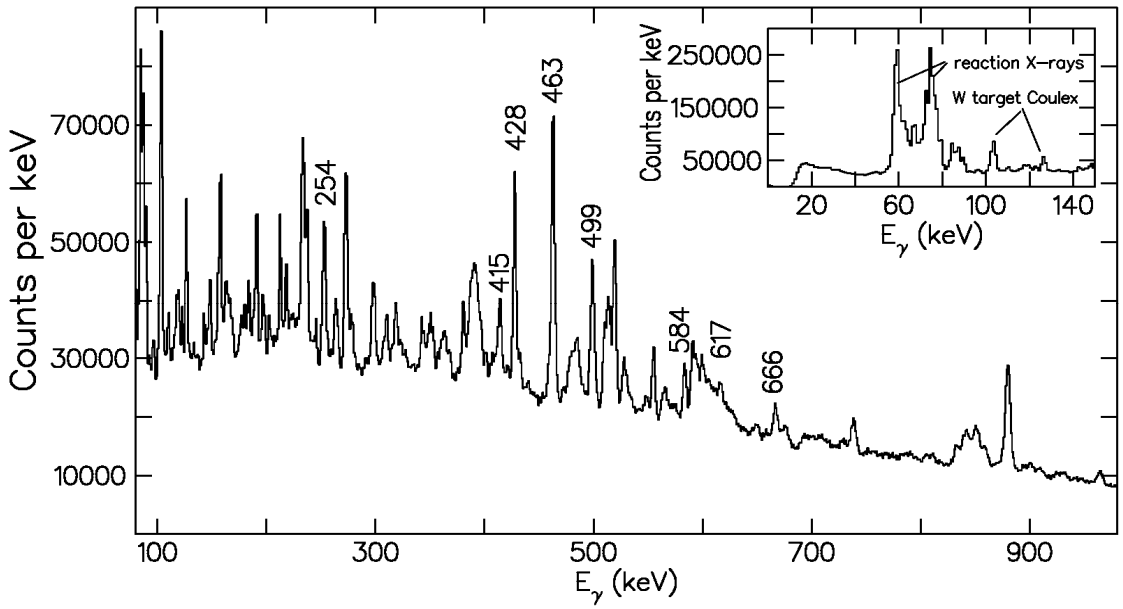

Figure 5:1. Total projection spectrum for the ^{180}W (^{20}Ne, 4n) ^{196}Po reaction of the CLOVER matrix. The known γ–rays of ^{196}Po are labelled with their energies. The observed X–rays corresponding to this spectrum are shown in the insert. This spectrum is not background subtracted.

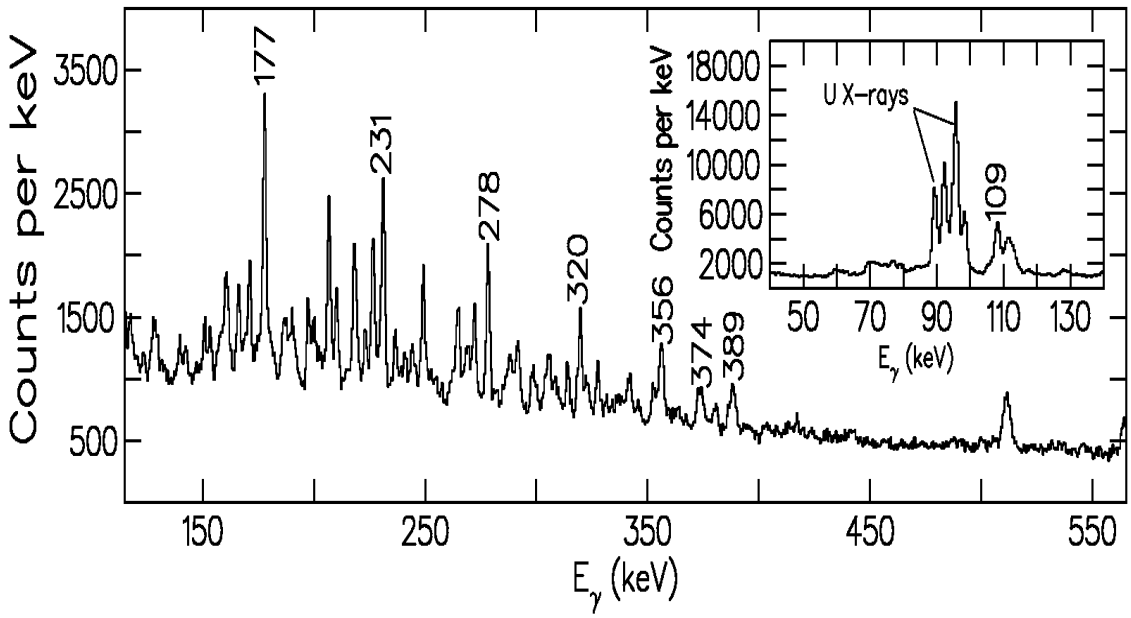

Figure 5:2. Total projection spectrum for the $^{232}Th(\alpha, 6n)$ ^{230}U reaction of the CLOVER matrix. The background is not subtracted. The known γ–rays of ^{230}U are labelled with their energies. The observed X–rays corresponding to this spectrum are shown in the insert.

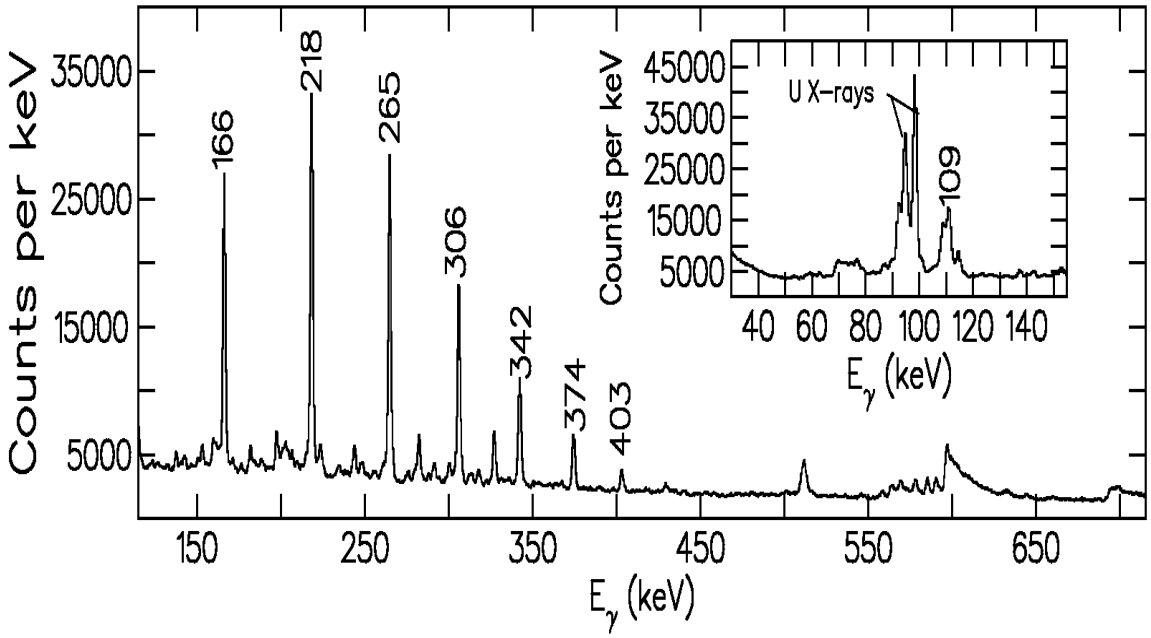

Figure 5:3. Total projection spectrum from the ^{232}Th (α, 4n) ^{232}U reaction for the CLOVER matrix. The known γ–rays of ^{232}U are labelled with their energies. The observed X–rays corresponding to this spectrum are shown in the insert. This γ–recoil gated spectrum is not background subtracted.

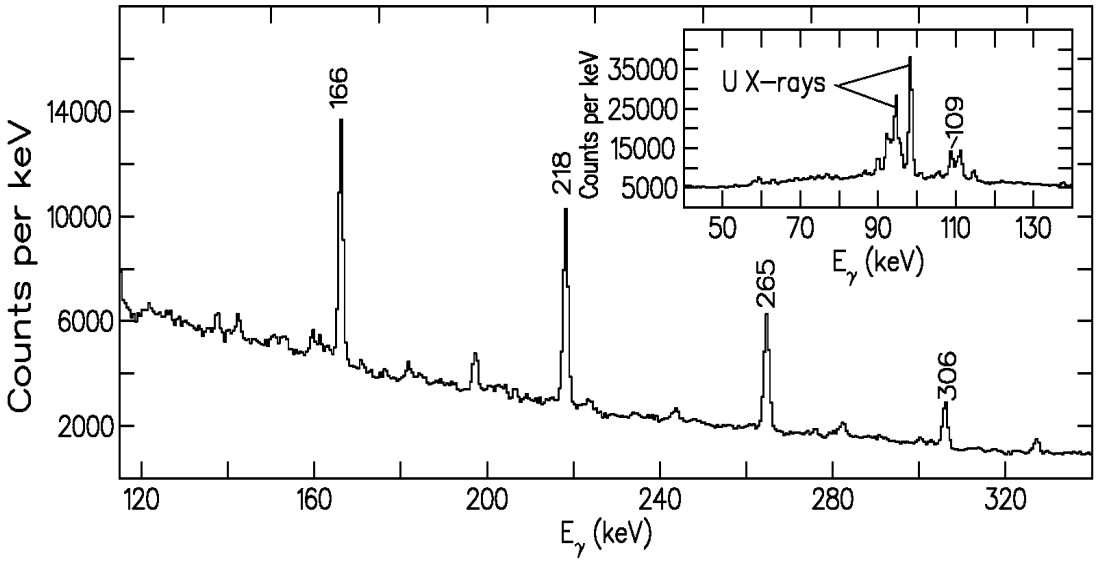

Figure 5:4. Total projection spectrum from the ^{232}Th (α, 4n) ^{232}U reaction for the LEPS matrix. The known γ–rays of ^{232}U are labelled with their energies. The observed X–rays corresponding to this spectrum are shown in the insert. This γ–recoil gated spectrum is not background subtracted.

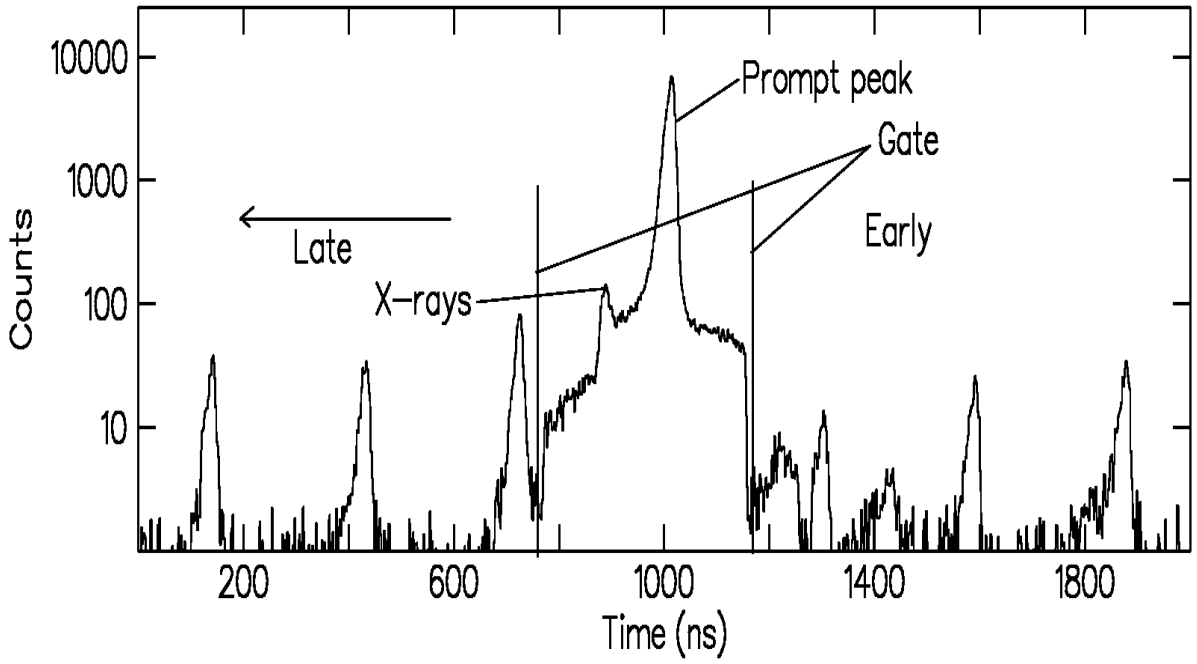

Figure 5:5. The prompt gate on the gain matched CLOVER time spectrum.

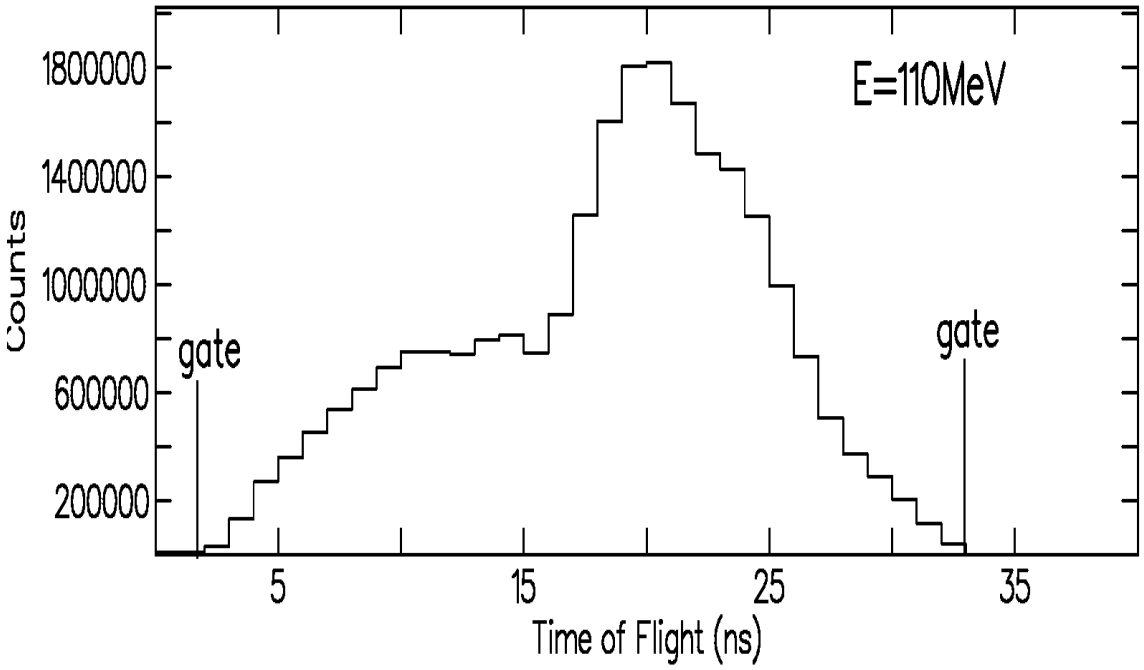

Figure 5:6. Time-of-flight measurements for the recoils produced in the $^{180}W(^{20}Ne, xn)$ reaction at E = 110 MeV.

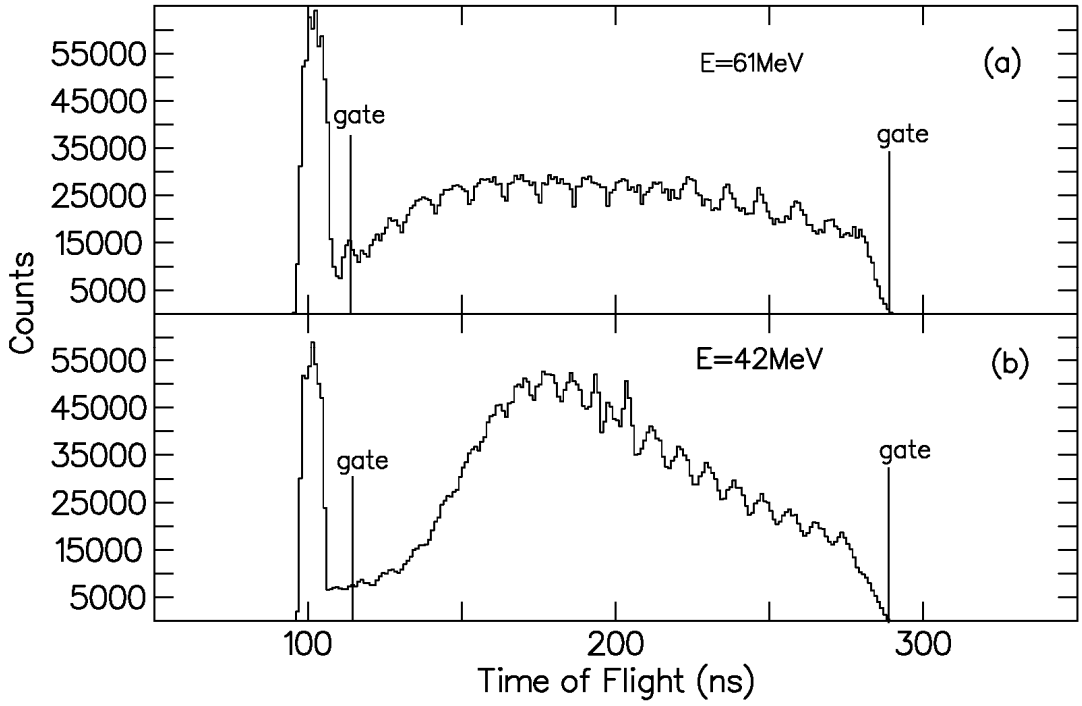

Figure 5:7. Time-of-flight measurements for the recoils produced in the $^{232}Th(\alpha, xn)$ reaction at (a) E = 61 MeV (b) E = 42 MeV.

5.2 The ^{196}Po level scheme

The ^{196}Po level scheme deduced from a previous study [Ber95] is known up to the 3647 keV state, see Figure 5:8. The ^{196}Po level scheme deduced from the current work is shown in Figure 5:9. Substantial changes to the earlier level scheme have been made. The summed spectrum of the transitions in the ground band of ^{196}Po is shown in Figure 5:10. The ^{196}Po results presented in this thesis contradict the placement of the 617, 388 and 668 keV γ–rays shown on the left hand side of Figure 5:8 [Ber95]. This is demonstrated in Figure 5:11 where the 617 and 666 keV gates are shown. It is clear that the 617 and 666 keV γ–rays transitions are not in mutual coincidence, contradicting the previous level scheme. In the spectrum gated on the 617 keV line the 390 keV γ–ray transition is seen, this implies the presence of a 49 keV transition which was not observed in this work, presumably due to internal conversion. The 592 keV line seen in the 666 keV gate in the Figure 5:11(b) results from ^{193}Pb contamination.

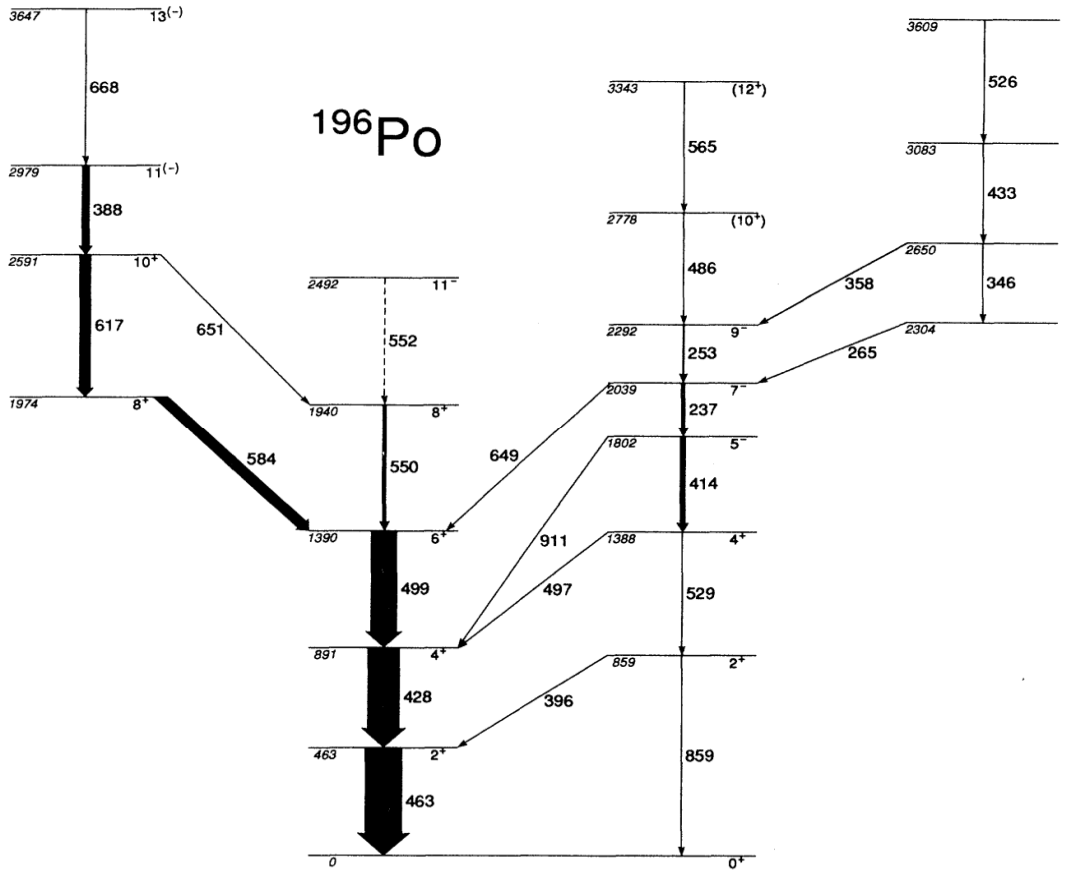

Figure 5:8. Partial ^{196}Po level scheme obtained in a previous measurement [Ber95]. The 11$^-$ state was taken from [Alb91].

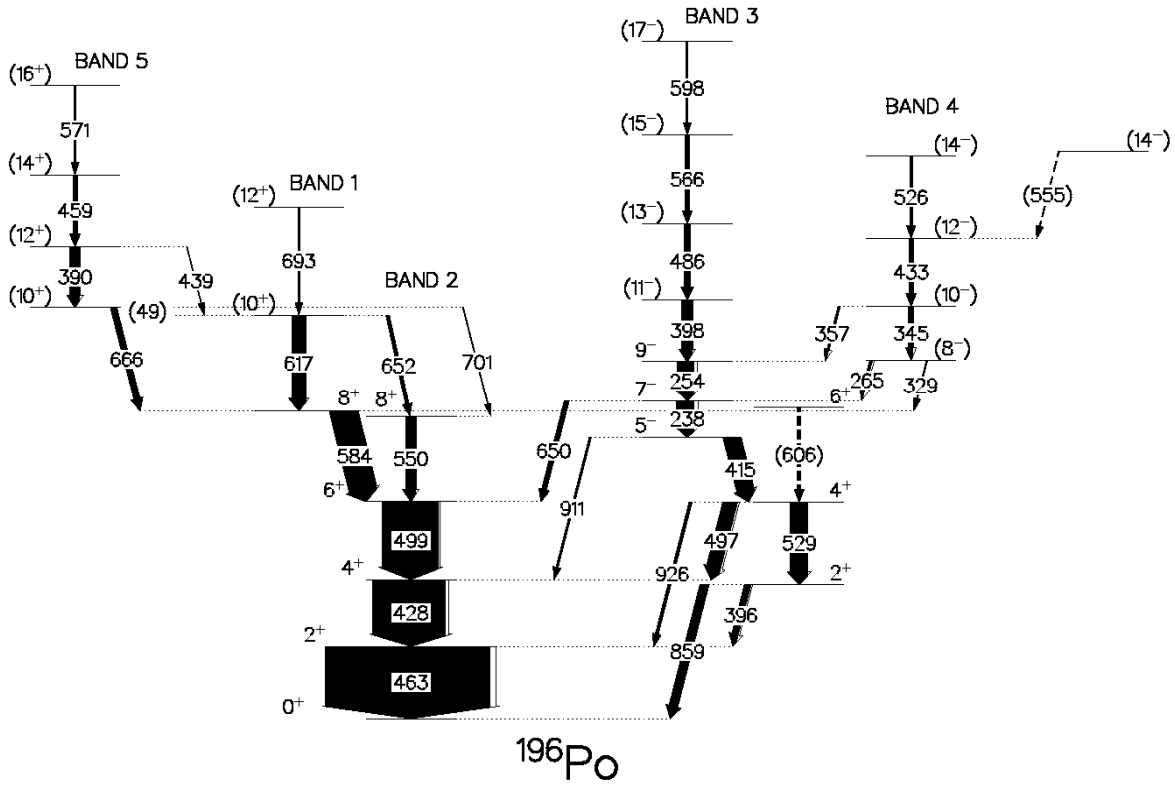

Figure 5:9. Partial level scheme of ^{196}Po deduced from this work.

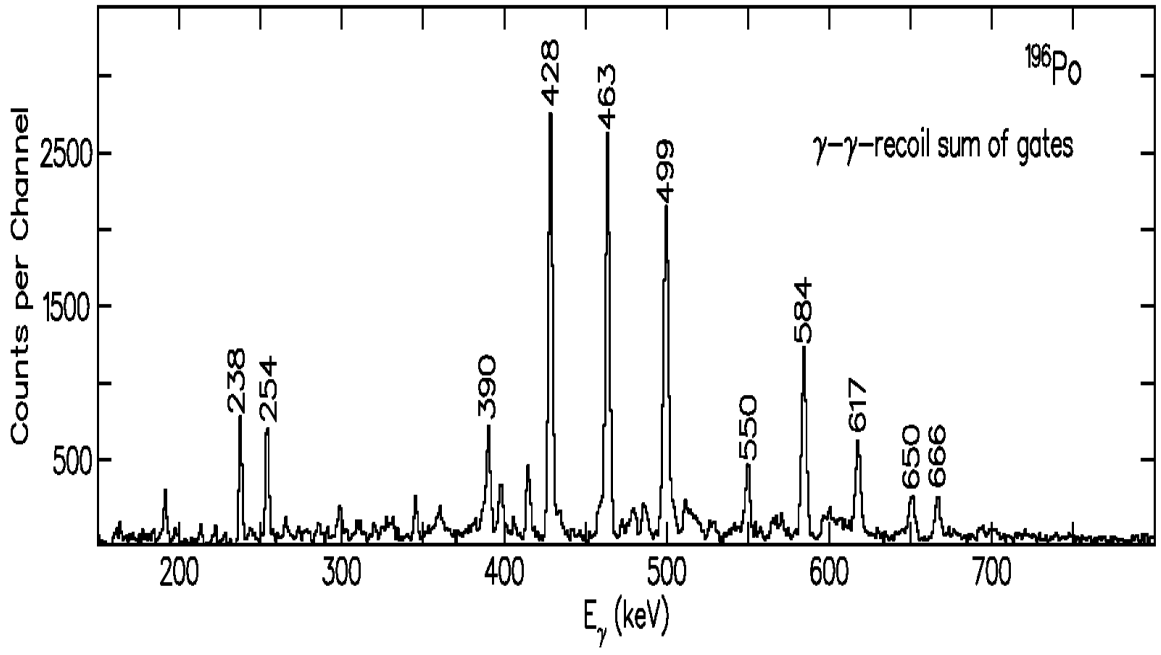

Figure 5:10. Summed γ–γ–recoil coincidence spectrum obatined in the ^{180}W(^{20}Ne, 4n) invistigation. Gates have been set on the 463 keV , 428 keV, 499 keV and 550 keV transitions.

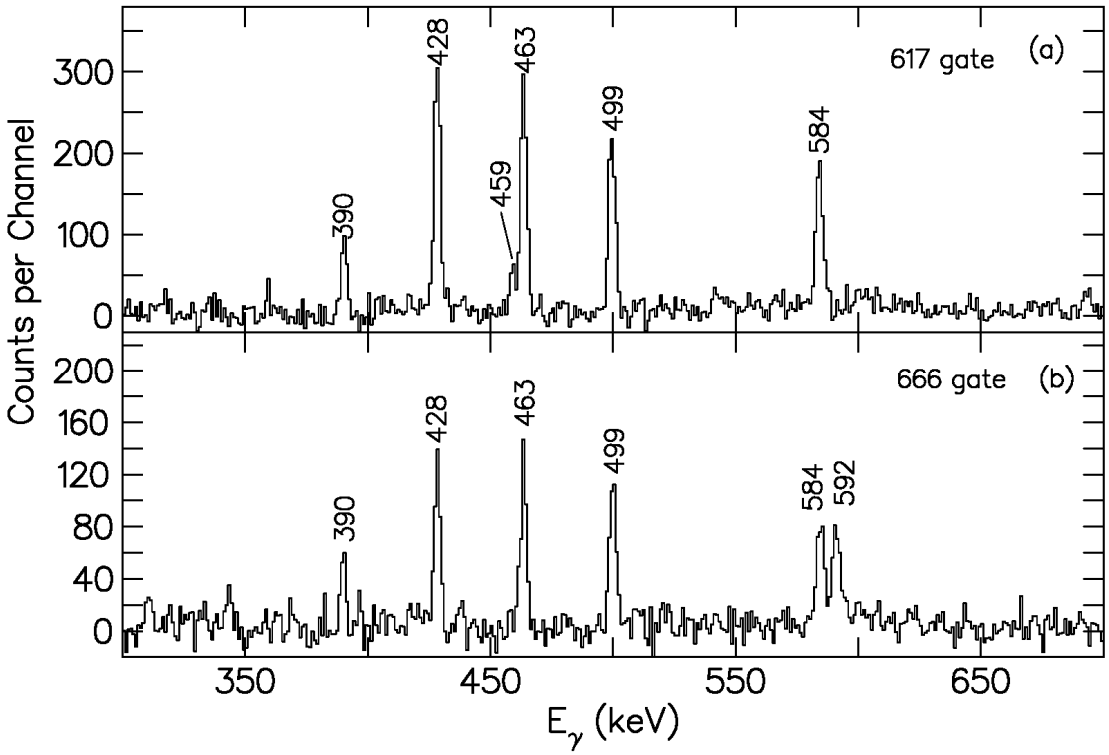

Figure 5:11. The γ–γ– recoil coincidence spectra obatined when gating on (a) the 617 keV and (b) the 666 keV γ–rays. All γ–rays seen in coincidence with the gating transition are labeled with their respective energies.

5.3 Search for hyperdeformed bands in ^{230,232}U

One of the main objectives of performing these experiments was to investigate the theoretically proposed hyperdeformed bands in the uranium isotopes [Ćwi94]. The peaks corresponding to transitions from hyperdeformed transitions should lie in the energy interval indicated in Figure 5:12. In this region, both reactions and target X–rays are dominant. Although the recoil detector allowed the fission background to be almost completely supressed, it did not reduce the target X–rays to a level required for a HD experiment. Therefore one could only expect to observe HD transitions in the energy region below 80 keV, just below the region of target and reaction X–rays (see dashed line in Figure 5:12). Unfortunately, with the CLOVER detectors, highly intense fluorescence X–rays were observed in this region, see Figure 5:12 and Figure 5:13. They include fluorescence X–rays from the recoil detector tungsten collimator, and a broad peak from the CLOVER suppression shields. Tin

absorbers were used to remove the W fluorescence X–rays, as can be clearly seen when comparing Figure 5:12(a) with Figure 5:12(b) and Figure 5:13(a) with Figure 5:13(b). On the other hand, the LEPS, did not have sufficient statistics to conduct this study, see Figure 5:14. Together with low statistics, these challenges frustrated the search for the hyperdeformed states. While efforts were made to ensure as low BGO threshold as possible, the Compton suppression could not be otherwise optimized, since it occurred in the RIS modules. As a result the investigation of this phenomena (hyperdeformation) was unsuccessful. We concentrated instead, on understanding whether the negative-parity bands in ^{230,232}U could be understood as tetrahedral structures.

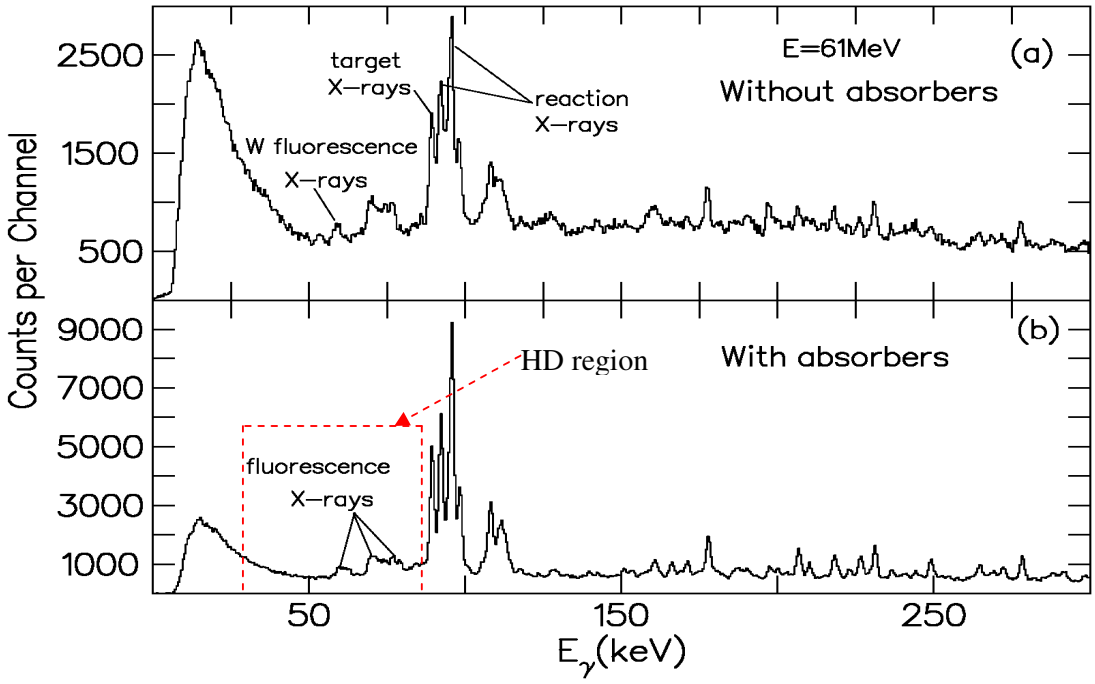

Figure 5:12. CLOVER spectra obatined (a) without tin absorbers and (b) with tin absorbers. The red lines indicate the HD region. Fluorescence X-rays are at low energies where the transitions of the hyperdeformed band are predicted in the U isotopes. These spectra were obtained at a beam energy of 61 MeV show the removal of the W X–rays.

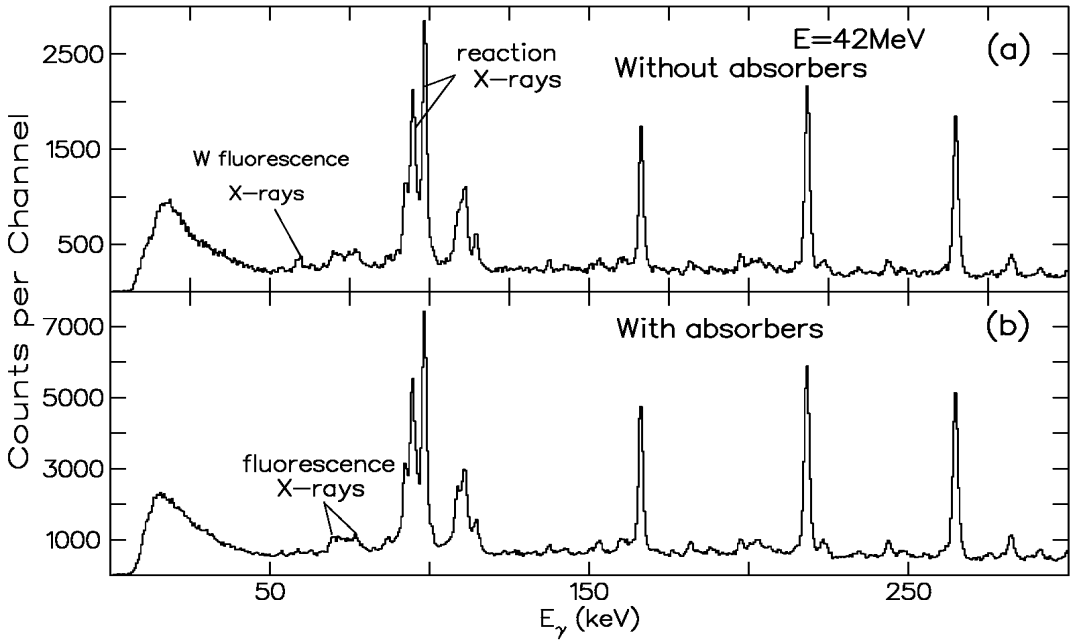

Figure 5:13. CLOVER spectra obtained (a) without tin absorbers and (b) with tin absorbers. Fluorescence X-rays are at low energies where the transitions of the hyperdeformed band are predicted in the U isotopes. These spectra were obtained at a beam energy of 42 MeV and show the removal of the W X–rays.

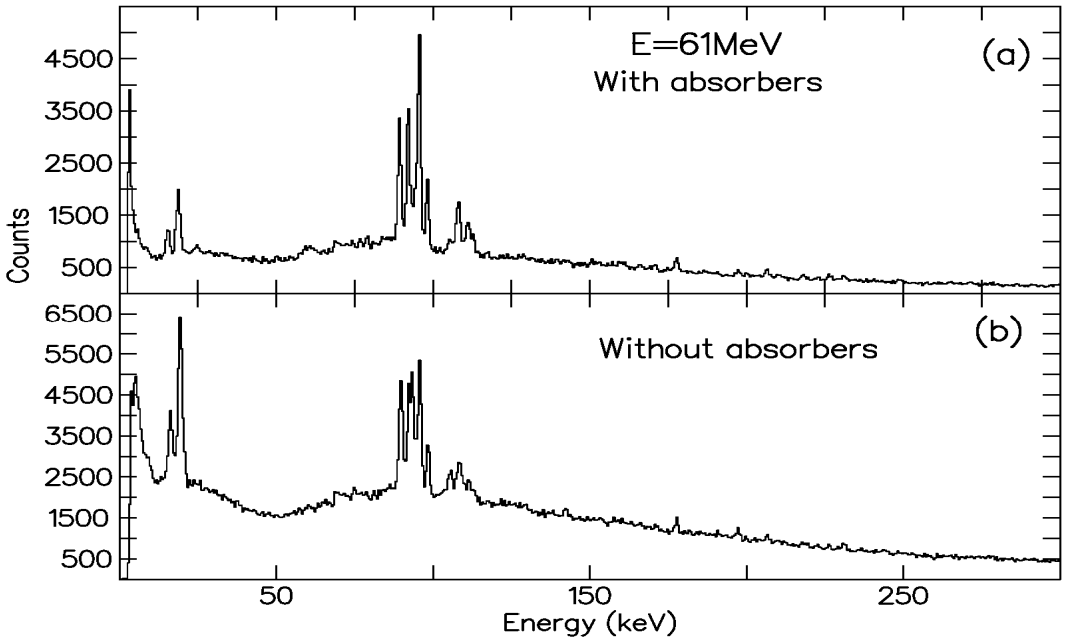

Figure 5:14. LEPS spectra spectra which were obtained at a beam energy of 61 MeV. There is high background at low energies where the transitions of the hyperdeformed band are predicted in the U isotopes.

5.4 The ^{232}U level scheme

In Figure 5:15 the level scheme of ^{232}U deduced from this work is shown. The summed coincidence spectrum displayed in Figure 5:16 confirms the presence of some of the ground state band transitions and E1 transitions linking it to the newly added levels of the negative-parity band. This spectrum was created by summing spectra obtained by gating transitions in the ground band up to the 16^+ state. Our ^{232}U level scheme extends the extensive work of [Zey87] and [Ack93]. The ground state band has been extended by 4 units of angular momentum. Most importantly, the data obtained in this work allowed to extend the lowest lying negative-parity band, identified as an octupole band as shown in the partial level scheme in Figure 5:17. In fact, a comprehensive set of E2 transitions has been successfully added to this band. The coincidence spectra confirming these findings are shown in Figure 5:18. In addition, numerous E1 transitions connecting this negative-parity sequence with the ground band have also been established. This includes both, $I \rightarrow (I-1)$ and $I \rightarrow (I+1)$ transitions, the latter are however weakly populated, see Figure 5:19 and Figure 5:20. Spectroscopic information on the transitions and levels observed in ^{232}U is given in Table 5:1.

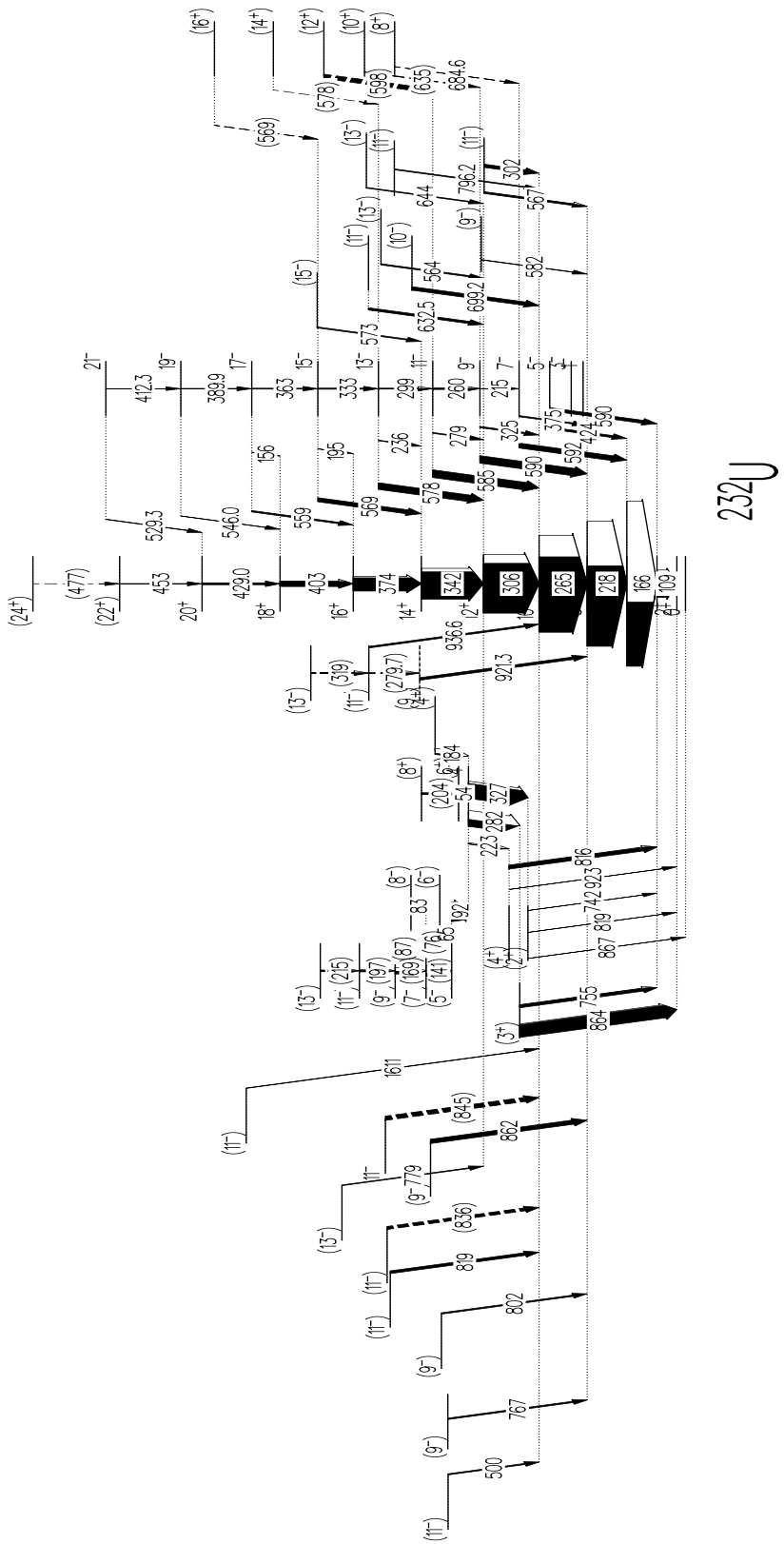

Figure 5:15. The whole level scheme of ^{232}U as deduced from this work. The widths of the arrows represent the relative intensities of the transitions.

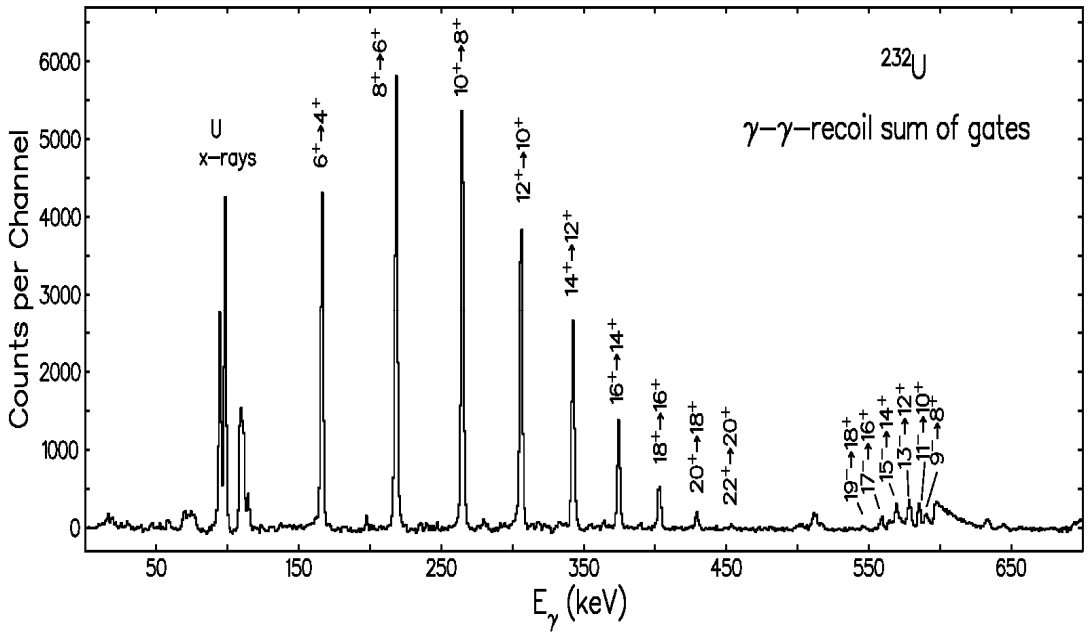

Figure 5:16. A coincidence spectrum showing the ground state band transitions and the E1 transitions observed by summing of spectra gated on transitions between the 4^+ to 16^+ states in ^{232}U.

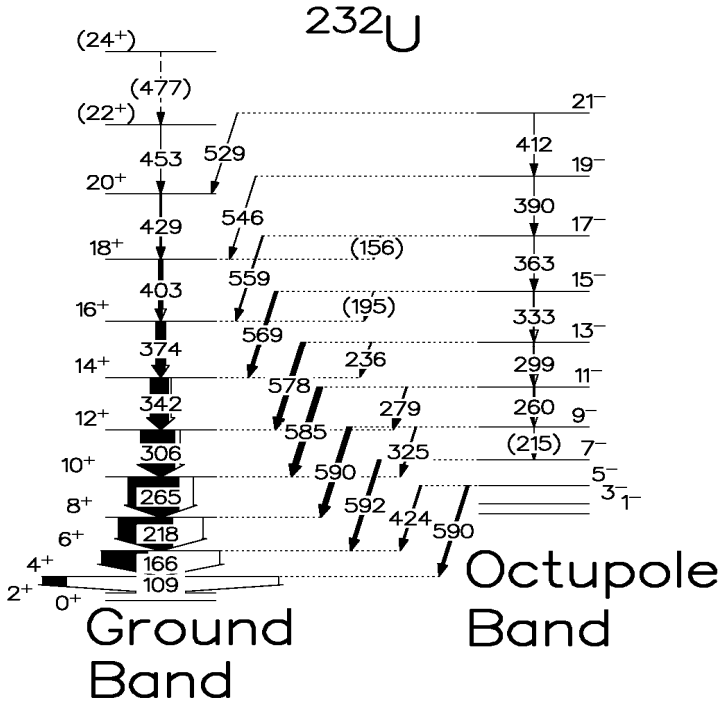

Figure 5:17. Partial level scheme of ^{232}U showing γ–rays related to the negative-parity band as observed in the present work. The widths of the arrows represent the relative intensities of the transitions.

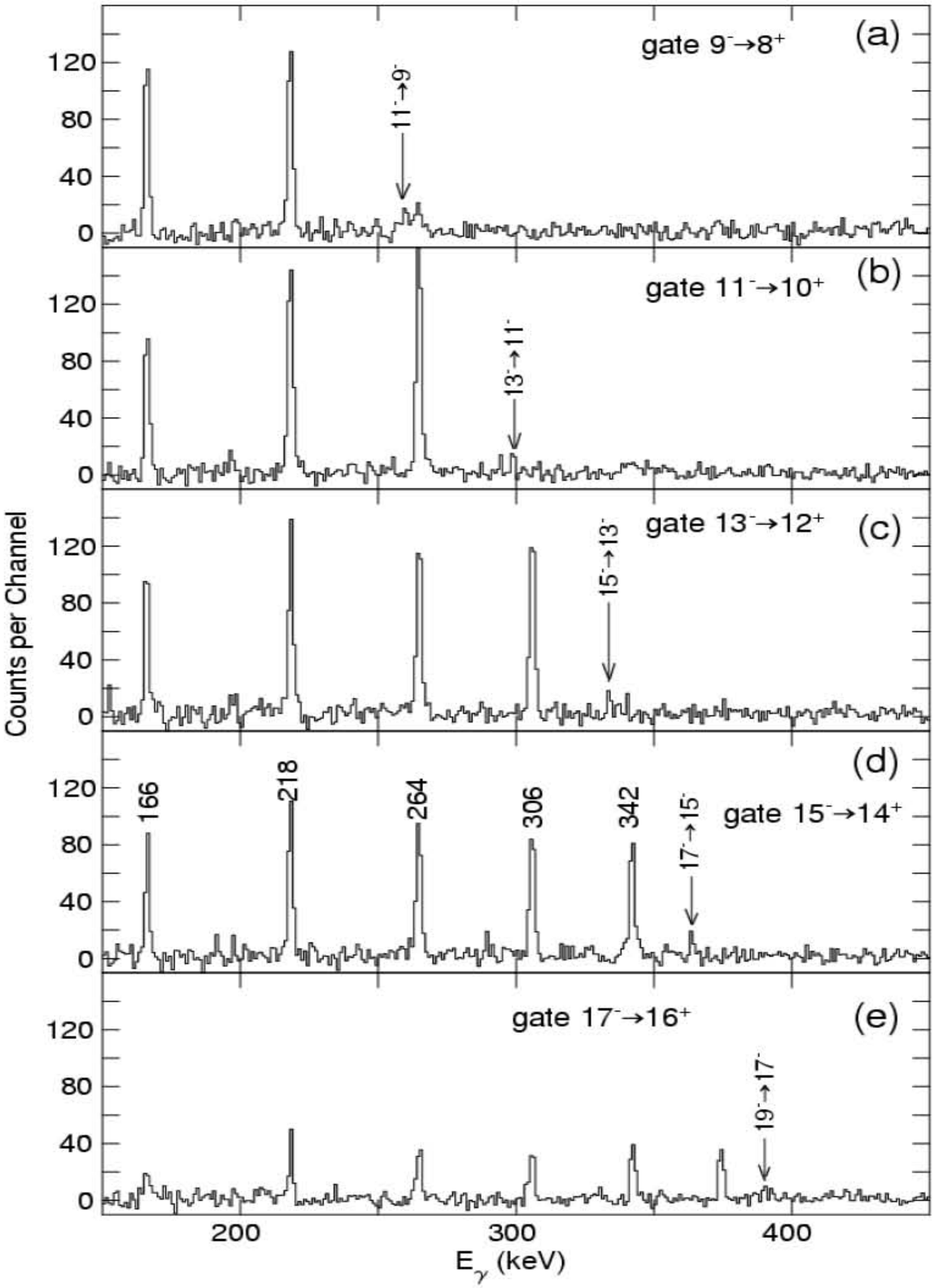

Figure 5:18. Coincidence spectra gated by selected E1, $I^- \rightarrow I^+ - 1$ transitions in ^{232}U showing in-band E2 transitions.

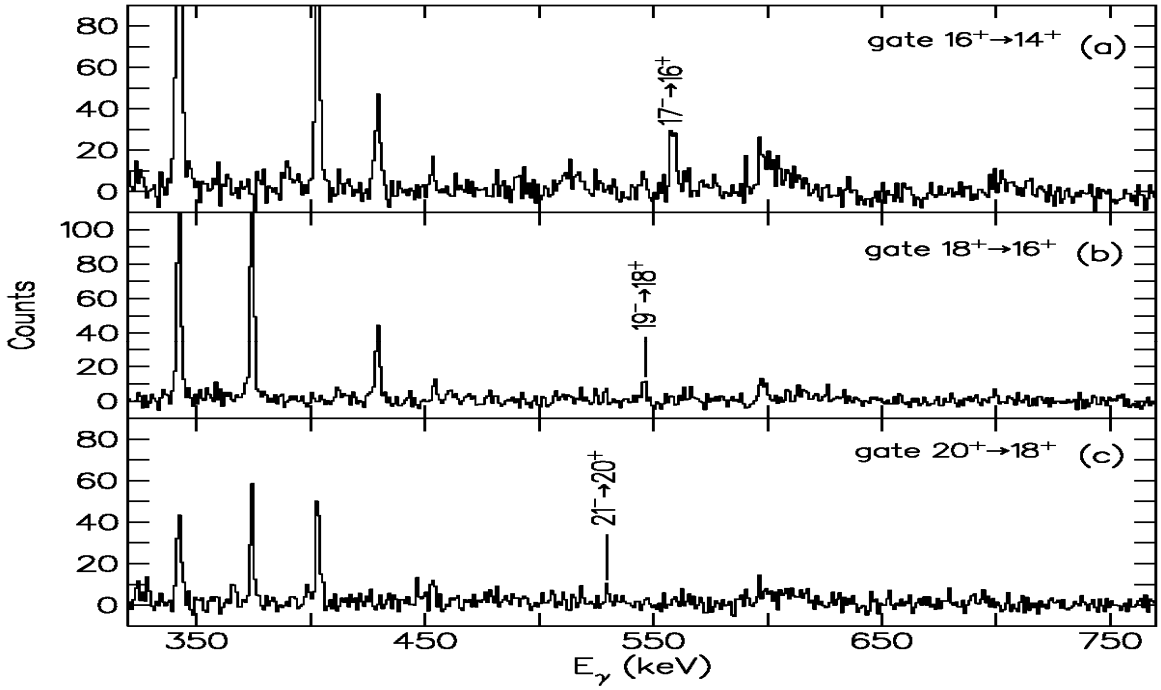

Figure 5:19. Coincidence spectra showing the E1 transition in ^{232}U which were observed for the first time in this measurement. The gating transition are indicated.

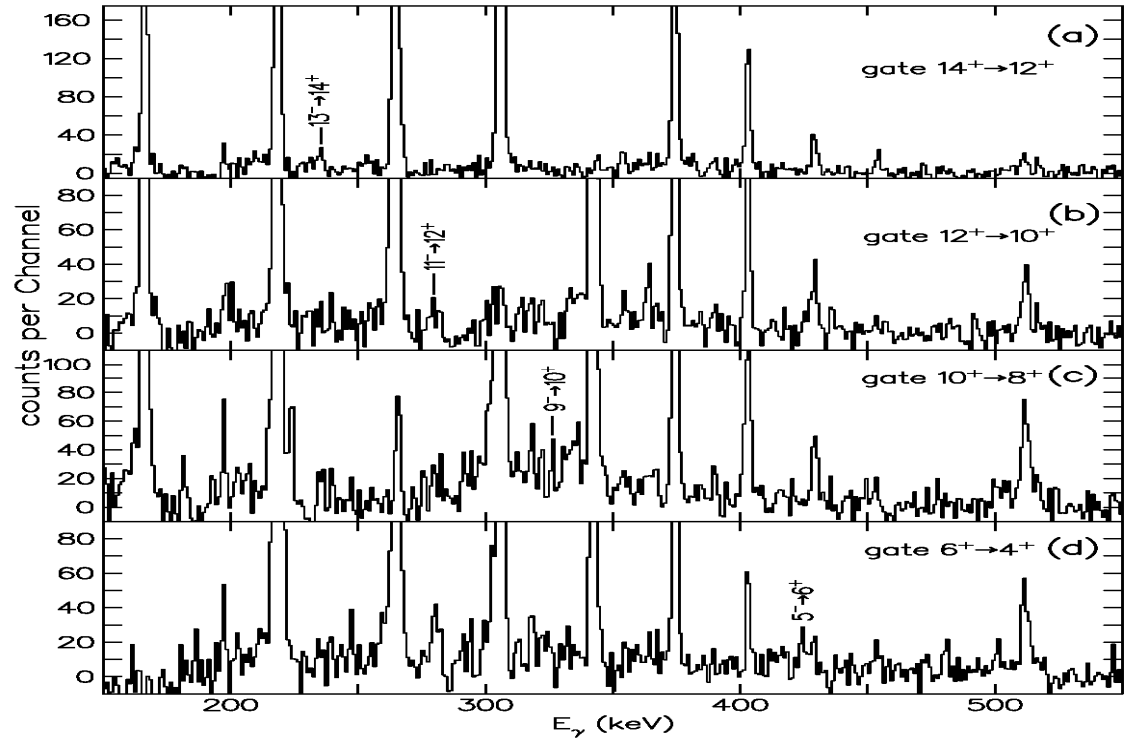

Figure 5:20. Coincidence spectra showing the $I^- \rightarrow I^+ + 1$ E1 transitions in ^{232}U. The gating transitions are indicated.

Table 5:1. Table of the measured transition energies and intensities for the ^{232}U partial level scheme shown in Figure 5:17. The γ–ray intensities were obtained by fitting the peak areas with the RADWARE program GF3 and subsequently efficiency corrections. The total transition intensities were obtained by correction for internal conversion from ESCL8R [Rad95].

Energies (keV)	$I_i^{\pi_i}$	$I_f^{\pi_f}$	**Multipolarity**	**Intensity (γ)**	**Intensity (total)**
109(1)	4^+	2^+	E2	55(13)	554(26)
165.9(3)	6^+	4^+	E2	217(15)	558(38)
218.0(3)	8^+	6^+	E2	283(10)	439(30)
264.5(3)	10^+	8^+	E2	271(9)	348(28)
305.7(3)	12^+	10^+	E2	176(6)	208(20)
342.0(3)	14^+	12^+	E2	100(5)	112(14)
374.1(4)	16^+	14^+	E2	51(2)	55(10)
402.8(5)	18^+	16^+	E2	20.0(9)	21(6)
429.0(8)	20^+	18^+	E2	8.2(5)	9(4)
453.50(19)	22^+	20^+	E2	3.0(3)	3(2)
477(1)	24^+	22^+	E2	1.5(5)	1.60(18)
590(1)	5^-	4^+	E1	17(6)	17(9)
592.50(3)	7^-	6^+	E1	13(3)	13(5)
589.90(12)	9^-	8^+	E1	24.5(16)	25(7)
585.10(8)	11^-	10^+	E1	23.3(13)	24(6)
578.10(7)	13^-	12^+	E1	18.2(10)	18(5)
569.10(8)	15^-	14^+	E1	12.2(11)	12(5)
558.60(16)	17^-	16^+	E1	5.2(5)	5(3)
546(1)	19^-	18^+	E1	1.0(3)	0.97(12)
559.30(25)	21^-	20^+	E1	0.9(1)	0.91(10)
424.10(10)	5^-	6^+	E1	8.7(12)	9 (4)
325.20(10)	9^-	10^+	E1	4.7(7)	5(3)
279.00(10)	11^-	12^+	E1	3.0(6)	3.2(4)
235.70(10)	13^-	14^+	E1	2.1(4)	2.2(2)
195.00(10)	15^-	16^+	E1	0.6(1)	0.71(9)
155.50(10)	17^-	18^+	E1	3.1(1)	3.7(8)
215.00(10)	9^-	7^-	E2	2.3(2)	3.6(9)
259.50(21)	11^-	9^-	E2	4.0(6)	5(3)
299.00(28)	13^-	11^-	E2	2.5(5)	3.0(2)
333.3(3)	15^-	13^-	E2	3.6(5)	4.1(3)

Energies (keV)	$I_i^{\pi_i}$	$I_f^{\pi_f}$	Multipolarity	Intensity (γ)	Intensity (total)
363.50(10)	17^-	15^-	E2	3.1(4)	3.4(2)
390(1)	19^-	17^-	E2	1.9(3)	2.1(2)
412(1)	21^-	19^-	E2	0.1(1)	0.16(5)

5.5 The ^{230}U level scheme

In Figure 5:21, the ground state band transitions observed by summing γ–recoil gated spectra of ground state band up to spin $14^+$are shown. The ^{230}U level scheme deduced in this work is shown in Figure 5:22. The ^{230}U ground state band has been extended by two transitions compared to the previous work of [Zey87] and [Ack93]. Compared to the ^{232}U data, the statistics were much smaller for this nucleus. As a result, it could not establish the in-band E2 transitions of the negative-parity band down to low spin states as was successfully done in ^{232}U. Only two in-band members of this band could be added viz, the $15^- \rightarrow 13^-$ and $17^- \rightarrow 15^-$ transitions 380 and 346 keV, see Figure 5:22 and Figure 5:23. The highly intense E1 transitions which de-excite from the octupole band to the ground band had been previously observed up to the 15^- state by [Zey87] and [Ack93]. In this work, a new transition connecting the 17^- member of the octupole band to the 16^+ member of the ground band have been observed. Figure 5:24 shows a spectrum which was used to confirm the existence of this newly identified E1 transition. The γ–ray intensities obtained in this measurement are given in Table 5:2.

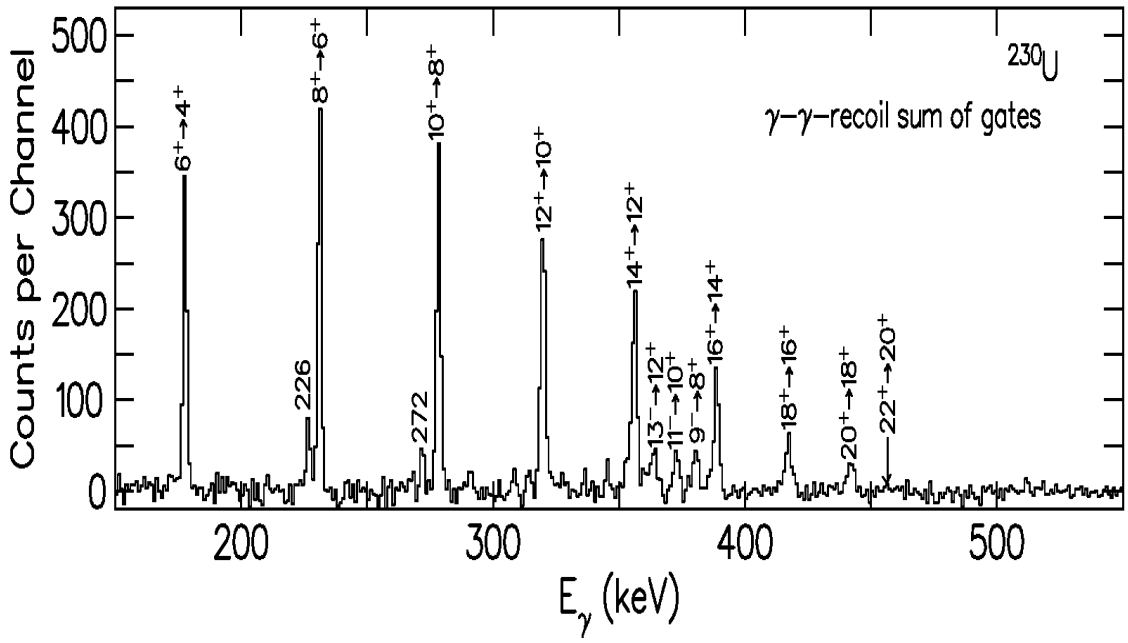

Figure 5:21. Spectrum obtained by summing γ–recoil coincidence spectra obtained by gating on the $6^+ \rightarrow 4^+$ *to* $14^+ \rightarrow 12^+$ *transition in the* ^{230}U *ground state band.*

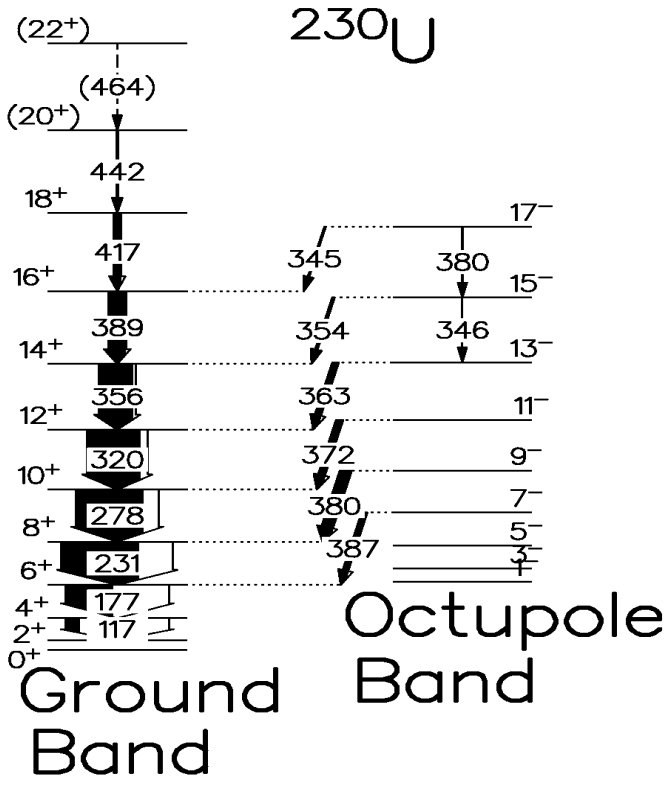

Figure 5:22. Partial level scheme of ^{230}U *showing γ–rays observed in the present work. Arrow widths indicate relative intensities.*

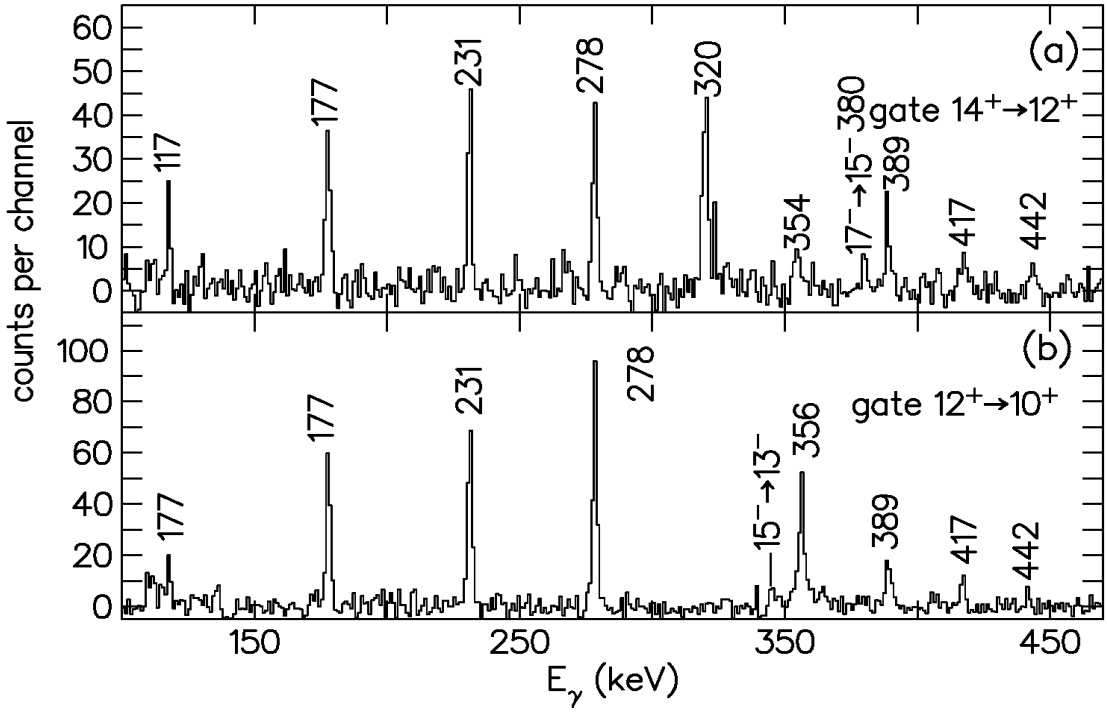

Figure 5:23. Concidence spectra showing new the in-band E2 transitions observed in ^{230}U. The gating transition are indicated.

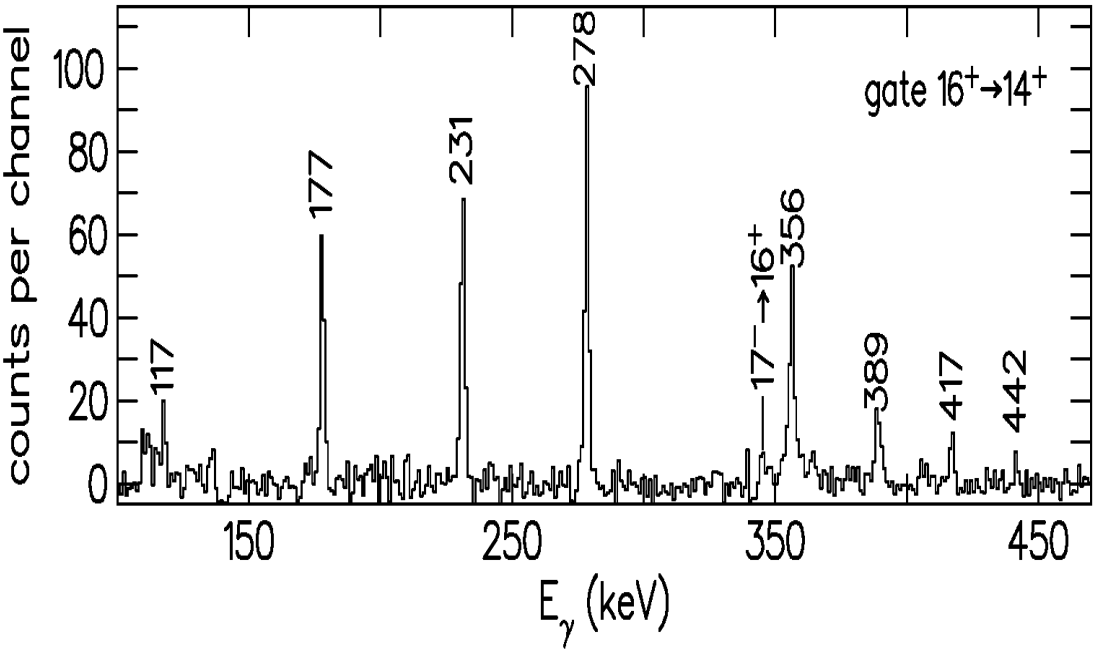

Figure 5:24. A coincidence spectum obatined by gating on $16^+ \rightarrow 14^+$ transition. The $17^- \rightarrow 16^+$ E1 transitions in ^{230}U which was observed for the first time in this measurement is indicated.

Table 5:2. Table of the measured transition energies and intensities in ^{230}U. The γ-ray intensities were obtained by fitting the peak areas with the RADWARE program GF3 and subsequent efficiency correction. The total transition intensities were obtained by correction for internal conversion from ESCL8R [Rad95].

Energies (keV)	$I_i^{\pi_i}$	$I_f^{\pi_f}$	**Multipolarity**	**Intensity (γ)**	**Intensity (total)**
117.41 (8)	4^+	2^+	E2	55 (7)	429(27)
177.46(5)	6^+	4^+	E2	382(52)	842(81)
230.93(5)	8^+	6^+	E2	539(41)	785(69)
278.07(5)	10^+	8^+	E2	445(26)	555(49)
319.54(5)	12^+	10^+	E2	346(25)	400(45)
356.06(6)	14^+	12^+	E2	200(13)	223(27)
388.55(9)	16^+	14^+	E2	101(9)	110(20)
417.04(14)	18^+	16^+	E2	35(7)	38(13)
442.0(10)	20^+	18^+	E2	19(9)	20(13)
464.42(10)	22^+	20^+	E2	2.4(10)	3(1)
386.9(11)	7^-	6^+	E1	34(22)	35(28)
380.31(2)	9^-	8^+	E1	74(15)	76(24)
372.2(20)	11^-	10^+	E1	50(10)	52(17)
363.5(19)	13^-	12^+	E1	37(7)	38(14)
354.2(20)	15^-	14^+	E1	30(7)	31(13)
345.16(18)	17^-	16^+	E1	23(4)	23(8)
379.5(7)	15^-	13^-	E2	25(7)	29(12)
346.0(15)	17^-	15^-	E2	13(4)	14(8)

5.6 Additional nuclei detected by the recoil detector

Although Experiment 2 was aimed at studying ^{230}U and ^{232}U, other nuclei were detected. The level schemes of the nuclei populated at 61 and 42 MeV beam energies in the reaction $^{232}Th(\alpha, xn)$ are shown in Figure 5:25 and Figure 5:26. Clearly, some of the nuclei were measured unexpectedly, as they were not supposed to be populated according to PACE calculations (see Figure 2:5). The way in which these nuclei were formed is thoroughly discussed in CHAPTER 6.

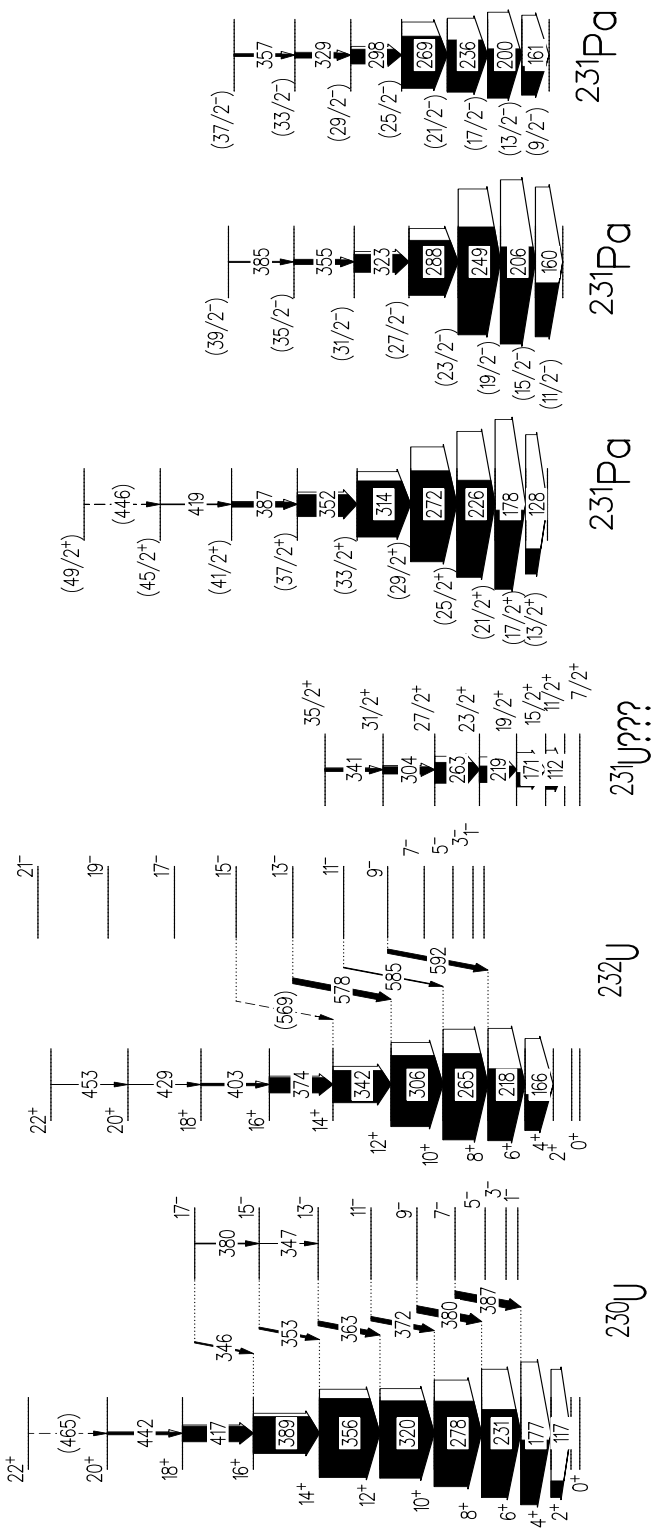

Figure 5:25. Partial level schemes, of U and Pa isotopes observed in the ^{232}Th(α, xn) reaction at 61 MeV. The widths of the arrows represent the relative intensities normalised for ^{230}U.

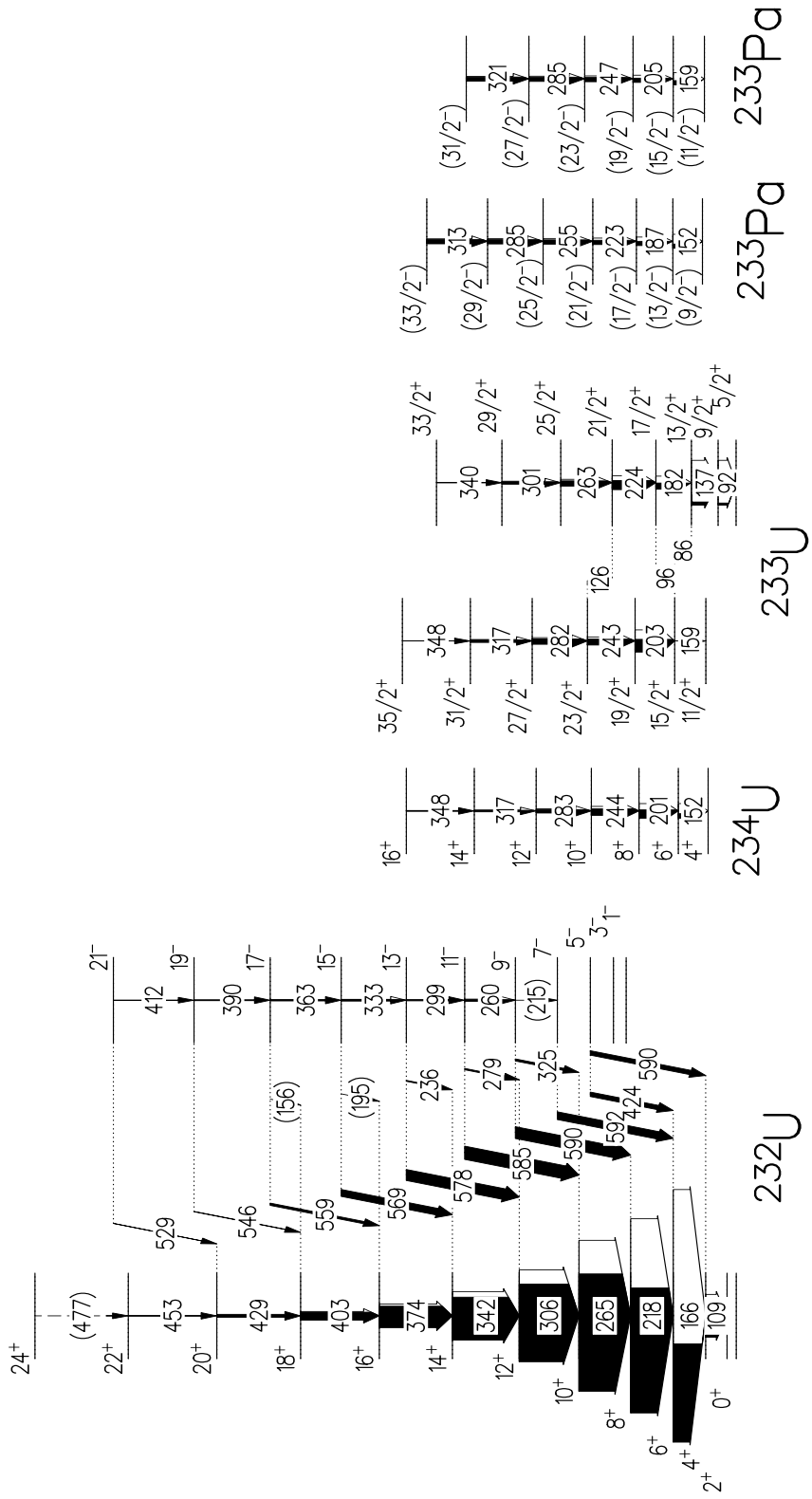

Figure 5:26. Partial level schemes of U and Pa isotopes observed in the ^{232}Th(α, xn) reaction at 42 MeV. The widths of the arrows represent the relative intensities normalised for ^{232}U.

CHAPTER 6 REACTION MECHANISMS

As mentioned in section 5.6, some nuclei which were not predicted by PACE calculations were detected. This CHAPTER discusses the reaction mechanisms which lead to the production of these nuclei.

6.1 The ^{180}W(^{20}Ne, xn) experiment

In the ^{180}W(^{20}Ne, xn) experiment, a number of nuclei were populated via a range of strong channels. These include the pure neutron evaporation channel leading to ^{196}Po, α3n to ^{193}Pb, 3α2n to ^{186}Pt and 4α2n to ^{182}Os. Mercury-190 evaporation residues populated via the 2α2n channel were also observed, but the cross-section was small compared to those of the other channels. Figure 6:1 shows spectra in which the different evaporation residues separated by the recoil detector are indicated. Recoiling nuclei with different time-of-flight are clearly separated by gating at different MCP time ranges. It is remarkable in Figure 6:1 that the strength of the 4α2n channel leading to ^{182}Os is comparable to that of the 4n fusion-evaporation channel leading to ^{196}Po. This is also evident in Figure 6:2 in which the projections of the MCP time of the recoil detector are compared. The time spectra were produced by gating on the third transition of the yrast line above the ground state of the indicated nuclei, respectively (see Figure 6:2(d)). Furthermore, the figure shows a bump located at 11 ns which is earlier than that expected for complete fusion residues (^{196}Po) observed at 20 ns. This is surprising since one would expect that if the ^{182}Os nuclei were populated via an α-induced incomplete fusion reaction at an energy of 22 MeV ($4/20\times110$ MeV), then they recoil with a velocity of $v = 0.0024c$ as compared with $v = 0.011c$ for the ^{196}Po recoils.

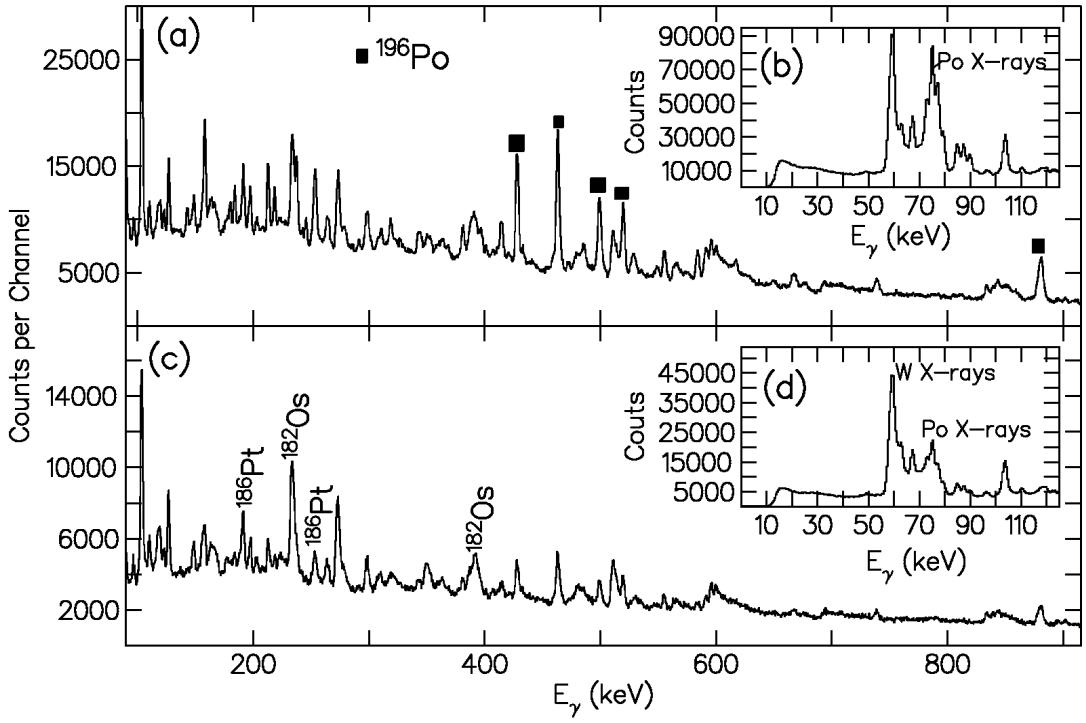

Figure 6:1. Comparison of γ-ray spectra obtained with different MCP time gates. Upper portion: MCP time gate was set on 15-32ns and lower portion: MCP time gate was set on 0-15 ns (seeFigure 4:28).

These calculations imply that the ^{196}Po and ^{182}Os should have times of flight of 19.6 ns and 92 ns, respectively. The 470 keV ^{182}Os recoils were not expected to be detected by the recoil detector due to the following reasons: (i) low energy which would not penetrate the 12 μg/cm^2 thick carbon foil and (ii) The time-of-flight of this recoil is 92 ns which falls outside the time gate. Additional information comes from an estimated average recoil velocity of the detected ^{182}Os products which were extracted by Mullins et al., [Mul09] from the Doppler shifted energies of the ground state band transitions of ^{182}Os. This was found to be $v = 0.02c$, which is faster than fusion, suggesting they are a product from other reaction mechanisms, in which an alpha particle is transferred to the ^{180}W target during a grazing collision (with subsequent emission of two neutrons), where upon the complementary ^{16}O beam fragment orbits and is ejected rearwards. Conservation of momentum leads to the forward going ^{182}Os binary partner travelling with $v = 0.019c$, in accordance with the measured energy shifts. This is also consistent with the bump at 11 ns in the recoil detector MCP time spectrum obtained when gating on ^{182}Os transitions. These calculations

lead to a conclusion that the ^{186}Pt was also produced via the same transfer reaction mechanism. It could be noted that the PACE calculation did not predict any ^{186}Pt and ^{182}Os. This is due to the fact that PACE does not take transfer reactions into account.

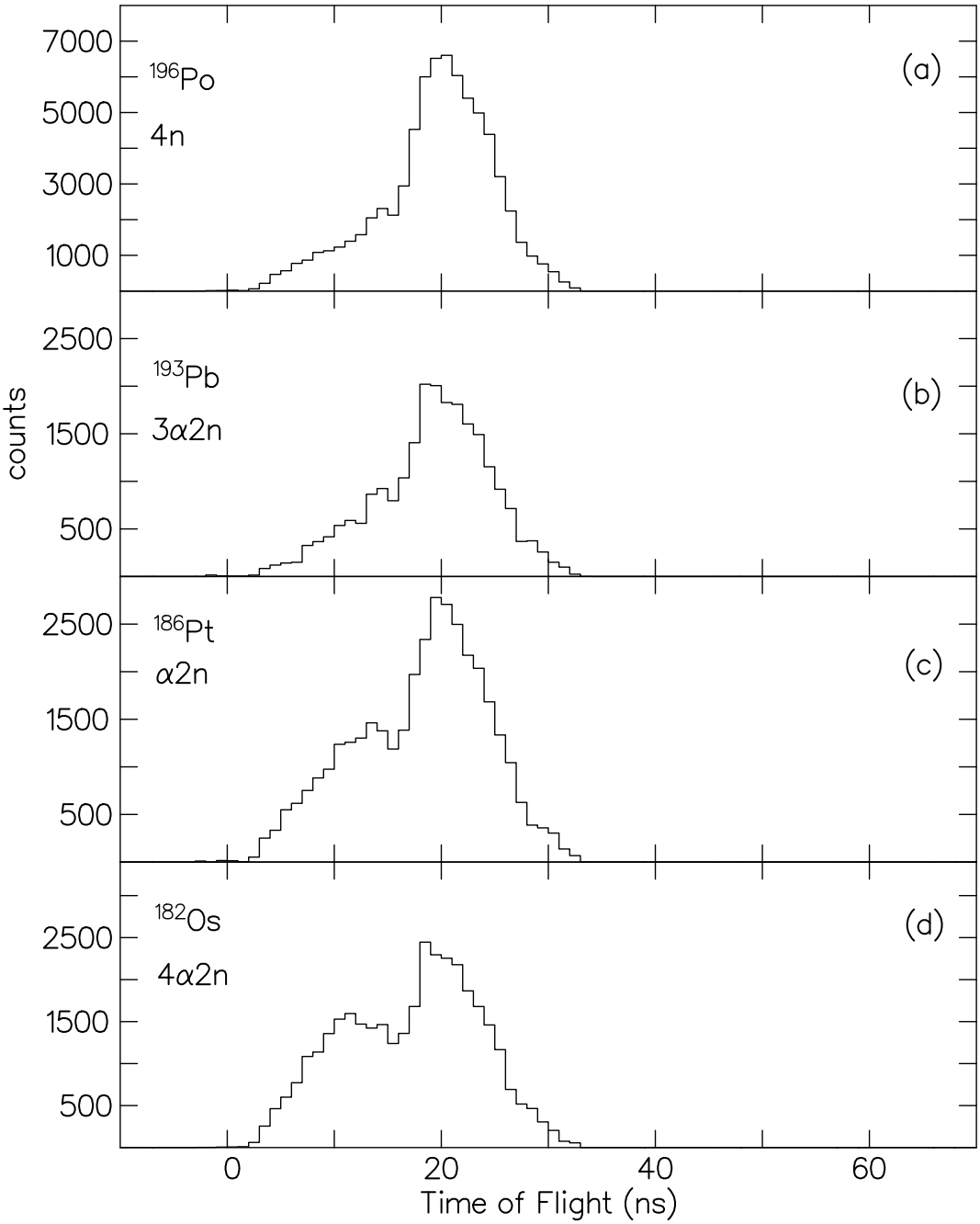

Figure 6:2. Projections of the MCP time spectra of the recoil detector selected by the third lowest ground state band transitions in (a) ^{196}Po (4n), (b) ^{193}Pb(α3n), (c)^{186}Pt 3α2n and ^{182}Os (4α2n).

6.2 The ^{232}Th(α, xn) experiment

In the ^{232}Th(α,pxn) measurement, the (α,pxn) channel was much stronger than the calculated cross-sections [Nis80] (see Figure 6:3). In the ^{232}Th(α, xn) measurements, the (α, pxn) channel was observed at both 42 and 61 MeV. The (α, pxn) products are ^{233}Pa and ^{231}Pa for 42 and 61 MeV, respectively. They were easily identified because their γ-rays transitions are known from previous studies [Lev96, Wur99, Abu02]. Figure 5:25 and Figure 5:26 show the Pa and the U isotopes populated at different beam energies. Remarkably the ^{231}Pa and ^{232}U are as strongly populated as the ^{230}U at 61 MeV beam energy – a contradiction to PACE calculations.

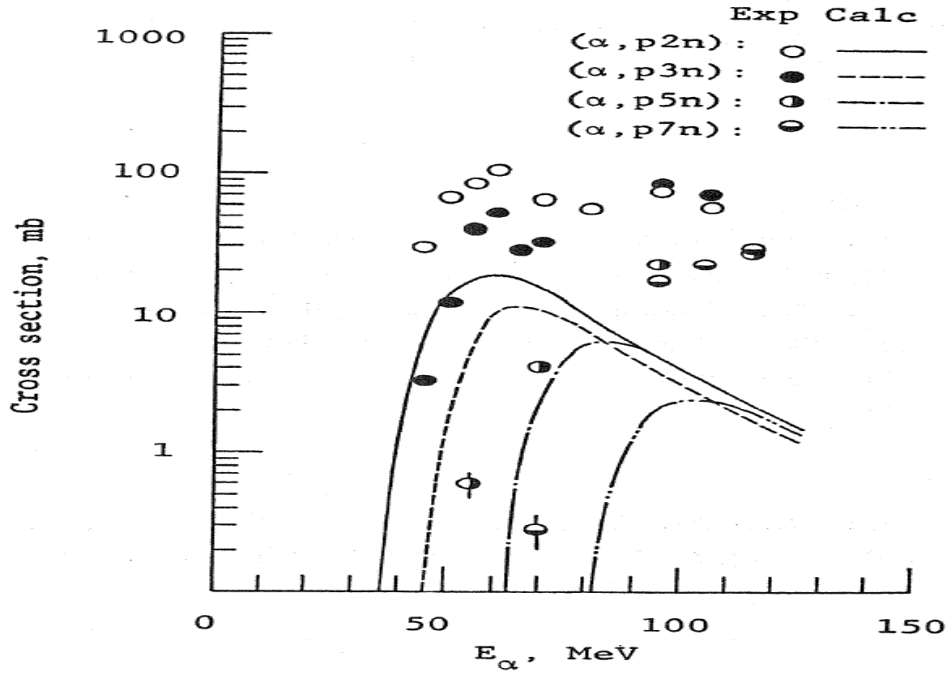

Figure 6:3. Excitation functions of the ^{232}Th(α, p2n)^{233}Pa, ^{232}Th(α, p3n)^{232}Pa, ^{232}Th(α, p5n)^{230}Pa, and ^{232}Th(α, p7n)^{228}Pa reaction [Nis80].

In addition, at a beam energy of 42 MeV, ^{234}U and ^{233}U are also more strongly populated than expected from the PACE predictions seen Figure 2:5. Figure 5:26 shows their yrast bands identified in our data; the spectra corresponding to the transitions in these nuclei are shown in Figure 6:4. They were also easily identified because they are well known from previous studies [New58, Ven85]. One signature branch of the $i_{11/2}$ band of ^{233}U is identical to the ground band of ^{234}U above the 4^+ level.

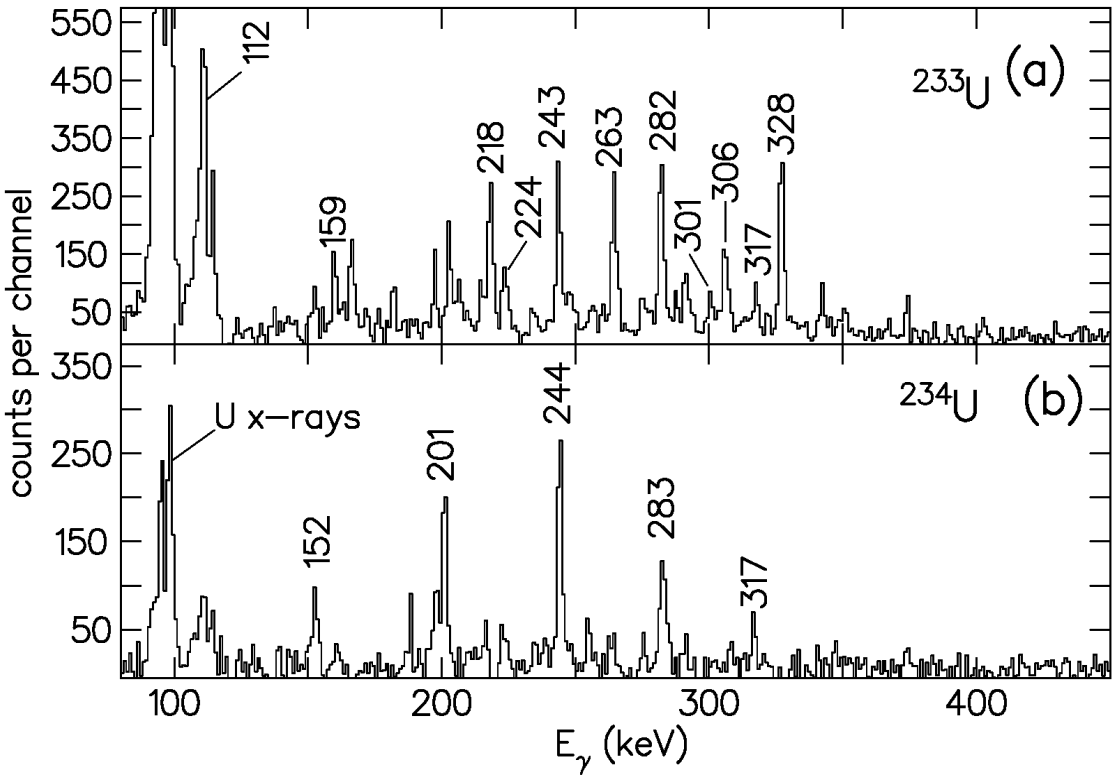

Figure 6:4. Coincidence spectra showing ground state band transition of (a) ^{233}U gated on the 203 keV,159 keV, 137 keV and 92 keV γ–ray transitions and (b) ^{234}U gated on the 201 keV and 152 keV γ–ray transitions.

Furthermore, in the $^{232}Th(\alpha, xn)$ reaction at 61 MeV, the ^{232}U ground state band, together with a few E1 transitions, were observed together with an unknown band very close in energy to the ^{232}U ground state band (see the level scheme in Figure 5:25). This is similar to the situation in our 42 MeV data, where the ^{233}U and ^{234}U were observed. In the 61 MeV measurement, ^{231}U was expected (according to PACE) to be the second strongest uranium channel, and no ^{232}U was expected to be seen at all, see Figure 2:5. Nevertheless, it comes as a surprise that ^{232}U was actually the second strongest channel instead of the proposed ^{231}U. Unlike the 42 MeV data, in this case we unable to confirm whether the mystery band belongs to ^{231}U, since the excited states of ^{231}U are practically unknown (except for α-decay work). We suggest that this band belongs to the nucleus ^{231}U. Figure 6:5 shows spectra obtained by setting different low energy gates which separates the ^{232}U from the proposed ^{231}U yrast band. The spectrum indicates that the ^{232}U remains present at an unexpected strength. To confirm the proposed ^{231}U band observed in our data, a new experiment

has been proposed. This experiment will be performed at an intermediate energy (55 MeV), where ^{231}U will be strongly populated (*see* Figure 2:5).

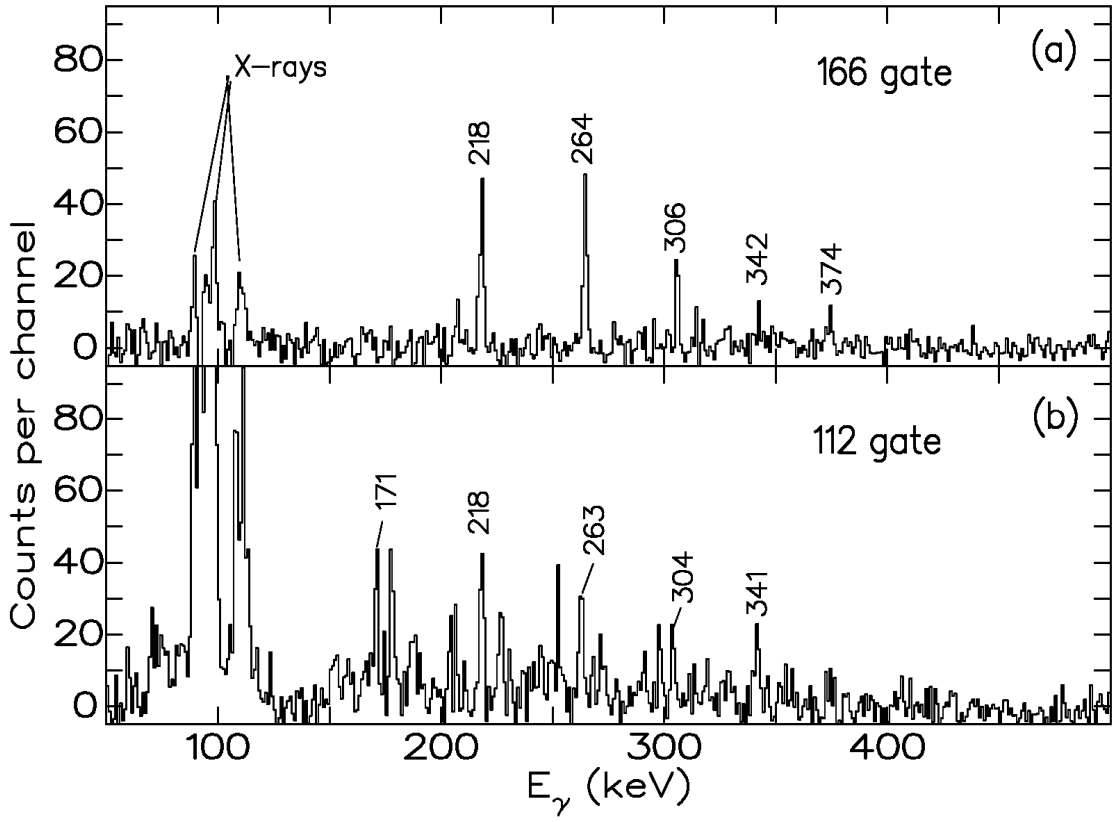

Figure 6:5. Coincidence spectra showing (a) the ^{232}U and (b) the proposed ^{231}U $i_{13/2}$ band populated using the ^{232}Th(α, xn) reaction at 61 MeV. The gating transitions are indicated.

In order to understand the unexpected strengths of ^{232}U at 61 MeV, further analyses were done. First, experimental and calculated cross-sections for all the (α, xn) reactions carried out at iThemba LABS in the past few years were compared. The measured ^{152}Sm(α, xn) cross-section was obtained from [Sch09] while the ^{197}Au(α, xn) and the ^{198}Pt(α, xn) were obtained from [Law09] and [Law08] respectively. These comparisons are shown in Figure 6:6, Figure 6:7, Figure 6:8, and Figure 6:9. The experimental cross-sections were obtained from relative γ–ray intensities of transitions in the yrast band of each nucleus. The strongest channel of each reaction, at each beam energy, was normalized to the calculated cross-section. Denoting the number of neutrons evaporated in the strongest channel at the highest energy by "x",

it can be seen that in all reactions at the highest energy, the cross-section of the channel with $x-2$ neutrons emitted is underestimated by PACE by approximately two orders of magnitude. This implies that the enhanced cross-section of the "$x-2$" channel is a general feature which does not depend on the target.

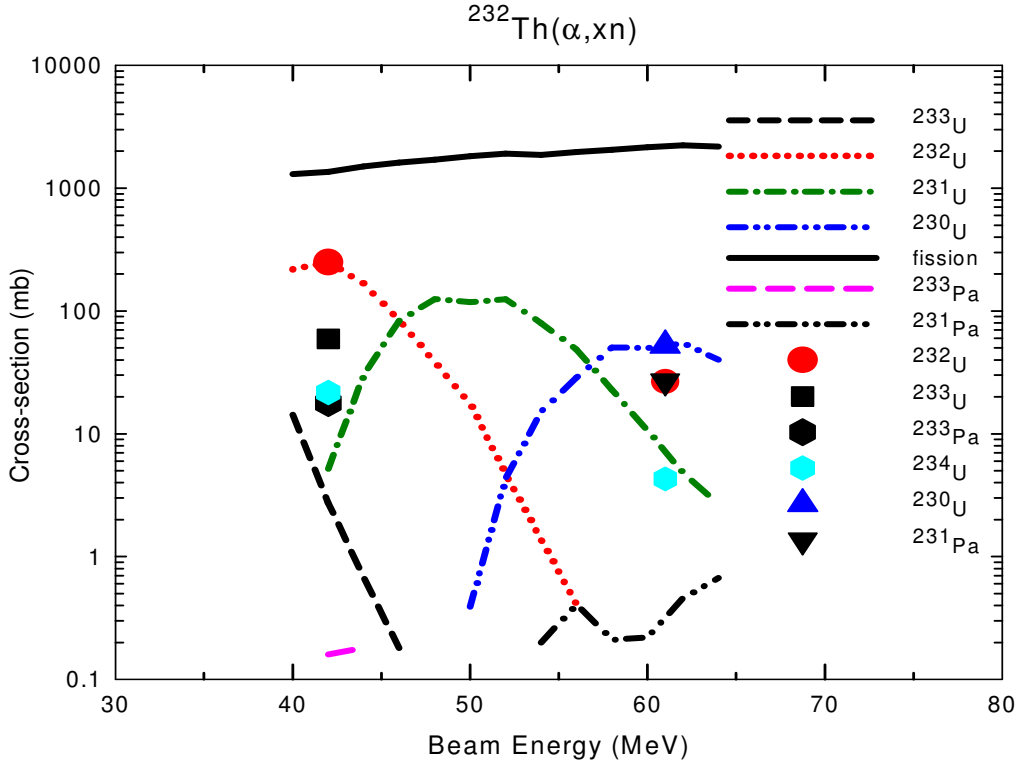

Figure 6:6. Camparison of calculated and measured cross-sections for U isotopes at different energies. The lines represent cross-sections calculated with PACE and the symbols measured cross-sections.

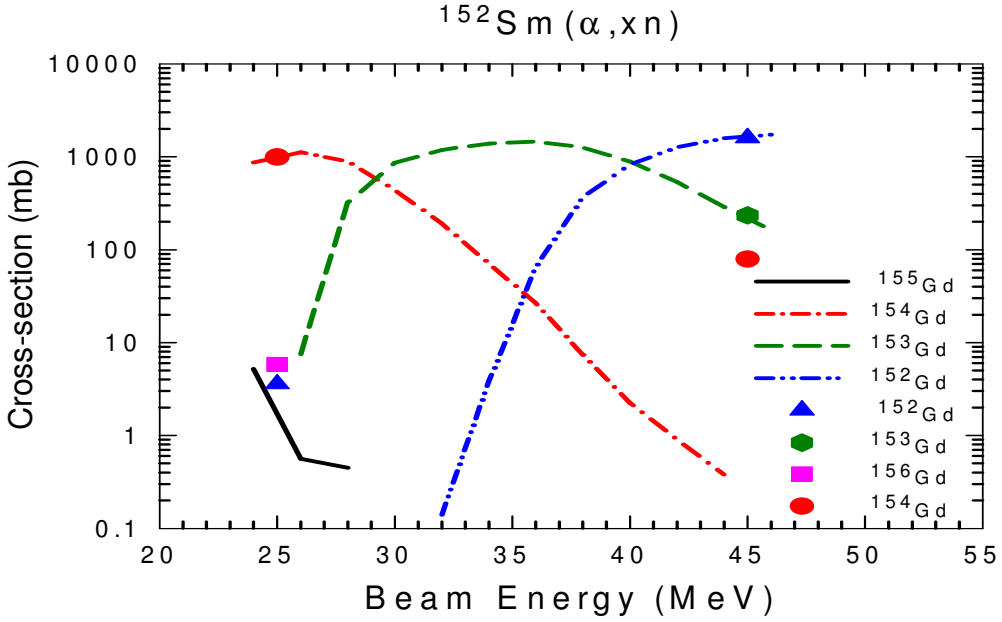

Figure 6:7. Comparison of calculated and measured cross-sections for Gd isotopes at different energies. The lines represent cross-sections calculated with PACE and the symbols are measured cross-sections.The measured cross-setions were obtained from [Sch09].

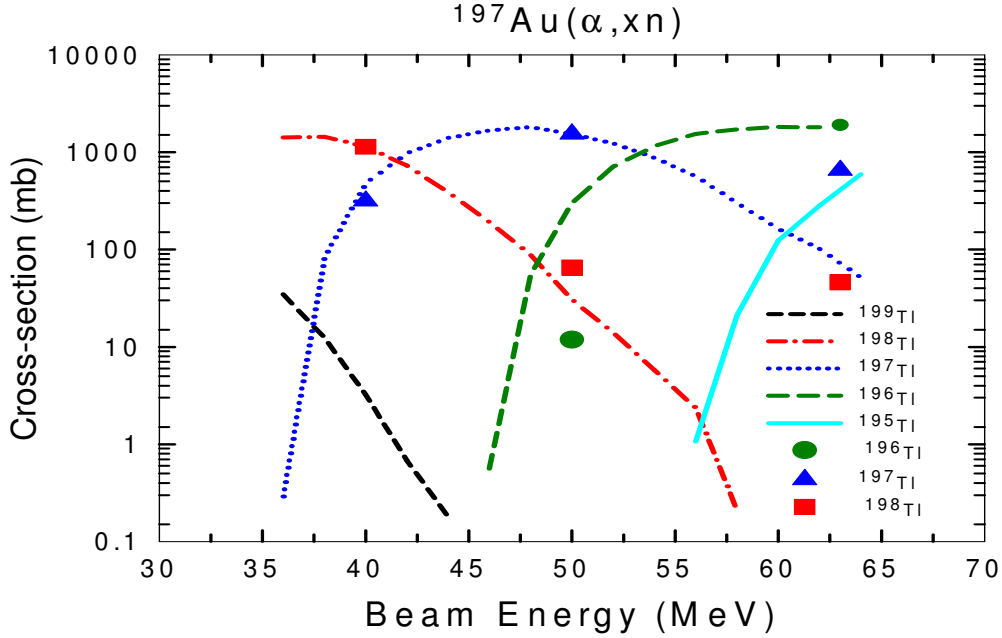

Figure 6:8. Comparison of calculated and measured cross-sections for Tl isotopes compared with measured cross-sections at different energies. The lines represent cross-section calculated with PACE and the symbols measured cross-sections. The measured cros setions were obtained from [Law09].

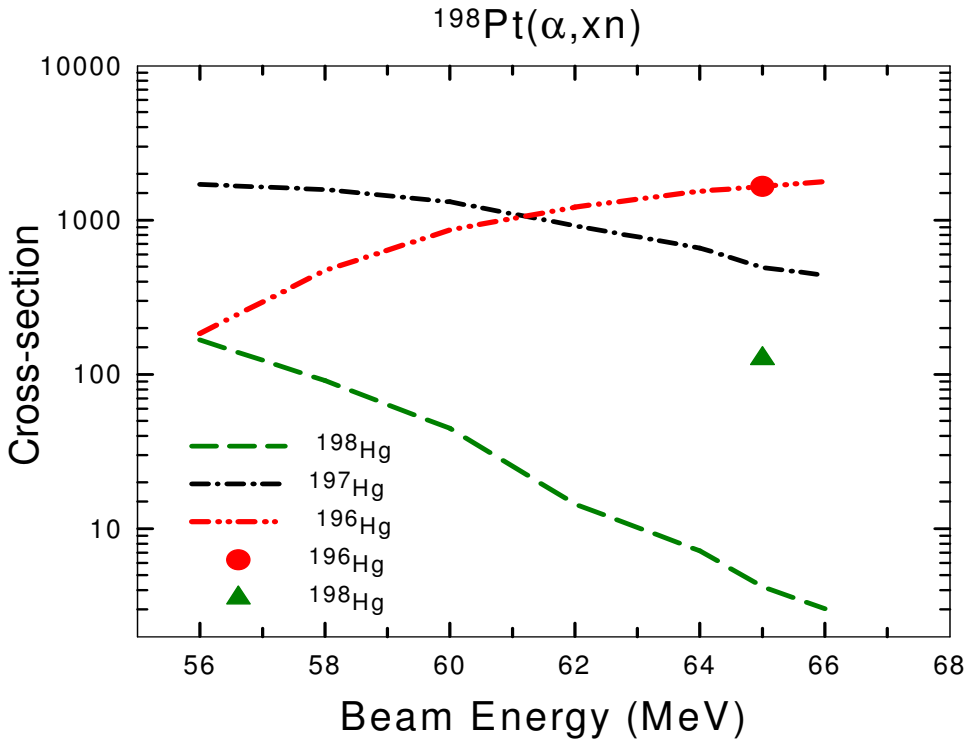

Figure 6:9. Comparison of calculated and measured cross-sections for Hg nuclei. The circle and the triangle represent the experimental results obtained for ^{196}Hg and ^{195}Hg, respectively, at beam energy of 65 MeV. The lines represent cross-sections calculated with PACE. The measured cros setions were obtained from [Law08].

The fact that PACE severely underestimates the strength of the "x-2" channel suggests that this channel could be produced by a mechanism other than fusion-evaporation. However, there appears to be no significant difference in the population as a function of spin between the "x" and "x-2" channels. In Figure 6:10 the ground state band intensities of the strongest U isotopes populated in the ^{232}Th(α, xn) reaction at 61 MeV are plotted as a function of spin. The intensities of the ground state band of ^{232}U populated at 42 MeV are also added to the plot. All the intensities were normalized to the intensity of the $8^+ \rightarrow 6^+$ transition of ^{230}U. The plots of the ground state band intensities follow the same trend, suggesting the formation of a compound nucleus.

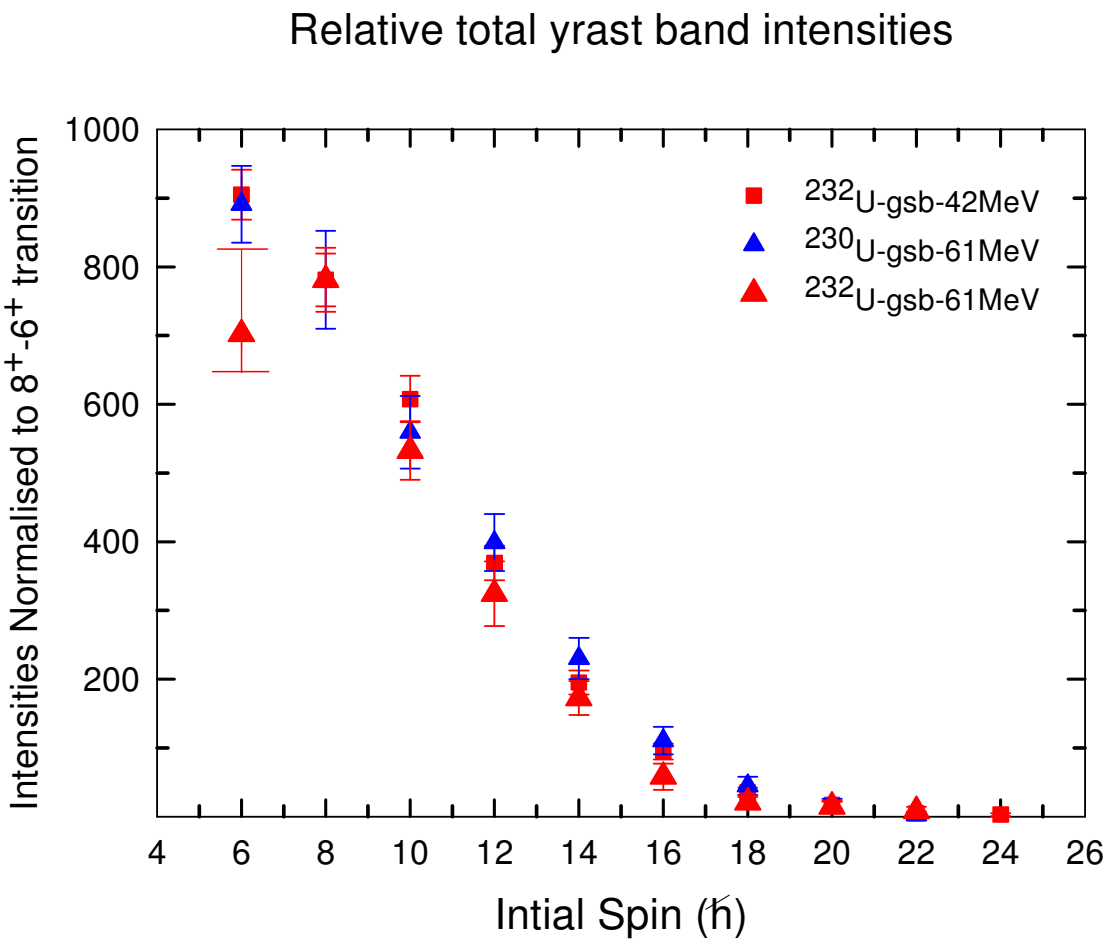

Figure 6:10. Normalized intensities of the ^{232}U ground state band at 42 MeV (squares), ^{232}U ground state band at 61 MeV (triangles) and ^{230}U ground state band at 61 MeV plotted as a function of spin.

More information on the reaction mechanism can be obtained by studying the time-of-flight spectra formed by gating on the yrast state band transitions of a nucleus and analyzing the measured MCP time spectrum. Figure 6:11 and Figure 6:12 show different MCP time spectra obtained when gating on the yrast band transitions of the indicated nuclei.

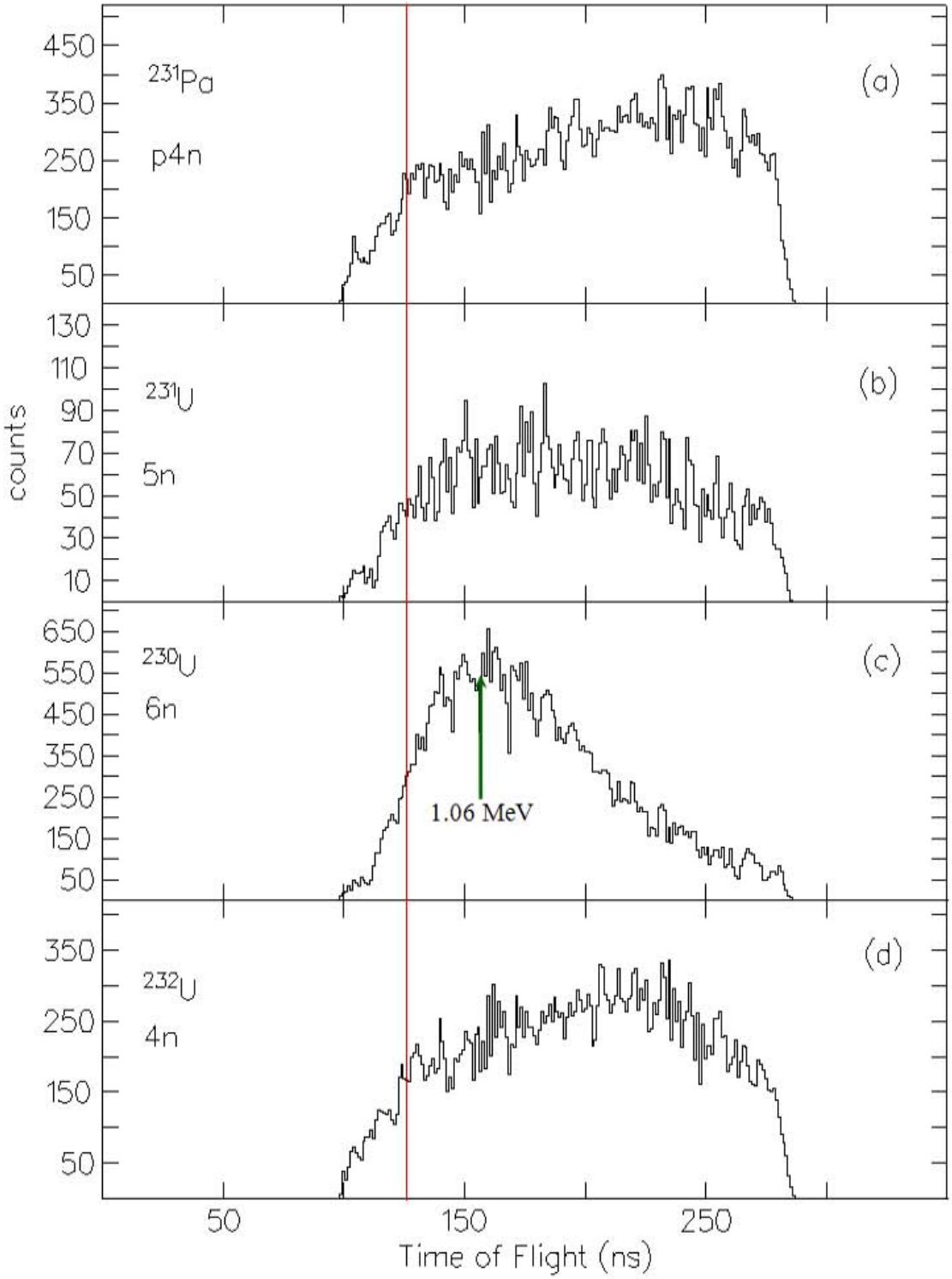

Figure 6:11. MCP time spectra obtained by gating on the yrast bands of the indicated isotopes in the $^{232}Th(\alpha, xn)$ reaction at 61 MeV. The red line indicates the starting time after neutron evaporation and the green arrow indicates the starting time before neutron evaporation corresponding to 1.06 MeV ^{230}U recoils.

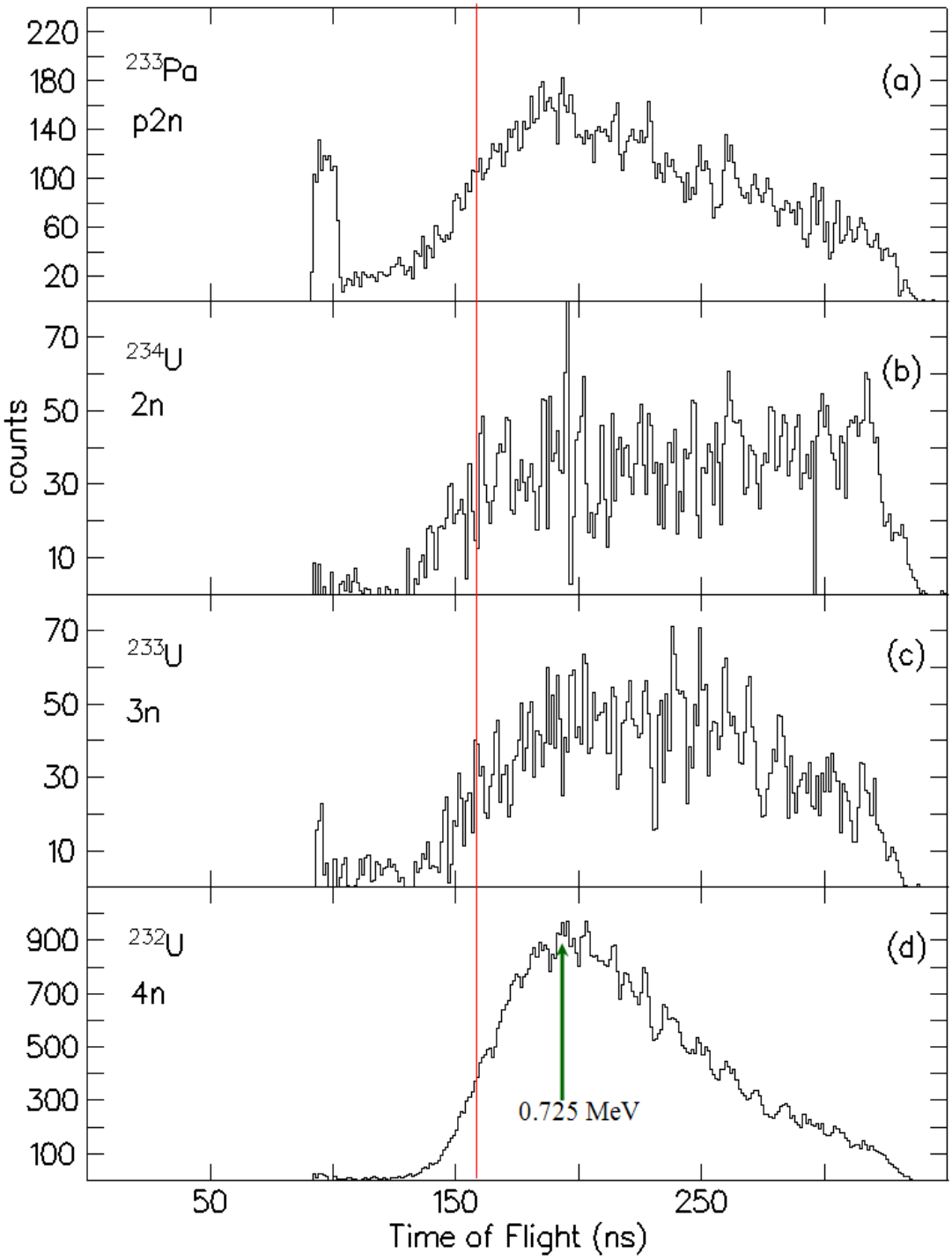

Figure 6:12. The MCP time spectra obtained by gating on the yrast bands of the indicated isotopes in the $^{232}Th(\alpha, xn)$ reaction at 42 MeV. The red line indicates the starting time after neutron evaporation and the green arrow indicates the starting time before neutron evaporation corresponding to 0.725 MeV ^{232}U recoils.

It can be seen from the spectra in Figure 6:11 that ^{231}Pa and ^{232}U arrive on average later than the ^{230,231}U products. Similarly Figure 6:12 indicates that the ^{232}U and ^{233}Pa are indeed faster than ^{234,233}U. This is confirmed in Figure 6:13 which shows γ–ray spectra formed using different MCP time gates on the 61 MeV data. In the slow gate, ^{231}U and ^{232}U are substantially enhanced. This is also observed in the ^{232}Th(α, 4n) reaction at 42 MeV where the ^{232}U was predicted to be the strongest channel. However, in the slow MCP time gate, ^{233}U and ^{234}U became substantially stronger (see Figure 6:14).

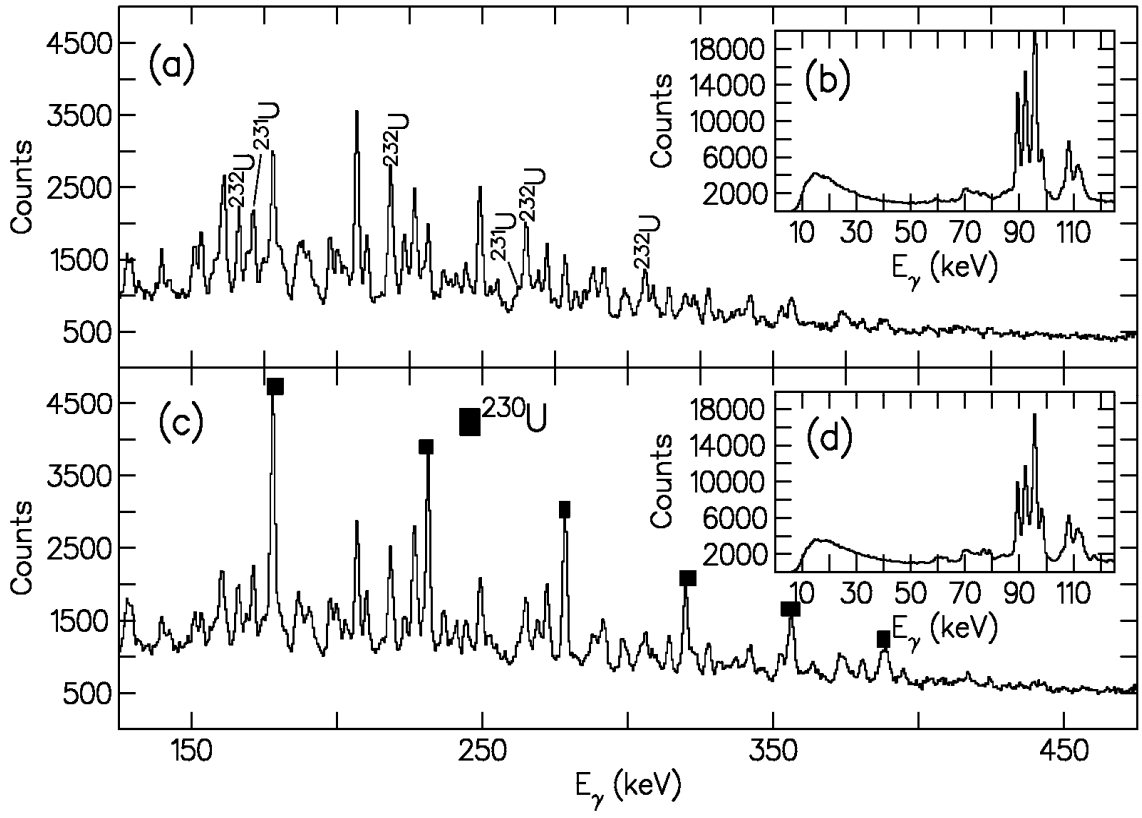

Figure 6:13. Comparison of the projection of MCP time gates in the ^{232}Th(α, xn) reaction measurement at 61 MeV. Upper portion: MCP time gate was set on 180-280 ns and lower portion: MCP time gate was set on 60-200 ns (see Figure 6:11).

The spectra of Figure 6:11 and Figure 6:12 have different shapes and these shapes imply that the nuclei were formed in different reaction mechanisms. Ideally, nuclei formed by complete fusion start with a definite momentum and spread out due to

particle evaporation and energy straggling in the target. This feature can be clearly seen in Figure 6:11(c) and Figure 6:12(a, d).

Indeed, the spectrum obtained by gating on the yrast band of ^{230}U (see Figure 6:15) with the calculated (see CHAPTER 4) time-of-flight spectrum for ^{232}Th(α, 6n) at 61 MeV are compared. The calculated time-of-flight spectrum is slightly wider than the measured time-of-flight spectrum, possibly due to an overestimate of the mean neutron evaporation energy, but is otherwise in substantial agreement with experiment (see Figure 6:15).

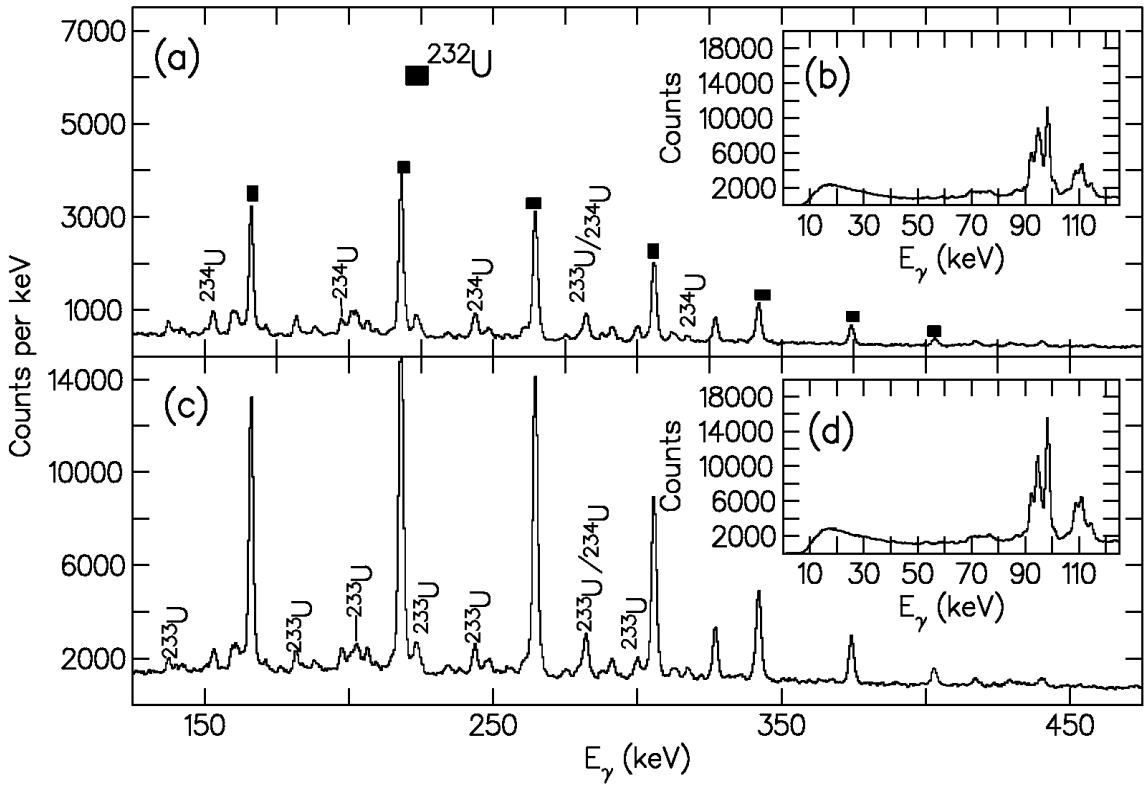

Figure 6:14. Comparison of the projection of MCP time gates in the ^{232}Th(α, xn) at 42 MeV reaction measurement. Upper portion:slow gate, MCP time gate was set on 180-280 ns and lower portion: fast gate, MCP time gate was set on 60-200 ns (see Figure 6:12)

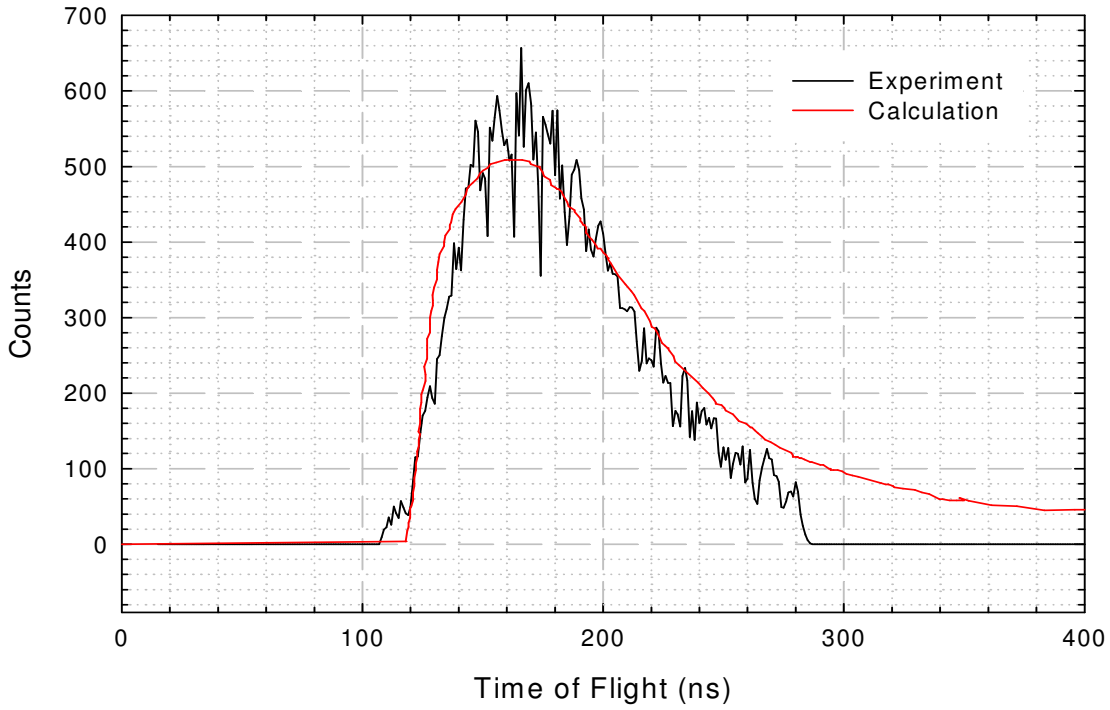

Figure 6:15. A comparison of the measured MCP time in $^{232}Th(\alpha,xn)$ reaction at beam energy of 61 MeV, spectra obtained by gating on the yrast band of ^{230}U (see Figure 6:11(c)) and the MCP time calculated taking into consideration the effect of evaporated neutrons and straggling in the target.

Furthermore, the calculated time-of-flight with the ungated MCP time spectra measured for ^{232}Th(α, 6n) at 61 MeV, Figure 6:16 are compared. These comparisons of the calculated MCP time spectra in Figure 6:15 and Figure 6:16 explain why the MCP time spectrum for the 61 MeV measurement looks relatively flat. It is because of the huge contribution from the products with "flat" time-of-flight spectra in Figure 6:11(a, b, d). Hence the calculation compared very well with the gated ^{232}U spectrum, see Figure 6:15 but not with the ungated MCP time spectrum.

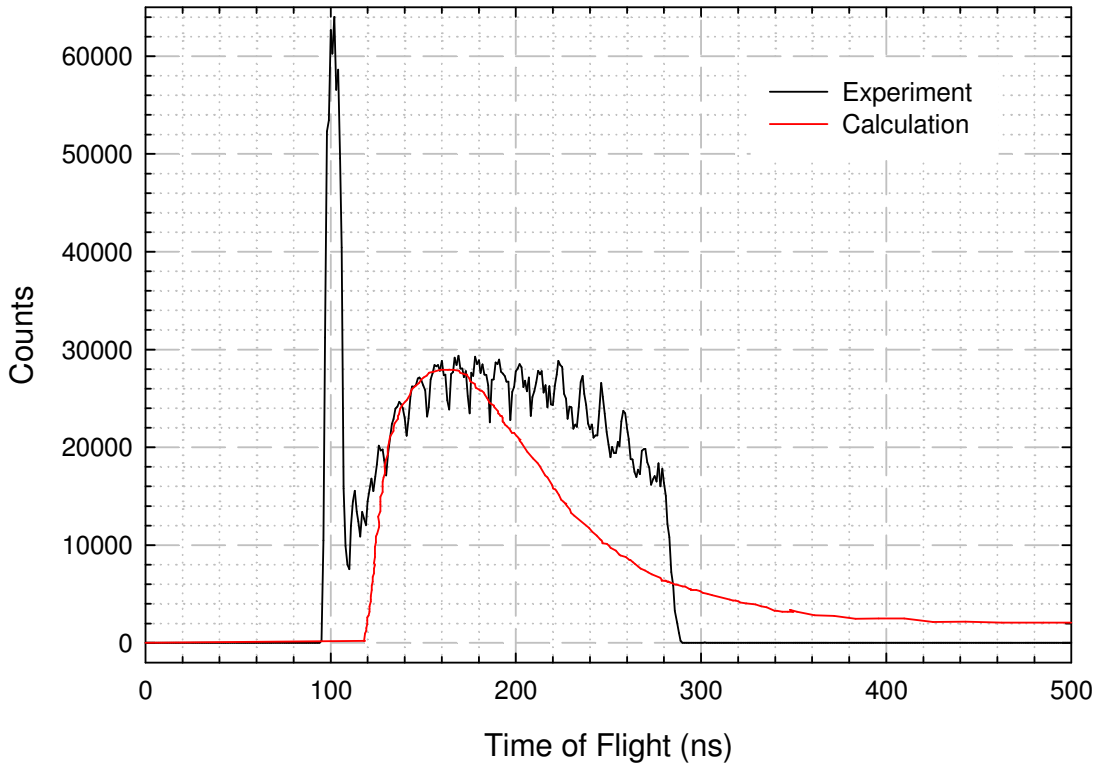

Figure 6:16. A comparison of the measured MCP time in $^{232}Th(\alpha,xn)$ reaction at a beam energy of 61 MeV and the calculated MCP time taking into consideration the effect of evaporated neutrons and straggling in the target. Note that the earliest arrivals come at about 100 ns =2.5 MeV.

The calculated starting time for the recoil from the complete fusion-evaporation is indicated by the green arrows in Figure 6:11(c) and Figure 6:12 (d). Figure 6:11 (b, d) and Figure 6:12 (b, c) show almost flat spectra and this suggests a huge distribution of initial velocities. As a result some recoils arrive slightly earlier than the recoils from fusion-evaporation: compare Figure 6:11(a, b, d) with Figure 6:11(c) or Figure 6:12(b, c) with Figure 6:12(a, d), while many others arrive much later.

The wide distribution of initial recoil velocities can be associated with transfer reactions. Consider, for example, Figure 6:17, in which recoil energies as a function of recoil angle are plotted for different recoil excitation energies for the reaction

^{232}Th(α,p)^{235}Pa at 61 MeV, as calculated using the kinematics program LISE [Baz02]. In Figure 6:17 the energy, angle acceptance of the detector, and the locus of points corresponding to the scattering of the proton at the grazing angle, θ_{gr} = 27°, are also indicated. Different recoil velocities are associated with different excitation energies, as expected. Ultimately, it is not ^{235}Pa that was observed, rather it was ^{231}Pa that was observed experimentally (see Figure 6:11 (a)). All of the above observations suggest a two-step, incomplete fusion mechanism. First, the transfer of three nucleons to the target, followed by equilibration and formation of a compound nucleus which decays by neutron evaporation:

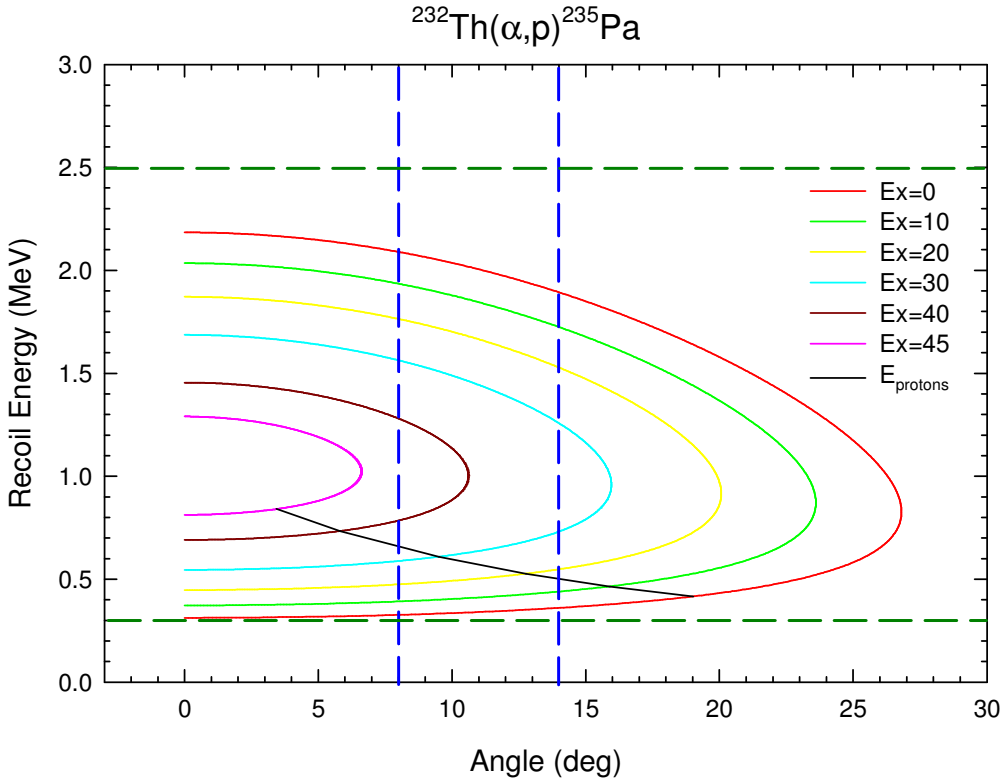

Figure 6:17. Recoil energy as a function of angle in ^{232}Th(α,p)^{235}Pa for different excitation energies of the recoil nucleus, calculated using LISE. The green and blue lines indicate time and angle acceptance respectively. The 100ns time-of-flight corresponds to ~2.5 MeV. i.e. the top dashed green line needs to move up to 2.5 MeV. The black line indicates to the scattering of the proton at the grazing angle, θ_{gr} = 27°.

$$^{232}Th + \alpha \rightarrow ^{235}Pa^{*} + p$$
$$^{235}Pa^{*} \rightarrow ^{231}Pa + 4n \qquad (6:1)$$

Uranium-232 can be formed in an analogous way:

$$^{232}Th + \alpha \rightarrow ^{235}U^{*} + n$$
$$^{235}U^{*} \rightarrow ^{232}U + 3n \qquad (6:2)$$

Within the acceptance of the recoil detector, excitation energies as high as ~42 MeV can be accommodated after the first step. This is not as high as complete fusion (~ 60 MeV offers better survival against fission. Incomplete fusion is often observed strongly in connection with alpha-cluster beams such as ^{9}Be, with the break-up of the beam occuring strongest near the grazing angle, [Bri61, Sur03]. Reactions near the grazing angle give rise to recoils with energies of around 500 keV (see Figure 6:17), which corresponds to a time-of-flight of around 230 ns. The time-of-flight spectra for ^{231}Pa and ^{232}U indeed support the incomplete fusion picture, with maxima at around 230 ns. Finally it is noted that the earliest arrivals of ^{231}Pa and ^{232}U correspond to an energy of about 1.7 MeV, as might be expected for complete fusion. Therefore a conclusion can be made that the various time-of-flight spectra may actually be composites of complete and incomplete fusion mechanisms.

CHAPTER 7 ELECTRIC DIPOLE MOMENTS IN ^{230,232}U AND IMPLICATIONS FOR TETRAHEDRAL SHAPES

7.1 Measurement of intrinsic electric dipole moment

To understand whether the U isotopes are tetrahedral or not, it would be ideally to measure the quadrupole moment Q_0 for this band. Since lifetimes cannot be measured, because of the weak population of the nuclei, energies, alignments and $|D_0|$ values of neigbouring nuclei were compared to see what conclusion can be made. In order to further establish the structural similarities in nuclei within the same isotonic chain, intrinsic dipole moments $|D_0|$ have been extracted for ^{230,232}U isotopes. The magnitude of the ratio of the intrinsic dipole to intrinsic quadrupole moment was extracted from the data through measurement of γ–ray branching ratios and the extraction of the $B(E1; I^- \rightarrow I^+ - 1) / B(E2; I^- \rightarrow I^- - 2)$ ratio of reduced transition probabilities. The rotational model gives for D_0 :

$$D_0 = \left[\frac{5(I-1)B(E1; I \rightarrow I-1)}{8(2I-1)B(E2; I \rightarrow -2)} \right]^{1/2} Q_0 \qquad (7{:}1)$$

The extracted $B(E1; I^- \rightarrow I^+ - 1) / B(E2; I^- \rightarrow I^- - 2)$ ratios of ^{230,230}U, together with magnitudes of the electric dipole moments $|D_0|$, are listed in Table 7:1 and Table 7:2. Our $|D_0|$ values were obtained using $Q_0 = 1000\, fm^2$ which is equal to the measured quadrupole moment Q_0 for the ground state band of the U isotopes [Bel60].

Figure 7:1 shows the experimental ratio of absolute magnitude of the intrinsic electric dipole moments $|D_0|$ as a function of spin for transitions de-exciting states of spin I in ^{230}U and ^{232}U. The measured $|D_0|$ values for both U isotopes are not constant over the range of measured spins. This suggests that the charge asymmetry and mass distribution in both isotopes change with increasing spin.

Table 7:1. $B(E1)/B(E2)$ ratios and dipole moments $|D_0|$ extracted from the ^{230}U data using the measured $B(E1)/B(E2)$ ratios, and the rotational model formulae.

$I_i^{\pi_i}(\hbar)$	$\frac{B(E1;I_i \to I_i-1)}{B(E2;I_i \to I_i-2)}\ (fm^{-2})$	$\lvert D_0\rvert$ $(e.fm)$
15	$9(9)\times10^{-8}$	0.15(7)
17	$1.0(8)\times10^{-7}$	0.16(6)
Weighted Mean		0.16(6)

Table 7:2. $B(E1)/B(E2)$ ratios and dipole moments $|D_0|$ extracted from the ^{232}U data using the measured $B(E1)/B(E2)$ ratios, and the rotational model formulae.

$I_i^{\pi_i}(\hbar)$	$\frac{B(E1;I_i \to I_i-1)}{B(E2;I_i \to I_i-2)}\ (fm^{-2})$	$\lvert D_0\rvert$ $(e.fm)$
9	$>55\times10^{-8}$	>0.12
11	$3.3(5)\times10^{-8}$	0.095(9)
13	$9.5(20)\times10^{-8}$	0.161(19)
15	$7.4(10)\times10^{-8}$	0.144(12)
17	$4.8(7)\times10^{-8}$	0.116(11)
19	$2.1(7)\times10^{-8}$	0.077(13)
21	$>4\times10^{-8}$	>0.12
Weighted Mean		0.1110(53)

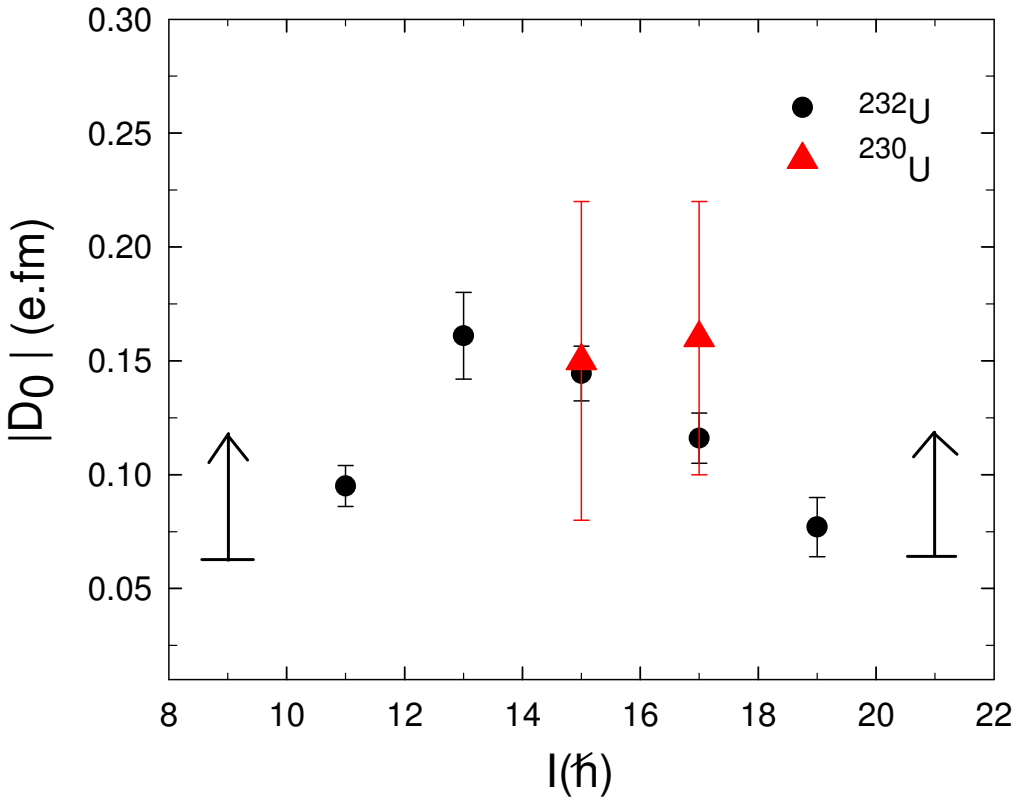

Figure 7:1. Plot of the experimental ratio of the absolute magnitude of the intrinsic electric dipole moments $|D_0|$ as a function of spin for transitions de-exciting states of spin I in ^{230}U and ^{232}U.

The use of the strong-coupling limit of the rotational model, as used to obtain equation (7:1), to extract the intrinsic dipole moments for ^{230,232}U is justified if the Coriolis mixing of the bands is small. In principle, the $B(E1; I^- \rightarrow I^+ + 1) / B(E1; I^- \rightarrow I^+ - 1)$ ratio, can be used to deduce the K-mixing present in the negative-parity band [Koc70]. Our values are within statistical uncertainty, consistent with a pure $K = 0$ assignment. The quadrupole moment Q_0 of the negative-parity band, in contradiction with the tetrahedral assumption, was assumed to be the same as that measured [Bel60] for the ground-state band.

In order to understand the results in the context of the systematics of the region, three plots were made. In the first two, shown in Figure 7:2 and Figure 7:3, the energies of the ground-state bands and the negative-parity side bands for the $N = 138$ and

$N = 140$ isotones of Ra, Th, and U nuclei are compared by aligning the energies of the 1^- states of the negative-parity bands. Remarkably, as first noted by Zeyen et al., [Zey87], one observes that, for $N = 138$, the bands are practically identical - the corresponding energies are indeed the same to within a few keV. The same correspondence is also seen for $N = 140$ between ^{232}U and ^{230}Th, although ^{228}Ra is only identical with these two nuclei at lower spin values.

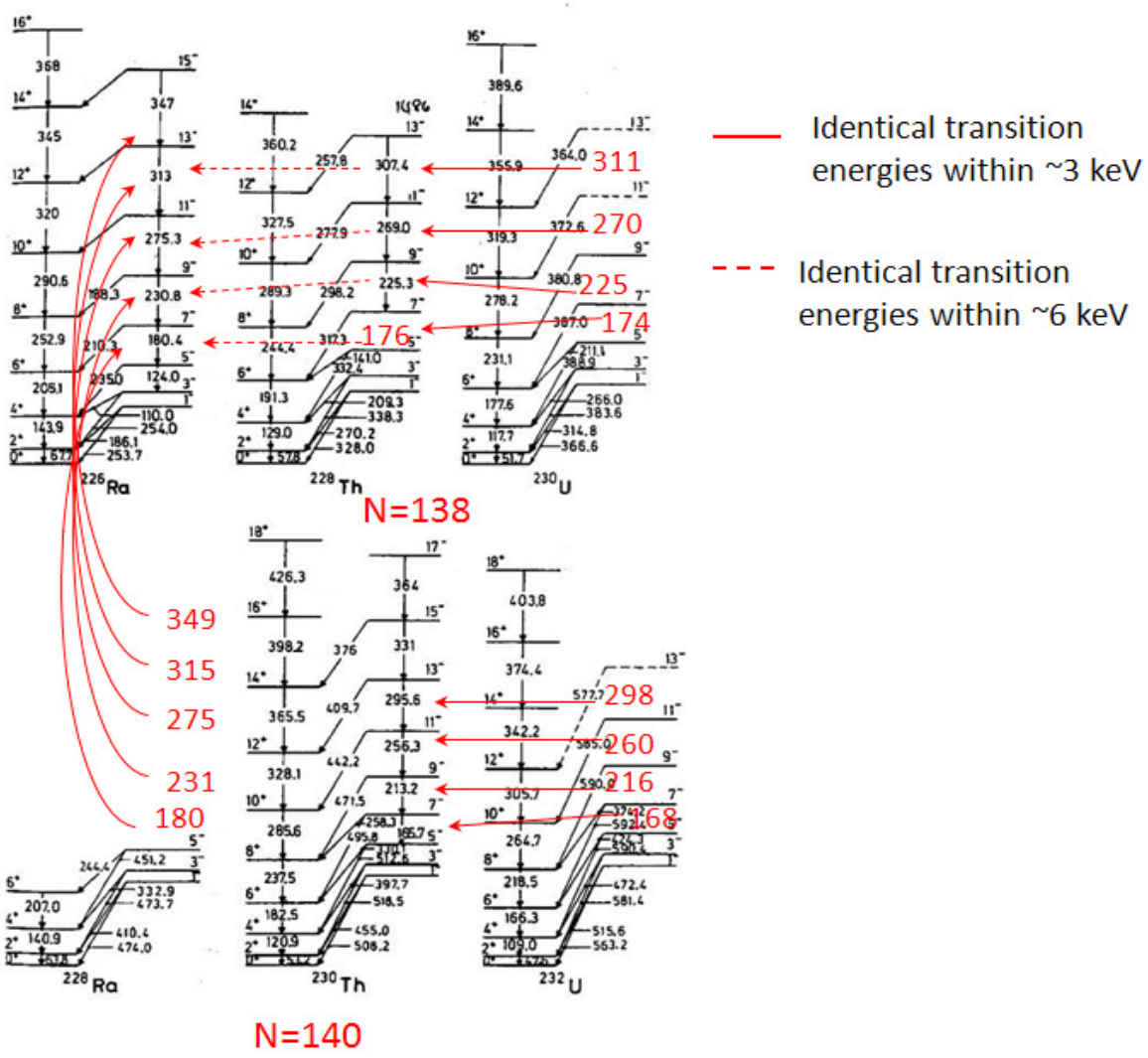

Figure 7:2. Comparison of the transition energies for the $N = 138$ and $N = 140$ isotones. Level schemes taken from [Zey87, Ack93]. The red numbers represent the energy of the γ-ray transitions connecting the levels. The figure is taken from [Bar10b].

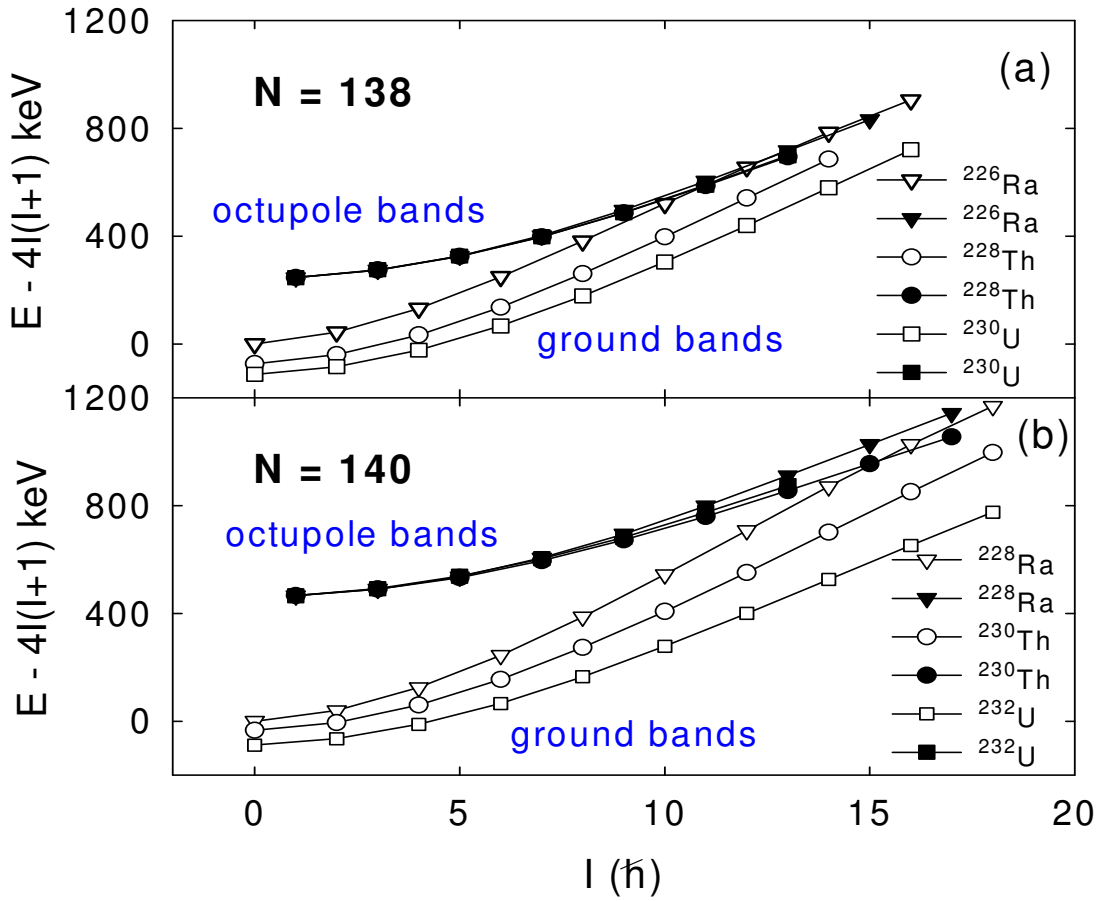

Figure 7:3. Energies of negative-parity octupole bands (solid symbols) compared with the energies of the ground-state bands (open symbols) for (a) $N=138$ and (b) $N=140$ isotones. A rigid-rotor reference has been subtracted and the energies of the bands have been aligned to the 1^- states of the octupole bands. Data taken from Refs: [Zey87, Ack93, Wol93].

In the third plot, Figure 7:4, the magnitude $|D_0|$ of the electric dipole moments of Ra , Th , and U nuclei, averaged over high-spin values (typically $I>7$) are compared as a function of neutron number. Our value of $|D_0|$ for ^{230}U is in good agreement with the tentative value obtained by Ackermann et al., [Ack93]. In the same figure, a staggering function evaluated for the 11^- states is also plotted (see the red lines in Figure 7:4). The staggering function is given by:

$$\Delta E(I) = [E(I) - 0.5(E(I-1) + E(I+1))] / E_{2^+} \qquad (7:2)$$

This function gives a measure of the splitting between the positive- and negative-parity bands and is normalized to the energy of the first 2^+ state [Bon05].

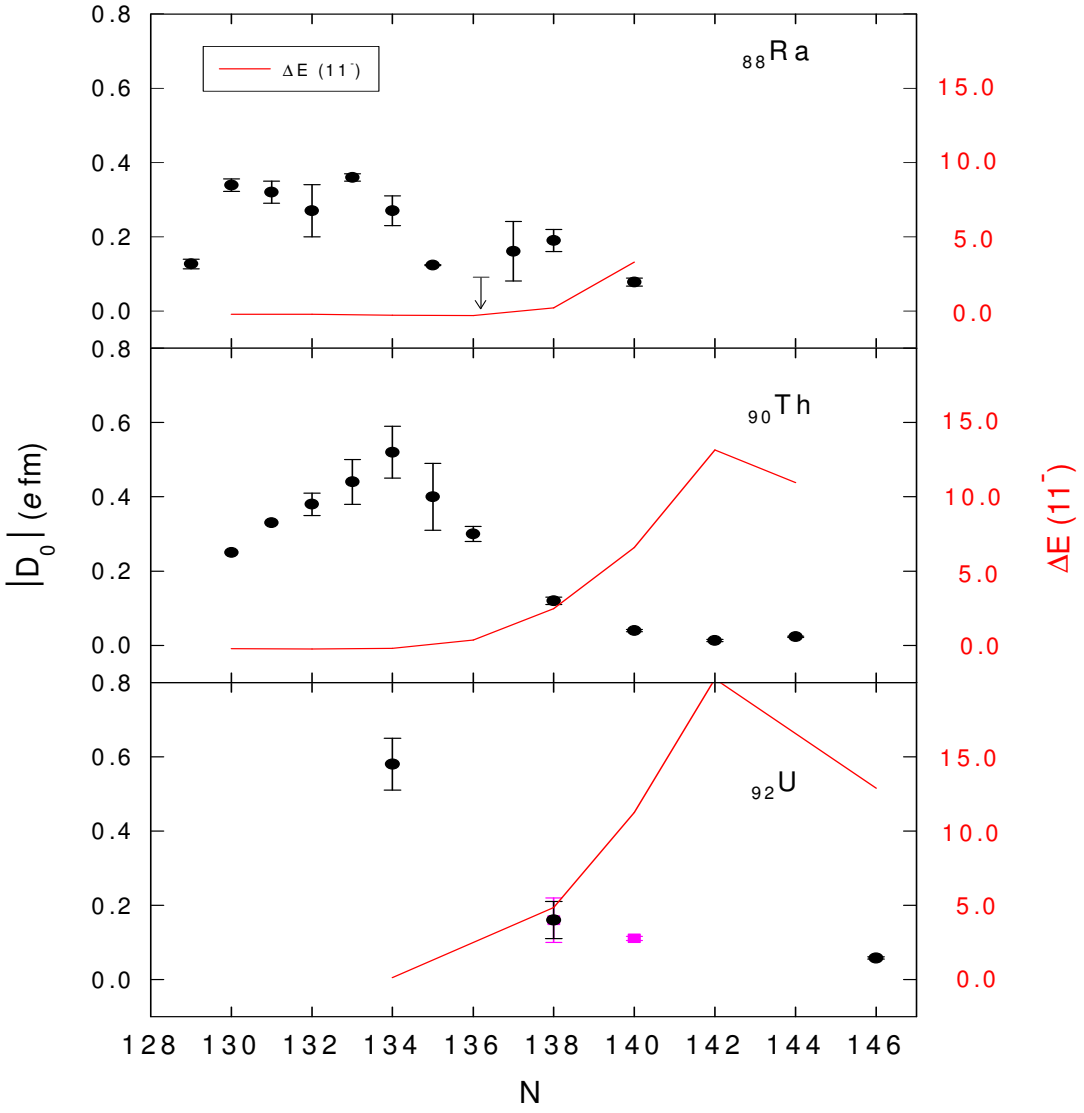

Figure 7:4. Systematics of experimental electric dipole moments (left hand scale) for Ra, Th, and U isotopes. Experimental $|D_0|$ *(black circles) values taken from the compilations of refs. [But96], [But91] and [Coc99], (*^{222,226,228}*Ra ,*^{234}*Th), [Ack93] (*^{232}*Th,*^{230}*U), [Gre98](*^{226}*U), and [War96] (*^{238}*U). The present work* $|D_0|$ *is indicated in pink squares, Right hand scale; experimental staggering function* $\Delta E(I)$ *given by equation (7:2) and the red lines are a plots of* $\Delta E(11^-)$.

An anticorrelation is observed between the staggering function and the dipole moments. Thus, the region traditionally associated with octupole deformation, $N<138$, is characterized by large dipole moments and negligible splitting between the bands, while the vibrational region, $N>140$, is characterized by large splittings and small dipole moments.

It can be seen that the $N=138$ and $N=140$ isotones lie near a transition region, where the large dipole moments of nuclei with $N<138$ give way to the small values above $N=140$ in the vibrational region. As the energies of the negative-parity bands of ^{230,232}U are similar to those of their isotones, also similar values of $|D_0|$ are observed.

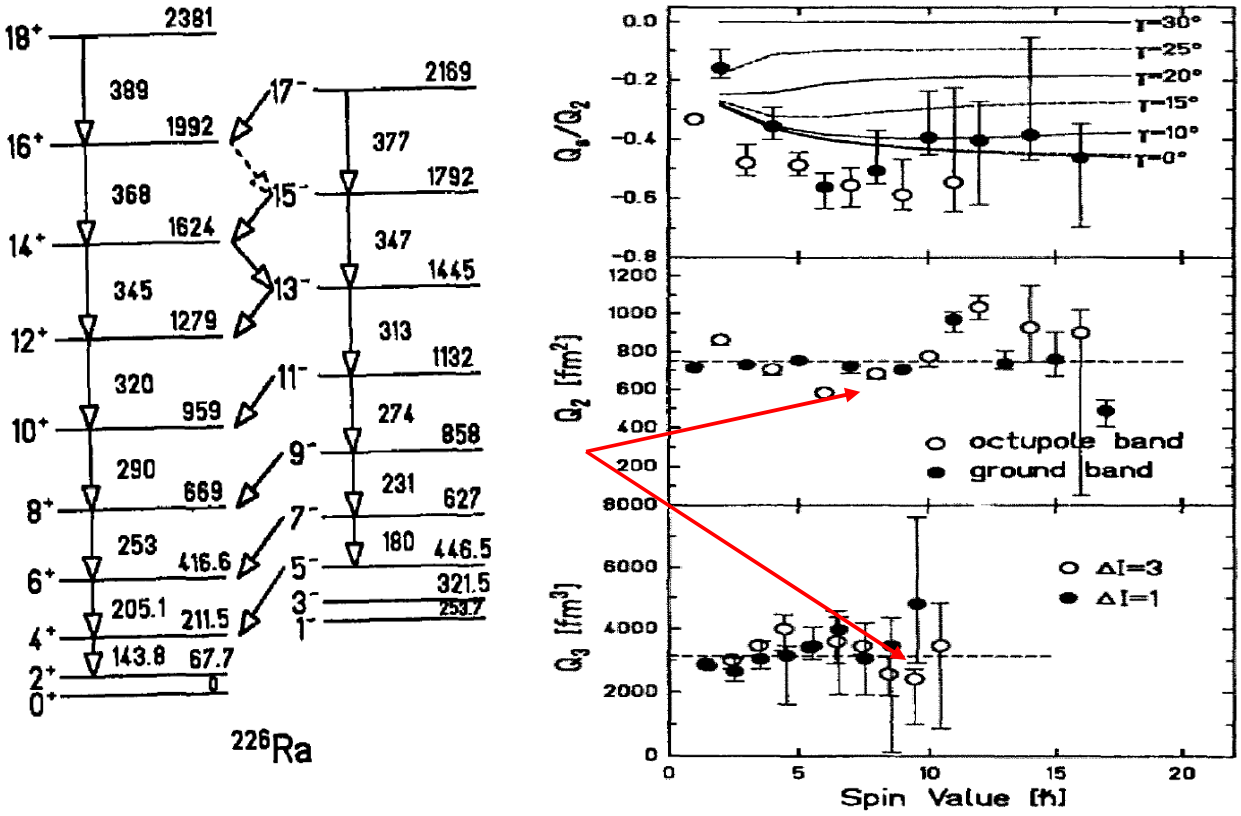

Figure 7:5. Coulomb excitation results of ^{226}Ra measured by Wollersheim et al.[Wol93].

An important point in connection with the possibility that the negative-parity bands of ^{230,232}U are tetrahedral rotors is that the Coulomb excitation of the $N=138$ isotone

^{226}Ra has been comprehensively studied by Wollersheim et al. [Wol93]. In this work, quadrupole and octupole moments of both the ground and negative-parity bands were measured and found to be equal as shown in Figure 7:5, with average values of $Q_2 = 750\,fm^2$ and $Q_3 = 3100\,fm^3$, respectively. Although the Q_3 value indicates an octupole deformation, the large value of Q_2 is inconsistent with that of a tetrahedral shape. Given the similarity in other properties of the ^{230,232}U bands with those of ^{226}Ra (see Figure 7:6), it would be remarkable if the quadrupole moments of the negative-parity bands of ^{230,232}U were zero and hence the shape tetrahedral. It can be concluded that the present data for ^{230,232}U fall inside the systematics of nuclei lying in the transitional region between those of stable octupole deformation and octupole vibrators.

The present data also allow a plausible explanation, without resorting to the tetrahedral assumption, of why the in-band E2 transitions were not observed in the earlier measurements [Zey87, Ack93]. In Figure 7:3 it can be seen that with increasing proton number, the negative-parity bands move further away from the yrast line, thus making their population in fusion-evaporation reactions less favorable. Furthermore, with essentially constant $B(E1)/B(E2)$ ratios between the isotones, and approximately constant $E2$ transition energies, the $E2$ transition rates would remain constant for these isotones, (assuming approximately similar quadrupole moments, as is the case for the ground state bands [Bel60]). However, the $E1$ transition decay energy would increase, causing the $E1$ transition rates to increase with E_γ^3. Thus, not only moving the negative-parity band further away from the yrast line would make it more difficult to populate it, but less of its population would be retained in the $E2$ transitions of the band due to increasing $E1$ decay rate.

Finally, in Figure 7:6, the measured values of $|D_0|$ are compared with the recent Skyrme Hartree-Fock calculations of Tsvetkov et al., [Tsv02]. These calculations are in substantial agreement with the earlier theoretical work of [Coc99] and [Egi92] for Ra and Th isotopes.

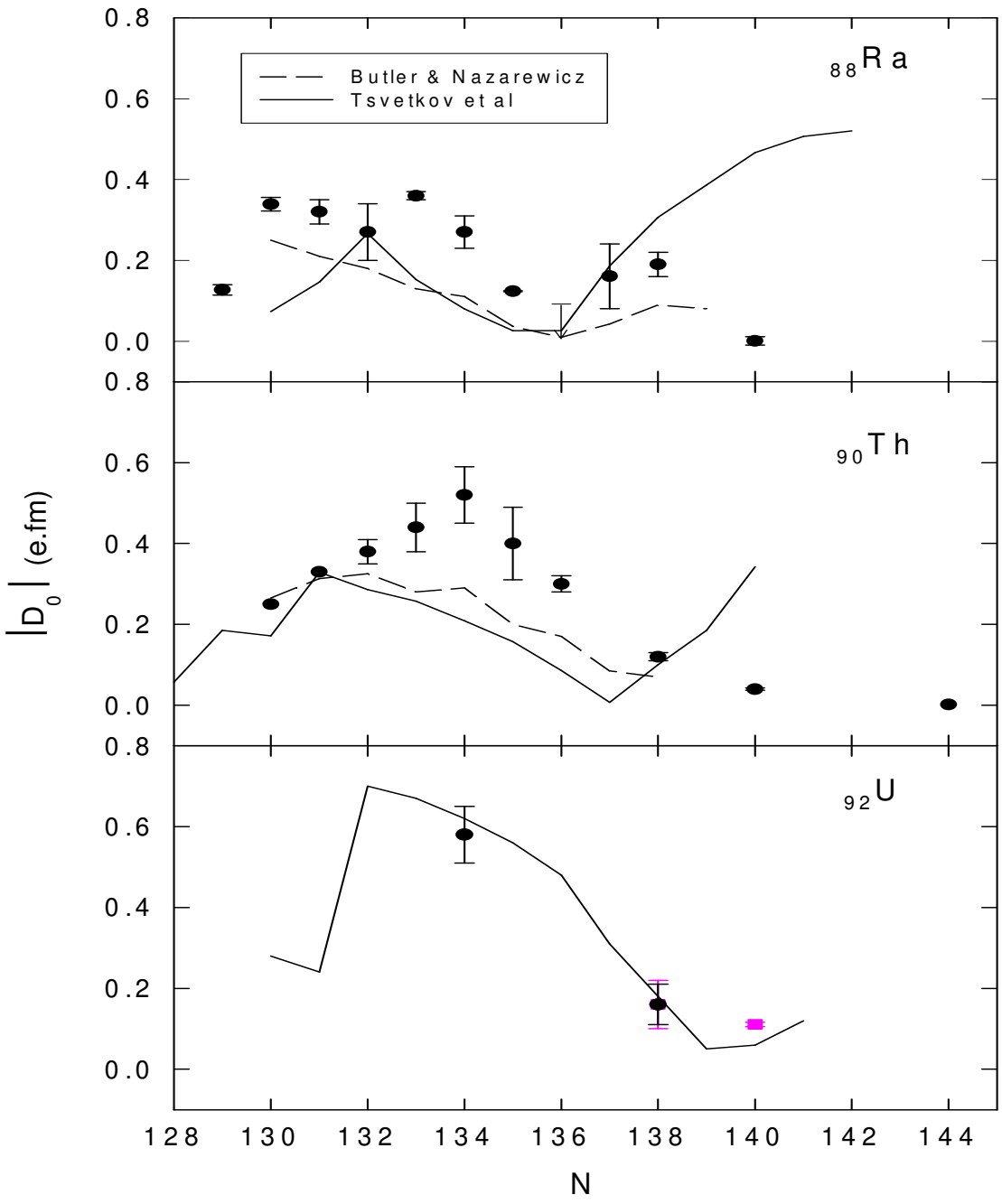

Figure 7:6. Systematics of experimental electric dipole moments compared to calculations of Tsvetkov et al.,[Tsv02] for Ra, Th and U isotopes. Experimental $|D_0|$ values (black circles) are taken from the compilation of Refs. [But96, But91, Coc99] (^{222,226,228}Ra, ^{234}Th),[Ack93] (^{232}Th, ^{230}U), [Gre98] (^{226}U), [War96] (^{238}U). The present $|D_0|$ are shown in pink squares.

Tsvetkov et al., included the triaxial quadrupole and octupole deformations, and extended the calculations of $|D_0|$ to U isotopes up to N=141. For the U nuclei their calculations are in good agreement with the experimental results. The calculations appear to overestimate the data for the heavier Ra and Th isotopes beyond N=138. It is interesting to note that the calculations of Tsvetkov et al. also predict increasing triaxial deformations with increasing spin which is qualitatively in agreement with the heart-shaped deformations implied by the octupole condensate picture discussed by Frauendorf [Fra08].

The close similarity in the energies and electric dipole moments of the negative-parity bands of the $N = 138$ and $N = 140$ isotones suggests a similar underlying structure, which by comparison with ^{226}Ra in particular, implies an octupole vibration picture contrary to the tetrahedral interpretation.

CHAPTER 8 SUMMARY AND FUTURE PROSPECTS

To study heavy nuclei, a recoil detector has been employed. This detector has been designed, developed, commissioned, tested and is now in operation at iThemba LABS. This device allows in a unique way to separate fusion-evaporation residues from fission background using the time-of-flight technique. With the help of this detector, heavy nuclei have been studied using ^{181}Ta(^{20}Ne, 6n) , ^{180}W(^{20}Ne, 4n) and ^{232}Th(α, xn) reactions.

In search for superdeformed states in ^{196}Po, the ^{180}W(^{20}Ne, 4n) reaction was used, from this work the known level scheme of ^{196}Po was confirmed but no superdeformation state was identified. This could be as a result of lack of statistics in our data or else superdeformed bands do not exist in ^{196}Po.

The ^{230,232}U isotopes were studied using the ^{232}Th(α, xn) reaction. The known level schemes of these uranium isotopes were confirmed and extended. For ^{232}U, a long sequence of in-band $E2$ transitions has been added to the negative-parity sequence identified as an octupole band. In case of ^{230}U, due to low statistics, only two in-band members could be added to what had been already measured in a previous investigation [Ack93].

Intrinsic electric dipole moments were extracted from the data using the measured ratios of $B(E1)/B(E2)$ reduced transition probabilities, and the rotational model formula, given in equation (7:1), assuming, $Q_0 = 1000\,fm^2$. The dipole moments were compared with the systematics of the neighbouring Ra and Th nuclei. Wollersheim et al., measured the quadrupole moments for the lowest-lying-negative-parity states in ^{226}Ra using Coulomb excitation [Wol93]. In Wollersheim et al., measurement these moments were found to be large (contrary to the assumption of a tetrahedral nuclear shape) and he also concluded that these states were of octupole nature. Since the features of ^{226}Ra are comparable to those of the other nuclei in the region, particularly to those of the ^{230,232}U nuclei studied in this work, it was concluded that ^{230,232}U are octupole bands and not tetrahedral.

In the ^{230,232}U data presented in this work, no hyperdeformed band was identified, this could be due to low statistics or ^{230,232}U do not have a hyperdeformed band. Furthermore in the ^{232}Th(α, xn) reaction, at 61 MeV, a very strong ^{232}U ground state band was observed. This was a surprise as it was expected from the calculation of the excitation functions that ^{231}U will be the strongest channel. However it was found that the reason for the above mentioned mystery is that the ^{232}U evaporation residues were a product of incomplete fusion reactions of which is not taken into account in the program PACE. Furthermore, a band very close in transitions energies to the ^{232}U ground state band was also observed. We propose this a low spin band in ^{231}U. It was not possible to assign it as the ^{231}U ground state band since the ground state of ^{231}U is still not known. As a result an experiment is planned at iThemba to further investigate ^{231}U by performing an experiment at intermediate beam energy where ^{231}U is the strongest channel. Besides confirming our ^{231}U candidate band it will be interesting to see how much ^{232}U will be produced when performing the proposed experiment.

The few percentage background from unknown source(s) in the recoil detector is still to be investigated and will hopefully be resolved. This will allow the use of high beam intensity and ultimately improve data statistics. This may enable experiments to search for hyperdeformed band in the U isotopes. Another plan to enhance production cross-section for hyperdeformed bands experiment is to use a radioactive ^{230}Th target. In order to use this kind of target, the recoil detector chamber will have to be modified.

APPENDIX A

Weisskopf estimates

The electric and magnetic transition rates, under the assumption that the transition is due to a single proton moving from one shell model state to another, can be estimated from

$$T(EL) = \frac{8\pi(L+1)}{\hbar L((2L+1)!!)^2}\frac{e^2}{4\pi\varepsilon_0\hbar c}\left(\frac{E_\gamma}{\hbar c}\right)^{2L+1}\left(\frac{3}{L+3}\right)^2 cR^{2L} \qquad \text{(A:0:1)}$$

and

$$T(ML) = \frac{8\pi(L+1)}{\hbar L((2L+1)!!)^2}\left(\mu_p - \frac{1}{L+1}\right)^2\left(\frac{\hbar}{m_p c}\right)^2\left(\frac{se^2}{4\pi\varepsilon_0\hbar c}\right)\left(\frac{E_\gamma}{\hbar c}\right)^{2L+1}\left(\frac{3}{L+2}\right)^2 cR^{2L-2} \qquad \text{(A:0:2)}$$

where μ_p , is the magnetic moment of the proton and m_p is the proton mass. The wave functions of the states were obtained using a square well potential. By taking $R = R_0 A^{1/3}$ and by setting the $\left(\mu_p - \frac{1}{L+1}\right)^2$ term in equation (A:0:2) to be equal to 10, estimates can be made for the lower multipole orders. These are known as the Weisskopf Estimates, and are given in Table A:1. These estimates are only realistic for pure single-particle transitions but not when collectivity plays a role.

Table A:1. Single-particle or Weisskopf estimates. The units are s^{-1} when the γ-ray energy E is expressed in MeV.

Weisskopf Estimates	
$T(E1) = 1.0\times10^{14} A^{2/3} E^3$	$T(M1) = 5.6\times10^{13} E^3$
$T(E2) = 7.3\times10^{7} A^{4/3} E^5$	$T(M2) = 3.5\times10^{7} A^{2/3} E^5$
$T(E3) = 3.4\times10^{1} A^{2} E^7$	$T(M3) = 1.6\times10^{1} A^{4/3} E^7$
$T(E4) = 1.1\times10^{-5} A^{8/3} E^9$	$T(M4) = 4.5\times10^{-6} A^{2} E^9$

Collective transition rates

The collective electric and magnetic transition probabilities for deformed nuclei have been deduced by Bohr and Mottelson [Boh75]. The reduced transition probabilities for $E2$ and $E1$ transitions, which are important in the context of this work, are given by equations (1:16) and (1:18) respectively. Table A:2 gives electric and magnetic transition rates in terms of the reduced transition probabilities for various multipolarities. They are obtained from equations (A:0:3) and (A:0:4) and they were used in this work to obtain the transition probabilities for the observed γ–ray transitions.

Table A:2 Transition rates expressed in terms of the reduced transition probabilities. The dimensions are: $T(\sigma L) - s^{-1}$, $B(EL) - e^2\,fm^{2L}$, $B(ML) - \mu_n^2\,fm^{2L-2}$, *and E is expressed in MeV.*

Transition Rates	
$T(E1) = 1.587\times10^{15}\,B(E1)E^3$	$T(M1) = 1.779\times10^{13}\,B(M1)E^3$
$T(E2) = 1.223\times10^{9}\,B(E2)E^5$	$T(M2) = 1.371\times10^{7}\,B(M2)E^5$
$T(E3) = 5.698\times10^{2}\,B(E3)E^7$	$T(M3) = 6.287\times10^{0}\,B(M3)E^7$
$T(E4) = 1.69\times10^{-4}\,B(E4)E^9$	$T(M4) = 1.87\times10^{-6}\,B(M4)E^9$

APPENDIX B

The process of mounting the carbon foil

One of the biggest challenges of using the recoil detector was the mounting and handling of carbon foils. The carbon foils used in the recoil detector were supplied by the Arizona carbon foil company from the USA. They were coated on $110 \times 110\ \mathrm{mm}^2$ support glasses with a parting agent in between. Due to being very thin and fragile special care was needed when removing the foils from their support glass and mounting them to the frame which is required by the experiment. The whole process was done by the iThemba LABS target maker, Mrs. N.Y. Kheswa at iThemba LABS. The equipment used during in the process are: 25ℓ water container, 15ℓ tank equipped with a tap, distilled water, alcohol, 1m long and 3 cm in diameter pipe, an aluminum stand to hold the glass plate at 45º and an aluminum holder to hold the frame vertically, where the foil was mounted.

The process involves the following procedures: A 25ℓ container filled with distilled water and 17% alcohol. The alcohol was necessary to reduce the surface tension of the water which has a potential to break the foil. The carbon-coated glass on its edges had to be scratched so that water will get access to dissolve the parting agent and allow carbon foil to release easily from the glass substrate.

The scratched carbon-coated glass was place on the 45º aluminum stand as shown in Figure B:1. The 45º aluminum stand shown in Figure B:1 and the aluminum frame holder were put at some distance parallel to each other in an empty 15ℓ tank as indicated in Figure B:2. A $100\ \mathrm{mm} \times 100\ \mathrm{mm}$ frame cleaned with alcohol was placed to its slots in the frame holder as indicated in Figure B:3. A pipe was used to slowly drain the distilled water and alcohol solution from the 25ℓ container into the 15ℓ tank. The water was taken out very slowly to avoid the damage of the foil by vibrations.

The tank was filled until the carbon foil was completely pulled off the glass and floating on the surface of water above the aluminum frame as depicted in Figure B:2. Thereafter the water from the tank was slowly drained using the tap until it reach the

top of the frame, with the carbon foil floating on it. The foil was directed to a frame by gently blowing on it until its edge was above the frame. While the edge of the foil was resting above the frame, water was removed through the tap until the foil was completely mounted in the frame. Empting the tank took about 1.5 hours. Figure B:4 shows a carbon foil after all the water in the tank has been removed. The mounted foil was kept in the tank for an hour to dry and thereafter it placed on safe place.

Anything that can cause vibration i.e. air conditioning was not encouraged in the target laboratory during the process of mounting carbon foil. On the big frame, we have successfully mounted 15 $\mu g/cm^2$ and thicker. For experiment two 4 $\mu g/cm^2$ thin carbon foils were required, small frames were designed since foils were breaking during mounting on bigger frames. Four of these small frame combined make the size of the big frame (see Figure 4:21). The 4 $\mu g/cm^2$ foil was mounted to the small frames with colloidal backing that was removed by heating.

Figure B:1. Carbon coated glass on a 45º aluminum stand.

Figure B:2. Carbon foil floating in the tank after the water level has risen above the frame. The foil has floated free of the substrate. The foil is then moved gently until one edge lies above the frame. The water is then moved slowly out of the tank.

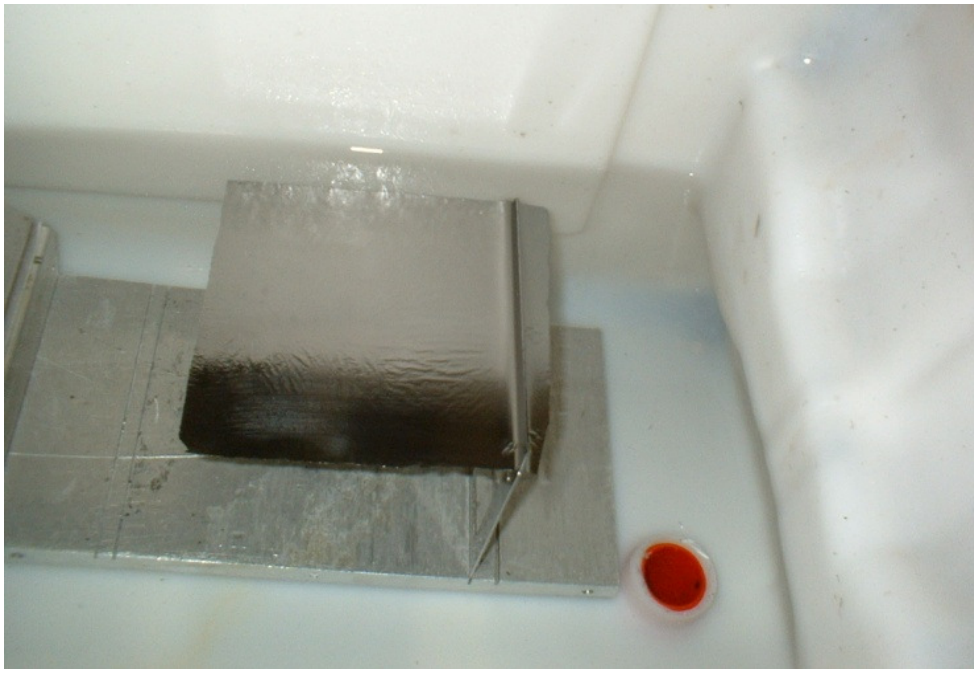

Figure B:3. The carbon foil, its edge resting on top of the frame, as water drained out of the tank slowly.

Figure B:4. The carbon foil fully mounted on a frame.

APPENDIX C

Derivations of some of the useful equations for recoil detector parameters

For particle of mass *m*, with charge *q* and speed *v* moving perpendicular to uniform magnetic field *B*, on a circular orbit with radius of curvature ρ, the Lorenz force is equal to centrifugal force:

$$qvB = \frac{mv^2}{\rho}$$

$$\rho = \frac{mv}{qB}$$

$$substituting\ m\ from\ p = mv$$

$$p = qB\rho \qquad \text{(C:0:1)}$$

The equation relating the total energy E of a particle and the momentum *p* of a particle is:

$$E^2 = p^2c^2 + mc^2 \qquad \text{(C:0:2)}$$

where $E = E_0 + E_k$ and $E = mc^2$

E_0 is the rest energy of a particle

E_k is the kinetic energy of a particle

c is the speed of light

$$\therefore B\rho = \frac{c^2 mv}{c^2 q}$$

$$B\rho = \frac{E\beta}{qc} \qquad \text{(C:0:3)}$$

where $\beta = v/c$ and with $\gamma = E/E_0$ where $\gamma = \frac{1}{\sqrt{1-\beta^2}}$

$$B\rho = \frac{E\sqrt{1-\gamma^2}}{qc\gamma}$$

$$Bp = \frac{\sqrt{E^2 - E_0^2}}{qc}$$

$$B\rho = \frac{\sqrt{E_k^2 + 2E_0E_k}}{qc}$$

$$B\rho = \frac{\sqrt{E_k^2 + 2E_0E_k}}{Qc} \qquad \text{(C:0:4)}$$

If a voltage is applied in an electron with charge e, the work done by the voltage is:

$$W = eEs$$

$$W = \frac{eVs}{s}$$

$$W = eV$$

$$W = \Delta U = \Delta K$$

$$\therefore \frac{1m_e v^2}{2} = eV$$

$$v = \sqrt{\frac{2eV}{m_e}}$$

$$v = 592.694 \times 10^3 \sqrt{V}\ (m/s)$$

$$v = 592.694 \times 10^3 \times 10^2 \times 10^{-9} \sqrt{V}\ (cm/ns)$$

$$v = 59.2694 \times 10^{-3} \sqrt{V}\ (cm/ns) \qquad \text{(C:0:5)}$$

The radius of curvature *(r)* in a uniform magnetic field (*B*):

$$F_B = F_C$$

$$ev \times B = \frac{mv^2}{r}$$

$$evB = \frac{mv^2}{r}$$

$$eB = \frac{mv}{r}$$

$$rB = \frac{mv}{e}$$

$$rB = 3.374 \times 10^{-6} \sqrt{V}\ (\text{from (9) in (Tm)})$$

$$\therefore rB = 3.374\sqrt{V}\ (\text{in(G cm)})$$

$$\therefore r = \frac{3.374\sqrt{V}}{B} \qquad \text{(C:0:6)}$$

Time-of-flight (t) over distance (d) in field-free region after acceleration by a voltage (V):

$$v = 59.2694\times10^{-3}\sqrt{V}$$
$$t = \frac{d}{v}$$
$$t = \frac{16.87d}{\sqrt{V}} \qquad \text{(C:0:7)}$$

Time-of-flight (t) for 180º bend:

$$v = 59.2694\times10^{-3}\sqrt{V}$$
$$d = \pi r = \pi\times\frac{3.374\sqrt{V}}{B} = \frac{10.5997\sqrt{V}}{B}$$
$$\therefore t = \frac{10.5997\sqrt{V}}{B}\times\frac{1}{59.2694\times10^{-3}\sqrt{V}}$$
$$t = \frac{178.849}{B}$$
$$t = \frac{179}{B} \qquad \text{(C:0:8)}$$

Time-of-flight when starting from rest in a uniform electric field ($E=V/d$):

$$F = qE$$
$$F = eE$$
$$m_e a = eE$$
$$a = \frac{eE}{m_e}$$
$$d = \frac{1at^2}{2}$$
$$t = \sqrt{\frac{2d}{a}}$$
$$t = \sqrt{\frac{2d^2 m_e}{eV}} = \sqrt{\frac{2\times9.11\times10^{-31}}{1.6\times10^{-19}}}\frac{d}{\sqrt{V}}$$
$$t = 33.7\frac{d}{\sqrt{V}} \qquad \text{(C:0:9)}$$

APPENDIX D

The vector field calculations for the recoil detector

A much improved understanding of the magnetic field distribution inside the recoil detector was obtained with numerical field analysis in 3D, using the program Vector Fields [Vec_1]. The field homogeneity could be much improved by minor changes in the geometry of the detector, as mentioned in section 4.1.5. Although perfect homogeneity was not achieved, the field around the centre of the chamber was about 22 G. In addition to the results shown in Figure 4:16, this section gives some of the results obtained by changing some parameters. Figure D:1 to D:5 gives the calculated field homogeneity on selected planes in the recoil detector chamber, without the addition of any shimming.

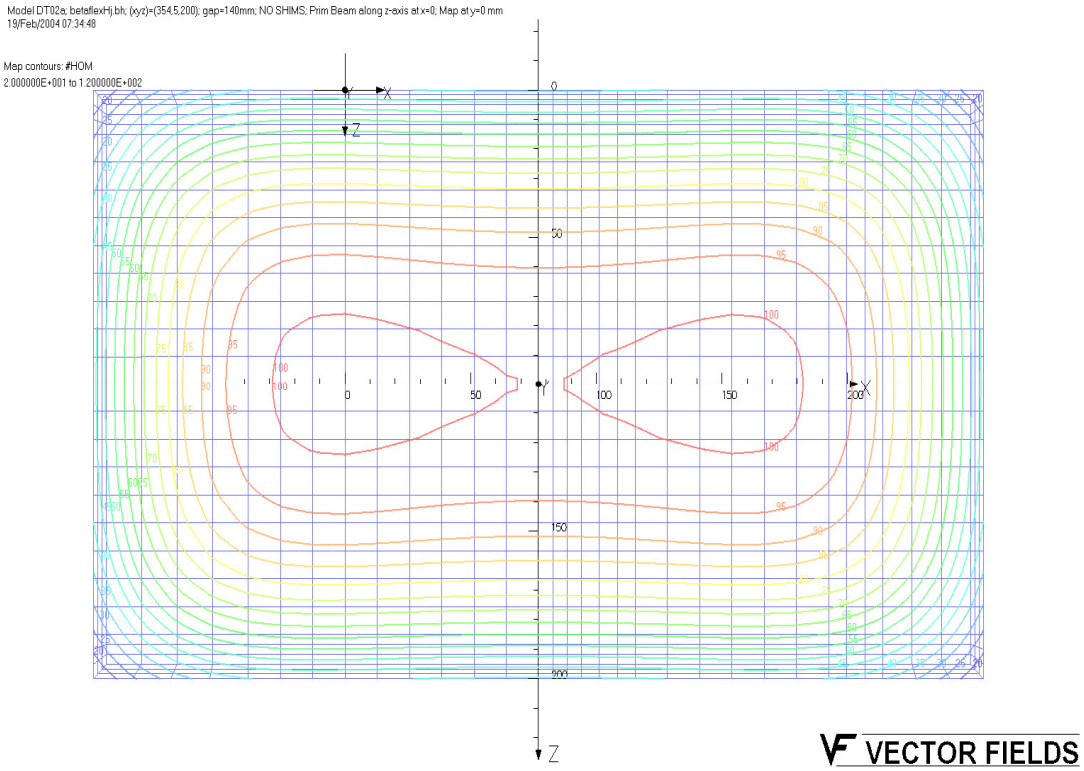

Figure D:1. A contour map shows the field homogeniety on the median plane (y=0 mm) of the recoil detector without any shimming of the magnetic materials, and expressed as a percentage of the magenetic field (22 G) at the center of the displayed map and with a step interval of 5%.

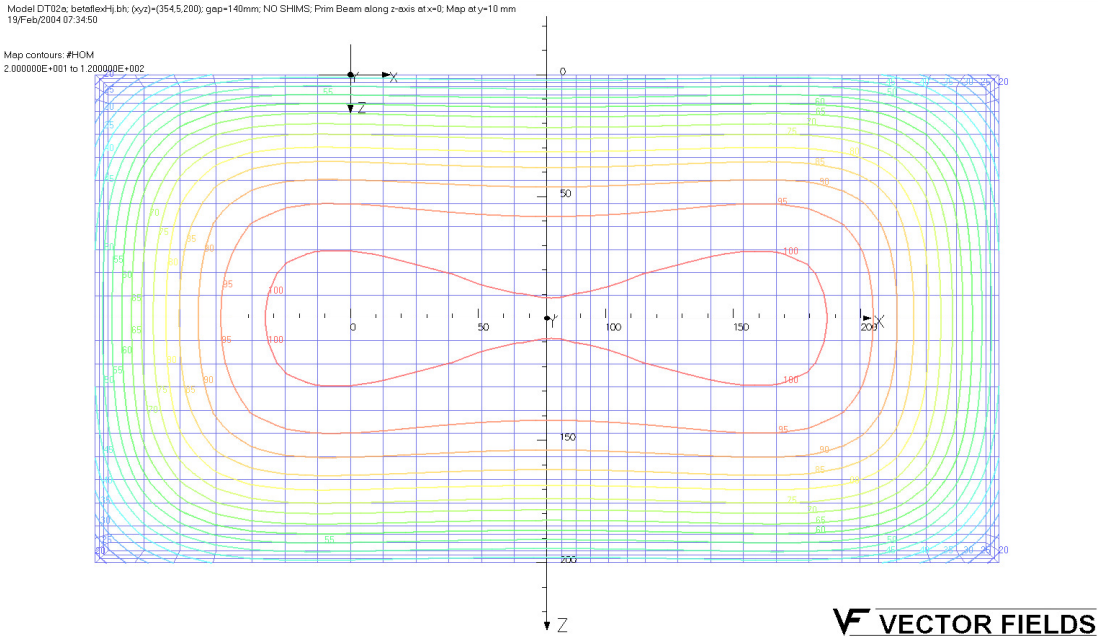

Figure D:2. A contour map shows the field homogeniety on the median plane (y=10 mm above the median plane) of the recoil detector without any shimming of the magnetic materials, and expressed as a percentage of the magnetic field (22 G) at the center of the displayed map and with a step interval of 5%.

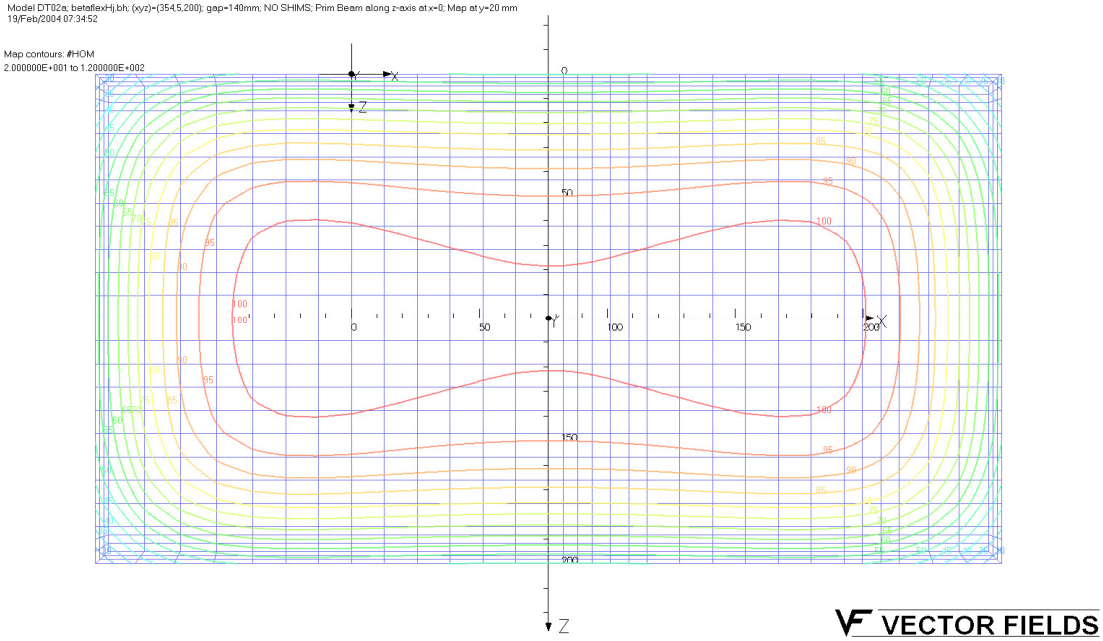

Figure D:3. A contour map shows the field homogeniety on the median plane (y=20 mm above the median plane) of the recoil detector without any shimming of the magnetic materials, and expressed as a percentage of the magnetic field (22 G) at the center of the displayed map and with a step interval of 5%.

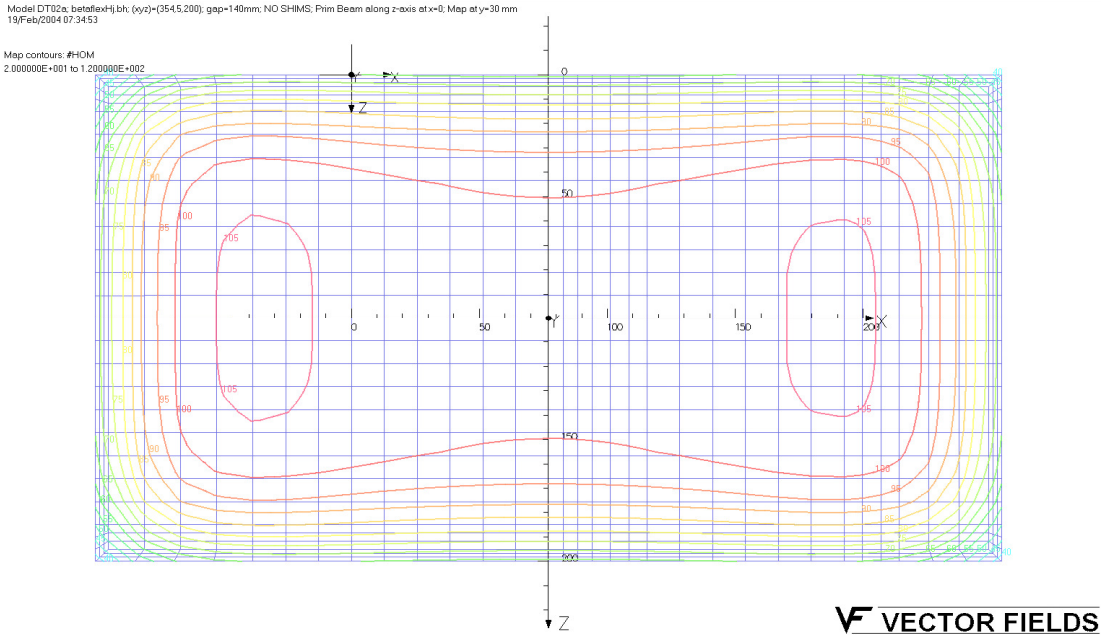

Figure D:4. A contour map shows the field homogeniety on the median plane (y=30 mm above the median plane) of the recoil detector without any shimming of the magnetic materials, and expressed as a percentage of the magnetic field (22 G) at the center of the displayed map and with a step interval of 5%.

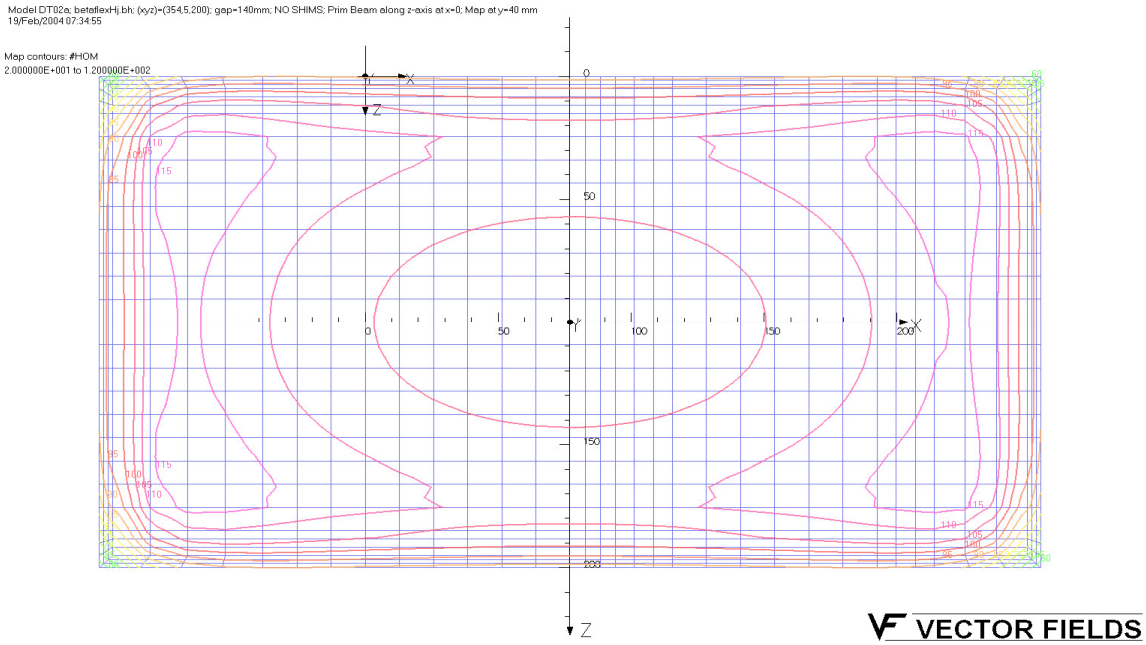

Figure D:5. A contour map shows the field homogeniety on the median plane (y=40 mm above the median plane) of the recoil detector without any shimming of the magnetic materials, and expressed as a percentage of the magnetic field (22 G) at the center of the displayed map and with a step interval of 5%.

APPENDIX D

The Figure D:6 to D:10 show calculated particle tracks in the detector, to illustrate the effect of the shimming of the magnetic material and to simulate expected outcomes when the incoming primary beam enters the detector chamber either slightly displaced or skew. Figure D:11 to D:13 show the wire grid and its calculated deflections on the secondary electrons from the target.

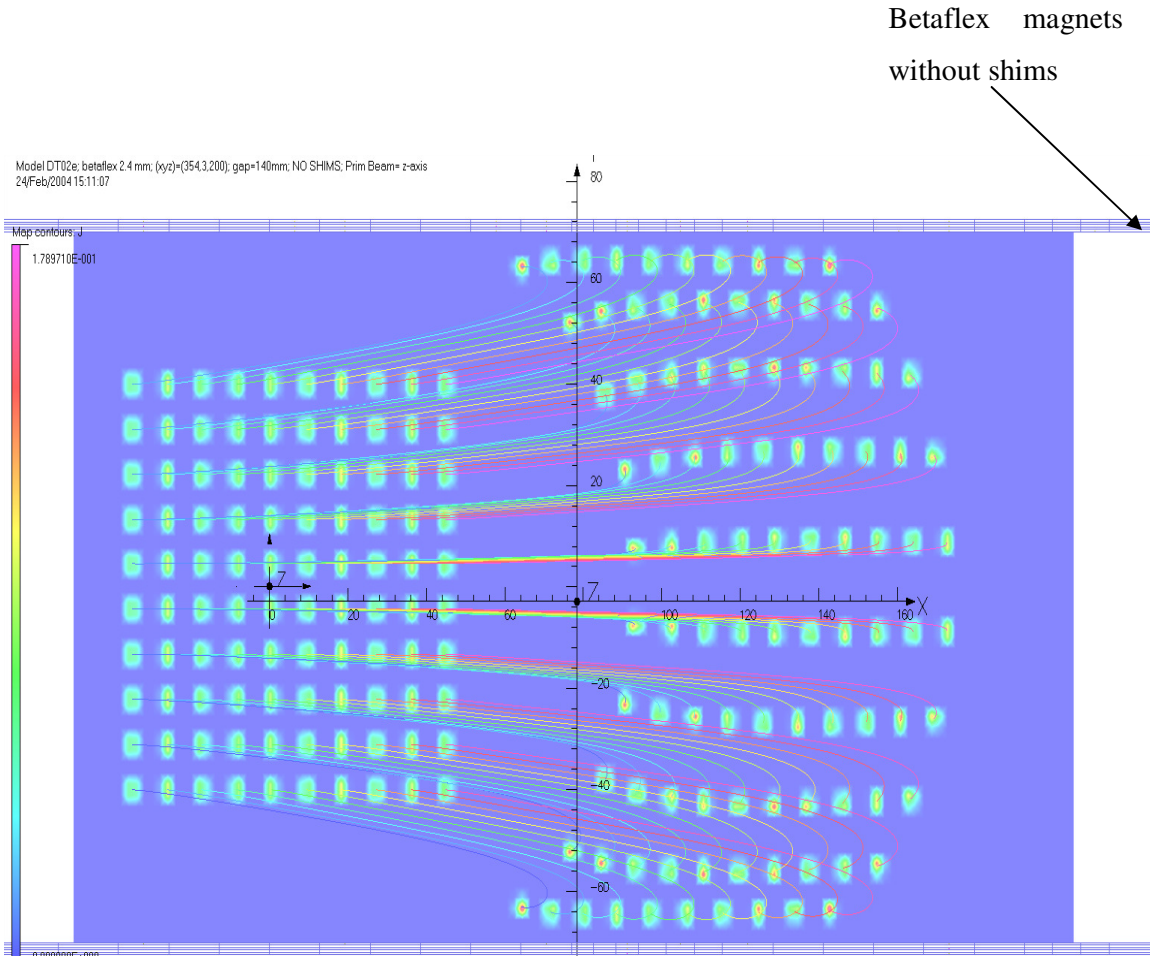

Figure D:6. The calculated particle tracks in the detector chamber with no shims, selected to start evenly-spaced from 80×80 *mm grid in the target plane (on the left side of the picture. The initial direction of the 100 particles (electrons) are all perpendicular towards the reader and then bend back to the same plane to the form an image of the initial grid (on the right hand side of the picture). The deformation in the image is a direct result of the inhomogeneity of the magnetic field. The coloured "spots" where each particle track interact with the target planes are selected. Statistical probabilty enhancements in order to simulate a more realistic nature of particle beams.*

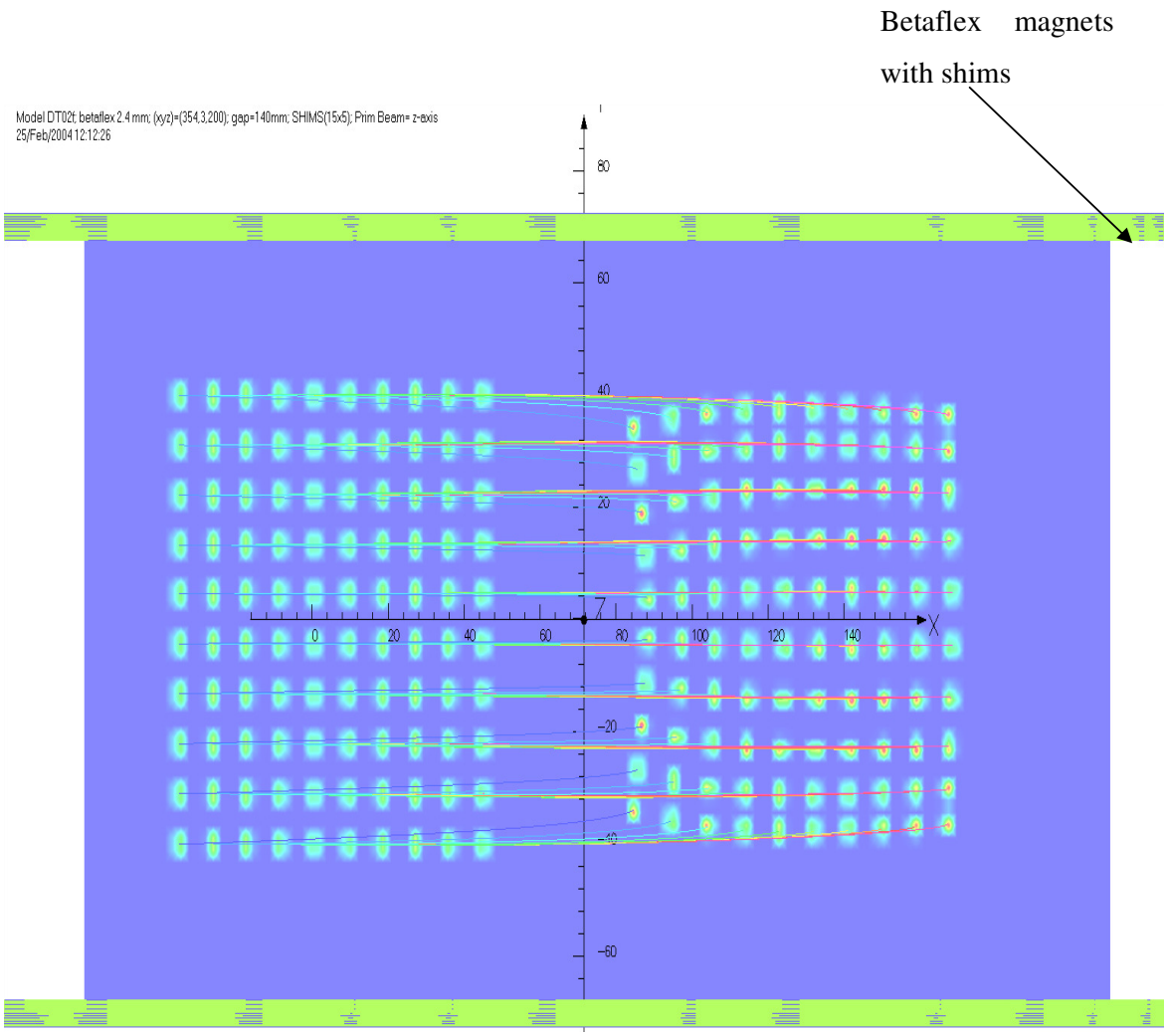

Figure D:7. The calculated particle tracks in the detector chamber with two 15×5 *mm shims, selected to start evenly-spaced from* 80×80 *mm grid in the target plane (on the left side of the picture. The initial direction of the 100 particles (electrons) are all perpendicular towards the reader and then bend back to the same plane to the form an improved image of the initial grid (on the right hand side of the picture).*

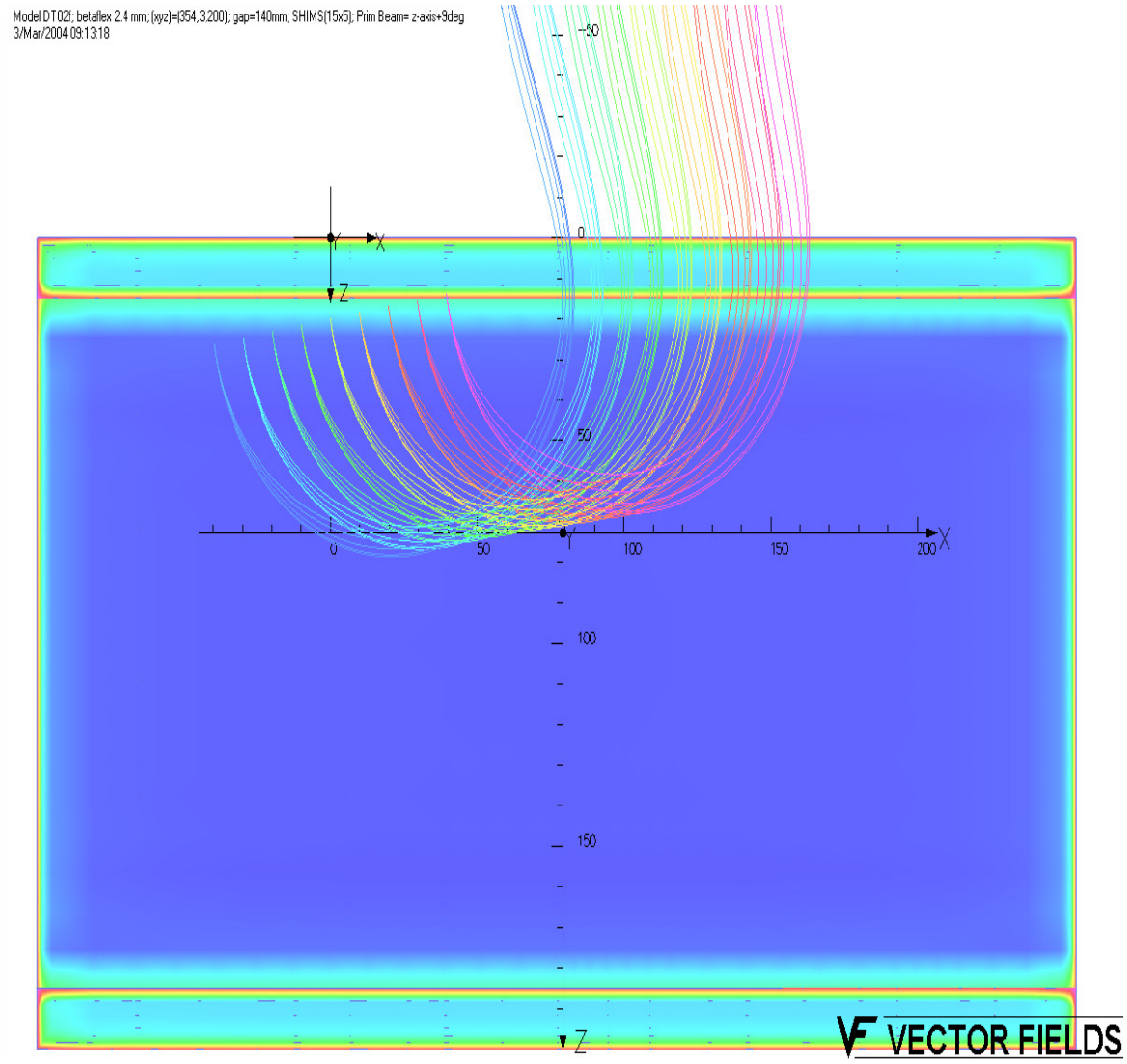

Figure D:8. Top view of the calculated particle tracks, all having an initial angle of 9º with respect to the normal to the target plane. The calculation is with two 15×5 *mm shims.*

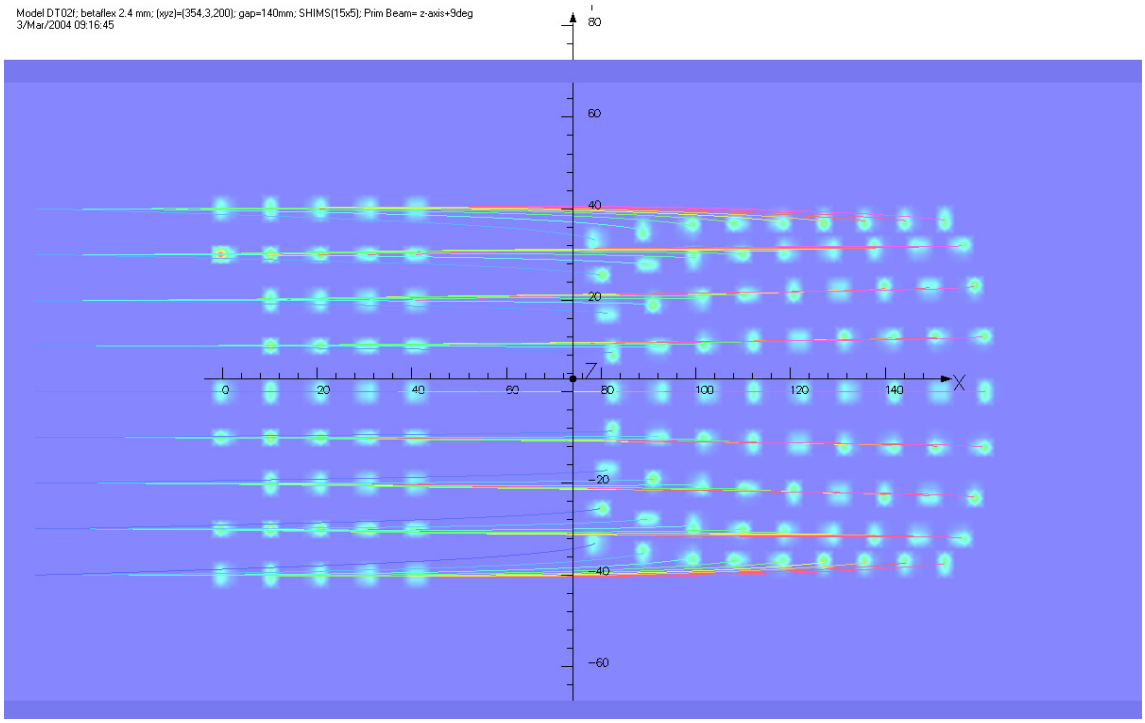

Figure D:9. Side view of the calculated particle tracks, all having an initial angle of 9º with respect to the normal to the target plane. The calculation is with two 15×5 *mm shims.*

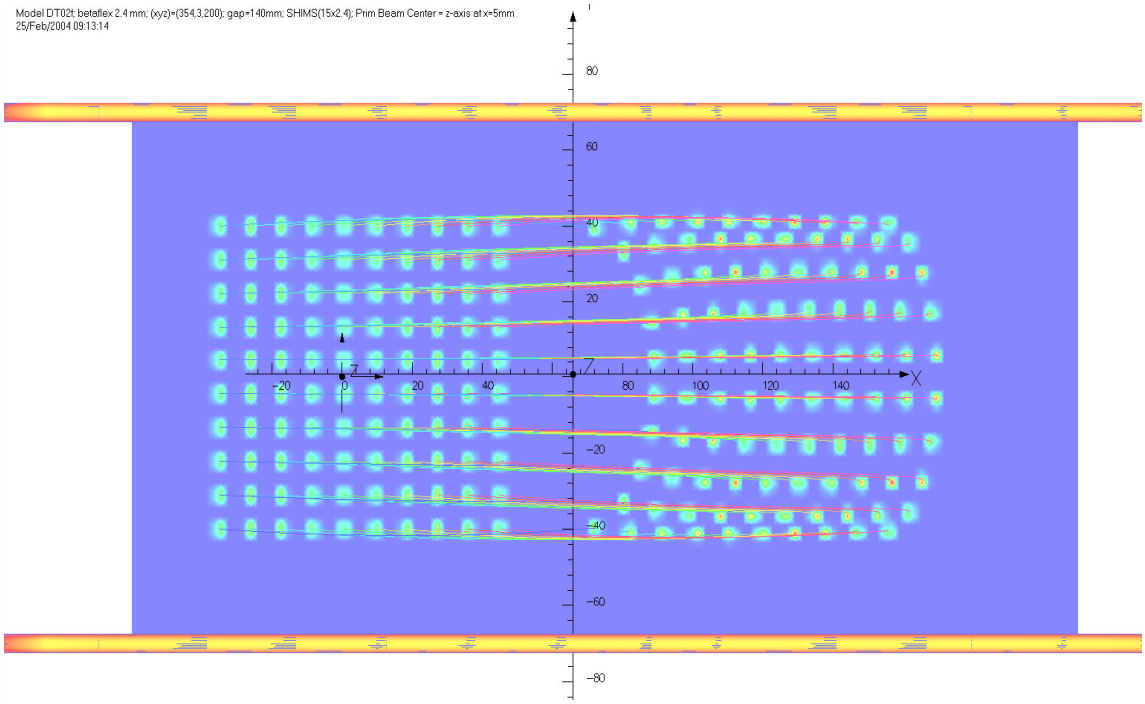

Figure D:10. Side view of the calculated particle tracks, all particles are 5 mm off from the x-axis. The calculation is with two 15×2.4 *mm shims.*

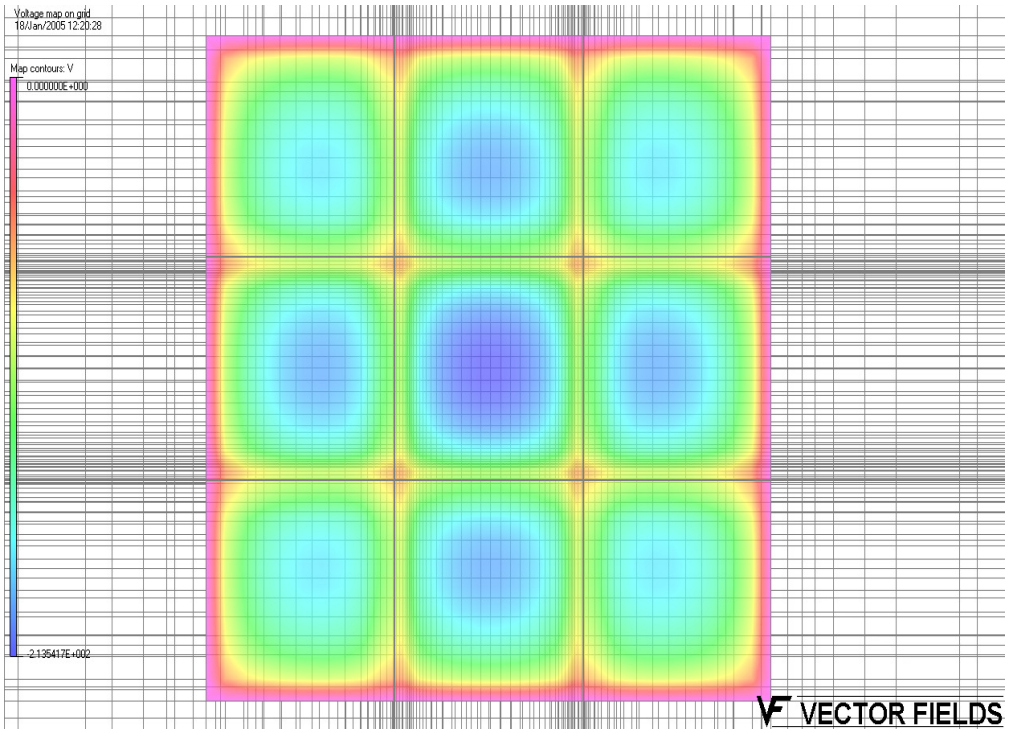

Figure D:11. Voltage map on the recoil detector grid 1.

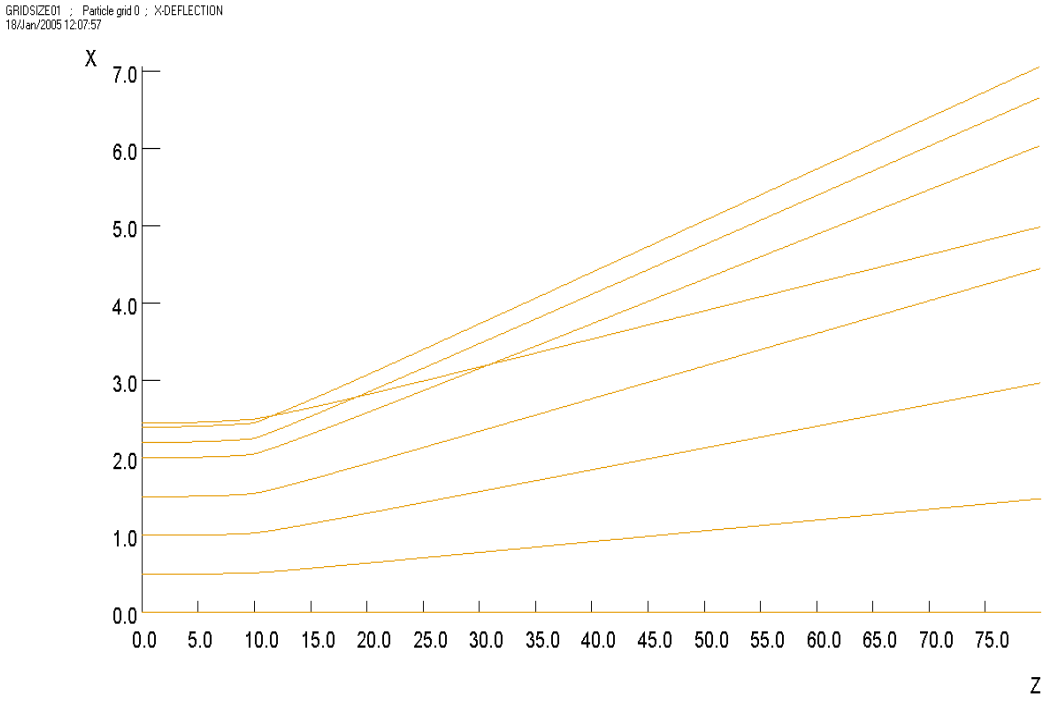

Figure D:12. Particle deflected in the grid in x-direction.

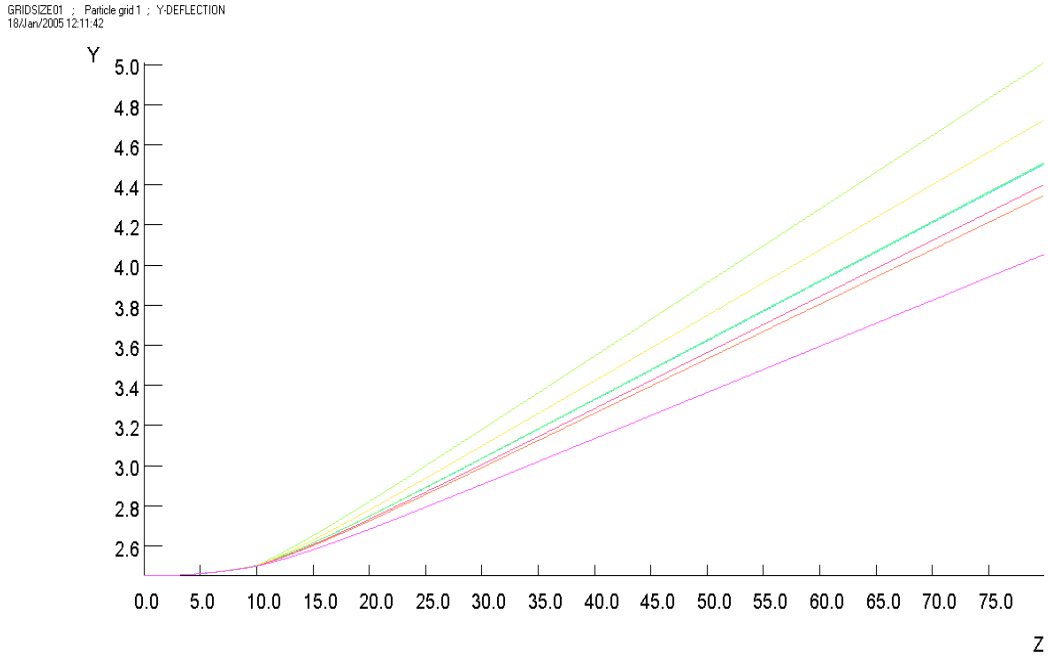

Figure D:13. Particle deflected in the grid in the y-direction.

REFERENCES

[Abu02] K. Abu Saleem, PhD thesis, Illionois Institute of Technology (2002)

[Ack93] B. Ackermann et al., Nucl. Phys. A 559, 61 (1993)

[Ahm93] I. Ahmad and P. Butler Ann. Rev. Nucl. Part. Sci 43, 71-116 (1993)

[Alb91] D. Alber et al., Z. Phys. A339, 225 (1991)

[Ald56] K. Alder, A. Bohr, T. Huus, B. R. Mottelson and A. Winther, Rev. Mod. Phys. 28, 432 (1956)

[Azj90] F. Azjenberg-Selove, Nucl. Phys. A506, 1 (1990)

[Bar10a] R. A. Bark et al., Phys. Rev. Lett. 104, 022501 (2010)

[Bar10b] R. A. Bark et al., Nuclear Structure Conference, Oral presentation, Lawrence Berkeley National Laboratory, (2010)

[Baz02] D. Bazin, M. Lewitowicz, O. Sorlin and O. Tarasov, Nucl. Instr. and Meth. A 482, 314 (2002), http://dnr080.jinr.ru/lise and http://www.nscl.msu.edu/lise

[Bec94] J. A. Becker, K. H. Maier, P. Fallon, A. O. Macchiavelii, J. A. Cizewski, C. J. Lister, E. F. Moore, A Recoil detector Fragments filter for GAMMASPHERE, (1994)

[Bel60] R. E. Bell, S. Bjørnholm and J. C. Severiens, Mat. Fys. Medd. K. Dan. Vidensk. Selk. 32, 12 (1960)

[Ben79] R. Bentsson and S. Frauendorf Nucl. Phys. A327, 139 (1979)

[Ben87] M. A. Bentley et al., Phys. Rev. Lett. 59, 2141 (1987)

[Ber89] J. F. Berger, M. Girod, and D. Gonny, Nucl. Phys. A502, 85c (1989)

[Ber95] L. A. Bernstein et al., Phys. Rev C52, 621 (1995)

[Bla52] J. M. Blatt and V. F. Wiesskof, *Theoretical Nuclear Physics*, John Wiley and Sons Inc., New York (1952)

[Blo75] J. Blons et al., Phys. Rev. Lett 35, 1749 (1975)

[Blo88] J. Blons et al., Nucl. Phys. A477, 231 (1988)

[Blo89] J. Blons at al., Nucl. Phys.A502, 121c (1989)

[Boh36] N. Bohr, Nature 137, 344 (1936)

[Boh57] A. Bohr and B. R. Mottelson, Nucl. Phys. 4, 529 (1957)

[Boh58] A. Bohr, B. R. Mottelson, Nucl. Phys. 9, 687 (1958)

[Boh75] A. Bohr and B. R Mottleson, *Nuclear Structure Volume II: Nuclear Deformations*, W. A. Benjamin Inc., New York (1975).

[Bon05] D. Bonatsos, D. Lenis, N. Minkov, D. Petrellis, and P. Yotov, Phys. Rev. C71, 064309 (2005)

[Bon83] W. Bonin et al., Z. Phys. 310, 249 (1983)

[Bre94] M. Brenner, Z. Phys. A349, 233 (1994)

[Bri61] H. C. Britt and A. R. Quinton Phys. Rev. C124, 877 (1961)

[Bro06] E. Browne and J. K. Tuli, Nuclear Data Sheets 107, 2649 (2006)

[Bru54] H. Bruining, Secondary Electron Emission, Pergamon Press, New York, (1954)

[Bur63] W. E. Burcham, *An Introduction to Nuclear Physics, Longmans 1st Publication* (1963)

[Bur79] W. E. Burcham, Elements of Nuclear Physics, Longman (1979)

[But91] P. A. Butler and W. Nazarewicz, Nucl. Phys. A 533, 249 (1991)

[But96] P. A. Butler and W. Nazarewicz, Rev. Mod. Phys. 68, 349 (1996)

[Cle73] H. G. Clerc, H. J. Gehrhardt, L. Richter and K. H. Schmidt Nucl. Instr. and Meth. 325 (1973)

[Coc96] J. F. C. Cocks et el., Acta Physica Polonica B27, 71 (1996)

[Coc97] J. F. C. Cocks et al., Phys. Rev. Lett. 78, 2920 (1997)

[Coc99] J. F. C. Cocks et al., Nucl. Phys. A 645, 61 (1999)

[Cre06] J. Cresswell and J. Sampson, http://nnst.dl.ac.uk/MIDAS/manual/MTsort/edoc033 (2006)

[Csi09] L. Csige, M. Csatlós, T. Faestermann, Z. Gácsi, J. Gulyás, D. Habs, R. Hertenberger, A. Krasznahorkay, R. Lutter, H. J. Maier, P. G. Thirolf, and H. F. Wirth , Phys. Rev. C 80, 011301 (R) (2009)

[Ćwi94] S. Ćwiok et al., Phys. Lett. B 322, 304 (1994)

[Dah88] M. Dahlinger et al., Nucl. Phys. A484, 337, (1988)

[DeS74] A. De Shalit and H. Feshbach, *Theoretical Nuclear Physics Volume 1: Nuclear Structure*, John Wiley and Sons Inc., New York (1974)

[Dud02] J. Dudek et al., Phys. Rev. Lett. 88, No.25, 252502 (2002)

[Dud06] J. Dudek, D. Curein, N. Dubray, J. Dobaczewski, V. Pangon, P. Olbratowski, and N. Schunck, Phys. Rev. Lett. 97, 072501 (2006)

[Dud07] J. Dudek et al., Phys. Pol. B38, 1389 (2007)

[Dud08] J. Dudek et al., private communications, (2008)

[Egi90] J. L. Egido and L. M. Robledo, Nucl. Phys. A518, 475 (1990)

[Egi92] J. L. Egido and L. M. Robledo, in Future Directions in Nuclear Physics with 4π Gamma Detection Systems of the New Generation-Strasbourg, 1991, AIP Conf. Proc. No.259, edited by J. Dudek and B. Haas (AIP, New York, p259 (1992)

[Eji89] H. Ejiri and M. J. A. de Voigt, *Gamma–ray and Electron Spectroscopy in Nuclear Physics*, Clarendon Press, Oxford (1989).

[Fra08] S. Frauendorf, Phys. Rev. C77, 021304 (2008)

[Fra81] S. Frauendorf. Physica Scripta 24, 349 (1981)

[Gal93] A. Galindo-Uribarri *et al.,* Phys. Rev. Lett. **71**, 231 (1993)

[Gar98] P. E. Garrett et al., Phys. Rev. C58 3734 (1998)

[Gav80] A. Gavron, Phys. Rev. C21, 230 (1980)

[Gav93] A. Gavron, Computational Nuclear Physics 2, Nuclear Reactions, Spinger-Verlag New York, Inc, 108 (1993)

[Gre98] P. T. Greenlees et al., J. Phys. G 24, L63 (1998)

[Gre99] P. T. Greenlees, PhD thesis, university of Liverpool, unpublished, 1999

[Hae77] D. R. Haenni et al., Phys. Rev. C16, 120 (1977)

[Haf38] L. R. Hafstad and E. Teller Phys. Rev. Lett. 54, 681 (1938)

[Ham85] I. Hamamoto, Treatise on Heay-Ion Science Vol.3, Plenum Press, New York, p.313-393, and reference therein (1985)

[Has92] D. Hasselkeamp. H. Rothard, K. O. Groeneveld, J. Kemmler, P. Varga, H. Winter, Particle Induced Electron Emission II, Springer Verlag, 123 97-145 (1992)

[Hee93] J. Heese et al., Phys. Lett. B302, 390 (1993)

[Hib93] I. M. Hibbert, PhD thesis, University of Manchester (1993)

[Jen10] M. Jentschel, W. Urban, J. Krempel, D. Tonev, J. Dudek, D. Curien, B. Lauss, G. de Angelis, and P. Petkov, Phys. Rev. Lett. 104, 222502 (2010)

[Jen95] H. J. Jensen, PhD thesis, University of Copenhagen, unpublished, 1995

[Jon95] P. M. Jones, L. Wei, F. A. Beck, P. A. Butler, T. Byrski, G. Duchêne, G. de France, F. Hannachi, G. D. Jones and B. Kharraja, Nucl. Instr. and Meth. in Phy. Res. A362, 556 (1995)

[Koc70] L. Kocbach and P. Vogel, Phys. Lett. B 32, 434 (1970)

[Kra88] K. S. Krane, Introductory Nuclear Physics, John Wiley and Sons, New York (1988)

[Kra98] A. Krasznahorkay et al., Phys. Rev. Lett. 80, 2073 (1998)

[Laf95] D. R. Lafosse et al., Phys. Rev. Lett. 74, 5186 (1995)

[Laf96] D. R. Lafosse et al., Phys. Rev. C54, 1585 (1996)

[Lam01] M. J. Lamey, Masters Thesis, Simon Fraser University, (2001)

[Lan95] G. J. Lane et al., Nucl. Phys. A586, 316 (1995)

[Law08] E. A. Lawrie et al., PR45 Experimental data (2008)

[Law09] E. A. Lawrie et al., PR60 Experimental data (2009)

[Lei95] M. Leino et al., Nucl. Instr. and Meth. B99, 653 (1995)

[Lei97] M. Leino, Nucl. Instr. and Meth. B99, 320 (1997)

[Lev96] A. I. Levon et al., Nucl. Phys. A598, 11 (1996)

[Lie09] E. O. Lieder et al., Nucl. Instr. and Meth. 607, 591 (2009)

[Lie78] R. M. Lieder, A. Neskakis, M. Muller-Veggian, Y. Gono, C. Mayer-Boricke, S. Beshai, K. Fransson, C. G. Linden, T. Lindbland, Nucl. Phys. A299, 255 (1978)

[Lie97] R. M. Lieder, in Experimental Techniques in Nuclear Physics, ed. D.N. Poenaru and W. Greiner, Walter de Gruyter, Berlin, p 137 (1997)

[Lob70] K. E. Lobner et al., Nuclear Data tables A7 (1970)

[Mab03] G. K. Mabala, PhD thesis, University of Cape Town unpublished, (2003)

[Met80] V. Metag, et al., Phys. Rep. 65, 1 (1980)

[Möl73] P. Möller and J.R. Nix, in Physic and Chemistry of Fission (IAEA, Vienna, 1973) Vol. 1, p.103

[Mos91] M. Moszyński and G. Duchêne et al., Nucl. Instr. and Meth. A308, 557 (1991)

[Mot60] B. R. Mottelson and J.G. Valatin, Phys. Rev. Lett. 5, 511 (1960)

[Mul09] S. Mullins, iThemba LABS, Project Advisory proposal, June (2009)

[Nak95] T. Nakatsukasa et al., Acta Physica Polonica B, 27, 59 (1995)

[Naz84] W. Nazarewicz, P. Olanders, I. Ragnasson, J. Dudek, G.A. Leander, P. Möller and E. Ruchowska, Nucl. Phys. A429 269 (1984)

[New58] J. O. Newton at al., Nucl. Phys. 5, 218 (1958)

[New98] R. T. Newman et al., Proceeding of Balkan School on Nucl. Phys, September1-10, 1998, Istanbul-TURKEY, Balkan Physics letters, 182 (1998)

[Nil95] S. G. Nilsson and I. Ragnarsson, "Shapes and Shells in Nuclear Structure", p60 (1995)

[Nis80] T. Nishi et al., RCNP Osaka Ann. Rep. p.119 (1980)

[Nol94] P. J. Nolan, G.A. Beck and D.B. Fossen, Ann. Rev. Nucl. Part. Sci., Vol. 45, 561-607 (1994)

[Nts07] S. S. Ntshangase and R.A. Bark, iThemba LABS, Project Advisory Committee report, June (2007)

[Ort_1] www-esd.fnal.gov/esd/catalog

[Pas71] V. V. Paskevich, Nucl. Phys. A169, 275 (1971)

[Pau03] E. S. Paul, Postgraduate Lectures, *Liverpool Nuclear Physics Group*. (2003)

[Pro95] V. M. Prozesky at al., Nucl. Instr. and Meth. B104, 36 (1995)

[Rad95] D. C Radford. Nucl. Instr. and Meth. A361, 297 (1995). *See also http://radware.phy.ornl.gov/*

[Reg03] P. Regan, Post Graduate Nuclear Experimental Techniques (4NET) Course Notes, University of Surrey, (2003)

[Rin80] P. Ring and P. Schuck, *The Nuclear Many-Body Problem, Springer-Verlag*, New York, (1980).

[Rob79] D. Robson et al., Phys. Rev. Lett. 42, no. 2, 876 (1979)

[Rut94] K. Rutz et al., Nucl. Phys. A590, 680 (1994)

[Sav96] H. Savajols et al., Phys. Rev. Lett. 76, 4480 (1996)

[Sch09] J. F. Sharpey-Schafer et al., PR135 Experiment data (2009)

[Sch80] J. Schou, Phys. Rev. B22., no.5, 2141 (1980)

[Sch83] D. Schwalm, Nucl. Phys. A396, 339c (1983)

[Shn02] T. M. Shneidman et al., Phys. Lett. B526, 322 (2002)

[Sli65] L. A. Sliv and I. M. Band, in Alpha-, Beta- and Gamma ray Spectroscopy ed. K. Siegbahn (North-Holland Publ. Co., Amsterdam, (1965) p. 1639

[Sri06] http://www.Srim.org, 2006

[Ste55] F. S. Stephens, F. Asaro and I. Perlman, "Low-lying 1- states in even-even Nuclei", Phys. Rev. 100, 1543 (1955)

[Str56] V. M. Strutinsky, Atom. Energyia 4, 150 (1956)

[Suj77] Z. Sujkowski et al.,Nucl. Phys. A 291, 365 (1977)

[Sur03] K. Surendra et al., J. Phys. G: Nucl. Part. Phys. 29, 1011-1022 (2003)

[Tec94] Technical information, MCP Assembly, Hamamatsu, May (1994)

[Thi02] P. G. Thirolf, D. Habs, Prog. Part. Nucl. Phys. 49, 245 (2002)

[Tjø85] P. O. Tjøm, R.M. Diamond, J. C. Bacelar, E. M. Beck, M. A. Deleplanque, J. E. Draper and F. S. Stephens, Phys. Rev. Lett. 55, 2405 (1985)

[Tsv02] A. Tsvetkov, J. Kvasil, and R. G. Nazimitdinov, J. Phys. G 28, 2187 (2002)

[Twi86] P. Twin et al., Phys. Rev. Lett. 57, 811 (1986)

[Vec_1] www. Vectorfields.co.uk, info@vectorfields.com

[Ven85] W. Z. Venema et al., Phys. Lett. B156, 163 (1985)

[Vog76] P. Vogel, Phys. Lett.B60, 431 (1976)

[Wad02] R. Wadsworth and P. J. Nolan, The influence of microstructure on rotational motion in nuclei, Rep. Prog. Phys. 65, 1079-1118 (2002)

[War83] D. Ward et al., Nucl. Phys. A 406, 591 (1983)

[War96] D. Ward et al., Nucl. Phys. A 600, 88 (1996)

[Whe39] J. A. Wheeler and N. Bohr Phys. Rev. 56, 426-450 (1939)

[Wie99] I. Wiedenhöver et al., Phys. Rev. Lett 102, 122501 (2009)

[Wol93] H. J. Wollersheim et al., Nucl. Phys. A 556, 261 (1993)

[Woo92] J. L. Wood et al., Phys. Rep. 215, p101, (1992)

[Wur99] M. Wurkner et al., Acta, Phys. Pol. B30, 1313 (1999)

[Zeb77] A. M. Zebelman, W. G. Meyer, K. Halbach, A. M. Poskanzer, R. G. Sextro, G. Gabor, and D. A. Landis, Nucl. Instr. and Meth.141, 439 (1977)

[Zey87] P. Zeyen et al., Z. Phys. A 328, 399 (1987)

[Zol75] D. R. Zolnowski et al., Phys. Lett. B 55, 453 (1975)